Università degli Studi di Firenze
European Laboratory of Non-Linear Spectroscopy (LENS)
International Doctorate in Atomic and Molecular Photonics

Towards a Dual-Species Atom Interferometer with Cadmium and Strontium

Candidate
Satvika Bandarupally

Satvika

Supervisor
Prof. Nicola Poli

Ph.D. Coordinator
Prof. Diederik Wiersma

ciclo xxxv, 2019-2022

Università degli Studi di Firenze, European Laboratory of Non-Linear Spectroscopy (LENS)
January 2023

Thesis submitted in partial fulfillment of the requirements for the degree of Doctor of Philosophy in International Doctorate in Atomic and Molecular Photonics.

Abstract

This thesis discusses the work done towards building a novel dual-species atom interferometer with ultra-cold cadmium and strontium at the Department of Physics and Astronomy, University of Florence, with special focus on the required laser systems and on the design of the dual-species vacuum chamber, which is thoroughly numerically simulated. Atom interferometry experiments based on alkaline-earth and alkaline-earth-like elements allow for precision measurements using their narrow-linewidth transitions. Furthermore, interferometric schemes such as multi-photon Bragg interferometry and emerging single-photon (clock) atom interferometry can be studied with both cadmium and strontium. Using these features, the dual-species interferometer provides the possibility to search for violations of the weak equivalence principle and to observe the effect of time dilation on quantum superpositions of clocks. In order to perform these experiments, the laser systems to access the singlet and triplet states of cadmium and strontium are developed and tested in order to be able to perform laser cooling, trapping and also for all the possible interferometric schemes. In the case of cadmium, all of these transitions lie in the ultraviolet region and this work also delves into the challenges in the production of the necessary high-power and continuous-wave light at 326 nm, 332 nm and especially the highly challenging deep ultraviolet light at 229 nm. In the cases of 326 nm and 332 nm, the light produced is at the Watt-level with sub-kHz linewidths. The developed laser sources are tested by performing spectroscopy on the novel atomic beam of cadmium, including making the first complete set of measurements of the isotopes shift of $^1S_0$ - $^1P_1$ transition at 229 nm. The measured properties of the developed laser sources are used to design and simulate a state-of-the-art apparatus for producing ultra-cold cadmium. This system is carefully designed to allow for direct loading of a magneto-optical trap on the narrow $^1S_0$ - $^3P_1$ of cadmium and is fully numerically simulated to validate and design the vacuum chamber. Finally, the full vacuum chamber of the cadmium-strontium apparatus is presented, including a calculation of a shifting lattice to launch these two atoms simultaneously in an atomic fountain.

Acknowledgements

The work presented in this thesis has been made possible with a contribution from lot of people. I would firstly like to thank Nicola Poli for giving me this opportunity to work and learn in an atomic physics lab as a PhD student, as I had long desired. His enthusiasm and optimism have always been crucial in moving forward against all the odds experienced, especially during the lockdown phase. His gregarious nature is not just limited to lab but also any outings or even during a table tennis match. Special thanks go to my colleague and dear friend, Jonathan Tinsley, with who I have been lucky to learn the critical skills and fundamental techniques required in experimental physics right from the very beginning of my course. There exists a calm and an unbiased approach in general matters like life, literature, music and lot more from Jonathan. His motivation and friendship has kept me going during my difficult times abroad. I thank Nicola and Jonathan for also carefully proofreading my thesis and giving it a good shape.

I would also like to thank Mauro Chiarotti mainly for his excellent work on the clock laser systems and also his timely help with the permanent magnetic measurements, along with being a helpful lab partner. Working with him is undoubtedly stimulating and progressing in nature, except, don't ask about his whereabouts! His quick-wit definitely leads to some chuckles in the lab and I cherish our time spent together at Trieste during our summer school. I would also like to thank Shamaila Manzoor mainly for the work done on the 326 nm laser system. Her constant perseverance and determination is certainly something to look up to. Another mention from the lab goes to Michele Sacco, thanks to him for all the work on electronics development required for our experiment. It is with him that I have learnt to make pasta from scratch like a true Italian, which I proudly treasure. During my program, I have also had an opportunity to work alongside few students at our lab for their diploma thesis. Important thanks go to Andrea Vignoli for his remarkable work done on characterizing the atomic oven. I thank Tommaso Rossetti for his work done in setting up the frequency doubling cavities for generating blue light and Gregorio Pekala for his early work on establishing the cadmium clock laser alongside Mauro. I would also thank Fabio Corti for his contribution to the electronics required for the experiments in the first year and also thank Leonardo Salvi for his help in the design of the electromagnetic coils. Particular thanks to Saïda Guellati-Khélifa for hosting me for my internship abroad at such short notice and for accepting to review my thesis. Special mention to the Department of Physics and Astronomy along with LENS for all the lab facilities provided with a notable thanks to the electrical and mechanical workshops for all their timely help.

Particular thanks to my parents, brother and my extended family back home including all the chirpy cousins who I am excited to meet soon along with Pranavi who has been a great friend right from my undergraduate times. I am especially grateful for my mother for her unwavering belief in me and her constant effort in checking upon me no matter what and my father for all the hard work he has put in over the years. Finally, I am forever indebted to have known and grown in the presence of the ones I have lost in the past three years, to all my lovely grandparents (ammama, bamma and tataya), my amazing fun uncle (Ramana mavaya) and to my first pet fish.

Contents

Chapter 1

Introduction

1.1 Matter-wave interferometry

About a century ago in 1924, Louis de Broglie introduced the concept of matter waves [1]. Interferometry with matter waves was first demonstrated with electrons in 1927 [2] and was also studied extensively with neutrons in the second half of the 20^{th} century [3]. A more recent and beautiful experimental validation of this theory came, however, from the interference of atoms, whose wavelengths are approximately four orders of magnitude lower than that of a visible photon. Atom interferometry continues to be a growing field with important applications to both fundamental and applied physics [4–6].

Norman Ramsey introduced the idea of performing interferometry by coherently controlling states of matter in 1950 [7]. This idea, where a superposition of the internal states of matter is generated by the interaction with light, forms the basis of atomic clocks. This later on was expanded to the superposition of external degrees of freedom, i.e., spatial superposition in separated interferometric arms. The initial illustration of the interference of such spatial superpositions was performed by Christian Bordé in 1984 [8]. It is this feature of interfering macroscopic spatial superpositions that distinguishes so-called atom interferometers from today's atomic clocks.

Further demonstrations of atom interferometry soon followed via diffraction gratings using Young's double-slit [9] and Mach-Zehnder schemes [10] and also by performing schemes with stimulated Raman transitions [11]. This last scheme relied on the then-new technique of laser cooling and trapping and atom interferometry has continued to accelerate alongside experimental techniques for producing ultra-cold and quantum degenerate samples of atoms. Nowadays, atom interferometric schemes are highly advanced and are employed routinely in a wide range of applications, for fields as diverse as macroscopic quantum mechanics [12] to civil engineering [13].

1.1.1 Light-pulse atom interferometry

This thesis focuses in particular on light-pulse atom interferometers. Such an atom interferometer is analogous to an optical interferometer where the splitting and recombination of the waves is done using temporally sequenced laser pulses instead of beam splitters and mirrors (Figure 1.1). This interferometric sequence exploits the wave nature of the employed quantum particles by using the laser beams to generate superpositions and to coherently change the centre-of-mass momentum and internal energy of the atoms. The atoms are firstly split into a superposition of momentum states and allowed free propagation over the required length scales and are then redirected towards each other before the waves finally recombine to form an interference pattern. Figure 1.1 shows the standard Mach-Zehnder interferometric scheme ($\pi/2$-π-$\pi/2$ laser pulse sequence) and the corresponding change in the expectation value of the atomic state population as a function of the acquired phase difference between the two arms.

A more detailed explanation of the differential phase acquired in the interferometer is given in Section 2.2, but in brief, the interference pattern which is formed depends on the physical environment the atoms pass through and on the direction of the interferometric beams. When the atoms interact with the interferometric laser beams, the phase of the lasers is imprinted onto the atoms. The interferometric lasers therefore serve as a phase reference for the atomic motion. As the interferometer is sensitive to positional changes on the scale $\sim 1/k_{eff}$, where k_{eff} is the effective wave vector of the laser beams, devices using optical pulses are therefore extremely sensitive to inertial forces and changes in inertial force.

For a terrestrial laboratory, atoms are affected by the gravitational pull of Earth and an atom interferometer is sensitive to this acceleration if the interferometric beams are aligned to the vertical (gravitational) axis. This allows a measurement of the acquired differential phase to be made, given as $\Delta\phi = k_{eff}gT^2$, where g is the gravitational acceleration and T is the time between the laser pulses interacting with the atoms. From this it is clear that maximizing the space-time area enclosed by the interferometer is crucial to accruing the largest possible differential phase. This is beneficial as for a given phase resolution of the measurement $\delta\phi$, device sensitivity ($\delta g/g = \delta\phi/\Delta\phi$) is improved with increasing $\Delta\phi$. In practice, this means that the momentum transferred to the atoms (i.e. k_{eff})

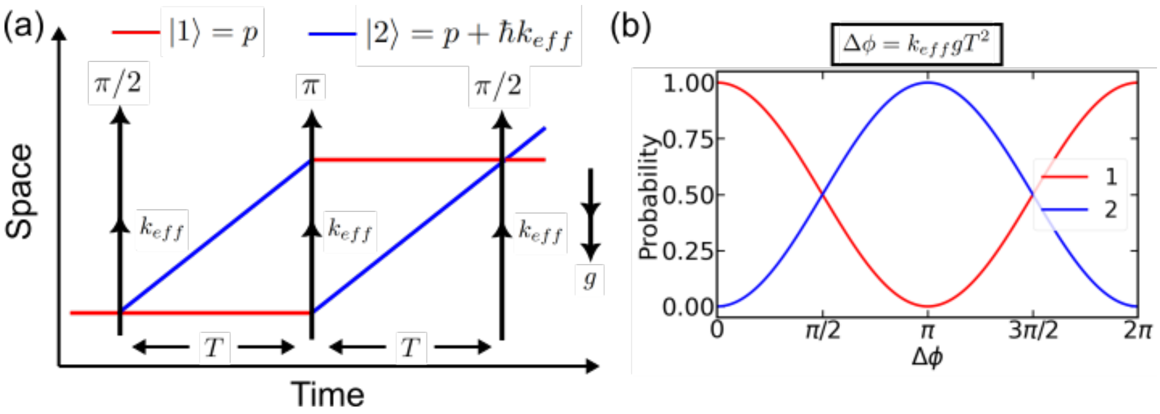

Figure 1.1: Basic idea of light-pulse atom interferometry on freely falling atoms. (a) The Mach-Zehnder atom interferometry sequence. (b) The resulting change in the expectation value of the state population as a function of interferometer phase difference.

and the interferometry time are crucial parameters for achieving the highest sensitivities.

With this result one tries to understand the forces acting on the atomic system by looking at the changes in the phase of the resulting fringe pattern. Especially with the plethora of atomic species options to choose from, increasingly precise atom interferometers are being developed and the limits of precisions are constantly being advanced.

1.1.2 Fundamental and applied physics with light-pulse atom interferometry

Using the basic principle outlined above, many experiments for the precision measurement of gravitational acceleration have been performed on a range of atomic species [14]. These include the initial tests with Raman transitions on freely falling sodium atoms [11] and with caesium atoms [15]. More recently, however, this field has been dominated by experiments using rubidium, for which high-power lasers are readily available.

These atom interferometers are capable of outperforming classical gravimeters, a result beginning with the first fully calibrated atom interferometry based gravimeter, which was able to observe tidal effects [15]. Gravity gradiometers using atom interferometry have become similarly advanced. One of the first gradiometers was performed with caesium atoms where gravity is measured simultaneously on two atomic ensembles [16]. Since then gradiometers have been used to measure a broad range of gravitational effects, including measurements of the gravitational curvature [17], even across the atomic wave packets themselves [18]. Gradiometers have also formed the basis of experiments measuring the gravitational constant G [19, 20] and the recent demonstration of the gravitational analogue to the Aharanhov-Bohm effect [21]. General relativistic effects have also been extensively studied and a network of underground gradiometers has been proposed for gravitational wave detection [22, 23].

However, these interferometers are not just limited to changes in the gravity across space and time, but also any inertial force fields which vary spatially across the space-time area of the atom interferometer. Many schemes for measuring rotations exist [24, 25] and point-source interferometers capable of measuring all inertial forces have been developed and studied [26, 27]. As these various force sensing applications imply, atom interferometers are increasingly used for real-world applications in geophysics such as climate research and also, interestingly, in determining soil properties [28]. A portable gravimeter to perform on-site measurements has been demonstrated [29] and more recently a gradiometer measuring underground features has been designed which considers the suppression of laser noise and seismic noise at micro-levels [13].

Modern atom interferometry applications are not merely limited to gravity and inertial force sensing, but due to the precisions achieved, they can be used to test fundamental physics. They have been used for determining the fine-structure constant [30, 31], which can additionally be used as a means for searching for dark matter [32]. Atom interferometry has also been used in providing new constraints on theories of dark energy [33]. Such fundamental applications will become more prevalent as the sensitivity of interferometers improve. One very interesting avenue is to study atom interferometers using squeezed states of the atoms [34, 35], thereby enhancing the intrinsic sensitivity, with a proof-of-principle experiment recently performed [36].

1.2 Atom interferometry with alkaline-earth and alkaline-earth-like atoms

Most of the experiments discussed in the preceding section have been performed with alkali atoms, which have only a single valence electron. More recently, atom interferometry with alkaline-earth and alkaline-earth-like atoms have gained considerable interest. These atoms possess two valence electrons and have both broad dipole-allowed transitions and narrow forbidden intercombination transitions. These intercombination transitions form the basis of many contemporary atomic clocks [37, 38], so there is a broad interest in studying cold samples of these atoms.

For atom interferometry specifically, alkaline-earth and alkaline-earth-like atoms (for example, Cd, Sr, Ca, Yb etc.) have several advantages and interesting features [39]. Most of the transitions of the singlet and triplet states of these elements lie in the blue-ultraviolet range, unlike for alkali atoms whose relevant electronic transitions lie in the infrared regime. This contributes to having a higher k_{eff} vector, ensuring larger momentum transfer to the atoms than the alkali elements and thereby results in a larger differential phase $\Delta\phi$. Another advantage is the zero angular momentum of the ground state ($^1\mathrm{S}_0$) which makes these elements insensitive to external electric and magnetic fields. Additionally, by using their narrow linewidth intercombination transitions, single-photon scattering can be suppressed in the interferometry sequence thereby increasing the coherence and atom number.

These features have been utilized in various experiments such as demonstration of a precision contrast interferometer using Bose-Einstein condensate with ytterbium atoms [40]. Large-momentum-transfer interferometers using Bragg transitions have also been demonstrated using strontium on the broad dipole-allowed transition [39] and also on an intercombination transition [41]. In addition to these, a long coherence time strontium interferometer, with T up to 1 s, has been demonstrated by using Bloch oscillations in an optical lattice [42].

Moreover, these species can be used to perform single-photon atom interferometry, as well as multi-photon Bragg diffraction, due to various narrow linewidth transitions available. Single-photon (or clock) atom interferometry has been suggested as a means to building very long baseline atom interferometers, because the laser phase does not change during propagation. This is not possible with multi-photon interferometers using counter-propagating beams, because the laser travel time introduces a noise term that cannot be canceled [43]. This feature means that single-photon atom interferometry has been proposed to detect gravitational waves [44, 45]. As single-photon interferometry requires the excited state to be long-lived (i.e. narrow linewidth), alkaline-earth and alkaline-earth-like atoms are an excellent option given the presence of clock transitions.

Single-photon gradiometers and gravimeters have been demonstrated on the 698 nm optical clock transition of ^{88}Sr [43, 46], and also on the 689 nm transition [47, 48]. Additional long-baseline interferometers are currently being built on Earth, with the aim to look for ultralight dark matter and gravitational waves [49, 50]. Also, several proposals exist to build such single-photon interferometers in space to make the baseline lengths considerably larger, to explore even higher sensitivities to e.g. gravitational waves in the 0.01-1 Hz frequency range [51, 52].

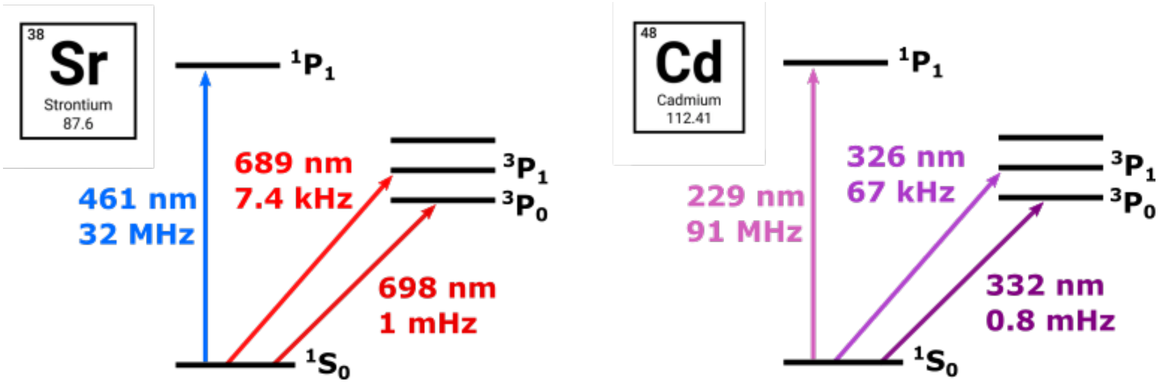

Figure 1.2: Simplified energy level diagrams and main optical transitions for strontium and cadmium.

1.3 A dual-species interferometer with cadmium and strontium

This thesis follows the line of a research proposal to build a dual-species atom interferometer using the alkaline-earth and alkaline-earth-like elements, strontium and cadmium, respectively [53]. This section outlines the reasons for this choice, with more details given in Section 2.3. Figure 1.2 shows a simplified energy level diagram of these two atoms, highlighting the dipole-allowed transitions and the intercombination transitions used for laser cooling, trapping, atom interferometry and optical atomic clocks.

Experiments with strontium have been very well demonstrated for atom interferometry as discussed in the previous section. However, cadmium is a relatively new species with lot of advantages and which also make it a potential candidate for future atomic clocks [54, 55]. Unlike strontium, the transitions in cadmium lie in the ultraviolet regime thereby allowing for results with higher intrinsic sensitivity. Furthermore, the shorter wavelength of ultraviolet light improves the collimation of the interferometry beams due to reduced diffraction effects and also helps in laser cooling by increasing the scattering force. Unfortunately, ultraviolet lasers are not commercially available at the same performance level as those of visible or infrared laser systems. Therefore, it is the task of the experimentalist to develop the high-power, narrow-linewidth laser systems needed in order to exploit these advantages in cadmium [56–59].

However, the choice of strontium as a pair with cadmium simplifies this technological challenge due to the transitions in strontium and cadmium having a near 2:1 ratio in their wavelengths.

From a technical perspective, the production of the laser light at 461 nm for strontium and 229 nm for cadmium is just one frequency doubling step away [57]. Similarly for the intercombination transitions, the required wavelengths are close to a frequency doubling step away from each other. This is useful as similar master laser technology can be used for the preparation of lasers to access both strontium and cadmium transitions. Furthermore, the well-known techniques and optics for strontium can be leveraged in the initial stages [59]. This 2:1 ratio can also reduce important technical noise in a dual-species interferometer (see Section 2.3.3).

Using this combination of atoms allows for testing a wide range of fundamental physics problems and for advancing atom interferometry based on intercombination transitions. Specifically, the weak equivalence principle tests with quantum probes [17] and searches for any time dilation effects in interferometric fringe contrast [60, 61] can be helpful in encapsulating and probing the intersection of the current theory of gravity with quantum mechanics.

1.4 Thesis outline

The rest of the thesis takes the following approach. Chapter 2 consists of the theoretical and experimental background required for the remainder of the thesis, including the relevant energy structures and properties of cadmium and strontium, as well as a more detailed description of the proposed experiments. Also presented is a description of the two-level atom-light interaction and its application in standard state-of-the-art cooling techniques like magneto-optical traps, molasses cooling and the optical dipole trap. It also consists of a brief explanation of atom interferometry.

There follows a discussion of the various laser sources developed for the interferometer. The development and characterization of the laser set-up for generating the light at 229 nm is discussed in Chapter 3. This chapter also focuses on the challenges in generating continuous-wave deep-ultraviolet light. The two laser systems developed for addressing the cadmium intercombination transitions at 326 nm and 332 nm are presented in Chapter 4. Chapter 5 presents the laser systems developed to address the relevant transitions for strontium at 461 nm, 689 nm and 698 nm. Chapter 6 focuses on testing some of these laser set-ups on a novel atomic cadmium beam which includes the characterization of the oven and spectroscopy on the $^1\mathrm{S}_0$ - $^1\mathrm{P}_1$ and $^1\mathrm{S}_0$ - $^3\mathrm{P}_1$ transitions. Details about the preparation of this ultra-high vacuum spectroscopy chamber are given in Appendix B.

The final part of this thesis relates to the design of the new vacuum chambers for this interferometer. The numerical simulations for the generation of ultra-cold cadmium atomic samples and a subsequent lattice launch in the 1 m interferometer is discussed in Chapter 7. The design of the upgraded strontium chamber and the combined cadmium-strontium chamber is presented in Chapter 8. This work is concluded in Chapter 9 in the form of a summary where the future prospects of the experiment are also discussed.

Appendix A gives a list of publications based on the work presented in this thesis.

Chapter 2

Theoretical background

This chapter provides the basic theoretical background required for the rest of this thesis. It begins with a description of the theory fundamental to the generation of ultra-cold atomic sources using laser cooling and trapping techniques. A more detailed discussion of light-pulse atom interferometry and the acquired phase difference is then presented. Finally, the relevant properties of cadmium and strontium are presented, focusing on the experimental aim of the dual-species interferometer. In particular, atom interferometry using their intercombination transitions are discussed and additionally the prospects for weak equivalence principle tests and quantum clock interference experiments are presented.

2.1 Theory of laser cooling and trapping

The advent of the methods to laser cool and trap neutral atoms has led to the Nobel Prize award in 1997 to Steven Chu, Claude Cohen-Tannoudji and William Phillips [62–64]. Reducing the velocity of matter from room temperature was first done with ions using electric fields, however cooling due to radiative forces was performed only after the invention of the laser, firstly on trapped ions [65] and later on freely moving atoms [66].

When an atom interacts with light of monochromatic radiation of frequency ω, broadly the atoms encounter two kinds of forces. One being the dipole force due to the induced dipole moment within the atom, and the second one being the radiation pressure force which arises due to the absorption and re-emission of the photons. This section will briefly discuss these two forces, with a focus on the laser cooling and trapping of atoms.

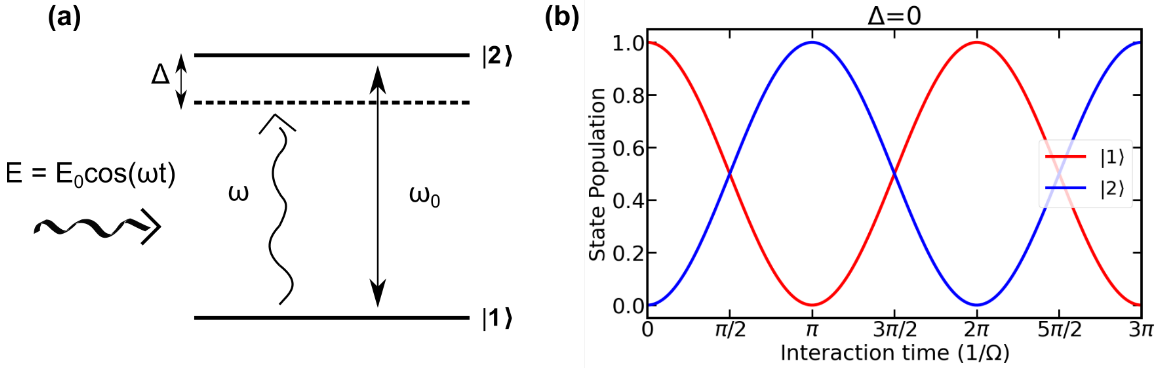

Figure 2.1: (a) Schematic of light with angular frequency ω interacting with a two-level atom. (b) Rabi oscillations between the two atomic states as a function of the interaction time with resonant light at $\Delta = 0$.

2.1.1 Rabi oscillations

For simplicity, a semi-classical approach is used where a two-level atom interacting with monochromatic light is considered [67], as shown in Figure 2.1. In this case, the Schrödinger equation of the atom wave function Ψ can be written as in equation 2.1 where the Hamiltonian is split into a steady-state component (H_0) and a time-dependent component $(H_I\,(t))$.

$$i\hbar\frac{\partial\Psi}{\partial t} = \left[H_0 + H_I\,(t)\right]\Psi \tag{2.1}$$

The eigenfunctions of H_0 represent those of the unperturbed atoms, which, for the two-level system, are labelled $|1\rangle$ and $|2\rangle$. These states have energies relating to the eigenvalues of H_0 of $E_1 = \hbar\omega_1$ and $E_2 = \hbar\omega_2$, respectively. The wave function at any moment in time can therefore be written as a linear summation of these states as shown in equation 2.2, where $c_1(t)$ and $c_2(t)$ are the state coefficients.

$$\Psi\left(\vec{r}, t\right) = c_1\,(t)\,|1\rangle\,\mathrm{e}^{-i\omega_1 t} + c_2\,(t)\,|2\rangle\,\mathrm{e}^{-i\omega_2 t} \tag{2.2}$$

Conversely, $H_I\,(t)$ describes the perturbation from the interaction of the atom with the incident light, which is considered as an oscillating electric field $\vec{E} = \vec{E}_0\cos\left(\omega t\right)$. In this case, the interaction Hamiltonian can be written as in equation 2.3 where $\vec{d} = e\vec{r}$ is the dipole operator, which will be discussed in more detail later in Section 2.1.6. In brief, however, it represents the energy of an electric dipole in the light field, where $\vec{r}$ is the position of the electron from the center-of-mass position of the atom.

$$H_I\left(t\right) = \vec{d}\cdot\vec{E_0}\cos\left(\omega t\right) \tag{2.3}$$

Equation 2.2 can be substituted into equation 2.1 to give the expressions for the state coefficients $c_1\left(t\right)$ and $c_2\left(t\right)$.

$$i\frac{d}{dt}c_1\left(t\right) = \Omega\cos\left(\omega t\right)e^{-i\omega_0 t}c_2\left(t\right) \tag{2.4}$$

$$i\frac{d}{dt}c_2\left(t\right) = \Omega^*\cos\left(\omega t\right)e^{i\omega_0 t}c_1\left(t\right) \tag{2.5}$$

where $\omega_0 = \omega_2 - \omega_1$ is the angular frequency difference between the two states. The Rabi frequency Ω is defined by the equation 2.6.

$$\Omega = \frac{\langle 1|\vec{d}\cdot\vec{E_0}|2\rangle}{\hbar} \tag{2.6}$$

To solve the equations 2.4 and 2.5, it is beneficial to write them in terms of complex exponential functions instead of trigonometric expressions. For example, equation 2.4 becomes,

$$i\frac{d}{dt}c_1\left(t\right) = \frac{\Omega}{2}\left[\mathrm{e}^{i\left(\omega-\omega_0\right)} + \mathrm{e}^{i\left(\omega+\omega_0\right)}\right]c_2\left(t\right) \tag{2.7}$$

Equation 2.7 can be simplified by using the rotating-wave approximation, which is a common approximation where the frequency of the laser is close to the atomic transition frequency ($\omega \sim \omega_0$). This means that the term $\mathrm{e}^{i\left(\omega+\omega_0\right)}$ averages out to zero, as it oscillates very fast in comparison to the interaction times. Following the application of the rotating-wave approximation, equation 2.8 can be derived, which is a second-order differential equation for $c_2\left(t\right)$.

$$\frac{\mathrm{d}^2}{\mathrm{d}t^2}c_2\left(t\right) + i\left(\omega-\omega_0\right)\frac{\mathrm{d}}{\mathrm{d}t}c_2\left(t\right) + \left|\frac{\Omega}{2}\right|^2 c_2\left(t\right) = 0 \tag{2.8}$$

If the initial state of the atom is assumed to be entirely in the ground state, it gives the initial conditions $c_1\left(0\right) = 1$ and $c_2\left(0\right) = 0$ and also the atomic state coefficients can be found. Also, for a transition between the two bound states, Ω is real, so $\left|\Omega\right|^2 = \Omega^2$ and the detuning $\Delta = \omega - \omega_0$ is defined. The solution to equation 2.8 for $c_2\left(t\right)$ is given below.

$$c_2\left(t\right) = -i\mathrm{e}^{-i\Delta/2}\frac{\Omega}{\sqrt{\Omega^2+\Delta^2}}\sin\left(\frac{\sqrt{\Omega^2+\Delta^2}t}{2}\right) \tag{2.9}$$

The population of the two states as a function of interaction time can therefore be written as shown in equations 2.10 and 2.11.

$$P_2\left(t\right) = \left|c_2\left(t\right)\right|^2 = \frac{\Omega^2}{\Omega^2+\Delta^2}\sin^2\left(\frac{\sqrt{\Omega^2+\Delta^2}t}{2}\right) \tag{2.10}$$

$$P_1(t) = |c_1(t)|^2 = 1 - |c_2(t)|^2 = 1 - \frac{\Omega^2}{\Omega^2 + \Delta^2}\sin^2\left(\frac{\sqrt{\Omega^2 + \Delta^2}t}{2}\right) \tag{2.11}$$

Equations 2.10 and 2.11 show the expected population oscillation between the two energy levels as a function of the interaction time. This phenomenon is known as Rabi oscillation or Rabi flopping and is shown in Figure 2.1 for the case of zero detuning. A very interesting and useful property of Rabi oscillations is highlighted in this figure. Specifically, the ability to make controlled superpositions of states by varying the interaction time. Two special cases are frequently used: firstly, pulses which generate a 50:50 split in the population, known as $\pi/2$ pulses because $t = \pi/2\Omega$; and secondly, π pulses which reverse the state populations for $t = \pi/\Omega$.

This ability to coherently alter the state population with light forms the experimental basis of not only light-pulse atom interferometry, but also a wide variety of other fields such as atomic clocks and quantum computation with atoms, ions and molecules.

2.1.2 Radiative force

While monochromatic light causes light to undergo coherent Rabi oscillations as described in the above section, a real system will also contain damping. For long interaction times this leads to a reduction of the quantum mechanical treatment to one of rate equations from the Einstein's formulation with the A and B coefficients [67]. In these conditions, the steady-state population of the excited state can be written as equation 2.12, where Γ is the linewidth of the excited state, which is inversely proportional to its lifetime.

$$\rho_2 = \frac{\Omega^2/4}{\Delta^2 + \Omega^2/4 + \Gamma^2/4} \tag{2.12}$$

As equation 2.12 shows, at high intensities the population tends to be split equally at 1/2 between the ground and excited states. The number of photons scattered by the atom is expressed according to the scattering rate R given in equation 2.13 where I is the input light intensity and I_{sat} is the saturation intensity of the transition. The saturation intensity is given by equation 2.14 where σ_0 is $3\lambda^2/2\pi$.

$$R = \frac{\Gamma}{2}\frac{I/I_{sat}}{1 + I/I_{sat} + 4\Delta^2/\Gamma^2} \tag{2.13}$$

$$I_{sat} = \frac{\hbar\omega_0\Gamma}{2\sigma_0} \tag{2.14}$$

The relation between Rabi frequency and the saturation intensity is given by the equation 2.15, a result which will be extensively used later in Section 2.2.

$$\Omega^2 = \frac{\Gamma^2}{2}\frac{I}{I_{sat}} \tag{2.15}$$

Atoms experience a force called the radiation pressure force as a result of this scattering (absorption and the re-emission of the photons) during their interaction with the light. Each absorption event gives the atom a recoil velocity $\vec{v}_r = \hbar\vec{k}/m$, where $\vec{k}$ is the wave vector of the light and m is the mass of the atom. The force from this recoil is obtained by multiplying the rate R at which the atom scatters the photons with the photon momentum $\hbar\vec{k}$.

The maximum radiation pressure force the atoms experience is therefore $\hbar\vec{k}\Gamma/2$, which occurs as $I \to \infty$, i.e., when the populations of both the internal atomic states approach 1/2 and the scattering rate (equation 2.13) is maximized. More generally, the radiative force is given by the equation 2.16.

$$\vec{F}_{rad} = \hbar\vec{k}R = \frac{\hbar\vec{k}\Gamma}{2}\frac{I/I_{sat}}{1 + I/I_{sat} + 4\Delta^2/\Gamma^2} \tag{2.16}$$

In the low-intensity regime, the I/I_{sat} term in the denominator of equations 2.13 and 2.16 can be ignored. In such regimes, the force due to the radiation pressure is given by the equation 2.17.

$$\vec{F}_{rad} = \frac{\hbar\vec{k}(\Gamma/2)^3 I}{(\Delta^2 + (\Gamma/2)^2)I_{sat}} \tag{2.17}$$

2.1.3 Optical molasses

The radiative force discussed above can be used to slow down, and therefore cool the atoms [68]. The simplest configuration to perform laser cooling on atoms moving with a velocity v, is to use red-detuned (frequency below the atomic resonance, Δ <0) counter-propagating laser beams, as shown in Figure 2.2. Usually the atoms have a velocity distribution in all the 3 dimensions, however here the 1 dimensional case is considered for simplicity and can be extrapolated.

The atomic motion leads to a Doppler shift where the atom sees a frequency of the radiation either red shifted or blue shifted depending on the direction of velocity relative to the laser propagation direction. This leads to a disparity in the force experienced by the atoms in both the directions. For a laser frequency detuning of Δ <0, if the $\vec{v}$ is in the direction opposite to $\vec{k}$, the Doppler shift increases the laser frequency thereby making it close to the resonance and increasing the scattering rate from this beam. Conversely, the counter-propagating laser beam which is in the same direction as the atom, will be blue shifted and therefore move further away from the atomic resonance. More

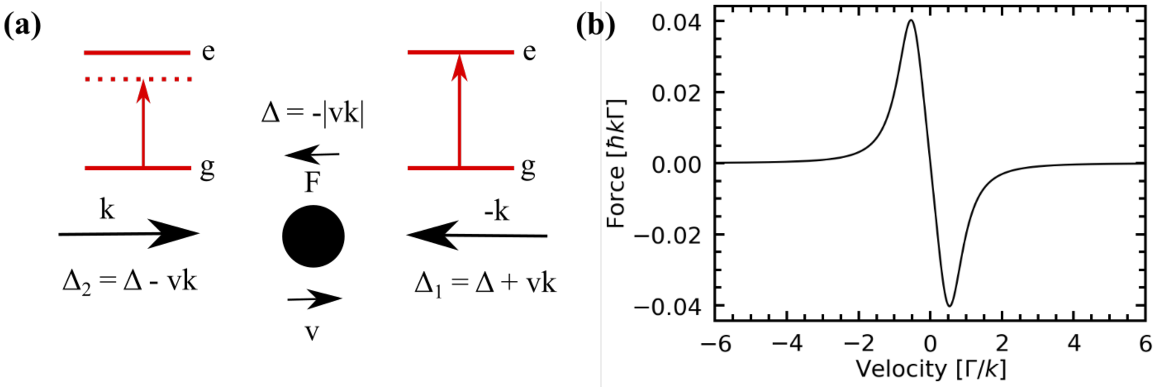

Figure 2.2: Figure (a) shows the two-level atom interaction with counter-propagating beams (optical molasses) and (b) shows the force experienced by the atom as a function of its velocity in the low-saturation regime.

technically, the beam opposite to the atomic motion is blue-shifted by kv ($\Delta_1 = \Delta + kv$) and the beam in the direction of the atomic motion is red-shifted ($\Delta_2 = \Delta$ - kv) and the atom will scatter more photons from the beam propagating counter to its motion. This leads to an imbalance in the radiation pressure forces and creates a damping effect on the atoms thereby decreasing their velocity.

The force experienced by the atom in this case can be derived by modifying equation 2.17 to include the Doppler shift and is given in equation 2.18. Again, this formula is valid for $I/I_{sat} < 1$, i.e, well below the saturation of the transition. This force is dependent on the atomic velocity and is basically the difference between the two Lorentzian profiles. The force is shown as a function of velocities in Figure 2.2 (b) for Δ = -$\Gamma/2$.

$$F_{rad} = \hbar k \left(\Gamma/2\right)^3 \left(\frac{1}{\left(\Delta - kv\right)^2 + \left(\Gamma/2\right)^2} - \frac{1}{\left(\Delta + kv\right)^2 + \left(\Gamma/2\right)^2} \right) \frac{I}{I_{sat}} \tag{2.18}$$

The damping coefficient for this motion ($F = -\alpha$v) is given by equation 2.19 and the damping time is given by τ = m/2α for all the atoms within the capture velocity range ($\pm\frac{\Delta}{k}$ or $\pm\frac{\Gamma\lambda}{4\pi}$, when Δ = -Γ/2) entering the optical molasses beams.

$$\alpha = 4\hbar k^2 \frac{I}{I_{sat}} \frac{-2\Delta/\Gamma}{\left[1 + (2\Delta/\Gamma)^2\right]^2} \tag{2.19}$$

2.1.4 Doppler cooling limit

There is a limitation in the temperature that the atoms can be realistically cooled down to, using the radiation pressure force, despite the formula implying otherwise and suggesting cooling down to zero velocities. In reality, there are various heating mechanisms occurring during the interaction which limit the temperature. However, the important one is due to the fluctuations in the scattering force from the radiation, which leads to a limit known as the Doppler cooling limit [69, 70].

While the absorption of a photon from the laser imparts momentum in a well-defined direction, subsequent spontaneous emission occurs in a random direction and each kick corresponds to a change in the momentum space by $\hbar k$. This motion is quite similar to the Brownian motion of microscopic particles [67]. This scattering event is assumed to follow Poissonian statistics, where the fluctuations in the scattering force cause a random walk in the velocity space along with the collective slowing of the atoms. This emission overall can be said to be isotropic when counter-propagating laser beams in 3 Cartesian dimensions are considered. This corresponds to a situation where $\overline{v} = 0$ but $\overline{v^2} \neq 0$.

This random walk in the velocity space of the atoms gives a minimum temperature of the atomic sample following slowing with a simple optical molasses beam set-up and is given by equation 2.20, where T_{Dop} is known as the Doppler temperature and k_B is Boltzmann's constant. This temperature is usually much higher in comparison to the recoil temperature, which is instead derived by considering the momentum imparted from a single photon.

$$T_{Dop} = \frac{\hbar\Gamma}{k_B} \tag{2.20}$$

An important and interesting characteristic is that this temperature depends only on the transition linewidth. From the increased scattering rate due to a higher linewidth, a faster random walk is generated.

However, laser cooling to temperatures less than those set by the Doppler limit is possible [71]. This sub-Doppler regime is acquired due to the degenerate structure of the electronic transitions [72, 73]. For example, ^{133}Cs at 852 nm can be cooled down to 2.5 μK, whereas the Doppler temperature is about 125 μK [74]. The general two-level atom approach isn't enough to explain the sub-Doppler temperatures attained and this experiment was performed when the Earth's magnetic field was cancelled out. In such a case, the temperature approaches the more fundamental recoil limit.

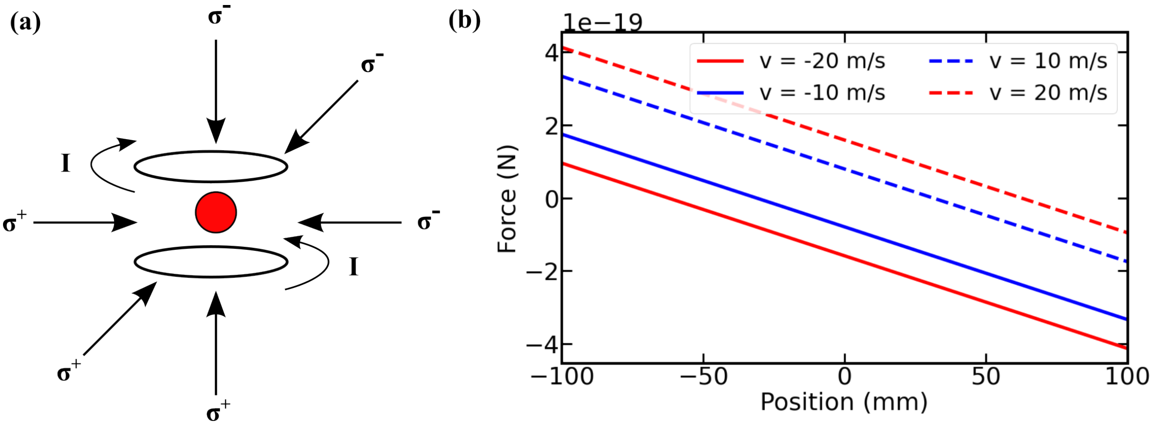

Figure 2.3: (a) Diagram of the set-up of a 3D MOT. (b) Force calculated for the 229 nm transition of cadmium according to equation 2.21, with a field according to equation 2.21, and $B_0 = 0.1$ T/m $\Delta = -\Gamma/2$, $s = 0.1$.

2.1.5 Magneto-optical trap (MOT)

The described optical molasses set-up slows the atoms down, but the atoms diffuse after eventually getting out of resonance with the molasses beams. Hence, in order to trap the atoms, a position varying force is additionally required. Such cooling and trapping can be done by introducing a position varying magnetic field in combination with circularly polarized laser beams [75]. This polarization is required in order to access the magnetic sub-state transitions whose degeneracy is lifted in the presence of magnetic field.

In this configuration, the force experienced by the atoms is a function of the velocity and position given by equation 2.21, where α is the damping coefficient given by the equation 2.19, g is the Landé g-factor, μ_B is the Bohr magneton, r is the distance of the atom from the center of the trap and B is the magnetic field.

$$F_{mot} = \alpha v - \frac{\alpha g \mu_B}{\hbar k} r \nabla |B| \tag{2.21}$$

The Zeeman splitting occurs due to the presence of the magnetic field whose strength increases radially from the center of the trap, thereby changing the atomic transition frequencies. This splitting is linearly dependent on the strength of the field at the location of the atom. In practice, magnetic coils in an anti-Helmholtz configuration, with the current circulating in opposite directions, allow for the generation of a suitable quadrupole magnetic field. This field is given in equation 2.22, where

B_0 is the field gradient about the center of the trap and allows for the trapping of atoms which are slowed due to the velocity-dependent radiation pressure force. This field gradient gives a linearly uniform position-dependent shift to the magnetic sub-levels (in both ground and excited states) which resonate with the laser beams ($\Delta E = \Delta m_l \mu_B B$, where m_l is the magnetic sub-level, μ_B is the Bohr magneton and B is the magnetic field).

$$\vec{B} = B_0 \left(-\frac{1}{2} x\hat{x} - \frac{1}{2} y\hat{y} + z\hat{z} \right) \tag{2.22}$$

The circularly polarized ($\sigma^{\pm}$) red-detuned laser beams, in a counter-propagating configuration along with the magnetic coils are shown in Figure 2.3. Assuming that the atom moves to the right from the center of the trap, the σ^- polarized laser beam interacts with the atom. As the laser frequency is red-detuned, it becomes resonant with $\Delta \mathrm{M}_J$ = -1 transition and slows the atom down and recoil kicks push the atom back to the trap center. For the atom traveling to the left, in the presence of the negative field, the σ^+ beam interacts with the $\Delta \mathrm{M}_J = +1$ sub-level as it comes in resonance with the red-detuned beam and gives the atoms a kick back in the opposite direction towards the center of the trap.

2.1.6 Optical dipole potential and force

This section describes the effect of the induced dipole caused by the interaction of the atom with light radiation. While the previous sections have discussed the method to trap atoms using the radiative scattering force, the remaining sections will look at the method to use dipole potential to trap neutral atoms. When considering the dipole potential, a classical approach can be taken [76], with only a small modification needed to return to the semi-classical approach used above [77].

The interaction and its effects are studied by considering the dipole approximation where the size of the atom is much smaller than the wavelength of the light, implying a negligible change in the electric field across the spatial extent of the atom. In this approach, the atom is modeled as a classical harmonic oscillator and the electric field of the light is given by equation 2.23, where ω is the frequency of the radiation and $\hat{\epsilon}$ is the unit polarization vector.

$$E^+(r) = \hat{\epsilon} E_0^+ \mathrm{e}^{-i\omega t} \tag{2.23}$$

The electric field and the subsequent displacement of the electron in the atom and other parameters in this classical formalism are considered to be complex quantities. The physical electric field therefore consists of positive and negative frequency elements, as shown in equation 2.24.

$$E(r,t) = E^{+}(r)\mathrm{e}^{-i\omega t} + E^{-}(r)\mathrm{e}^{i\omega t} \tag{2.24}$$

The displaced electron within the atom in the presence of the electric field thereby creates a dipole moment $\vec{d} = -e \cdot r$, where e is the charge of the electron and $r = \vec{r} \cdot \hat{\epsilon}$ being the displacement in the direction of $\hat{\epsilon}$. This is encapsulated by the polarizability α, which is the ability of an atom to experience an internal dipole moment in the presence of an external electric field given by equation 2.25.

$$\vec{d} = \alpha \vec{E} \tag{2.25}$$

The effect of the induced dipole moment within the atom can be calculated by solving the equation of motion of the electron using Newtonian mechanics from which the polarizability is derived which is given by equation 2.26, where ω_0 is the transition frequency of the atom and m is the mass of the electron.

$$\alpha\left(\omega\right) = \frac{e^2}{m} \frac{1}{\omega_0^2 - \omega^2 - i\omega\Gamma_\omega} \tag{2.26}$$

where Γ_ω is defined according to,

$$\Gamma_\omega = \frac{e^2\omega^2}{6\pi\epsilon_0 m c^3} \tag{2.27}$$

This leads to more familiar form of polarizability which is given by equation 2.28, where $\Gamma = \left(\omega_0/\omega\right)^2 \Gamma_\omega$.

$$\alpha\left(\omega\right) = 6\pi\epsilon_0 c^3 \frac{\Gamma/\omega_0^2}{\omega_0^2 - \omega^2 - i\left(\omega^3/\omega_0^2\right)\Gamma} \tag{2.28}$$

In the case where saturation effects are neglected, this classical approach gives an identical result to the semi-classical case. When considering the semi-classical case, the only change is that Γ should be the natural linewidth of the transition [77].

The interaction potential of the induced dipole moment is expressed in terms of the polarizability as shown in equation 2.29, where $I\left(\vec{r}\right)$ is the intensity dependence of the electric field on position.

$$U_{dipole}\left(\vec{r}\right) = \frac{1}{2\epsilon_0 c} \mathrm{Re}\left(\alpha\right) I\left(\vec{r}\right) \tag{2.29}$$

Substituting equation 2.28 into equation 2.29 gives the dipole potential as equation 2.30.

$$U_{dipole}\left(\vec{r}\right) = -\frac{3\pi c^2}{3\omega_0^3}\left(\frac{\Gamma}{\omega_0 - \omega} + \frac{\Gamma}{\omega_0 + \omega}\right) I\left(\vec{r}\right) \tag{2.30}$$

The sign of this dipole potential is dependent on the frequency of the incident radiation relative to the transition frequency, which is expressed as detuning ($\Delta = \omega - \omega_0$). This makes the atom either attracted or repulsed by the harmonic potential. The optical dipole force experienced is the change in the potential ($\vec{F}_{dipole}$ = -∇U_{dipole}) and is directly proportional to any intensity gradient of the light field. This dipole force experienced by the atoms is fundamental to optical dipole traps which are discussed in more detail below in Section 2.1.7.

It is to be noted that the polarization of the incident light determines the dipole pattern within the atom. When the light is linearly polarized ($\hat{\epsilon} = \hat{k}$), this creates an oscillating dipole, whereas in the case of circularly polarized light ($\hat{\epsilon} = (\hat{i} \pm i\hat{k})/\sqrt{2}$), there is a rotating dipole. Using this polarization dependence on the induced dipole, the Poynting vector is written using the normalized angular distribution of the radiative dipole emission which gives the total power radiated from the dipole as a function of polarizability given in equation 2.31.

$$P_{rad} = \frac{\omega^4 |\alpha(\omega)|^2}{6\pi\epsilon_0^2 c^4} I \tag{2.31}$$

2.1.7 Optical dipole trap

The application of the optical dipole potential to atom trapping is now considered in more detail. The potential described in equation 2.30 arises from the conservative force which is dependent on the intensity gradient. In a real system, the presence of scattering corresponds to heating of the atoms within the trap. While the dipole force is due to the real part of the polarizability, the scattering instead is due to the imaginary part, as given in equation 2.32, where c is the speed of light in vacuum.

$$R_{dipole}\left(\vec{r}\right) = \frac{1}{\hbar\epsilon_0 c} \mathrm{Im}\left(\alpha\right) I\left(\vec{r}\right) \tag{2.32}$$

By using the polarizability from 2.28 in equation 2.32 gives the scattering rate as equation 2.33.

$$R_{dipole}\left(\vec{r}\right) = \frac{3\pi c^2}{2\hbar\omega_0^3} \frac{\omega^3}{\omega_0^3} \left(\frac{\Gamma}{\omega_0 - \omega} + \frac{\Gamma}{\omega_0 + \omega}\right)^2 I\left(\vec{r}\right) \tag{2.33}$$

The heating or photon scattering effect can be reduced by being far off resonance with the atom, which matches the assumption used to derive these equations of a low number of scattering events well below saturation.

In the case when $\Delta = \omega - \omega_0$ fulfills the criterion $|\Delta| << \omega_0$ (i.e. when the laser is relativity close to the transition), the rotating-wave approximation can be applied, as previously discussed in Section 2.1.1. This simplifies equations 2.30 and 2.33 to the following forms.

$$U_{dipole}\left(\vec{r}\right) = \frac{3\pi c^2}{2\omega^3} \frac{\Gamma}{\Delta} I\left(\vec{r}\right) \tag{2.34}$$

$$R_{dipole}\left(\vec{r}\right) = \frac{3\pi c^2}{2\hbar\omega^3}\left(\frac{\Gamma}{\Delta}\right)^2 I\left(\vec{r}\right) \tag{2.35}$$

Equations 2.34 and 2.35 show that the dipole potential scales inversely with Δ, while the scattering rate scale inversely with Δ^2. Consequently, the farther the frequency of the light from the transition frequency, lower the scattering rate of the trap relative to the trap depth. Large detunings are therefore to be preferred, if the consequent reduction in the trap depth can be counteracted by a sufficient increase in the intensity of the light.

From equation 2.34 one can further see that for red-detuned light, where the frequency of the driving field is less than the transition frequency, the atoms experience an attractive potential. The dipole force is oriented towards higher intensities in this case. The opposite is the case for blue-detuned light which generates a repulsive force.

There can be many configurations of forming an optical dipole trap. With a single focussed Gaussian beam, the dipole potential allows for the trapping only in the radial direction and has a long spread along the axial direction. For such a single beam configuration, it's better to avoid the wave vector in the direction of gravity and place the beam horizontally. The efficiency of loading in the trap however is dependent on the temperature of the atomic ensemble. If the temperature of the ensemble is much lower than the trap potential, the atoms see a cylindrically symmetric potential as shown in equation 2.36, where r and z represent the radial and axial directions and w_0 and z_R are the waist and the Rayleigh length of the Gaussian beam, respectively. The trap frequency in the radial dimension is $\omega_r = (4\hat{U}/m\omega_0^2)^{1/2}$ and in the axial dimension is $\omega_z = (2\hat{U}/mz_R^2)^{1/2}$

$$U_{sin}(r,z) = -\hat{U}\left[1 - 2\left(\frac{r}{w_0}\right)^2 - \left(\frac{z}{z_R}\right)^2\right] \tag{2.36}$$

To attain better trapping, a crossed beam trap can be used where a tight confinement can be achieved in two dimensions. For this the angle of the crossed beams can be varied, but for an angle of 90° and equal waist of w_0 beams of orthogonal polarizations, the dipole potential is given by the equation 2.37, where the effective trap depth here is $\hat{U}/2$ and the trapping occurs in the x-y plane.

$$U_{CB}(x,y,z) = -\hat{U}\left(1 - \frac{x^2 + y^2 + 2z^2}{w_0^2}\right) \tag{2.37}$$

2.1.8 Optical lattice

In addition to the crossed configurations of the optical dipole traps discussed above, lasers beams can be used in a counter-propagating manner in order to create an interference pattern where the atoms can be trapped in the nodes or the anti-nodes of the standing wave pattern. In the retro-reflected configuration, the wavefront curvature and the polarization can be assumed to be conserved and a periodic potential (standing wave) is formed with a period of $\lambda_L/2$, where λ_L is the wavelength of the lattice laser beam. Assuming the polarization is in the x dimension and the propagation is in the z dimension, the electric field is given by equation 2.38, where the amplitude is position dependent and gives an intensity pattern of $4I_0\cos^2(k_L z)$ along the z axis, where I_0 is the intensity of the beam.

$$E\left(z,t\right) = 2\epsilon_x E\left(z\right) cos\left(\omega_L t\right) \tag{2.38}$$

The standing wave formed has a dipole potential given by the equation 2.39, where the effective potential depth is $\hat{U}/2$. There is a strong dipole force in the nodes and anti-nodes formed axially and the trap depth potential in the retro-reflected configuration is four times larger than the peak formed with a single traveling wave. The axial trap frequency is $\omega_z = \hbar \mathrm{k}(2\hat{U}/m)^{1/2}$ and varies when moved away from the waist of the Gaussian beam.

$$U(r,z) = -\hat{U}cos^2\left(k_L z\right)\left[1 - 2\left(\frac{r}{w_0}\right)^2 - \left(\frac{z}{z_R}\right)^2\right] \tag{2.39}$$

These standing wave lattices can be generated in a 2D or a 3D structure where every lattice site acts as a tight harmonic oscillator. The angle between these beams can be altered and are termed as Kagomé lattices where the frequency of the radiation is altered to get the desired trap depth potential. The atoms in the lattice can be described using the Bloch wave terminology with a crystal momentum q from the solid-state physics formulation. Atoms are treated in a quantum-mechanical manner and they can undergo jumps or tunneling into the nearby lattice sites. Larger trap depths can help avoid these atomic losses due to tunneling (see Section 8.4).

2.2 Theory of atom interferometry

2.2.1 Basic principle of atom interferometry on freely falling atoms

In this section, the case of freely falling atoms interacting with interferometric laser beams aligned along the gravitational axis is considered. These beams are assumed to be in a general manner and a specific scheme, e.g. Bragg interferometry or single-photon interferometry, is not assumed. The laser beam is simply considered to have an effective wave number k_{eff}.

To observe interferometic phenomenon, the atoms are required to be split and evolved for a time period T and then recombined in order to obtain a fringe pattern. This is obtained in a general

$\pi/2 - \pi - \pi/2$ pulse sequence, with equal free evolution time T between the pulses, which is a Mach-Zehnder interferometry scheme (Figure 1.1). From the earlier discussion on Rabi oscillations (see Section 2.1.1), this means that the first $\pi/2$ pulse generates an equal superposition between the two states. However, the part of the wave packet which has changed state has also received momentum of $\hbar k_{eff}$ and therefore the two arms of the interferometer will begin to spatially separate with evolution time. In this way, the interaction with the laser can generate a coherent superposition between spatially separated arms (or more formally, momentum states of the atom). The central π pulse acts as a mirror, flipping the momentum of the two arms and bringing them back together. The final $\pi/2$ pulse closes the interferometer.

The probability of the atoms in the ground and excited states at the point of detection is shown in equations 2.40 and 2.41, whose oscillation is periodically dependent on the acquired phase difference, $\Delta\phi$.

$$P_g = \frac{1}{2}\left[1 + cos\left(\Delta\phi\right)\right] \tag{2.40}$$

$$P_e = \frac{1}{2}\left[1 - cos\left(\Delta\phi\right)\right] \tag{2.41}$$

The final phase difference $\Delta\phi$ acquired in this case is dependent on the internal atomic phase which is acquired during the free-propagation of wave packets ($\Delta\phi_{prop}$), any asymmetries arising at the point of overlap within the interferometer ($\Delta\phi_{sep}$), and from the laser beams ($\Delta\phi_{light}$). The phase can be separated into these individual components as in equation 2.42.

$$\Delta\phi = \Delta\phi_{prop} + \Delta\phi_{sep} + \Delta\phi_{light} \tag{2.42}$$

Formal treatments which consider the classical trajectories of the full Lagrangian and taking a Feynman path integral approach are available in the literature [78–81]. However, in the case of perfect overlap between the two arms of the interferometer, $\Delta\phi_{sep} = 0$. This requires the correct calibration of the time between the pulses to assume the final $\pi/2$ pulse is applied when the two interferometer arms are exactly spatially overlapped. Similarly, $\Delta\phi_{prop} = 0$ when the gravitational field is considered to be uniform (in the absence of gravity gradients).

However, $\Delta\phi_{light}$ is not in general zero and gives the leading order phase shift of the interferometer. This laser phase depends on the frequency of the lasers and the position of the atomic wave packet, but also on other factors such as if the laser frequency is away from the transition frequency or even the presence of state-dependent shifts like the AC Stark shift.

2.2.2 Derivation of leading-order phase shift

To investigate $\Delta\phi \approx \Delta\phi_{light}$, the standard case of a light-pulse Mach-Zehnder interferometer operating on freely falling atoms is considered. In this configuration, atoms experience acceleration due to gravity and interact with laser beams along the axis of gravity as shown in Figure 1.1. In this case the phase difference is given by the equation 2.43

$$\Delta\phi = \phi\left(z_1, t_1\right) - \phi\left(z_2^I, t_2\right) - \phi\left(z_2^{II}, t_2\right) + \phi\left(z_3, t_3\right) \tag{2.43}$$

where $\phi\left(z, t\right)$ is the phase imprinted by the interferometry laser pulse at time t on the atoms at position z. For the two $\pi/2$ pulses the two arms of the interferometer are assumed to be perfectly overlapped and therefore there is only a single term for these pulses. For the central π pulse however, the atoms are in a spatial superposition and there are two contributing terms. The phase $\phi\left(z, t\right)$ due to the laser beam interaction assuming negligible transverse velocities is given by the equation 2.44.

$$\phi(z, t) = -k_{eff}z + \omega_{eff}t + \phi_{eff} \tag{2.44}$$

where k_{eff}, ω_{eff} and ϕ_{eff} are the effective wave number, angular frequency and phase of the interferometric laser beam, e.g. Raman, Bragg or single-photon lasers. Considering the Newtonian trajectories of the freely falling atoms [82],

$$z_1 = 0 \tag{2.45}$$

$$z_2^I = v_0 T - \frac{1}{2} g T^2 \tag{2.46}$$

$$z_2^{II} = \left(v_0 + v_R\right) T - \frac{1}{2} g T^2 \tag{2.47}$$

$$z_3 = 2\left(v_0 + v_R\right) T - 2 g T^2 \tag{2.48}$$

where v_0 is the initial velocity of the atoms and v_R is the recoil velocity from the laser. Applying this to the first term of equation 2.44, the well known phase shift of an atom interferometer for gravity measurements is shown in equation 2.50.

$$\Delta\phi = -k_{eff}\left(z_1 - z_2^I - z_2^{II} + z_3\right) \tag{2.49}$$

$$\Delta\phi = k_{eff} g T^2 \tag{2.50}$$

From this equation it can be noted that the sensitivity to g of the interferometer is enhanced by increasing k_{eff} and T to generate a larger phase difference. In practical terms, this requires using shorter wavelength transitions to enhance the momentum transferred by the laser beams. Alternatively, so-called large-momentum transfer techniques can be used to apply $n\hbar k_{eff}$ at each stage and therefore enhance the sensitivity by n.

Enhancing the sensitivity using T means increasing the free flight time by utilizing, for example, a fountain configuration, where the atoms are launched upwards, allowing for the free fall distance to be effectively doubled (the atom travels upwards and then downwards the same height h). This gain is limited by the acceleration due to gravity which means $T \propto \sqrt{h}$, so increasing the height of a fountain by a factor 10 only increases the free flight time by a factor ∼3. For this reason, trapped atom interferometers, where the atoms are held in an optical lattice, or space-based missions are also pursued.

2.3 Prospects for a dual-species atom interferometer

2.3.1 Relevant properties of cadmium and strontium

Overview of strontium

Experiments with strontium and their applications as an accurate atomic clocks have been extensively studied [83]. Very recently, strontium has been used as a source for optical clocks with record fractional frequency precision down to 10^{-20} level [84, 85] and for making the first continuous Bose-Einstein condensate [86]. Previously, all four natural isotopes of strontium have been cooled to quantum degeneracy [87]. Strontium is also an increasingly common source for atom interferometry, with special interest on interferometry on the ultra-narrow ^{1}S$_0$ - ^{3}P$_0$ clock transition, as discussed earlier in Section 1.2.

One very interesting feature is that ^{88}Sr, the most abundant isotope of strontium, has a negative cold collision cross-section (a_r = -2a_0, where a_0 is the Bohr magneton) in the ground state, which leads to a reduced decoherence in longer interferometric sequences and also lower collisional losses. The advantages of this property have been demonstrated in trapped atom interferometers [42] and long lived Bloch oscillations have been observed up to 10s of seconds in a vertical optical lattice structure [88, 89]. Trapped atom interferometers with caesium have recently shown very long interferometry times (up to one minute) by using an optical cavity to form the trapping lattice [90, 91] and ^{88}Sr is an interesting candidate to further these experiments.

The main transitions required for cooling and trapping and atom interferometry are shown in

Table 2.1: Abundances, mass, spin and magnetic moment values of all the cadmium isotopes.

Isotope	Mass (amu)	Abundance	Spin	Magnetic moment
^{106}Cd	105.91	1.25 %	0	
^{108}Cd	107.90	0.89 %	0	
^{110}Cd	109.90	12.51 %	0	
^{111}Cd	110.90	12.81 %	1/2	-0.5943
^{112}Cd	111.90	24.13 %	0	
^{113}Cd	112.90	12.22 %	1/2	-0.6217
^{114}Cd	113.90	28.72 %	0	
^{116}Cd	115.90	7.47 %	0	

Figure 1.2. In addition to this the so-called magic wavelength at 813 nm should also be considered important. In particular, atom interferometry will benefit from high-power and high mode quality beams at 461 nm, 689 nm and 698 nm, for the reasons discussed below in Section 2.3.2. High powers at 461 nm and 689 nm are also needed for efficient cooling and trapping. While the saturation intensity of the 689 nm transition is very low, so is the velocity range of its cooling force (equation 2.18). Magneto-optical traps on $^1S_0$ - $^3P_1$ therefore typically require the laser to be frequency modulated [92], which increases the power demands of the system.

Overview of cadmium

Cadmium is a soft transition material with an atomic number of 48 and it consists of eight isotopes in total (out of which six are abundant). It most commonly finds its applications in electroplating, batteries and pigments, and is water-insoluble along with being toxic for humans. Of the eight isotopes, six are spin-0 bosons and the other two are spin-1/2 fermions (see Table 2.1).

From an atomic physics perspective, cadmium is an alkaline-earth-like element with two electrons in the outermost orbit. This gives rise to a singlet and a triplet structure, thereby allowing for a dipole-allowed wide transition at 229 nm and a linewidth of 90.9 MHz [93], an intercombination transition at 326 nm with a 66.6 kHz linewidth [94], and the clock transition at 332 nm with a 7 mHz level of linewidth [95]. Unlike strontium, the generation of ultra-cold cadmium is relatively novel. Indeed, degenerate sources such as a Bose-Einstein condensate (BEC) has not been prepared.

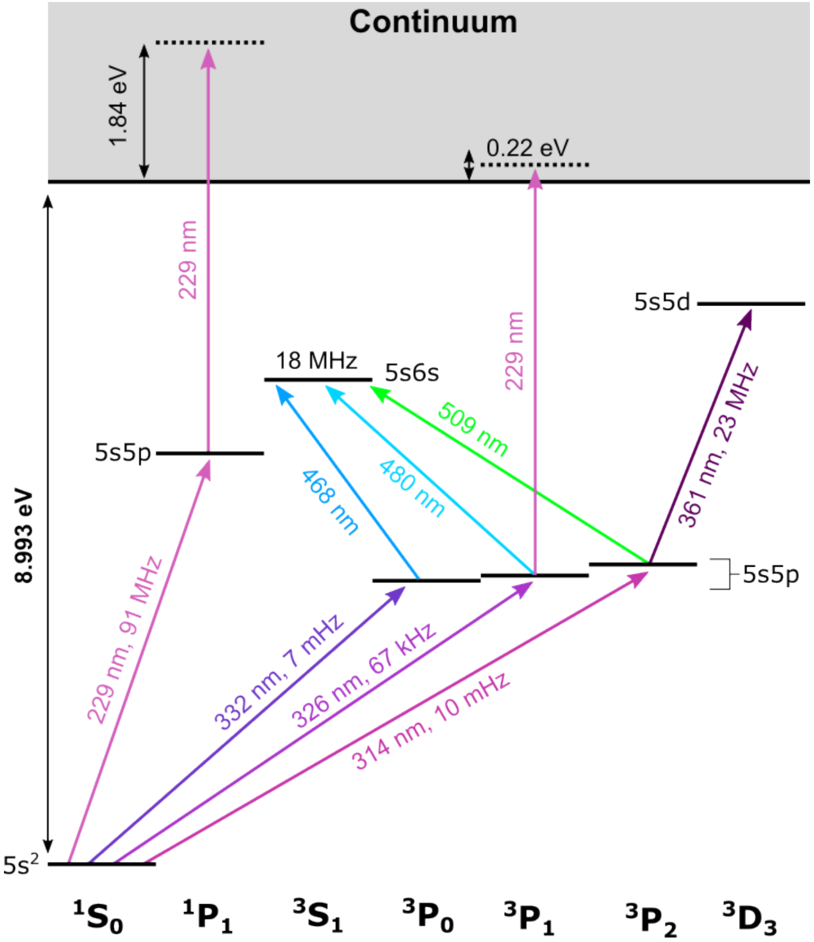

Figure 2.4: Electronic transition structure of bosonic cadmium

Its basic transitions are shown in Figure 2.4.

The clock transition in cadmium occurs at 332 nm which is in the ultraviolet regime. There is significant metrological interest in using cadmium as a clock due to its reduced sensitivity to black-body radiation [96], an order of magnitude less than strontium. This black-body frequency shift usually contributes to a significant systematic error in atomic clocks [97] and this lower sensitivity will reduce the need for cryogenics in the experiment [98]. The higher frequency of the transition will also increase the intrinsic sensitivity of both atomic clocks and atomic interferometers using this transition.

The singlet transition is the main Doppler-allowed cooling transition at 229 nm. Production of the DUV at this wavelength is the most challenging one and the characterization and challenges faced in development of the laser system at this wavelength are discussed in Chapter 3. Nevertheless, given its high scattering rate and low wavelength it has the ability to slow down atoms over very short stopping distances and is therefore potentially very useful for bringing the atoms from room temperature to mK levels. The first magneto-optical trap of cadmium was indeed performed on the 229 nm transition, with atoms loaded from an atomic vapor [99]. Here the most dominant loss mechanism of the MOT was also studied, which is the photo-ionization occurring from the $^1P_1$ state. These losses caused by 229 nm pose a challenge in designing a state-of-the-art atom source comparable to those of strontium (Chapter 7).

Eventually the first MOT on the intercombination was also performed and studied [54]. The atoms are loaded from a cadmium dispenser and the two MOTs on the 229 nm and the 326 nm transitions are performed at the same location. This eventually allows for an atomic ensemble close to the 1.58 μK Doppler temperature, with atoms cold enough in order to load them into a magic-wavelength lattice to ultimately perform clock spectroscopy.

Recently, theoretical interest has also increased in cadmium. Calculations on the clock states at the magic wavelengths and their magnetic dipole and electric quadrupole polarizabilities are performed in [55] and the magic wavelength was also measured as 420 nm [54]. It has also very recently been highlighted that cadmium is an excellent choice for making King's plots to search for new particles and physics [100] and estimations of mass and field shift parameters of the clock and other intercombination transitions are studied in [101].

2.3.2 Atom interferometry with intercombination transitions

This section discusses some of the advantages and laser requirements when performing atom interferometry with intercombination transitions. In particular, the cases of multi-photon Bragg interferometry and single-photon (or clock) atom interferometers are considered and discussed in more detail. The technological requirements for accessing these intercombination transitions is highlighted, in particular, the requirement of high-power, narrow-linewidth lasers in order to drive efficient transitions [59].

Bragg interferometry

Light-pulse atom interferometry in the multi-photon scheme is performed with counter-propagating laser beams where one beam excites the atom and it undergoes stimulated emission into the other

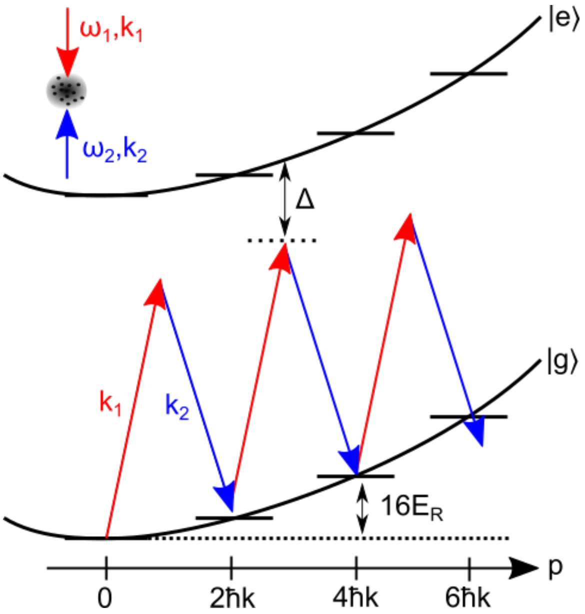

Figure 2.5: Light-pulse Bragg interferometry. The diffraction order in the case shown is $n = 2$.

beam and thereby undergoes a momentum change equal to the even number of exchanged photons. There are many different ways to perform these momentum changes, such as stimulated Raman transitions [11], Raman adiabatic rapid passage [102] and Bragg beams [103]. With Raman schemes the momentum change occurs along with a change in the internal hyperfine structure within the atom, whereas only the external momentum state change is acquired in the case of Bragg interferometry. Since the internal electronic state of the atoms remains constant in the Bragg procedure, errors from the Stark shift and some density dependent state shifts can be avoided. Due to the absence of hyperfine structure in the ground states of cadmium and strontium, the remaining discussion is restricted to the Bragg scheme.

While Bragg beams do not change the internal electronic state of the atom, the interferometric beams are coupled to a transition, as shown in Figure 2.5. The resonance condition for the two beams to perform diffraction is shown in equation 2.51, where $E_R = \hbar k/2m$ is the recoil energy, $\delta = \omega_1 - \omega_2$ is the angular frequency difference between the two Bragg beams and n is the diffraction order.

$$n\hbar\delta = 4n^2 E_R \tag{2.51}$$

The Rabi frequency of the Bragg interaction is shown in equation 2.52, where Ω_0 is the Rabi frequency from the individual beam component as defined earlier in equation 2.15 and Δ is the detuning shown in Figure 2.5.

$$\Omega_B = \frac{\Omega_0^2}{2\Delta} \tag{2.52}$$

An interesting property of intercombination transitions using Bragg beams is the number of atoms lost due to single-photon scattering (spontaneous emission). These losses occur because the Bragg beams can also cause standard scattering events as defined earlier by the scattering rate R (equation 2.13). For a standard Mach-Zehnder sequence the total interaction time is $2\pi/\Omega_B$ so the expected number of scatters S is $2\pi R/\Omega_B$. This is given in equation 2.53.

$$S = 2\pi R \frac{1}{\Omega_B} = 2\pi \left(\frac{\Gamma}{2} \frac{I/I_{sat}}{1 + I/I_s + 4\Delta^2/\Gamma^2} \right) \left(\frac{4\Delta}{\Gamma^2} \frac{I}{I_{sat}} \right) \tag{2.53}$$

Equation 2.54 shows that these losses S do not depend on the intensity of the Bragg beams, but only on the relative detuning by considering that at large detunings $I/I_{sat} \ll 4\Delta^2/\Gamma^2$ and so the denominator of the scattering rate can be written as $4\Delta^2/\Gamma^2$.

$$S \approx 2\pi \left(\frac{\Gamma}{2} \frac{I/I_{sat}}{4\Delta^2/\Gamma^2} \right) \left(\frac{\Delta}{4\Gamma^2} \frac{I}{I_{sat}} \right) \approx \pi \frac{\Gamma}{\Delta} \tag{2.54}$$

This means that to reduce losses and maximize coherence, large relative detunings Δ/Γ should be used. As the linewidth for intercombination transitions is much less than the dipole transition's linewidth, this means that smaller absolute detunings Δ are needed. This is a major practical advantage as small detunings are much simpler to achieve experimentally, as shown already in strontium [41]. Figure 2.6 shows this advantage in the case of the ^{1}S$_0$ - ^{1}P$_1$ and ^{1}S$_0$ - ^{3}P$_1$ transitions of cadmium, assuming they have the same Rabi frequency and same absolute detunings.

Figure 2.6 shows another advantage of using the intercombination transitions of cadmium and strontium for Bragg interferometry. Assuming the same relative detuning and intensity of the Bragg beams, a higher Rabi frequency can be achieved with the intercombination transition than the dipole-allowed transition. To see this consider that for a fixed relative detuning and intensity, the Rabi frequency scales as shown in equation 2.55.

$$\Omega_B \propto \frac{\Gamma}{I_{sat}} \tag{2.55}$$

As the saturation intensity is also proportional to the natural linewidth, equation 2.14 can be used to show that $\Omega_B \propto \lambda^3$. Therefore the intercombination transition will result in a higher Rabi frequency as shown in Figure 2.6 in the case of cadmium. In Figure 2.6, Δ=500 Γ and the beam waist w = 5 mm, which shows that high power Bragg lasers are needed if fast Rabi frequencies (>kHz) are to be achieved.

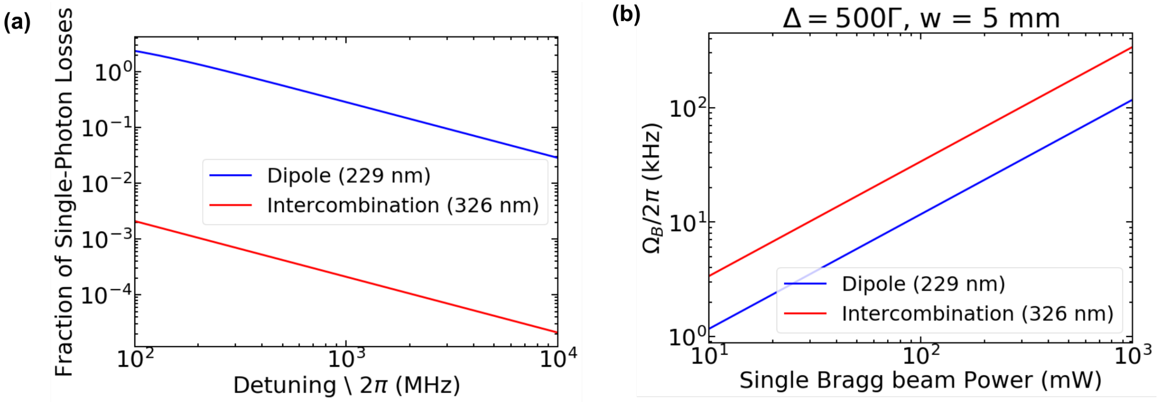

Figure 2.6: (a) Expected losses from single-photon scattering in a Bragg interferometer as a function of absolute detuning. (b) Expected Rabi frequencies as a function of Bragg beam power.

While the intrinsic sensitivity may be lower when using intercombination transitions, the faster Rabi frequencies and especially reduced spontaneous emission losses make them an excellent practical choice for Bragg interferometry.

Single-photon Atom Interferometry

The earlier discussions have assumed perfect interferometry lasers and therefore control of the atomic states. In reality, many things reduce this perfect control, including atom temperature and laser noise. One way to mitigate this is to use high Rabi frequencies, which is useful in improving pulse fidelity in both the cases of non-zero temperature (momentum width) [104] and in the presence of laser noise [59]. This requires high intensity interferometry beams.

In practice for an atom interferometer, high intensity means high power. This is because the beam cannot be made arbitrarily smaller as this will lead to wavefront curvature and therefore phase variations across the atomic cloud. Tight focusing will likewise lead to intensity variations and therefore Rabi frequency variations across the cloud. Both these effects will lead to a systematic effect in the differential phase shift. In the ideal case, the atoms would be interacting with plane waves with smooth flat intensities, which is approximated when the beam is much larger than the atom cloud and the Rayleigh length is much larger than the interferometry region. However, making the interferometric beam larger will also lead to reduced intensity and therefore reduced Rabi frequencies and can also lead to increased diffraction when the beam passes through the vacuum

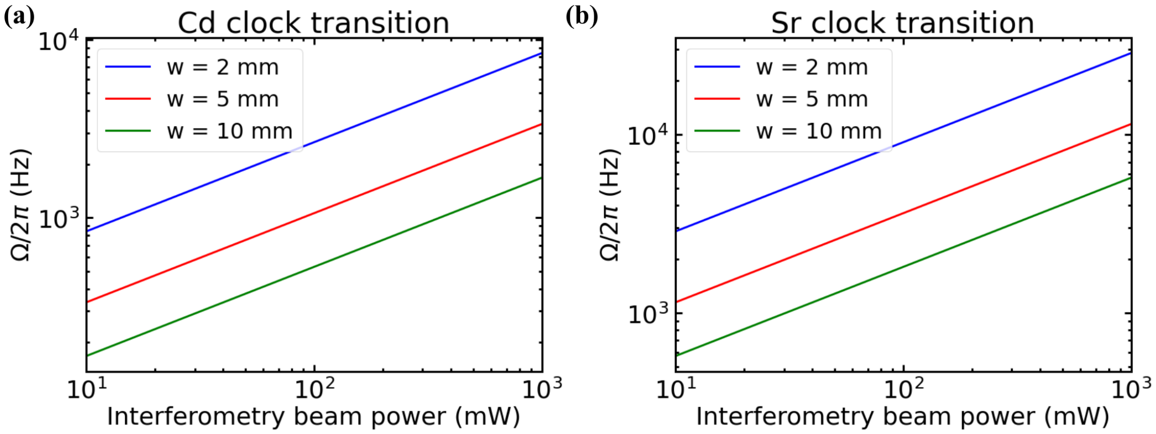

Figure 2.7: Calculated Rabi frequency for resonant interaction of laser light with clock transitions as a function of interferometric beam power for different waists for (a) cadmium and (b) strontium.

chamber viewports [105], as calculated for the dual-species interferometry chamber in Section 8.3.

For clock atom interferometers, the demand for high power represents an important practical difference with atomic clocks. The role of laser noise and Rabi frequencies for clock atom interferometers has recently been studied [59], but here the basic power requirements can be demonstrated by showing the calculated Rabi frequencies, according to equation 2.15, for cadmium and strontium as shown in Figure 2.7. As can be seen for the desired large beams (w >5 mm), >100 mW of power are required for $\Omega/2\pi >$ kHz. For this reason, it has been suggested to use cavities to build up power for clock atom interferometers [106], but here work on clock lasers with > 1 W power is presented (Sections 4.3 and 5.2).

2.3.3 Test of the weak equivalence principle

This section focuses on the possibility of using the cadmium-strontium atom interferometer to search for violations of the weak equivalence principle (WEP) or the universality of free-fall (UFF). General relativity, still the latest and current theory of gravity, is centered around these two principles, so it is important to understand and look for deviations around this principle to enhance any further extensions to the current understanding of gravity, especially its combination with quantum physics. As laboratory interferometers are invariably sensitive to gravitational acceleration, atom interferometry with two species is a natural testbed for understanding the effects of gravity on

Table 2.2: Estimation of effective k_{eff} vector ratio (by using suitable Bragg order n for each atom) for dual-species interferometer tests of UFF. Maximum common-mode noise rejection is obtained by setting the same interrogation times $T_A = rT_B$, where $r = \sqrt{k_B^{\text{eff}}/k_A^{\text{eff}}}$

A	B	λ_A (nm)	λ_B (nm)	$r = \sqrt{k_B^{\text{eff}}/k_A^{\text{eff}}}$
Rb	K	780.2	766.7	1.009
Yb	Rb	398.9	780.2	1.011
Sr	Cd	460.9	228.8	1.004
Sr	Cd	689.4	326.1	1.028

different masses.

Deviations from WEP can be quantified using the Eötvös parameter, which is expected to be zero according to general relativity. Current leading WEP values come from the MICROSCOPE collaboration, which recently published the final results using classical test masses on a satellite [107]. No violation of WEP was observed down to the 10^{-15} level of the Eötvös parameter. Along with this, the precision measurements performed with lunar ranging experiments have also measured down to 10^{-14} [108] with no violations recorded.

In the realm of atom interferometry, violations have most commonly been looked for by using two rubidium isotopes undergoing free-fall [109–112]. The best limit on the UFF from atom interferometry is currently at the 10^{-12} [111]. Clearly, this limit is much worse than tests done with other techniques as discussed above. Instead, dual-species interferometry has been done with rubidium and potassium [113] and proposed for ytterbium and rubidium [114]. The later suggests a theoretical sensitivity to violations down to the order of 10^{-13}. For higher accuracies to rival e.g. MICROSCOPE, performing such dual-species interferometers in space may be required, as this can provide longer interferometry times.

However, atom interferometry allows for WEP tests in unique ways, not accessible to experiments using classical masses. For example, simultaneous atom interferometry with rubidium atoms in different hyperfine states [112, 115], different spin states [116], and using rubidium atoms in a superposition of hyperfine states [117] has been studied which can provide insight on the quantum domain of WEP. Different isotopes of strontium have also been studied, taking advantage of using

^{87}Sr and ^{88}Sr and therefore one fermion and one boson (rubidium isotopes are both bosons), to investigate spin-gravity coupling [118]. This experiment limits this phenomenon to the 10^{-7} level.

For this purpose, atomic cadmium with six bosons and two fermions can be utilized. Bosonic isotopes of these elements can be used to perform Bragg interferometry and can be used to test the universality of free fall. The common-mode noise rejection in the large-momentum-transfer Bragg interferometry of the two species can be maximally cancelled if the interrogation times have a unit ratio (r=T_A/T_B). This ratio r is $\sqrt{k_B/k_A}$, with k_A and k_B being the effective k vectors of the interferometry beams for both species [119]. By selecting a suitable order of Bragg diffraction, the momentum transfer on both the atomic species (i.e. the effective k vectors) can be made as close to equal as possible and the common-mode noise rejection can be maximized. For the dipole-allowed ^{1}S$_0$ - ^{1}P$_1$ transitions of cadmium and strontium (229 nm and 461 nm, respectively), this ratio is 1.004. In comparison to the above-mentioned Rb-K (780.2 nm, 766.7 nm, r = 1.009) or Yb-Rb (398.9 nm, 780.2 nm, r = 1.011), the Sr-Cd ratio r is better. These results are summarised in Table 2.2.

2.3.4 Quantum interference of clocks

Another striking feature of general relativity is the gravitational redshift or time dilation effect. This law states that the speed of a clock depends upon the strength of the gravitational potential of its position. This prediction of general relativity has been experimentally verified many times, including the use of optical clocks on the laboratory scale [120]. Very recent demonstrations have shown changes in strontium optical clocks with changes of height of few cm [85] and a few mm [84]. These measurements are so sensitive that they have been practically used for geodesy using transportable clocks, for example inside a mountain [121] and at different floors of a skyscraper [122]. In addition to these demonstrations, gravitational time dilation has some interesting fundamental implications that can be checked when combining optical clocks with atom interferometers.

General relativity considers the flow of proper time to vary with space-time trajectories, while such defined paths are forbidden according to quantum mechanics. In the classical state of motion regime of the atom in a quantum clock, the clocks experience time dilation in the weak field and low velocity limit in accordance with the general relativity [123]. However, quantum effects like the dependence of the interferometric fringe visibility on the gravitational time are significant and cannot be treated as a systematic error, but instead require a quantum change to the general relativistic notion of proper time [60]. Changes in phase-shift also occur simultaneously and a dual-species atom

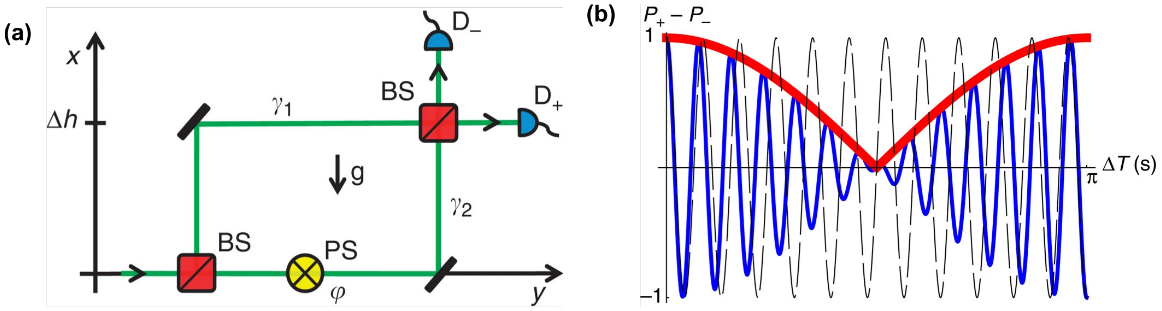

Figure 2.8: (a) Idea of experiment to test for gravitational-induced decoherence of a clock interferometer. (b) Expected signal as a function of interferometer time. Adapted from [60].

interferometer could be ideal to perform the precision measurements of the phase-shift parameter and subsequently the induced decoherence can be studied. The idea that this might be a kind of decoherence mechanism got some theoretical discussion a few years ago [124–126] and has been recently studied in more detail for clock atom interferometers [127] and for atom interferometers more generally [61, 128]. The possible quantification of time dilation effects using the coherence of quantum superpositions could lead to an understanding of the notion of proper time in the realm of quantum mechanics or even a quantum twin paradox. The clock states of cadmium could be an ideal species to test this principle with, as the transition lies in the ultraviolet regime thereby providing higher intrinsic sensitivity of the clock interferometer.

The non-destructive measurement of the quantum state of the atom prior to any interferometric measurement explains the complementarity principle [129]. These measurements are however performed on the external state of the atoms, mainly in the position and the momentum space, where general relativistic effects in the path of the interferometric arms are ignored. Theoretical understanding of the interferometric output considering the time dilation effects arising from the spatial separation of the arms is being studied [60].

Recently, there have been some groups studying about such time dilation effects in a broad range of phenomena related to clocks and spectroscopy. For the observed frequency shift in the ion trap atomic clock, an additional shift is also predicted thereby showing the deviations from the ideal theoretical clock model [130]. Another theoretical demonstration is discussed where the uncertainty in the time measured (due to the entanglement in the internal state of the atom and the external degrees of freedom) is lost by delocalizing the clock and a better precision is regained back by performing a measurement on the clock state. This quantum time dilation is further illustrated where the clock in a superposition state of the momentum wave packets [131]. The consequence of quantum dilation shows up as a change in the atomic emission spectrum. The quantum Doppler shift in a hydrogen-like atom clock scales as v/c, which is different from the emission rate of atoms which are in the superposition of the momentum states as v^2/c^2 [132].

By performing precision spectroscopy on the clock transition with the help of velocity-selective Bragg diffraction, the internal clock state and the external degrees of freedom of the atoms can be manipulated independently. This allows for the possibility to perform atom interferometry on an ensemble of atoms which have been prepared in a superposition of clock states. If the two arms of this interferometer are at different gravitational potentials (e.g. heights), then the gravitational time dilation can provide which-path information and therefore lead to a reduction in contrast. In the case of strontium, a similar idea is proposed which uses the magic wavelength of 813 nm to perform the large-momentum-transfer Bragg transitions, which demands higher powers [61].

Figure 2.8 shows the idea of an interferometer formed from two atomic clocks in a superposition at different heights. The decoherence is predicted to be observed in the interferometric signal as a periodic signal with a period $\mathrm{p} = \pi\hbar/\Delta E$, where ΔE is the energy difference of the two states. This signal can be seen fully in the interferometric output if $\mathrm{h}\Delta T = c^2/gf$, where h is the difference in height of the two interferometric arms and ΔT is the total time spent at those arms and c, g and f are the speed of light, gravitational acceleration and the clock transition frequency. For cadmium and strontium these values are 10 ms and 21 ms. In the case of cadmium, a 2 m height arm distance and a ΔT of about 5 s is enough to observe the periodic decoherence in the fringe output [60]. Strontium can potentially act as reference to confirm that the loss of coherence is really due to this effect and not e.g. background gas collisions etc.

Chapter 3

Infrared vertical-external-cavity surface-emitting laser as a master source for the $^1S_0$ - $^1P_1$ transition of cadmium

This chapter focuses on the development of a laser system to access the broad $^1S_0$ - $^1P_1$ transition of cadmium. In particular, a novel infrared vertical-external-cavity surface-emitting laser (VECSEL) is presented, developed specifically for this purpose in collaboration with a commercial company (Vexlum) [57]. The VECSEL offers easy tunability in the approximate range of 910 - 930 nm, meaning that it can act as a master source for the $^1S_0$ - $^1P_1$ transition of both strontium and cadmium, highlighting the technological synergy between these species. The main focus of this chapter is the development of the 229 nm light required for cadmium, but the performance of the system at 461 nm is also shown. As both the VECSEL at these wavelengths and the production of 229 nm were relatively undeveloped at the time of commencement of the experiment, a more historical approach is taken to guide and explain the technological challenges and how they were overcome. A more recent version of this VECSEL, where some of the limitations of this first-generation model have been solved, has been optimized for 461 nm and is presented briefly later in Section 5.1.

3.1 Introduction: Vertical-external-cavity surface-emitting lasers (VECSELs)

The wavelengths of the $^1S_0$ - $^1P_1$ transition are 229 nm and 461 nm for cadmium and strontium, respectively. This broad transition is useful in slowing and trapping the atoms in the form of Zeeman slowers, 2D/3D magneto-optical traps (MOTs) and optical molasses, and may also be used to perform Bragg interferometry. In order to enable the above techniques, the important requirements are to have a high-power, low-noise, single-frequency tunable laser source with good spatial mode quality [57]. It would be helpful and advantageous to have a compact yet robust source which can be easily maintained and is portable [133].

There are however, a limited number of laser sources in the wavelength regime of 450 - 470 nm. A stable laser source at these wavelengths would help in generating the deep ultraviolet (DUV) light at 229 nm via second-harmonic generation (SHG). Narrow-linewidth lasers are useful when using high-finesse, resonant cavities to perform this frequency doubling. In the recent times, there have been laser diodes emitting up to 1 W of power at 460.86 nm in the market, which are mainly designed to access the main cooling transition of strontium. These laser systems use a master external-cavity diode laser (ECDL) to inject a slave diode system. The longevity of this laser is determined by injection percentages into the slave diode and also the lifetimes of the employed diodes [128].

An alternative to direct production in the blue is to begin in the infrared (IR) regime. Expensive laser systems in the infrared region at 900 - 940 nm such as Ti-sapphire and neodymium-doped fiber systems are available, but come with large footprints and considerable expense. A smaller-scale laser source could be the usage of ECDLs coupled into tapered amplifiers before frequency doubling of the IR light. It is possible to achieve around 70 % coupling into the tapered amplifier from the infrared and to produce powers up to around 2 W [134]. Here, however, the poor and variable mode quality of the tapered amplifier output means that it is difficult to efficiently couple this power into a doubling cavity. Powers produced in the visible region are therfore limited to 500 - 1000 mW.

Here a vertical-external-cavity surface-emitting laser is employed, termed as VECSEL [135]. This laser produces high-power and narrow-linewidth IR radiation with an excellent mode quality and single-frequency operation. The low-noise operation of VECSELs is due to the low carrier lifetime, which is crucially less than the photon cavity lifetime [135]. It has a relatively simple configuration and is quite compact along with being lower in cost, in comparison to the above mentioned systems (cf. the Ti-sapphire laser presented in Section 5.2). The footprint of the laser is about 19 × 32 cm^2

and is just one key-turn away from lasing at the desired settings, provided the internal drivers and wavelength selecting elements are at the right temperature setting [57].

There are low-noise tunable VECSELs that have previously been applied in the atomic physics community but were not commercialized and have not gained widespread adoption. Experiments using these lasers sources include the generation and manipulation of magnesium ions to perform quantum information processing experiments. By using two-successive frequency doubling stages, light at 285.3 nm resonant with $^1S_0$ - $^1P_1$ transition in magnesium atoms is produced by a VECSEL with an intra-cavity lithium tri-borate crystal. Also light for the Doppler cooling of $^{25}Mg^+$ is generated with the same technique, specifically for the cycling and re-pumping transitions at 279.6 nm and 280.4 nm respectively [136]. An AlGaInP-based VECSEL system has been used to access the narrow-linewidth intercombination transition of strontium atoms at 689 nm. It operates with sub-kHz linewidth and can be applied to laser cooling, trapping and interferometric purposes with neutral strontium atoms [137]. Finally, two VECSELs were used to generate ultraviolet light at 235 nm and 313 nm for the purpose of photo-ionization of beryllium atoms. They are also used to laser cool these $^9Be^+$ ions and to perform quantum information processing experiments with trapped beryllium ions [138]. The laser also demonstrated the capability to produce high-fidelity quantum gates [138].

This chapter is mainly focused on the performance characterization of a VECSEL based on a novel gain chip design and operating at 915 nm. It will also delve into the details of the production of the second-harmonic blue at 458 nm and another frequency doubling stage to produce the deep ultraviolet (DUV) light at 229 nm using home-made bow-tie cavities. With the DUV produced, precision frequency measurements are performed via spectroscopy on a novel cadmium atomic beam, as reported in Chapter 6. The results of the characterization of this novel system have been previously reported in [57].

3.1.1 Laser internal and external set-up

The developed VECSEL was produced by the company Vexlum and characterized at the University of Florence. It is capable of lasing with W-level output powers in the wavelength range 910 - 928 nm. This laser is based on a novel gain chip mirror design which emits in the 900 - 930 nm range of the spectrum and is pumped by a semi-conductor diode laser at 808 nm with output powers up to 15 W. The combination of this gain chip along with a birefringent filter, etalon and a curved mirror with a piezo electric transducer (PZT) form an optical resonant cavity. Figure 3.1 shows the

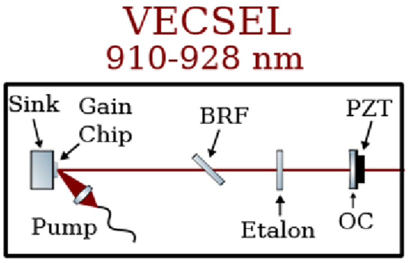

Figure 3.1: Internal components of the laser: Laser cavity - consisting of a gain chip mounted onto a heat sink along with frequency selective elements - birefringent filter (BRF), etalon and a piezo electric transducer (PZT) on the out-coupling mirror (OC).

internal structure of the laser cavity which gives an idea of how these wavelength selecting elements are placed within the cavity.

The gain chip is a monolithic semi-conductor structure which rests on a high thermal conductance $3 \times 3 \times 0.3$ mm^3 diamond heat-spreader. The disk shaped geometry of the heat spreader aids in efficient heat extraction from the pump laser to the thermoelectric element (TEC) stabilized cooling mount. The heat is further transmitted to a heat-sink which is cooled down with a chiller maintained at 20 °C.

This gain chip is grown on GaAs substrate and the active region of this substrate consists of GaInP window and multiple quantum wells made up of GaInAs. These quantum wells are placed at the anti-nodes of the emission, which enhances stimulated emission and prevents amplified spontaneous emission [135]. Figure 3.2 shows the schematic of the gain mirror and its cooling assembly.

The new semi-conductor is coated with an anti-reflection using ion-beam sputtering in order to minimise the reflections of the pump light. It also helps in protecting the semi-conductor surface from the tightly focused, high power 808 nm pump beam. With this gain mirror and a curved out-coupling mirror, a 12 cm cavity is formed. The transmission of the curved mirror is 1.5 % with a radius of curvature of 200 mm. Using this, the waist size of the pump beam on the gain chip is matched to the waist of the cavity for efficient coupling of the stimulated emission to the waist of the cavity. This cavity is not under vacuum but is tightly sealed from the external environment.

The tunability ranges of the frequency selective elements within the laser cavity are shown in Table 3.1. The most coarse selection is obtained by manually rotating a birefringent filter for which

Table 3.1: Frequency selective elements of VECSEL internal set-up and their tuning range

Element	Frequency range
Gain chip	–
BRF rotation	10 - 0.1 THz
BRF temperature	1 - 0.1 THz
Etalon temperature	100 - 1 GHz
PZT	0 - 1 GHz

there is a separate outlet on the top of the laser housing to access it. This gives a coarse tuning from 10 - 0.1 THz. This feature is generally used while changing the laser frequency to access one of the two cooling transitions at 229 nm (for cadmium) or at 461 nm (for strontium). This alteration can also be achieved in a more refined way by changing the temperature of the birefringent filter, between values of 27 - 40 °C. With this tuning, 1 - 0.1 THz of range is achieved.

Finer tuning is achieved by varying the temperature of the etalon, whose presence also helps to ensure single-frequency emission. Changes in the etalon temperature lead to changes in the optical path length of the beam and therefore the frequency. The etalon works in a temperature range of 27 - 80 °C corresponding to frequency tuning range of 100 - 1 GHz. Figure 3.3 shows how changes in the temperature in the birefringent filter the and etalon leads to a corresponding change in the laser emission frequency and also the respective power. As can be seen, there is a range of tunable temperatures of these frequency selective elements, which correspond to a varying optical power

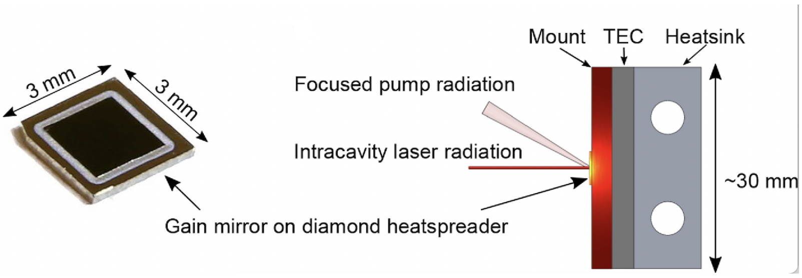

Figure 3.2: Gain chip on a 3 × 3 × 0.3 mm^3 diamond heat spreader, schematic of the cooling body of the gain chip which shows the TEC and heat sink.

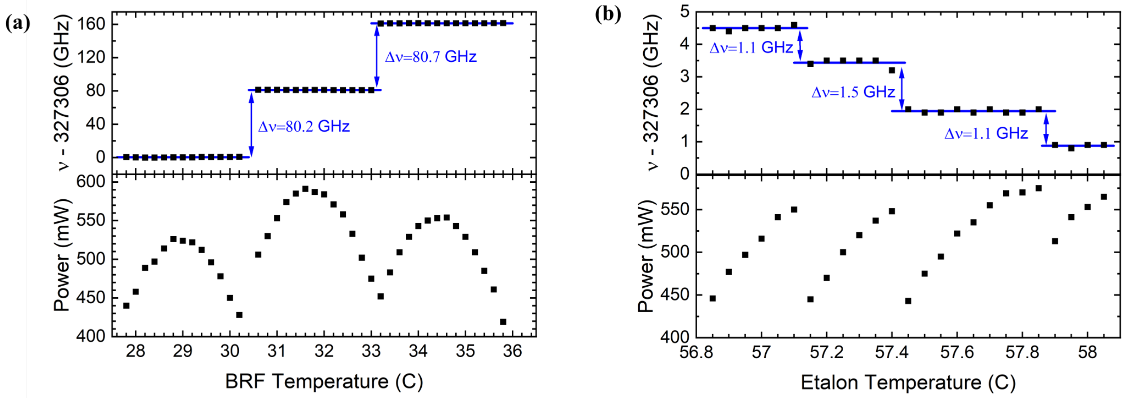

Figure 3.3: Frequency and power change in the laser emission with respect to the change in (a) the birefringent filter and (b) etalon temperature.

output while maintaining approximately constant emission frequency.

The finest tuning element is the length of the cavity which is adjusted by the piezo-electric transducer (PZT) on the curved mirror. It is a continuous tuning method, whereas the previous methods are discrete in nature, and allows for a continuous frequency change within the free spectral range (FSR) of the etalon. When the PZT on the output coupler is tuned the frequency is changed smoothly within the mode of the etalon. Once the edge of the etalon mode is reached, a mode hop is observed thereby showing up as a discontinuity in the frequency domain. This is experimentally seen as a sudden jump in the power. The mode-hop free scan is therefore the FSR of the etalon which is 1.2 GHz (Figure 3.3). However, it is possible to change the temperature of etalon at the same time as moving the PZT which means one would be able to stay on resonance with a single etalon mode for a longer range (as changing the temperature changes the length of the etalon and hence its central frequency). This PZT has a measured sensitivity of 14.2 MHz/V and is used to actively stabilize the laser. It has a bandwidth of 50 kHz, measured by looking at the amplitude modulation of the output laser light.

While all the above methods generally exhibit hysteresis, with these wavelength-selective elements, a continuous frequency control over 1.2 GHz free spectral range (FSR) in the infrared (IR) and across a full range of 20 nm is achieved.

The set-up described above consists of a laser head, a control unit and a chiller. The control unit head allows us to set the temperatures of the laser driver's thermoelectric cooler (TEC), gain chip, etalon and the birefringent filter (BRF) and is easy to operate, close to a turn-key system. There are two channels in the laser housing which allow the inflow and outflow of distilled water which helps in maintaining the overall temperature of the laser head and all the elements in it at 20 °C. The chiller employed not only ensures constant temperature but also helps in keeping the length of the laser cavity stable thereby reducing the relative intensity noise (RIN) and the frequency noise of the laser. This makes the laser resistant to variable atmospheric conditions and helps in producing constant powers.

Finally, it has been observed that there is some absorption due to the water vapor molecules in the air at 900 - 930 nm wavelength. To avoid any water traces the cavity is purged with nitrogen. The absorption due to the water molecules reduces the circulating power within the cavity which decreases the output lasing powers. The master laser head therefore has an aluminium housing with an inlet for, a very low pressure flow of nitrogen gas, <2000 sccm with a tube of 6 mm diameter. The outlet pipe also allows to connect, for example, another laser in series which could require the nitrogen flow, compromising with a reduced pressure of the flow.

3.2 Laser behaviour and primary second-harmonic generation (SHG) at 458 nm

3.2.1 VECSEL characterization

The VECSEL emits with a nearly circular Gaussian beam with excellent mode quality, with a measured M^2 value of less than 1.02. Figure 3.4 (a) shows the output power produced as a function of emission wavelength. This laser can produce powers greater than 1 W in the region of 908 - 915 nm and greater than 2 W between 915 - 928 nm. It is observed that the higher powers are produced at higher wavelengths until dropping down rapidly, with a maximum of ~3 W are obtained at around 925 nm.

Figure 3.4 (b) shows the output power produced with respect to the current of the pump laser diode at both 915 nm and 922 nm emission, relevant for the main cooling transitions for cadmium and strontium, respectively. The vertical error bars correspond to the systematic error arising from the accuracy of the power meter used for the measurement. It is 3 % as specified by the manufacturer. The wavelength is measured with a commercial wavemeter (WaveMaster, Coherent). The maximum power this master laser can emit is ~2 W at a wavelength of 915 nm. The produced power can

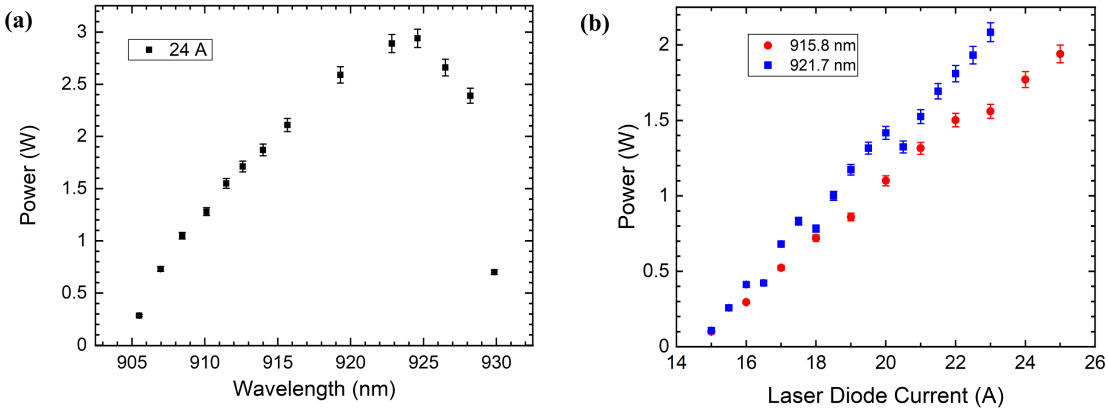

Figure 3.4: (a) VECSEL optical power produced with respect to wavelength of emission at a pump laser diode current of 24 A. (b) VECSEL power produced with respect to laser diode current close to the target wavelengths (blue squares at 921.7 nm, and red circles at 915.8 nm). Error bars are from the systematic error of the power meter.

be enhanced by lowering the gain chip temperature. Figure 3.5 shows such a measurement and the highest power obtained being 2.01 W at 18 °C.

During the power measurement at the highest laser diode current of 25 A at a wavelength of 921.724 nm, there was irreparable damage to the gain chip. It was initially misunderstood as a loss of alignment and several trials were made by tweaking the out-coupler mirror in order to retrieve the lost power. Figure 3.6 shows the functioning chip without damage first and then in the next panel one can observe the non-circular nature of the illuminated spot by the pump laser on the gain chip, confirming the predicted damage. The laser was sent back to the company and had the gain chip replaced with a new design. The Vexlum company made upgrades to the gain chip design due to the excess heating observed at these wavelengths. For this reason, a more recent model has been implemented for addressing the $^1S_0$ - $^1P_1$ of strontium (see Section 5.1).

The frequency noise and the intensity noise properties of the laser are studied. A stable power production is observed over 1 hour at a pump diode current of 25 A. The power is measured to be within ± 0.5 % of the initial starting value throughout this time period [57]. This and the relative intensity noise (RIN) is described in more detail in Section 3.2.2.

Figure 3.7 shows the spectral density of the frequency noise of the free-running laser. To perform

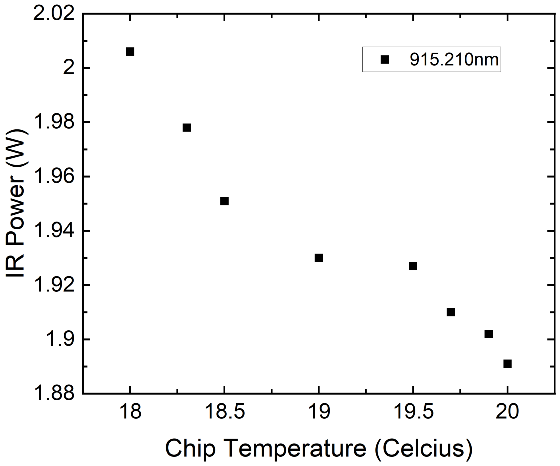

Figure 3.5: Power of emission at 915.21 nm as a function of the gain chip temperature.

this measurement of the free-running laser, the VECSEL is aligned to a home-made bow-tie cavity. The error signal is generated using the Hänsch-Couillaud locking technique from the reflected signal from the cavity. The electronic circuit board for generating this signal consists of a polarizing beam-splitter and small-area photodiodes at both transmission and reflecting outputs, which are then connected to trans-impedance amplifiers and subtracted. The cavity acts as a frequency reference and the obtained error signal contains the information about the frequency fluctuations of the laser with respect to the frequencies the cavity is resonate with.

The slope of the error signal is calibrated by using the linewidth of the cavity. The linewidth of the cavity is measured by using side bands spaced at 10 MHz with an electro-optical modulator (EOM). The value is measured to be approximately 2 MHz. The error signal measurement is taken at various frequency ranges using an oscilloscope. Figure 3.7 shows the frequency noise measurement of the free-running laser and the background. The background measurement (dashed black line) is performed when the laser is tuned out of resonance with the cavity. From the power spectral density of the frequency noise (red line) and the background, a peak at 1 kHz is observed. This peak arises from the electrical noise of the supply from the pump diode laser and can be removed by filtering this electronic signal. Linewidth of the emission can be characterized in multiple ways, one such evaluation is based on the phase noise spectral density function, also termed as fast linewidth. This

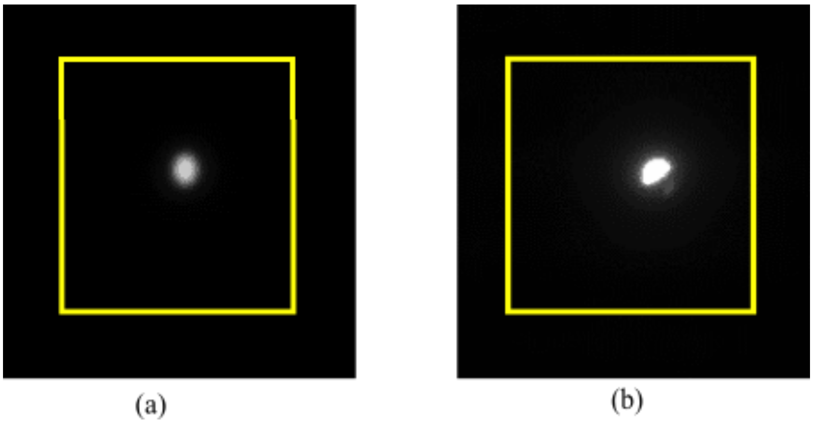
(a) (b)

Figure 3.6: Image of the (a) functional gain chip and (b) of the burnt gain chip (non-circular emission observed). The yellow square represents the approximate area of the gain chip.

linewidth $\Delta\nu$ is defined as given in equation 3.1 [139]:

$$\int_{\Delta\nu/2}^{f_{max}} S_\Phi(f)\, df = 1 \tag{3.1}$$

where the phase noise is given by equation 3.2, within which $S_\nu(f)$ is the measured power spectral density of the frequency noise:

$$S_\Phi(f) = \frac{S_\nu(f)}{f^2} \tag{3.2}$$

The linewidth is estimated to be 8 kHz according to the definition from the equation 3.1. The root-mean-squared linewidth is also considered at different timescales by integrating $S_\nu(f)$:

$$\Delta\nu_{rms}^2 = \int_{1/t}^{f_{max}} S_\nu(f)\, df \tag{3.3}$$

This method gives linewidths of 4 kHz and 100 kHz at timescales of 100 μs and 100 ms, respectively. This result is in agreement with the linewidth calculated from the beta-line estimation method [140] which is about 1 kHz at 100 μs timescale. This value is much less in comparison to the transition being addressed which is about 32 MHz and 90.9 MHz for strontium and cadmium, respectively. However, this low linewidth helps in better coupling efficiencies by using almost 90 % of the IR power for the second-harmonic generation purpose, which is discussed in the next section. In any experiments where one requires narrower linewidths at such frequencies, there is also a possibility of locking this laser to a high-finesse cavity. This represents a major improvement with respect to ECDL and tapered amplifier based schemes, where the linewidth is typically much higher (>100 kHz).

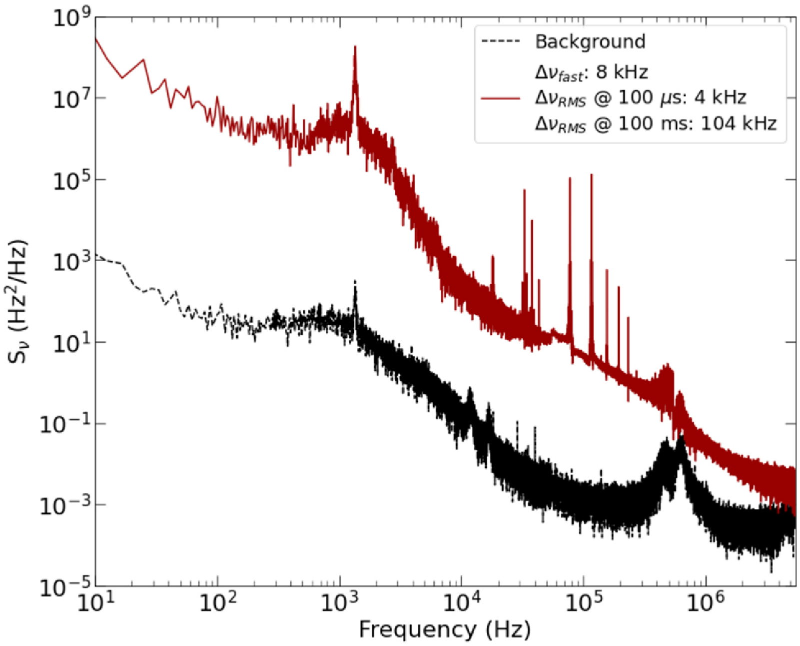

Figure 3.7: Power spectral density of the frequency noise of the free-running VECSEL (red line) measured from the error signal of the Hänsch-Couillaud locking system and the background measurement taken while the laser is out of resonance with the cavity (black dotted line).

3.2.2 SHG production in a resonant lithium triborate (LBO) cavity

For the production of the second-harmonic generation light (SHG) at 458 nm, the infrared light at 915 nm is mode matched to a home-made bow-tie cavity using a nonlinear crystal as the doubling medium. This section begins with the theoretical description of SHG production in a resonant cavity before the cavity design and performance is discussed. The SHG power is given by equation 3.4, where P_ν is the fundamental power and E_{nl} is the nonlinear coefficient of the crystal:

$$P_{2\nu} = E_{\text{nl}} P_\nu^2 \tag{3.4}$$

It is clear that increasing the produced SHG is dependent upon maximizing E_{nl} and especially P_ν due to the square dependence. The nonlinear coefficient of the crystal is given by equation 3.5 [141], where d_{eff} is the nonlinear coefficient of the crystal, l is the length of the crystal, n_ν and $n_{2\nu}$ are the refractive index of the crystal for the fundamental and SHG, α is the absorption in the crystal and

λ is the wavelength of the fundamental light:

$$E_{\mathrm{nl}} = \frac{16\pi^2 d_{\mathrm{eff}}^2 l}{\epsilon_0 c \lambda^3 n_\nu n_{2\nu}} e^{-\alpha l} h_m \tag{3.5}$$

For phase matching condition, $n_\nu = n_{2\nu}$. The parameter h_m is the Boyd-Kleinman coefficient which depends on the walk-off angle of the crystal and the ratio of the crystal length to the Rayleigh length of the focused input [142]. To maximize the Boyd-Kleinman coefficient, the waist of the input beam must be carefully selected depending on the crystal length, walk-off and input wavelength. The Boyd-Kleinman factor can be further optimized by considering an elliptical waist [143], but this is not considered in the cavity design described here.

On the other hand, to maximize P_ν a resonant cavity is used. The circulating power in the cavity is given by equation 3.6 [141], where T is the transmission of the input coupling mirror, ηP is the power coupled to the cavity, l_c is the linear losses in the cavity excluding the input coupler:

$$P_c = \frac{T\eta P}{\left(1 - \sqrt{(1-T)(1-l_c)(1-E_{\mathrm{nl}}P_c)}\right)^2} \tag{3.6}$$

From this, it can be noted that reducing the linear losses of the cavity is very important to maximising the SHG. This means the finesse of the cavity should be as large as possible.

The final consideration is the input coupler. There exists an optimum input coupler for any cavity design and input power. This is given by equation 3.7 [141]. Typically, trials with different input couplers about this value is made and the relative SHG production is maximized.

$$T = \frac{l_c}{2} + \sqrt{\frac{l_c^2}{4} + E_{\mathrm{nl}}\eta P} \tag{3.7}$$

A home-made doubling cavity has been designed based on these discussed considerations, and inspired by a similar frequency-doubling system which produces 1 W of light at 399 nm from a continuous Ti-sapphire laser at 798 nm [141]. The design of this cavity has been presented previously in [57, 144]. In brief, however, a compact home-made bow-tie cavity is constructed with a lithium triborate (LiB_3O_5, LBO) crystal as the doubling medium. Although crystals like potassium titanyl phosphate (KTP) are available with higher nonlinear coefficients, the LBO crystal was chosen as it is meant to be durable and long-lasting. For example, there is an age-related damage process in KTP called grey-tracking which leads to decrease in performance with time [145]. The cavity is built in a monolithic aluminium housing, which can be tightly sealed and the cavity region evacuated. This design is made for enhanced thermal and mechanical stability, with the mirror mounts directly screwed into the bulk of the material.

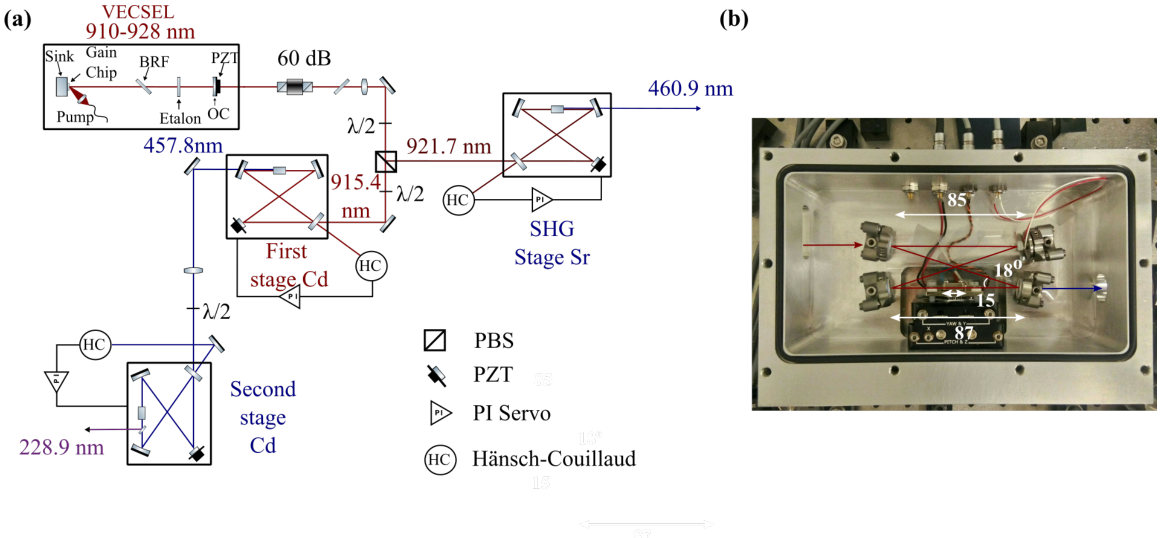

Figure 3.8: (a) Optical schematic of the laser system for generating light at 229 nm or 461 nm. The laser operates at either 915 nm or 922 nm and does not produce these two colours simultaneously. For 229 nm generation, firstly the IR output of the VECSEL is shaped and frequency doubled to 458 nm which is used to generate ultraviolet light at 229 nm. (b) Photograph of the opened home-made bow-tie cavity along with the dimensions expressed in mm.

Figure 3.8 (b) shows the internal image of the LBO frequency doubling cavity highlighting the distances between the plane mirrors and the curved mirrors and also the crystal length (15 mm). The two concave mirrors have a radius of curvature of 75 mm, an angle of incidence of 9° and are separated by 87 mm. The tangential and saggital waists between the curved mirrors are estimated to be 40 μm and 42 μm, respectively. The calculated Boyd-Kleinman factor is 0.28 which is close to the maximum for this given wavelength and the length of the crystal [142]. The design optical path length is 362 mm and the free spectral range is 829 MHz.

The secondary waist is formed at the mid-point between the two plane mirrors and is about 220 μm in the tangential plane and 244 μm in the saggital plane. One of these plane mirrors is used for incoupling the light and the other has a PZT attached to it to finely vary the length of the cavity. The transmission of this in-coupling mirror is about 1 % (nominal and measured), from which the theoretical value of the finesse is calculated to be about 450, as estimated from the roughly expected linear losses in the cavity, such as the reflectivity of the mirror coatings and the absorption in the crystal. The plane mirror on which the PZT is mounted has a diameter of 6.3 mm, compared to 12.7 mm for the remaining mirrors. This smaller diameter is chosen to minimize the mass or the mechanical load for the PZT. The first mechanical resonance of this PZT mirror is estimated to be at approximately 100 kHz.

The LBO crystal (Raicol) is cut for Type-I phase matching at 25 °C at an angle of 21.7°, the value required for the second-harmonic generation of 458 nm. The crystal has an anti-reflection coating on both sides for both the fundamental and SHG and a 1° angled cut is employed on the input and output faces to avoid etalon effects. The crystal is placed at the mid-distance between the two curved mirrors and is set to be at a constant temperature of 25 °C through feedback via a thermoelectric cooler attached to the crystal mount.

This cavity is capable of working for both 915 nm and 922 nm, with the mirrors coated for both wavelengths and negligible changes to the cavity's optical parameters. Each time the emission wavelength is altered, the phase matching angle to the crystal has to be adjusted for optimal performance. To match for the wavelengths for cadmium and strontium cooling transitions, the crystal angles are optimized for both the cases where one can simply alter the crystal position for the best performance. For this, a five-axis aligner is used which allows independent translation about all three coordinate axes to position the crystal precisely in the x, y and z directions. There are tip and tilt control screws from two independent positions in each case, which means in addition to translation, the crystal can be angled in the two transverse directions. Finally, it is also possible to translate the crystal in the axial direction to centre it at the cavity focus.

Light is sent to this cavity as shown in Figure 3.8 (a). The first component in the optical set-up is a 60 dB Faraday isolator which helps in preventing any back reflections to the laser cavity. A bi-convex lens of 500 mm focal length is used to match the IR beam to the secondary waist within the cavity. Very high coupling efficiencies of up to 90 % are achieved, due to the excellent mode quality of the VECSEL (see Section 3.2.1).

The performance of the cavity is optimized by measuring the finesse in gradual steps. Firstly, the input beam is aligned by removing the in-coupling mirror to make sure the height is at the center of the cavity mirrors and to confirm if the beam hits the center of the remaining three mirrors. This process is done iteratively. The power of the SHG is optimized in this single-pass configuration before closing the cavity. This is done by adjusting the position of the crystal carefully. Once the optimum position of the crystal is achieved, the in-coupling mirror is placed and the cavity is closed. This helps in building up the power in the closed cavity configuration and the SHG is maximized by tweaking the mirrors, but not moving the crystal position. Once the power has been optimized with the mirrors, the phase matching angle of the crystal is re-optimized and this process can continue iteratively.

In each of these steps, the finesse is measured by observing the transmission peaks and compared to the theoretical value which gives an idea of which component is responsible for power losses observed, if any. Following this optimization procedure a finesse of around 400 is measured, slightly lower than the theoretical maximum given above. The finesse measurement is performed by introducing side bands at 10 MHz by using an electro-optical modulator (EOM) and then fitting the cavity resonance to a Lorentzian to estimate the linewidth. With this EOM, the spacing of the side-bands is used as a frequency reference in calibrating the resonance peaks from the cavity.

When the cavity is not under vacuum, in one full triangular sweep (i.e. both up and down in frequency), the transmission peaks from the cavity do not look symmetrical. During a sweep up in frequency, the peak looks thinner and sweep down the peak looks wider than the usual. This is attributed to a pushing and pulling effect due to the high-circulating powers causing a heating effect [56]. This shows up as a change in the optical path length and the symmetry breaking with respect to the change in frequency of the laser results in the varying transmission peaks while changing the sweep. When the cavity is under vacuum, this problem is solved and uniform peaks are observed. For the vacuum, a rubber O-ring and a Swagelok along with a membrane pump is used to reduce the pressures to the 1 mbar level. This vacuum also protects the cavity from acoustic noise and helps in generating better and more stable locks.

The cavity is locked to the laser by using the Hänsch-Couillaud locking mechanism [146]. The derived error signal is sent to the PZT within the cavity to keep it on resonance with the laser via an optimized proportional-integral controller. Figure 3.9 (a) shows the SHG power produced as a function of the fundamental IR light coupled into the cavity at both the wavelengths of interest, 915.5 nm for cadmium and 921.7 nm for strontium. The cavity can produce powers greater than 1 W at 461 nm which can be used directly for strontium atoms. The power is slightly less in the case that the cavity is producing 458 nm for cadmium atoms since the power produced by VECSEL at the respective IR wavelength is lower (Figure 3.4). However, higher conversion efficiencies in the cavity for 458 nm are observed which is attributed to higher finesse and circulating powers or perhaps better alignment and phase matching of the crystal. The shaded region represents the uncertainty from the fitting. This data is fit by varying the linear losses of the cavity whilst holding the other parameters fixed, by theory. From these fitted linear losses, the finesse of these cavities is extracted

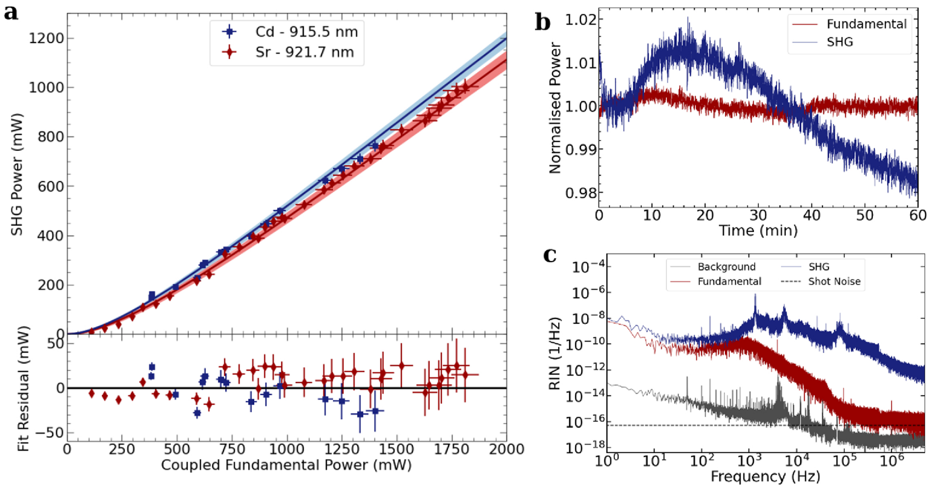

Figure 3.9: (a) Blue SHG power is plotted against the coupled IR fundamental power at both input wavelengths of 915.5 nm and 921.7 nm and below is the residue plot from the fit (performed by varying the linear losses of the cavity) to the observed values. The error bars in the above graphs represent the error coming from the systematic uncertainty in the measurement of power by the power meter (±3 %). (b) The normalized power stability of the fundamental IR and the subsequently produced SHG over a 1 hour time scale. (c) The relative intensity noise (RIN) of the IR produced from the laser and also how it reflects onto the SHG blue. Background RIN measurement is also shown which is taken while the light going to the photodiode is blocked. The dotted line is the shot noise limit.

as 387 ± 6 and 367 ± 7 for cadmium and strontium cavities, respectively. These values are lower than previously mentioned values which we obtained from determining the linewidth. This suggests that the performance of these cavities can still be improved, and higher SHG powers attained by optimization. The current understanding is that the angle of the crystal is not perfectly normal to the input incident beam, which reduces the circulating power as the coatings and the cavity are designed for the angle of incidence of 0°. Fundamentally, there is nothing limiting the performance of the cavities in terms of the power produced, i.e, more SHG powers can be expected by increasing the circulating power. This is expected because there are no heating effects or any sign of saturation observed in the SHG power produced as shown in Figure 3.9 (a).

Figure 3.9 (b) shows the power stability measurement of the SHG produced for a period of 1 hour. This measurement is performed using an amplified biased photodiode and shows power stability within 2 %, while the fluctuations from the VECSEL is about 0.5 %. This is further characterized by studying the relative intensity noise (RIN). The measurement shown in Figure 3.9 (c) is made by using a small-area, amplified photodiode with a bandwidth of approximately 100 MHz. This RIN measurement graph shows the intensity noise measurement with respect to the frequency of the fundamental, SHG and the background. It is observed that until 1 kHz, the RIN of the fundamental and the SHG are almost at similar level. However, due to the limited bandwidth of the electronics used, at higher frequencies, RIN of the SHG is much higher and a peak at 1 kHz is also observed. This peak is caused by the previously discussed peak in the frequency noise of the VECSEL (see Figure 3.7), which is not fully actively compensated here and is then being converted to amplitude. The intensity noise of the fundamental decreases at higher frequencies, however, reaching the shot-noise limit at a Fourier frequency of $\sim 10^6$ Hz. The shot-noise limit given by $S(f) = 2h\nu/P$, where P is the power used in the measurement, which in this case was 8.5 mW.

3.3 Second-stage second-harmonic generation of 229 nm

3.3.1 Deep ultraviolet production and implementation: Problems and solutions

For the cadmium system a second doubling stage is required to make the needed 229 nm light. However, making deep ultraviolet (DUV, <280 nm) is difficult due to a number of important technical reasons.

Firstly, purchasing high-quality anti-reflection and high-reflectivity coatings at these wavelengths is not easy. For example, it is experimentally observed that optics with oxide coatings display worse power degradation in comparison to those using fluoride coatings, as tested at 244 nm [147]. Furthermore, the rate of power degradation increases with increasing circulating powers. In order to compensate for the surface oxide depletion of the coatings, the optics are flushed with oxygen which leads to a rapid recovery in performance. However each time the oxygen replenishment is performed, the recovery is only partial and the performance degrades irreversibly with use. Slight changes in alignment can help in recovering the lost power, similar to what we experienced with our doubling crystals (see Section 3.3.3), but again this is only a temporary solution.

Tight focusing of DUV light will exacerbate the above depletion problems, but this is required for high intensities in the crystal and therefore conversion efficiencies. One possibility is to use elliptical focusing to optimize the Boyd-Kleinman coefficient [143], while keeping the spot size relatively large. Such elliptically focused doubling cavities have been demonstrated [148], but they remain in their infancy. There is also evidence that cesium lithium borate - $CsLiB_6O_{10}$ (CLBO) is less prone to UV-induced damage than beta barium borate crystals (β-BaB_2O_4, BBO) [149, 150], however unfortunately it cannot be used for phase matching down to 229 nm and BBO must be selected in the present case.

In the following section the design and characterisation of the doubling cavity for producing DUV is presented, with emphasis on how we have tried avoid or minimize these problems.

3.3.2 Design of the doubling cavity for 229 nm production

The 458 nm produced in the home-built frequency-doubling cavity is itself doubled in a resonant optical bow-tie cavity. In this case, a commercial bow-tie cavity (Agile Optic) specially designed for this purpose is used. To try to help with stable DUV production, the cavity uses vacuum-compatible feedthroughs to control the mirrors and crystal holders so that the cavity is isolated from the lab environment. The cavity can also be sealed with indium and has gas inlet ports to allow for the flow of clean air or oxygen to help prevent the degradation discussed above.

The mechanical design is based upon a monolithic and stable structure previously used for producing 313 nm [151], although the size of cavity is enlarged to increase the waist within the doubling crystal, sacrificing some conversion efficiency to try to reduce DUV-induced damage. The radius of curvature of the focussing mirrors is 200 mm and the focussed waist is 70 μm and 43 μm in the tangential and sagittal directions, respectively. The Boyd-Kleinman coefficient is estimated as 0.038. The incoupling waist is nearly circular with waists of 200 μm and 203 μm in the tangential and sagittal directions, respectively.

The employed nonlinear medium is BBO. Due to the hygroscopic nature of BBO, this 10 mm long crystal is maintained at a temperature of 40 °C throughout the experiment, via a heating-only element controlled via a home-made temperature controller box. Maintaining the crystal at a higher temperature may help to prevent UV-induced damage [149], as has been observed in a CLBO-based 261 nm system [150]. The effective non-linear coefficient of this crystal is 1.39 pm/V and for Type-I phase matching, which occurs at an angle of 61.2 ° at the operating temperature and wavelengths.

The crystal is cut at Brewster's angle for the blue light which is sent to the cavity with p-polarization. This particular choice is done to reduce the need for anti-reflective coatings on the crystal and therefore to protect them from UV-induced damage. As Type-I phase matching is employed, however, the SHG is produced with s-polarisation and therefore some fraction is reflected from the rear BBO surface ($R = \sin^2(\pi/2 - 2\theta_B) \sim 22\%$) [151]. This light can still be accessed if the side of the crystal is polished. The crystal is placed in an aluminium housing which can be moved using two sets of screws: three on the side; and two more screws on the top to tip. Since the tip and tilt translation provided by these screws are not independent, the alignment procedure can be cumbersome and and it is not always a straightforward mechanism to get the crystal into the optimal position.

The 229 nm light is coupled out of the cavity using a dichroic filter placed immediately after the crystal. This removes the DUV light from the cavity as soon as it is produced, to protect the cavity mirrors and coatings. Again to reduce the need for coatings, the dichroic is placed at Brewster's angle for the blue light and has only a reflective coating for 229 nm.

3.3.3 Production of 229 nm in a beta barium borate (BBO) cavity

In order to mode match the 458 nm light to the above cavity, it is first necessary to shape the beam. It is best to take care to shape the beam properly due to the nonlinear dependency of SHG production on input power, so small gains in coupled power can significantly enhance the produced 229 nm. As the 458 nm light is itself produced via SHG, the walk-off in the LBO crystal means that the beam is highly astigmatic and not truly Gaussian, making the shaping procedure especially important. The mode matching is performed by using a combination of cylindrical and spherical telescopes and then by a single bi-convex mode-matching lens. For this, firstly, a pair of cylindrical lenses is chosen in a telescopic arrangement to correct for the elliptical nature. A 150 mm focal length for the vertical direction and 400 mm focal length for the horizontal direction is used. After this the waist ratio in the horizontal and the vertical direction is about 1.05. Figure 3.10 shows the beam profile after shaping the blue beam with the cylindrical telescope.

Once the beam is shaped, the next step is to match the waist of the beam to the secondary waist of the cavity, such that maximum coupling to the BBO cavity is achieved. For this, a telescope consisting of a convex and a concave lens of focal lengths 100 mm and −50 mm, respectively, are utilized. The beam profile after these lenses is also shown in Figure 3.10. Following this, a plano-convex lens of focal length 750 mm is used to focus the beam into the 229 nm cavity. The target waist is about 200 μm and from Figure 3.10, it can be noted that the beam now is close to the target waist. This combination of spherical telescope and the mode-matching lens helps in generating a waist of about 200 μm from an original highly astigmatic beam. From the profile of the beam after the spherical telescopic and the mode matching lens, the waists in the vertical and horizontal regions

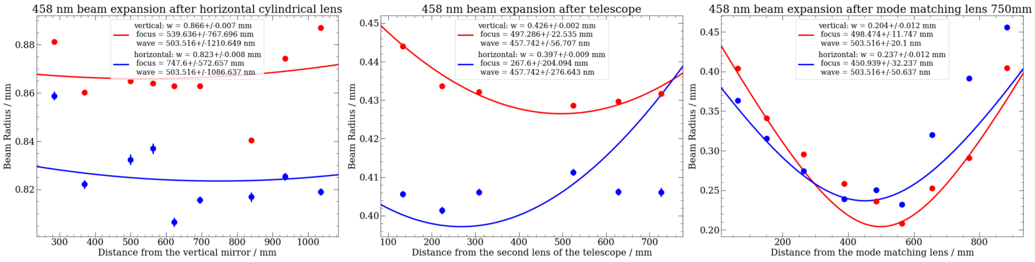

Figure 3.10: Beam profile of 458 nm after (left plot) shaping with cylindrical lenses to correct for the elliptical nature arising from the walk-off, and then (center) using a telescope, before finally (right) producing a beam of waist approximately 200 μm to be coupled to the secondary waist of the cavity.

have successfully been made similar to each other and focal positions are also close. Following this procedure, a coupling efficiency of 70-80 % to the BBO cavity is obtained.

An in-coupling mirror with nominal transmission of 1 % is selected according to equation 3.7. The finesse is measured in several different configurations to understand the linear loss mechanisms within the cavity. Firstly, without the crystal or the dichoric Brewster plate, a finesse of > 400 is measured after proper alignment and cleaning of the mirrors, first with acetone and then with methanol. Once the crystal and dichoric are inserted, the finesse is found to be highly dependent upon the angle of incidence on these elements and any inclination of the circulating light. That is, the losses must be very carefully optimized in a single-pass configuration to ensure the crystal and dichroic are really at Brewster's angle and that the light beam circulates perfectly parallel to the cavity base.

Unfortunately, performing second-harmonic generation to the ultraviolet regime was not as straightforward as for the visible light. In trying to find good working conditions, BBO crystals from three different companies have been employed and the cavity performance characterized. This helps in understanding the current situation of the optical damage mechanisms with the mirrors and the crystals involved in the ultraviolet regime. An overview of the results from the trials with different crystals is given in Table 3.2 and the remainder of the section discusses the results of these trials.

Table 3.2: Overview of the results of the trials with different BBO crystal manufacturers.

Manufacturer	Finesse	Maximum Usable 229 nm	Comments
Castech	262 ± 16	12.5 mW	Rapid degradation
Raicol	224 ± 10	∼2 mW	Slow degradation
Eksma	350 ± 6	>50 mW	Stable (hour timescale)

Castech

Firstly, BBO crystals from the company Castech are selected, which have been used in previous DUV demonstrations. The maximum achieved finesse was only 262 ± 16 from which a maximum of 12.5 mW is obtained with a conversion efficiency of 5%. Figure 3.11 shows the SHG produced with respect to the coupled power and the simulated power curve based on the measured finesse and shows reasonable agreement. However, this finesse is lower than the design and target value of ∼350 provided by the company, and also what should be achievable based on the finesse measured when using only the mirrors and the measured single-pass losses of the dichroic and crystal (∼0.1 %). At higher coupled powers, Figure 3.11 also shows that the SHG power doesn't increase quadratically and the conversion efficiency into the DUV seems saturated. This can be understood by the localised heating effects within the BBO crystal [56].

More critically, the produced power is not stable. The stability of the DUV produced is observed by measuring the power over a 15 minute time period. In Figure 3.11, it is seen that within 15 minutes the DUV reduces to ∼25 % of what is present initially, from the mW to 100 μW level. This power can be regained by modifying the cavity, mainly by changing the horizontal crystal angle and translating the crystal. Moreover, this degradation begins almost immediately when the cavity is locked.

There are several possible speculations about why this could be happening. They include the alignment drift within the cavity, which gives rise to finesse alterations and reductions in coupled power. Perhaps also the lack of a clean environment or insufficient oxygen content in the cavity might be resulting in excessive UV-induced chemical damage (see Section 3.3.1). Also there is the possibility of the crystal itself being defective in nature, which can exacerbate the problems [56].

In order to understand the source of this power reduction, the cavity was re-optimised and the finesse remeasured at 210 ± 10. A power stability measurement was performed again but while

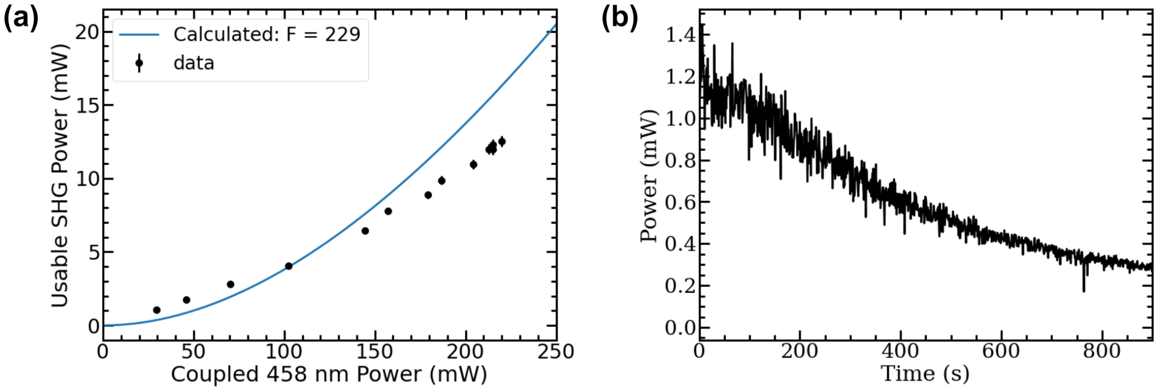

Figure 3.11: (a) SHG produced with the Castech BBO crystal as a function of the coupled blue power. Error bars are the systematic error of the power meter. (b) Power stability measurement of the DUV produced over a period of 15 minutes. The cavity is locked at T=0 s.

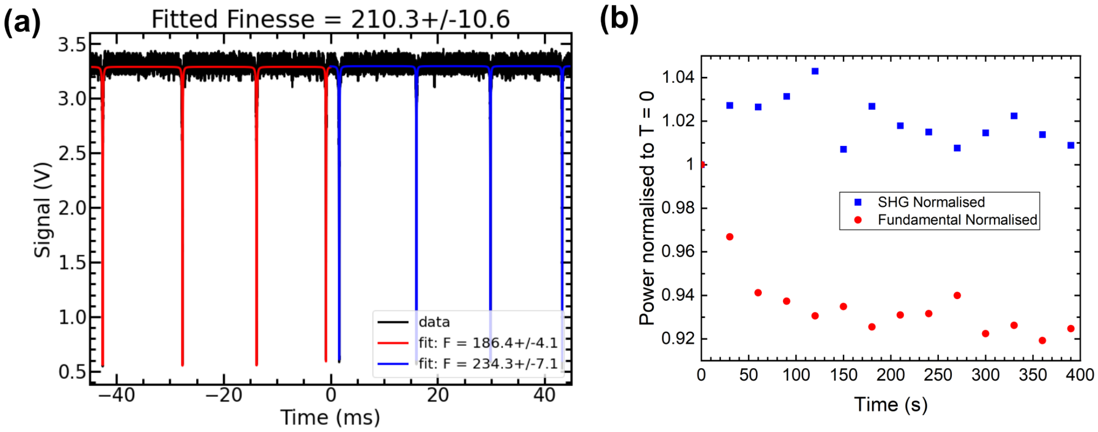

Figure 3.12: (a) Finesse measurement using the reflected beam from the BBO cavity. (b) The normalized peak powers produced for the SHG and the fundamental blue light while the PZT of the unlocked cavity is being swept. No decrease of the produced SHG or degradation of the cavity finesse is observed in this configuration.

simultaneously also monitoring the input blue power and the circulating power. The circulating power is measured via the fundamental blue leakage from one of the cavity mirrors. A photodiode is placed and calibrated to give an idea of the circulating powers. Figure 3.13 shows the results of this measurement. It is noted that the rapid SHG power reduction is not due to the input blue power sent to the cavity as it is pretty much stable over the approximate 6 min time period, whereas there is a decrease in the circulating power by 60 %. Also during this measurement, a clear drop in the coupling efficiency is observed despite having the fundamental blue nearly constant over the 6 min time period.

These results suggest that the reduction in SHG is due to a decrease in the circulating power and a degradation of the cavity. This is supported by performing a finesse measurement immediately after this experiment, where the finesse has decreased to 143 ± 5 (Figure 3.13).

To check that the damage is due to the cavity degradation and not e.g. alignment drifts, the cavity is re-optimized and the produced DUV is monitored over the same time period, but without locking the cavity. This is done by sweeping the cavity and by looking at the resonant DUV peaks produced and also the fundamental blue input normalised power over a 5 minute time period. In this case, there was no decrease in the SHG production efficiency observed in the unlocked configuration (Figure 3.12). This strongly suggests it is indeed the continuous production of 229 nm which is causing damage within the cavity.

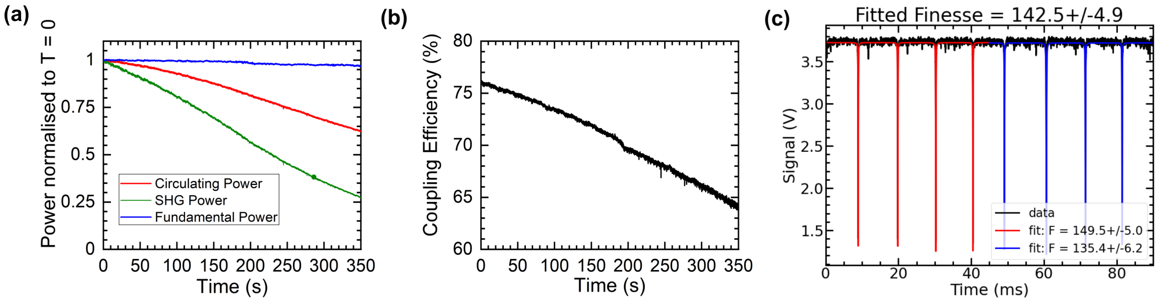

Figure 3.13: (a) Normalized SHG power, fundamental blue input power and circulating power. The cavity is locked at T=0 s and the SHG at this time is ∼1 mW. (b) Estimated coupling efficiency to the cavity as a function of lock time. Both (a) and (b) show a clear and immediate reduction in performance. (c) Finesse measurement after the lock, showing degradation (cf. Figure 3.12 (a)).

Raicol

After significant trials in optimizing the BBO cavity and experiencing exponential power degradation problems, the next crystal was chosen from a different company, Raicol. A coupling of 86 %, which is higher than the previous measurements was achieved. However, the finesse obtained was only 224 ± 10 (Figure 3.14) and the power reduction was also similar to the case above. The power degradation is not as fast as the measurement with the crystal from Castech, but it is still considerable as shown in Figure 3.14. It is seen to be approximately at a stable level with a slow decline when producing power at 2 mW. It can be noticed in locked region of the figure at 800 - 900 s. However, high stable power levels could not be achieved.

It was decided to try to understand the cause of this decline in finesse which had now been observed in multiple crystals from both Castech and Raicol – the prime suspect was DUV-induced damage on the crystal or dichroic. The crystal was removed from the casing to examine any obvious signs of damage. We noticed a few spot marks on the front and especially on the rear surfaces of the BBO crystal where the DUV is present. Figure 3.14 (b) shows the images of the crystal surfaces where damage on the rear surface is visible, strongly suggesting that the crystal is being damaged by the produced 229 nm.

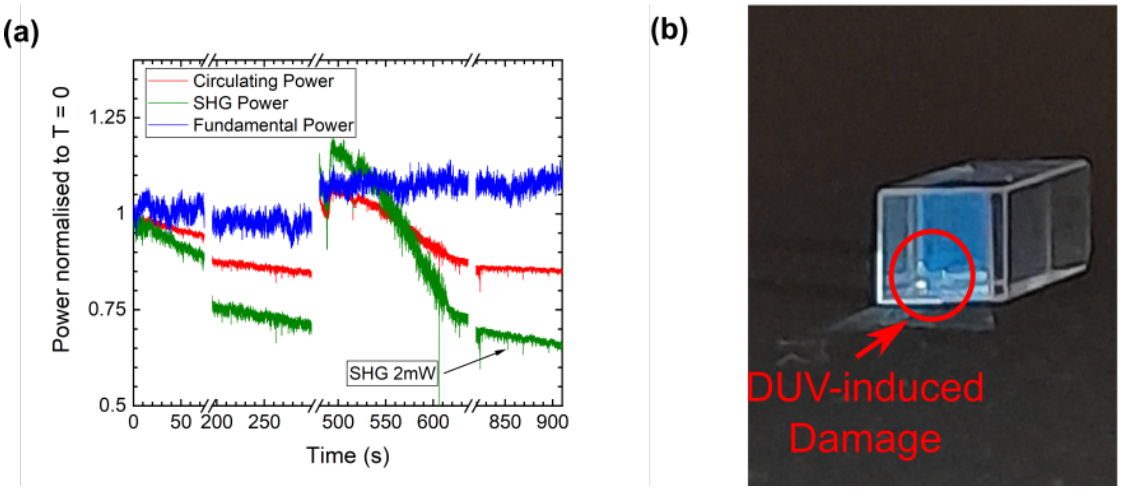

Figure 3.14: (a) Normalized power stability measurement over a period of time of 900 s showing the circulating fundamental power, SHG produced power and the input fundamental power. Breaks are for the laser coming off lock. (b) DUV-induced spot marks on the rear surface of the BBO crystal.

Eksma

Having experienced power degradation problems with the crystals from Castech and Raicol, and having observed the clear damage to the Raicol crystal, a new BBO crystal from the company Eksma Optics was trailed. The cavity was re-established by using the same incoupler with transmission of 1 %. We obtained a finesse of 350 ± 6 which is the best value attained so far and close to the design value. This was achieved after very careful alignment of the input blue beam and the Brewster's angles of the dichroic and the crystal. Figure 3.15 shows the DUV production with respect to the coupled blue at 458 nm and the finesse measurement. A maximum power of up to 50 mW and a conversion efficiency of ∼30 % is obtained, limited by the available blue power at the time of this measurement.

To study the SHG power stability, a DUV power measurement is performed, as can be seen in Figure 3.15 (c). The decreases in power are a result of the cavity coming out of lock, rather than due to the crystal as the power is recovered once the cavity is re-locked. This is shown in the vertical jumps. This crystal seems to have much better DUV production without immediate degradation. In the previous cases, the crystal had to constantly be translated to recover the initially observed power, but this is not the case in this instance. Also, more interestingly, long-term DUV production data at about 30 mW for about 50 min is taken which can also be seen in the figure. The power is more or less stable and there is no sign of degradation other than the occasional un-locking of

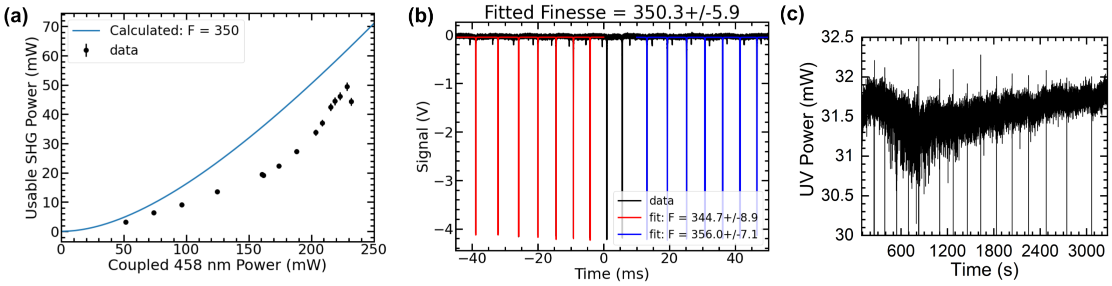

Figure 3.15: Charactrization of the cavity with the BBO crystal from Eksma. (a) Usable SHG produced as a function of the coupled fundamental power. (b) The respective finesse measurement of the cavity from fitting the reflected signal. In this case the design finesse can be reached and the 229 nm is produced in usable quantities. (c) DUV power variation over one hour when the BBO cavity is locked to the LBO cavity with around 31 mW usable SHG power.

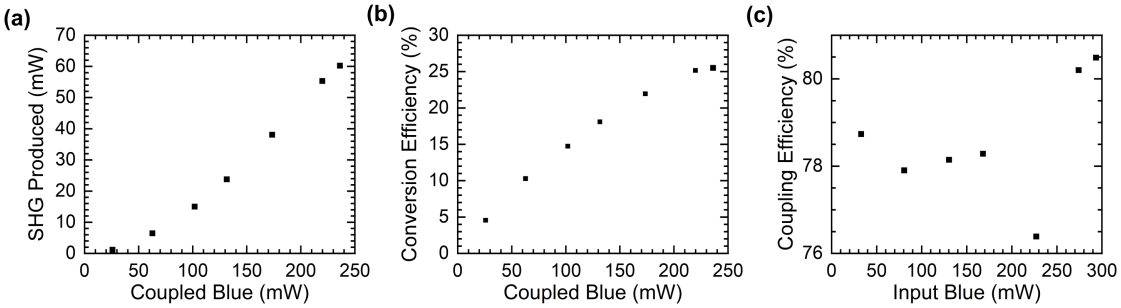

Figure 3.16: SHG power production (a), conversion efficiency (b), and input power coupling efficiency (c) are shown after moving the laser set-up to the clean room.

the cavity. The behaviour is therefore observed to be much better than the previously employed crystals.

Finally, due to the repeated damage caused to the crystal and optics from the various UV sources, the experiment has been moved to a clean room. This should greatly aid in the stable production of high-power UV and DUV. After moving the laser system to the clean room, with the same crystal, slightly higher powers were observed. After some re-optimization following the shifting of the set-up, a power measurement is performed at the usable position in the optical set-up, i.e, after two mirrors and a cylindrical lens which is placed to shape the DUV beam in order to perform spectroscopy (see Section 6.2) and not accounting for the SHG reflected from the crystal rear surface (∼22%). A maximum conversion efficiency of 25 % as shown in Figure 3.16 and powers up to 100 mW have been obtained when coupling in more blue power. The coupling efficiency to the BBO cavity is about 80 %.

The information obtained from these tests is that having a good crystal is crucial to stable and high-power DUV production. This aligns with what has previously been reported [56]. The best process currently is a trial-and-error method, as it has been performed by trying multiple crystals from multiple manufacturers. For example, good Castech crystals have been successfully employed at this wavelength in the past [56], even if the ones sourced here were not suitable. This unpredictable behaviour of the crystals highlights that there is much more work to be done in terms of DUV optical technology and understanding better the damage mechanisms at such unprecedentedly low wavelengths.

Chapter 4

Laser systems for the $^1S_0$ - $^3P_0$ and $^1S_0$ - $^3P_1$ intercombination transitions of cadmium

This chapter reports the development and characterization of the two laser systems developed for addressing the intercombination transitions of cadmium. Specifically, the $^1S_0$ - $^3P_0$ and $^1S_0$ - $^3P_1$ transitions at 332 nm and 326 nm, respectively. Previous continuous-wave demonstrations at and around 326 nm and 332 nm were based on third-harmonic generation for powers up to 100 mW [152] or second-harmonic generation for powers around 50 mW [54]. The lasers presented here are instead based on a novel design, using external-cavity diode lasers in the infrared which are stabilized to the sub-kHz level, before being amplified and then frequency quadrupled. With this architecture, powers around the Watt-level in the UV are achieved, meaning the systems demonstrate the high power and narrow linewidths needed for atom interferometry. The details and characterization of these two laser sources have been reported in recent publications which form the basis of this chapter [58, 59].

4.1 Visible Raman fiber amplifiers

The two lasers for the intercombination transitions are based on frequency quadrupling high-power light in the infrared, specifically at 1328 nm and 1305 nm for the $^1S_0$ - $^3P_0$ and $^1S_0$ - $^3P_1$ transitions,

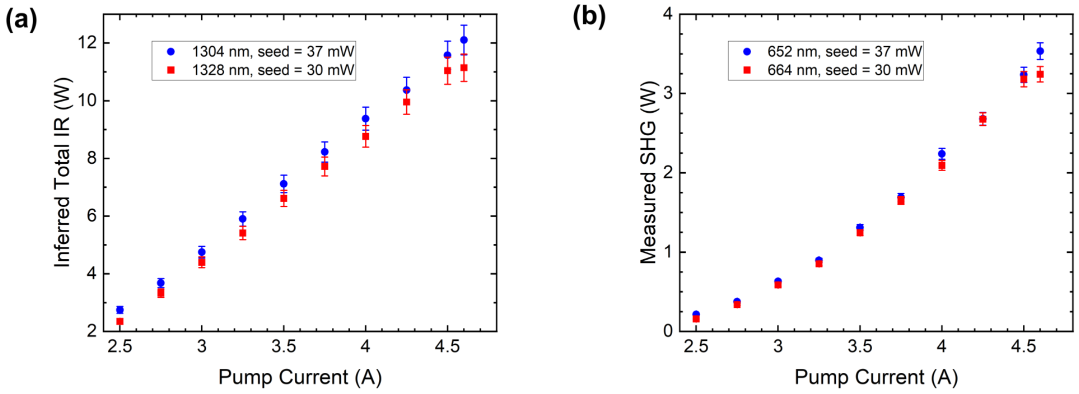

Figure 4.1: Power output of the two Raman fiber amplifiers for (a) the fundamental IR and (b) the visible SHG. Over 3 W of SHG is achieved for both systems. Error bars are the systematic uncertainty of the power meter.

respectively. The amplification and the first doubling stage is performed in two commercial visible Raman fiber amplifiers (VRFA, MPB Communications), specialized for each wavelength respectively. These amplifiers require a seed laser power of 10 - 50 mW in a polarization-maintaining fiber, which is then amplified in 300 m of fiber. The fiber is pumped with multi-mode lasers which radiate with ∼30 W, centered at 1112.5 nm and 1130 nm for the 1305 nm and 1328 nm systems, respectively.

The visible Raman fiber amplifiers firstly amplifies the infrared light from the seed up to a maximum of 12 W before a single-pass frequency doubling stage to the red light using a periodically-poled MgO:LiNbO3 crystal (PPLN). Although not currently used, the unconverted IR light is also accessible (∼8 W) and may be used to seed another PPLN or doubling cavity in the future. A maximum SHG power of 3.4 W at 652 nm is generated with these amplifiers, with a similar value achieved at 664 nm. Figure 4.1 shows the total amplified IR power and SHG for variable pump laser currents in both systems.

The frequency and intensity noise properties of the amplifiers have also been tested. A beat note taken between the unamplified master and amplified infrared light showed a 20 Hz linewidth, suggesting that the amplifiers do not introduce significant frequency noise. The amplifiers do, however, introduce significant intensity noise [58, 153], which is due to the high intensity noise of the pump lasers. This necessitates active stabilization of the intensity after amplification, which can be performed in the visible with an acousto-optical modulator (AOM) at the cost of some reduction in the usable optical power.

4.2 Laser for the $^1S_0$ - $^3P_1$ transition at 326 nm

A novel laser system built for the generation of light resonant with the $^1S_0$ - $^3P_1$ intercombination transition in cadmium at 326 nm is has been constructed and characterized [58]. This transition's natural linewidth is about 66.6 kHz and can be employed to perform the cooling and trapping of cadmium, Bragg transition interferometry, and also for precision spectroscopic measurements. It is an extremely useful transition in the generation of the ultra-cold atomic ensembles which allows the atoms to be cooled down towards the Doppler temperature of 1.6 μK [54], as simulated in Chapter 7.

A detailed explanation of the laser set-up can be found in [58]. As an overview, this narrow-linewidth, high-power laser is generated by a two-stage frequency-doubling set-up of master light emitted at 1304.8 nm from a home-built external-cavity diode laser (ECDL). This master light is amplified and frequency doubled using a visible Raman fiber amplifier to generate 652.4 nm radiation, which in turn is doubled in a BBO cavity. The suitability of the produced UV light for the $^1S_0$ - $^3P_1$ transition of cadmium has been demonstrated by performing spectroscopy on the novel atomic beam, which is presented in Chapter 6.

Figure 4.2 shows the optical schematic of the laser set-up. The master ECDL is based upon a gain chip (Innolume) centred at 1300 nm and with a broad emission spectrum of about 60 nm. This gain chip is mounted in a Littrow configuration, with the diffraction grating attached to a PZT actuator. An aspheric collimation lens with focal length 4.59 mm is placed in front of the gain chip

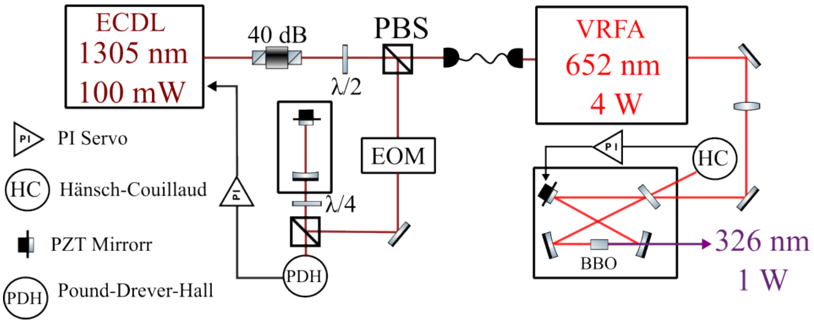

Figure 4.2: Experimental set-up of the laser system for generating 326 nm. See text for details.

and in this configuration the laser emits a maximum power of ∼100 mW in a single-mode operation at 1304.8 nm. A small fraction of this power is used for frequency stabilization (∼mW), while the remainder is coupled into a single-mode polarization-maintaining fiber and sent to the visible Raman fiber amplifier (∼30 mW).

The master ECDL is frequency stabilized to a Fabry-Pérot cavity under mild vacuum by use of the Pound-Drever-Hall (PDH) method [154]. A feedback bandwidth of about 1 MHz onto the ECDL is achieved, by feeding back onto the laser current and PZT. This allows for a reduction in the emission linewidth of the master laser down to the sub-kHz level. This signal is sent to a spectrum analyser and the power spectral density of the frequency noise ($S_\nu(f)$) is measured as a function of frequency as shown in Figure 4.3. A fast linewidth (see equation 3.1) of 0.3 kHz of the seed laser is measured from the error signal from the lock to the stabilization cavity. Assuming no further frequency broadening, this gives an estimate of the linewidth of the 326 nm light (quadruple of the seed laser frequency) as 16 times the measured master laser linewidth, i.e 4.8 kHz which is conveniently lower than the transition's linewidth to be accessed.

A final frequency doubling step is performed with the visible light, with which a maximum produced power of 1 W at 326 nm is generated. The visible light is first passed through an AOM to allow the intensity of the zeroth-order to be stabilized with a bandwidth of $\sim 10^4$ Hz, before being directed to a bow-tie cavity (Agile Optic) with a Brewster-cut BBO crystal (Raicol). This cavity is

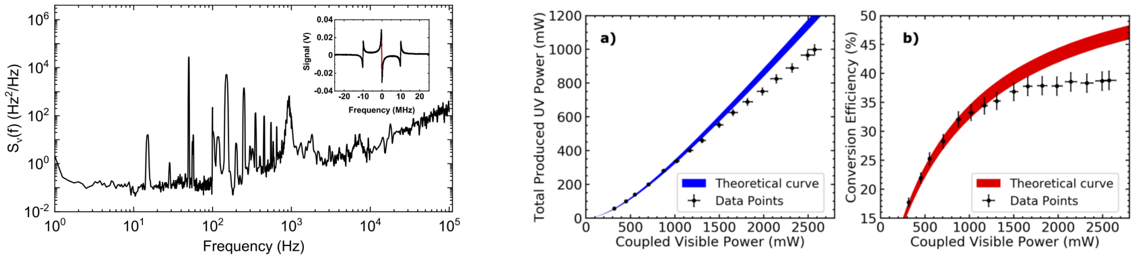

Figure 4.3: Left: Measured frequency noise of the master laser at 1304 nm when stabilized to the Fabry-Pérot cavity. The inset shows the calibrated error signal used to measure the spectral noise density. Right: Generated UV in the BBO cavity and corresponding conversion efficiency in terms of power as a function of the light coupled into the BBO cavity. The theoretical fit is calculated according to the equations presented in Section 3.2.2 and using the measured finesse value. Adapted from [58].

specifically designed for working in the UV and for long-term mechanical stability [151]. The finesse of the cavity is measured as 225±4 and the visible light is coupled with an efficiency of around 85%.

About 2.5 W of light at 652.4 nm is coupled to the non-linear bow-tie cavity and a maximum produced power of 1 W at 326 nm is achieved, giving a maximum conversion efficiency of 40 % from the crystal (Figure 4.3). The produced SHG is in agreement with the theoretical values for low coupled powers, but at higher coupled powers a deviation is observed, with the conversion efficiency saturating. This implies the possibility of heating effects within the crystal leading to thermal lensing effects [155].

In any case, these power of the produced UV is compatible with Bragg interferometry, being able to drive fast Rabi oscillations ($\Omega/2\pi \sim 10$ kHz) with large beams (see Figure 2.6). Likewise there is more than sufficient UV power for the broad range of cooling techniques planned with 326 nm on the new cold cadmium apparatus (see Section 7.3.3).

4.3 Laser for the ^{1}S$_0$ - ^{3}P$_0$ clock transition at 332 nm

As discussed in Section 2.3.2, in order to use the clock transition (^{1}S$_0$ - ^{3}P$_0$) to perform large-momentum transfer atom interferometry, it is necessary to have a high power, Hz-level linewidth laser system with excellent mode-quality and low relative intensity noise. As for the 326 nm laser presented above, such a system is not currently commercially available and therefore it has been developed specifically for this project. A detailed explanation of this laser and its locking electronics can be found in [59, 156].

The optical schematic of the laser for the production of the required 332 nm light is shown in Figure 4.4. As can be seen, a very similar optical set-up to the 326 nm laser is utilized. Again, the seed laser is a home-made external cavity diode laser arranged in Littrow configuration which is frequency stabilized by sending about 1 mW of power to a medium-finesse Fabry-Pérot pre-stabilization cavity ($\mathcal{F} \approx 5000$) using the PDH method. The derived error signal allows for feedback with a bandwidth of up to 700 kHz onto the laser. The majority of the power (about 35 mW, 1328 nm) of the seed laser is sent to the Raman fiber amplifier where the infrared light is amplified (~10 W, Figure 4.1) and then frequency doubled to the red at 664 nm (about 3 W) using a single-pass waveguide containing a PPLN crystal.

Whilst the above is very similar to the 326 nm case, further reduction in the laser frequency noise is required. Therefore, an acousto-optical modulator (AOM) is introduced onto the 664 nm light.

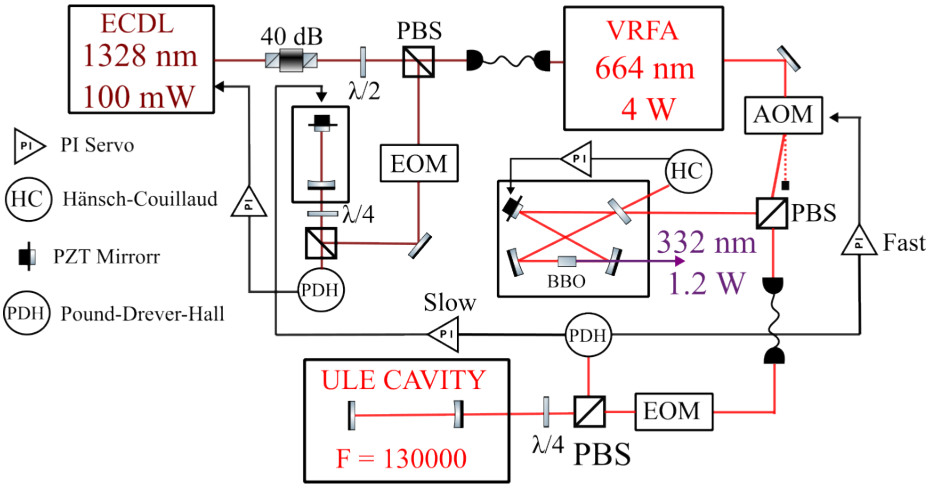

Figure 4.4: Experimental set-up of the laser system for generating 332 nm. See text for details.

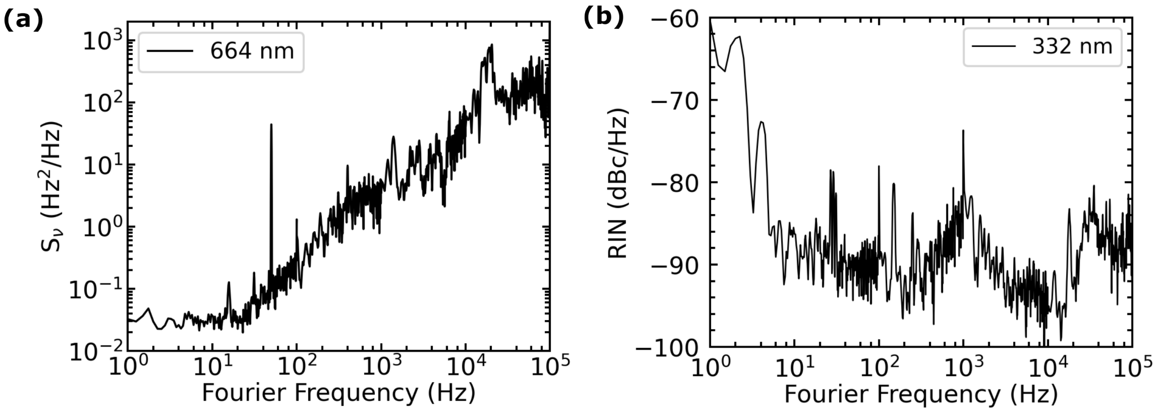

Figure 4.5: (a) Measured frequency noise of the laser at 664 nm after stabilization to the ULE cavity. (b) Free-running relative intensity noise of the 332 nm output.

A small portion of the first-order mode from the AOM is sent to a stable, super high-finesse cavity and is locked using the PDH locking scheme. This cavity is under ultra-high vacuum and is made of ultralow expansion glass (ULE) and has a measured finesse of 130000 at 664 nm. The cavity is known to be ultra-stable due to previous measurements and use in a strontium optical clock [157]. The use of an AOM has the additional advantage that it can control the intensity as well as the frequency, allowing for the simultaneous compensation of the amplitude noise added by the visible Raman fiber amplifier.

The PDH error signal is generated by use of an electro-optical modulator (EOM) on the red light. This error signal is split and the fast feedback (up to 50 kHz) is sent to the AOM in the visible and the slow-feedback is sent to the PZT of the pre-stabilization cavity. In this way, the excellent long-term stability of the super-high finesse cavity laser is transferred to the pre-stabilization cavity and the laser frequency noise can be further suppressed. The error signal from the super-high finesse cavity is used to perform an in-loop measurement of the frequency noise. The power-spectral density measurement of the frequency noise at 664 nm is shown in Figure 4.5. This measurement gives a fast linewidth calculation of 2 Hz in the visible, thereby about 8 Hz in the UV regime.

The remaining major portion of the visible light is sent to a non-linear bow-tie cavity with a Brewster-cut BBO crystal and about 1.2 W of light at 332 nm is produced with a ∼Hz-level linewidth. Figure 4.6 shows the produced UV as a function of visible power coupled into the cavity. The free-running relative intensity noise of the UV is shown in Figure 4.5. The noise excess around

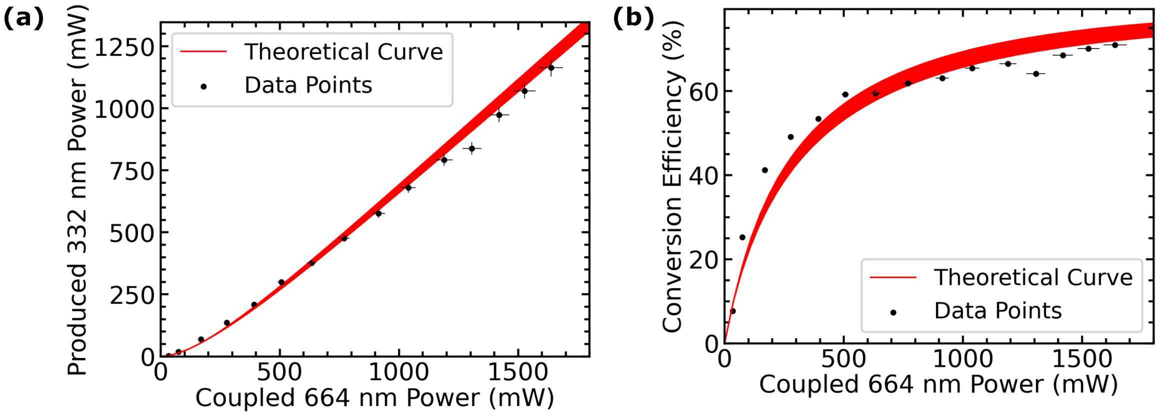

Figure 4.6: Generated 332 nm in the BBO cavity in terms of (a) power and (b) conversion efficiency. Shaded regions represent that uncertainty of the calculations (see Section 3.2.2).

1 kHz is from acoustic noise, which remains after passively shielding the cavity in an additional protective housing and mounting on vibration damping sorbothane. The spike is believed to be due to a mechanical resonance due to the screws in the mount for the PZT-mounted mirror.

With these measured frequency noise and relative intensity noise values, we calculate that the laser is suitable for performing state-of-the-art clock interferometry [59]. Specifically, we have calculated that it is suitable for performing large-momentum-transfer clock atom interferometry up to the order of $n = 10$ and that Rabi frequencies of $\Omega/2\pi \sim$ kHz can be achieved (cf. Figure 2.7).

Chapter 5

Laser sources for strontium transitions at 461 nm, 689 nm and 698 nm

This chapter presents the new laser sources which have been developed for atom interferometry with strontium. Firstly, another frequency-doubled laser at 461 nm based on an upgraded master VECSEL is briefly presented, where the problems identified at 922 nm in Chapter 3 have been resolved. Secondly, a Ti-sapphire laser capable of addressing both the $^1S_0$ - $^3P_0$ and $^1S_0$ - $^3P_1$ intercombination transitions, at 689 nm and 698 nm respectively, is presented. Details of the stabilization of this laser to a super-high-finesse ULE cavity are reported, as previously presented also in [59].

5.1 Upgraded VECSEL for 461 nm transition

The laser and optics used for generating the 461 nm light needed for the $^1S_0$ - $^1P_1$ transition of strontium is essentially the same as presented in Chapter 3. However, due to the newness of the technology, there are some significant changes in the master VECSEL as this is a more recent model. The performance obtained in the wavelength regime of 910 - 930 nm led the Vexlum company to further develop the gain chip in order to produce higher powers, specifically to counter the runaway heating effects which damaged the chip when operating at high powers at 922 nm (see Figure 3.6). With this updated gain chip functionality, the main improvement is in power and stability at 922 nm,

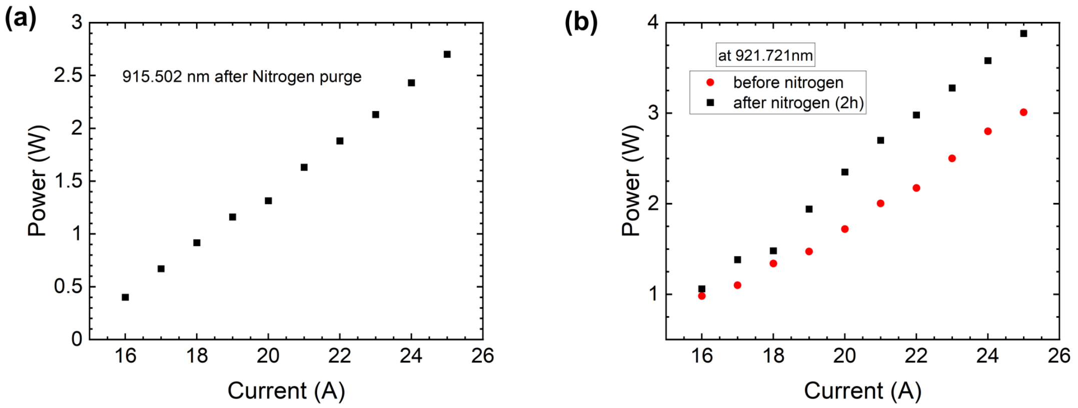

Figure 5.1: Power generated by the VECSEL as a function of laser diode current at a wavelength of (a) 915.50 nm and (b) 921.72 nm after purging the laser cavity with low-flow nitrogen. Purging with nitrogen can give about a 1 W gain in power at 921.72 nm.

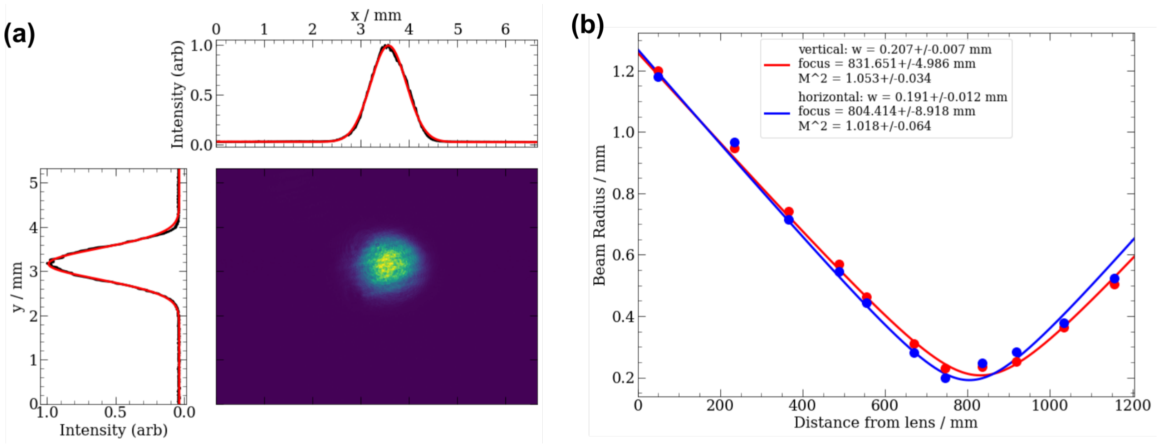

Figure 5.2: (a) Image of the VECSEL beam profile when operating at 922 nm. (b) Beam profile of the IR beam after the mode-matching lens used to attain a waist of approximately 200 μm to couple to the LBO frequency doubling cavity to generate blue light at 461 nm. The fits give a measured M^2 =1.05 ± 0.03.

so we use this laser to generate blue light at 461 nm.

Mechanically, the design of this laser is almost completely similar to that of the previously described VECSEL in Chapter 3. It comes with a water cooling chiller which keeps the aluminium casing and the components within the laser at 20 °C. The footprint of the laser is exactly identical to that of the previous one, which allows us to easily interchange between the two optical set-ups. Keeping in mind the grander purpose of this experiment, i.e, building a dual-species atom interferometer with cadmium and strontium, this is useful as the same master laser technology can be easily tuned for producing either 229 nm or 461 nm. For this purpose and also for comfortable movement of the laser systems, the optical set-up is compactly mounted up on a 75 cm × 75 cm breadboard.

Figure 5.1 shows the power produced as a function of pump laser diode current at both 922 nm and 915 nm. The laser begins to lase at about 13 A of pump laser diode current. This master laser used to produce 461 nm light is capable of producing high powers up to 3.88 W at 922 nm and 2.7 W at 915 nm, this represents gains similar to 1.8 W and 0.7 W, respectively, compared to the previous VECSEL (cf. Figure 3.4 and Figure 5.1). This is therefore a major power enhancement at the required wavelength for strontium, so this system can be specialized for this atom.

The high-power IR beam from the master laser is shaped and aligned to the home-made bow-tie cavity with an LBO crystal mounted on the translation stage. The mechanical design, optics and dimensions of the cavity are the same as described in Section 3.2.2, except that the LBO crystal

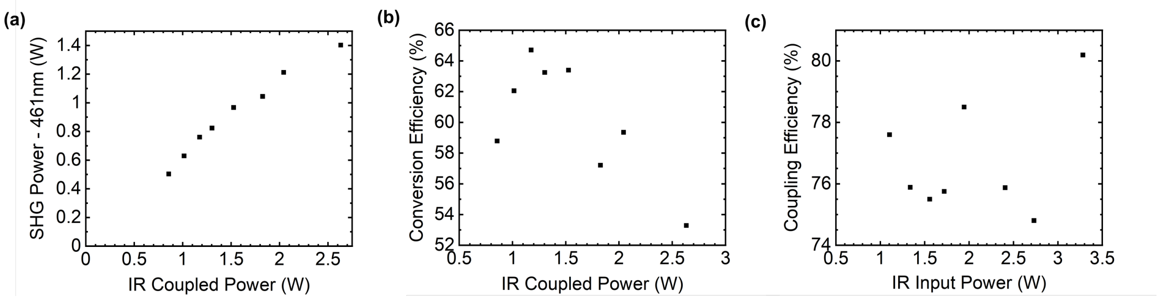

Figure 5.3: (a) SHG produced at 461 nm as a function of IR coupled power. A maximum of 1.4 W of blue is observed. (b) Conversion efficiencies up to 65 % are observed with this cavity and is plotted against IR coupled power and (c) coupling efficiencies up to 80 % is observed and is plotted as a function of the IR input power.

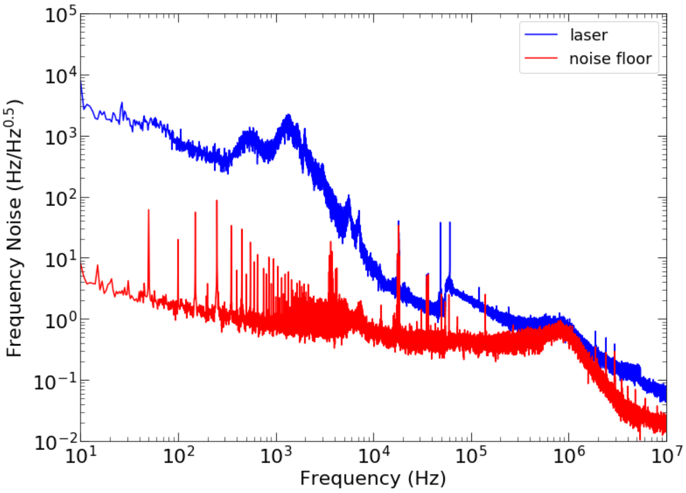

Figure 5.4: Frequency noise of the free-running VECSEL at 922 nm measured using the error signal from the Hänsch-Couillaud locking system (blue line). The noise floor (red line) is measured when the laser is tuned out of resonance with the cavity. The measurement results in a linewidth of 6 kHz.

is specialized for producing 461 nm. This results in the crystal being cut with a slightly different phase-matching angle, but more substantially having a different anti-reflection coating. With an electro-optical modulator (EOM), side-bands on the laser frequency are generated, spaced at 10 MHz which is used to measure the linewidth, which is estimated to be 1.88 MHz. The secondary waist of this cavity is calculated to be 200 μm between the two plane mirrors and the laser is matched with a single from the bi-convex (f = 400 mm), mode-matching lens placed at an approximate distance of 63 cm from the cavity waist. Figure 5.2 shows the beam profile measured from the lens. The M^2 value is measured as 1.05 ± 0.03, taken from the weighted mean of the M^2 in the horizontal and vertical directions. This again shows the excellent mode quality typical of VECSELs and allowing the target waist to be well-matched with this single singlet lens as shown in Figure 5.2.

Figure 5.3 shows the SHG produced at 461 nm as a function of the IR in power coupled into the cavity, which are measured as 75 - 80 %. A maximum of 1.4 W is obtained at the highest VECSEL laser diode current of 25 A. The conversion efficiencies range from 52 - 66 % with this LBO crystal from Raicol company and Figure 5.3 shows the conversion efficiency change as a function of the circulating power. At these higher powers than Figure 3.9, the conversion efficiency seems to have saturated, suggesting the possibility of inhomogeneous temperature changes in the LBO, like in the case of the cadmium intercombination lasers (Figure 4.3).

The frequency noise of this laser has also been measured. The frequency noise measurement is performed by looking at the change in the laser frequency with respect to the resonant frequencies the cavity can withstand by generating an error signal from the dips of the reflected signal using the Hänsch-Couillaud locking scheme. This error signal is calibrated using the linewidth of the cavity which is known by generating side-bands on the laser frequency at 10 MHz. The error signal measurement is taken over a range of Fourier frequencies and is shown as the blue data in Figure 5.4. The background (red) in the graph is measured when the laser is out of resonance with the cavity. With this measurement, we estimate a fast linewidth of 6 kHz (equation 3.1), very slightly reduced compared to the previous VECSEL, but with a similar spectrum (Figure 3.7).

5.2 Ti-sapphire laser for intercombination transitions of strontium

A commercial titanium-sapphire laser (Matisse, Sirah Lasertechnik) is used to generate light at 689 nm and 698 nm allowing to access the intercombination transitions in strontium, especially for generating the high powers required for atom interferometry on these transitions (see Section 2.3.2). This laser was selected due to its excellent power, noise and mode quality features. This laser emission band is around 670 nm–1020 nm which makes it unsuitable to produce the 652 nm and 664 nm light (to generate 326 nm and 332 nm, respectively) required to access the intercombination transitions of cadmium. This means the 689 nm transition is also towards the edge of the operation. It should be noted, however, that this laser model is compatible with replacing the Ti-sapph crystal with a dye module allowing wavelengths down to 550 nm to be reached.

The internal structure of the laser is shown in Figure 5.5. It consists of a temperature cooled Ti-sapph crystal acting as the lasing medium pumped with up to 25 W of green light at 532 nm (Millennia eV, Spectra-Physics). As in the VECSEL systems presented earlier, there is additionally a birefirngent filter (BRF) for wavelength selectivity and a thin etalon for ensuring single-mode operation. Unlike the VECSEL, however, there is an additional intra-cavity etalon to ensure the light only circulates in one direction in the cavity. The continuous and fine tuning of the laser frequency is performed by two piezo-electric transducers (PZT) mounted on mirrors. One is optimised for low-frequency changes and the other for fast frequencies with a bandwidth up to ∼100 kHz. An electro-optic modulator (EOM) can optionally be placed inside the laser cavity for frequency control

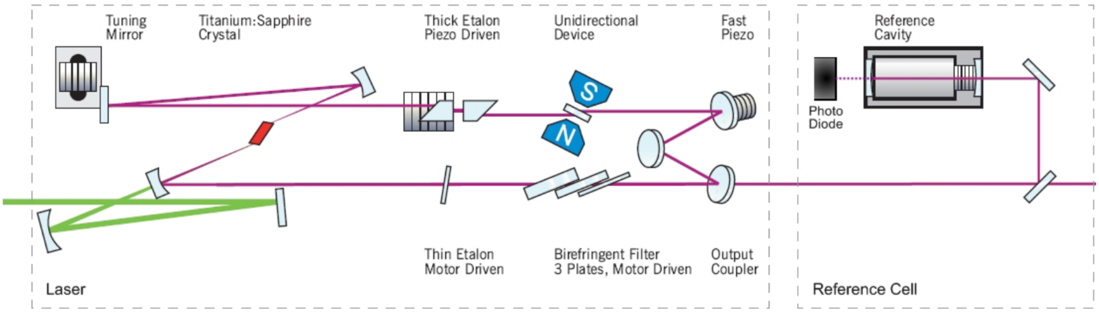

Figure 5.5: Optical set-up of the Ti-sapphire laser. See text for details. From [158].

with a bandwidth >10 MHz.

The power and noise qualities of this laser have been tested at 689 nm, 698 nm and also at 813 nm, which is the magic wavelength of the strontium clock transition. Although not discussed in detail in this thesis, this could be useful for generating a magic-wavelength lattice for trapping strontium, or even for Bragg interferometry on atoms in a superposition of the two clock states [61]. The powers and the linewidths at these different wavelengths are shown in Table 5.1. These linewidth measurements were performed by stabilizing the laser to a broadband, low finesse Fabry-Pérot cavity ($\mathcal{F} \sim 50$) using the PZTs on the mirrors and the side-of-fringe method. The error signal of this lock is used to determine the reported root-mean-squared linewidths of <40 kHz.

As can be seen in Table 5.1, substantial powers are available even with the introduction of the EOM. For comparison, previous clock atom interferometry experiments with strontium used a tapered amplifier system which generated a maximum power 300 mW at 698nm, so this system represents an order of magnitude increase. Moreover, the tapered amplifier suffered from severe ageing and mode quality issues [43], which are not present in this system.

Further relevant optical properties of the laser are tested at the clock transition wavelength of 698 nm as shown in Figure 5.6. The relative intensity noise of the laser at 698 nm is measured using a small-area photodiode and is shown in Figure 5.6 along with the background measurement where the light hitting the photodiode is blocked. This noise is integrated between 10 Hz - 10 MHz to give an root-mean-squared value of just 0.04%. The beam quality is also measured and is nearly circular and close to diffraction-limited with a measured M^2 <1.1, determined from the beam profile measured following focusing by a single spherical lens.

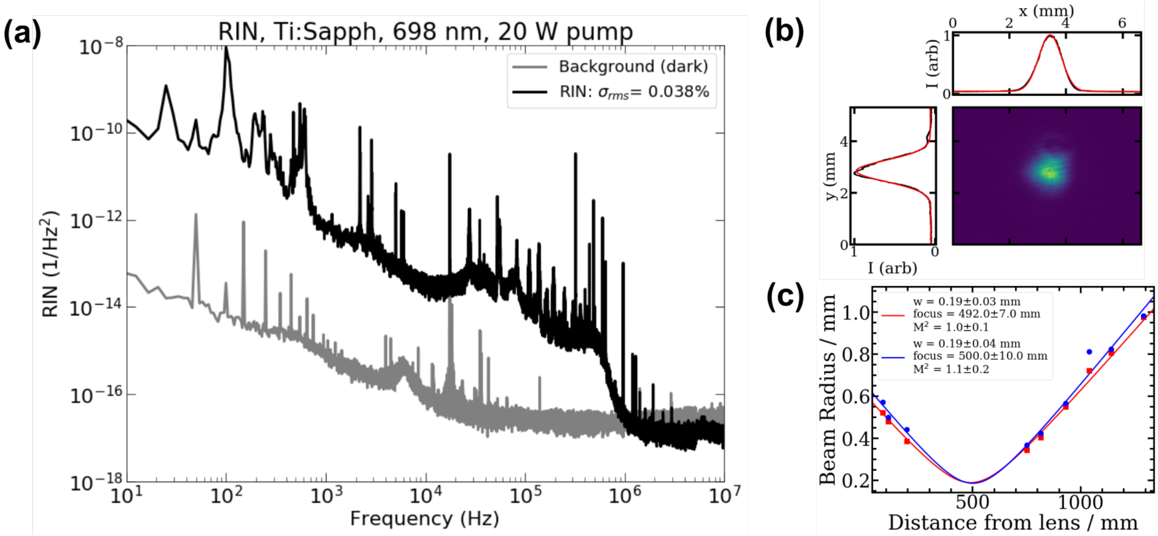

Figure 5.6: Properties of the Ti-sapph laser measured at 698 nm. The laser shows (a) low RIN and (b) a nearly circular, Gaussian output. (c) Measured M^2 in the horizontal (red line and squares) and vertical (blue line and circles).

Table 5.1: Overview of Ti-sapph properties at relevant wavelengths. Linewidth is when stabilized to the reference cavity.

Wavelength	Power Without EOM	Power With EOM	Linewidth Stabilized
689 nm	4.2 W	3.5 W	40 kHz
698 nm	5.6 W	4.1 W	40 kHz
813 nm	8.7 W	–	18 kHz

5.2.1 Stabilization to the ULE cavity

In order to achieve the Hz-level linewidth to access the clock transition $^1\mathrm{S}_0$ - $^3\mathrm{P}_0$ in strontium, a small fraction of the power at 698 nm from Ti-Sapphire laser is sent to the same stable super-high finesse, ultra-low expansion (ULE) cavity as was used for the stabilizing the cadmium clock laser (Section 4.3). The finesse of the ULE is estimated to be about 410,000 from previous measurements at this wavelength and was used as the reference for an strontium optical clock [157]. The error signal from this cavity is generated in the same way as discussed in that chapter.

The optical set-up of the stabilization to the ULE cavity is shown in Figure 5.7. A small portion of the power is sent to a Fabry-Pérot pre-stabilization cavity to stabilize the laser to the ~kHz level. This lock is performed by the slow and fast PZTs present in the Ti-sapph laser cavity. Another fraction of the laser is sent to the ULE cavity using the Pound-Drever-Hall method and the error signal is split. The fast error signal is sent as a feedback to the electro-optic modulator (EOM) in the laser cavity, while the slow one is sent to the PZT within the pre-stabilization cavity. The use of the EOM means that an external AOM is not required as in the case of the cadmium clock laser. Likewise, the low RIN of the Ti-sapph means it does not require active suppression as was the case with the Raman fibre amplifiers.

When the laser is stabilized to the ULE cavity, the error signal is utilized to perform an in-loop frequency noise measurement and the results are shown in Figure 5.7. The power spectral density

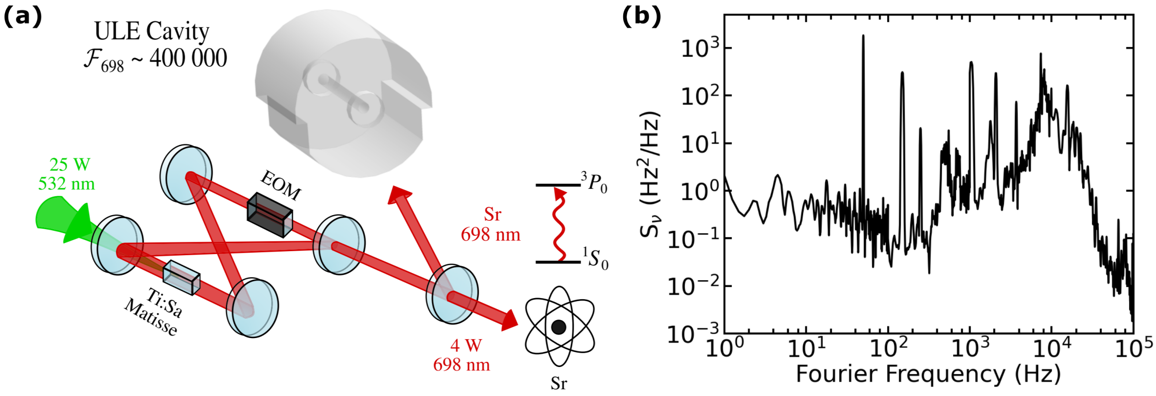

Figure 5.7: (a) Optical set-up for locking the Ti-sapph to the super-high finesse ULE cavity at 698 nm. See text for details. Adapted from [59]. (b) Power spectral density of the frequency noise of the laser when locked to the ULE cavity. The deduced linewidth from this measurement is 10 Hz.

of the frequency noise gives an estimated linewidth of 10 Hz at 698 nm when integrating according to equation 3.2. This can be used to estimate the large-momentum transfer possible with this laser, which should be viable up to $n = 100$ [59]. This around an order of magnitude higher than for the cadmium set-up, due to the higher power and wavelength allowing for faster Rabi oscillations ($\Omega/2\pi \sim 2$ kHz). This laser therefore seems to be an excellent choice for clock atom interfetometry experiments.

Chapter 6

Spectroscopy of cadmium on a atomic beam

This chapter presents the vacuum set-up built for high resolution spectroscopy of cadmium transitions. The experimental system consists of an oven, with a geometry optimized to produce a collimated and intense atomic beam of cadmium. The oven has been mounted and tested in a vacuum chamber specialized for performing spectroscopy, the design of which is described. Spectroscopy on both the broad $^1S_0$ - $^1P_1$ transition at 229 nm and the narrow $^1S_0$ - $^3P_1$ transition at 326 nm is shown. In particular at 229 nm, the absolute frequency of the ^{114}Cd transition and the isotope shifts relative to this transition are determined, with some of these shifts measured for the first time [57]. This transition is also used to characterize the atomic beam's properties, such as flow rate and divergence. Spectroscopy at 326 nm instead focuses on generating an error signal to allow the laser presented in Section 4.2 to be frequency stabilized to the 66.6 kHz wide transition.

6.1 Oven and spectroscopic chamber design

6.1.1 Oven for generating a cadmium beam

Compact and efficient atomic beams are useful and advantageous for the production of ultra-cold atoms and for precision spectroscopy. These ovens in combination with an ultra-high vacuum chamber help in the production of collimated sources of atoms which can be used directly for performing spectroscopy or as the main source for the efficient loading of magneto-optical traps. This rep-

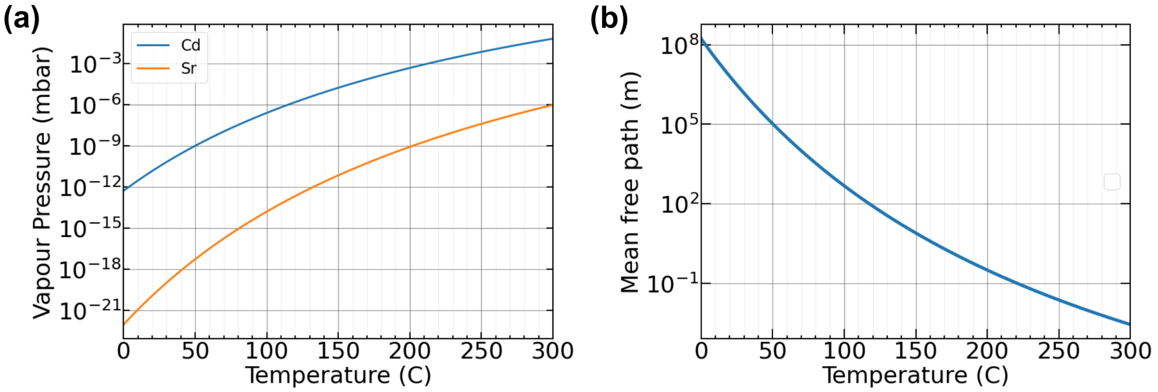

Figure 6.1: (a) Vapor pressure of cadmium and strontium as a function of temperature. (b) Mean free path length of the cadmium vapor, modeled as an ideal gas. The mean free path is orders of magnitude larger than the capillary length (8 mm) for T <200 °C.

resents the first step in experiments for metrological purposes, tests fundamental physics, atom interferometry and much more.

For the production of ultra-cold atoms, it is advantageous to have an oven which is capable of producing a high flux of atoms while consuming less power and more importantly with a good heat management within the system. A fully characterized oven can help us in estimating the expecting loading rates and trap efficiencies of the cooling techniques involved (see Chapter 7).

Cadmium has a higher vapor pressure in comparison to other alkaline-earth and alkaline-earth-like elements such as strontium and ytterbium, which makes it easier to generate high-flux collimated beams at much lower temperatures. Figure 6.1 compares the vapor pressure values of cadmium and strontium giving an idea of the required temperatures and shows that there is about a 7 orders of magnitude difference between the vapor pressures of cadmium and strontium at 100 °C. Also the higher mass of cadmium allows for lower beam velocities making it easier to slow and trap the atoms for the generation of ultra-cold atoms. Working at lower oven temperatures is advantageous for maintaining lower pressures in the overall vacuum system. The melting temperature of cadmium is 321.1 °C. Hence, only temperatures comfortably lower than this value are considered.

A novel atomic oven is developed for cadmium whose design is based on [159], but with several upgraded features. This oven is made of a stainless steel reservoir and its internal schematic design is shown in Figure 6.2, within which the cadmium cylindrical sample is placed. This reservoir is wrapped up with tantalum wires threaded through an insulating ceramic multi-bore tube. The cylindrical opening of the reservoir has the capacity to withhold 120 capillary tubes with a length of 8 mm and with an internal radius of 100 μm. The diameter of this aperture is 10 mm whereas the length is 34 mm. An aluminium heat shield is placed around the reservoir and ceramic tube, to reduce the radiative heat transfer from the oven to the rest of the chamber.

The oven has four feedthroughs out of which two are used for heating the cadmium sample via running current through the tantalum wire. The other two ports are used for temperature read out via a thermocouple inserted into the base of the flange where the cadmium is placed. These feedthroughs are compatible with ultra-high vacuum, allowing external control of the oven without compromising the vacuum level.

For the best performance, it is assumed that this oven is operated in Knudsen regime, where collisions among the atoms are neglected which means that the divergence of the emitted atomic beam is determined by the capillaries and not increased by the intra-atomic collisions. This is justified by the mean free path being much larger than the capillary length at the operating temperatures. The initial simulations of this atomic oven designed for the MOT of cadmium atoms, estimates the efficiencies of 10^6 - 10^7 atoms at a temperature of about 100 °C [160]. This can be validated by considering the mean free path of cadmium, modeled as an ideal gas, at a typical operating temperature of 100 °C. This is calculated as ~500 m and therefore is much larger than the capillary length, as shown in Figure 6.1. At 250 °C the mean free path is only around 2 cm, so it is advisable to stay below such temperatures.

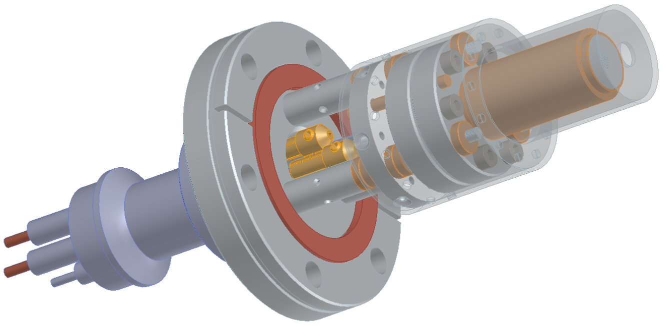

Figure 6.2: CAD of the oven design.

6.1.2 Vacuum environment for spectroscopy

The oven is inserted in a vacuum chamber suited for spectroscopy and the design of the chamber is shown in Figure 6.3. The oven is connected to the left of the spectroscopic chamber using a standard CF40 flange. The design also allows for optics to be put inside the chamber for improved collection efficiency (solid angle). A concave mirror placed at the bottom of a chamber and a plano-convex lens placed at the top are inserted into the vacuum chamber to maximize the fluorescence signal collected through the top viewport (see Section 6.2).

Ultra-high vacuum levels are typically requested for atomic physics experiments, to minimize the interactions of the atoms with the environment. This is done by removing the atmospheric gas inside the chamber with a series of vacuum pumps and also by baking the chamber at high temperatures. This procedure is outlined in detail in Appendix B, but in brief, the chamber is first cleaned with distilled water and acetone by hand and subsequently, for small parts, in a heated ultra-sonic bath. A scroll pump and a turbo pump are connected via a valve to reduce the pressure to the high vacuum regime, while an ion pump is permanently attached to the chamber. The chamber is baked at approximately 120 °C for at least two weeks to remove water vapor and other contaminants from the system. Following this procedure, the background pressure of this chamber while the oven is at room temperature is measured to be 10^{-10} mbar according to the calibrated current of the ion pump. At the working temperature of 100 °C, the pressure goes up to about 10^{-9} – 10^{-8} mbar.

6.2 Spectroscopy of the ^{1}S$_0$-^{1}P$_1$ transition at 229 nm

6.2.1 Optical set-up of spectroscopic measurements

Spectroscopy on the atomic beam aiming at the ^{1}S$_0$ - ^{1}P$_1$ transition is performed using the 229 nm radiation generated from the frequency-quadrupled VECSEL (Chapter 3). For these measurements, it is important that the properties of the light being sent to the atoms is well known. Since there is a dearth of cameras which are used for a generic beam profile at such low wavelengths, we use the knife-edge approach [161] to measure the waist of the beam (vertical and horizontal axes) at various distances. This experiment was performed with utmost care to ensure protection from the scattered 229 nm photons. The blade is attached in a vertical and horizontal fashion and measurements are taken at different distances to order to verify the size and focus of the beam. Figure 6.4 shows the beam profile of the UV coming out the BBO frequency doubling cavity at 3 different locations.

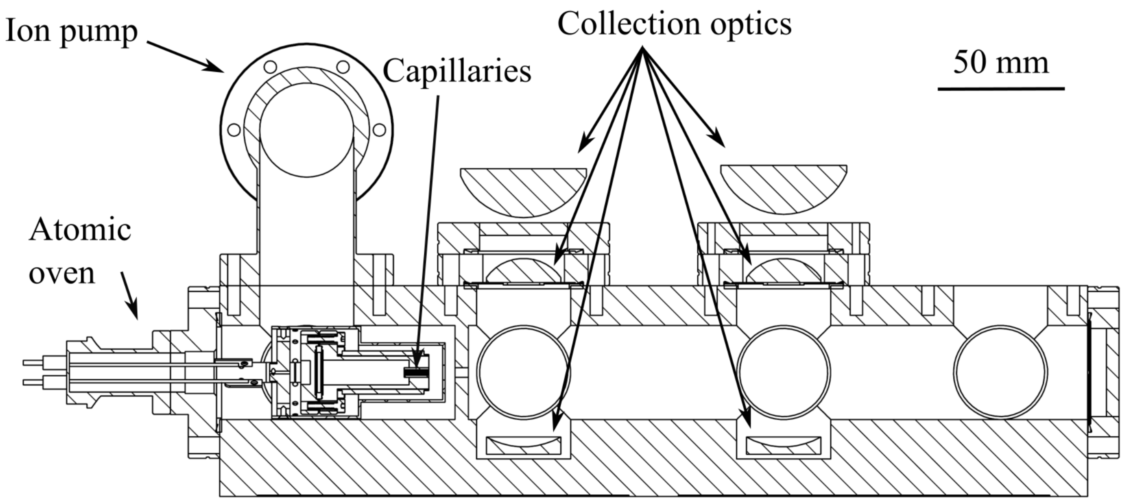

Figure 6.3: To-scale cross-sectional drawing of the spectroscopic chamber to which the oven is connected onto the left. The bottom part of the chamber allows space for optics which are helpful in collecting the fluorescence emitted by the photons. The left top part of the chamber is used for connecting the ion pump. Light is sent through the viewports on the side (not shown) and viewports on top are used for detection purposes.

The beam waist in the horizontal direction is estimated to be 32 μm centred close to the crystal position and is therefore highly divergent outside the cavity (Rayleigh length $\sim$14 mm). The beam appears to be approximately collimated in the vertical direction, however, and the waist is measured to be 420 μm. In order to send a collimated beam to the atomic beam, a 200 mm focal length horizontal cylindrical lens is placed approximately at the focal length from the BBO crystal. The beam profile is performed precisely at the distance where the DUV beam interacts with the atoms in the chamber. A single measurement was performed at the approximate middle-distance of the two beam sent to the atomic beam (input and retro-reflected). The power is split using a polarizing beam splitter and the transmitted power is sent to the knife-edge measurement. The reflected beam was used to monitor the produced UV power to correct for power variations during the knife-edge measurement. Figure 6.5 shows the beam profiles where the fitting offset and the amplitude is fixed to remove any errors from the tail of the fit. These fits give the beam diameters to be 1.10 ± 0.02 mm and 2.88 ± 0.12 mm in the horizontal and vertical dimensions, respectively, and value of 3.1 ± 0.3 mm^2 for the beam area.

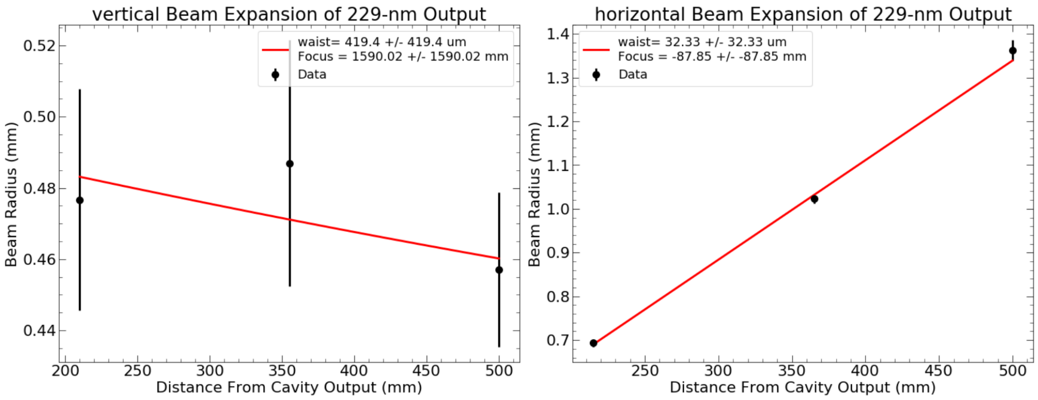

Figure 6.4: Beam profile from the knife-edge measurement of the UV light after the BBO cavity

Figure 6.6 (a) shows the optical schematic of the experiment. The power used to do spectroscopy is generally low (about 1 mW) in order to stay well below the saturation intensity (I_{sat} =0.99 W/cm^2). The beam is sent through a half-wave plate and then retro-reflected. The beam polarization is set to be horizontal, which is optimized by maximizing the fluorescence from the atoms with the half-wave plate. Since we are looking at the dipole emission, in the ideal case, there would be no emission in the direction parallel to the polarization of light and it is instead maximized in the vertical direction [67].

The light emitted by the atoms is collected by a photomultiplier tube (H9307, Hamamatsu) placed on the top of the spectroscopic chamber. Since the light emitted by the atoms is of the order of nW, optics are placed within the chamber to maximize the solid angle of the collected fluorescence. We place a 30 mm concave mirror underneath the beam and a 40 mm focal length plano-convex lens in order to collimate the collected light, which is finally focussed onto the photomultiplier tube using a 60 mm focal length plano-convex lens, placed outside the chamber. A narrow optical filter is also placed directly before the photomultiplier tube to block any external light. The schematic of the collection optics is shown in Figure 6.6 (b). This device has gains of the order of 10^5 and is dependent on wavelength of the radiation.

Using a triangular wave sent to the VECSEL PZT, the frequency of the UV light sent transversely to the atomic beam is altered. This sweep takes place after locking the LBO cavity to the VECSEL and then subsequently locking the BBO cavity to the LBO cavity. While these cavities are in resonance with the master laser, the VECSEL PZT is slowly swept up to a peak-to-peak voltage of 80 V which allows at least 3 GHz of sweep in the UV regime. To monitor the power fluctuations in

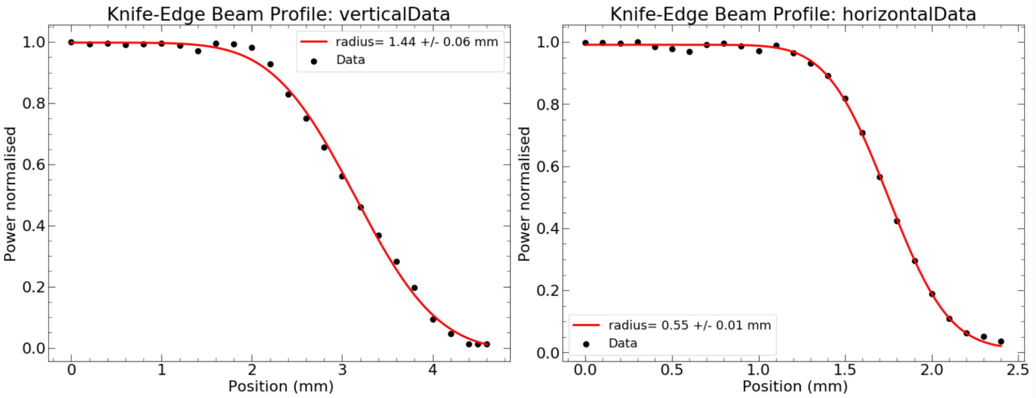

Figure 6.5: Beam profile from the knife-edge measurement of the 229 nm light to determine the size of the beam interacting with the atoms.

the UV, a portion of the UV power is sent to a photodiode while performing the experiment. This also acts as a good monitor everyday, in order to better understand the behaviour of the cavities and also the BBO crystal.

We estimate the angle that the UV interacts with the atomic beam, which should be orthogonal to minimise the Doppler shift. This is done by overlapping the reflection from the vacuum viewports and the input beam, assuming that the atomic beam is traveling straight and therefore parallel to the viewports. Based on this measurement, the deviation from orthogonality between the laser beam and the atomic beam is estimated to be <4 mrad.

6.2.2 Oven characterization

From the fluorescence signal obtained from the atoms, the height and width of one of the peaks is used to determine the flux, flow rate and divergence of the atomic beam at various temperatures [162].

From a single sweep of up to 3 GHz in the DUV, we observe the signal from all the 8 isotopes of cadmium (see Section 6.2.3). To determine the properties of the oven, one of the dominant peaks is selected, which is due to ^{114}Cd and which has negligible contributions from the other isotopes. This peak is fit with the method of least squares to a Voigt profile, which is a convolution of Gaussian and Lorentzian distributions representing the Doppler broadening and the natural linewidth distributions, respectively. In the performed fit, the Lorentzian width is set to be constant at the known natural linewidth and from the fitted Gaussian, we obtain the Doppler spread of the atoms,

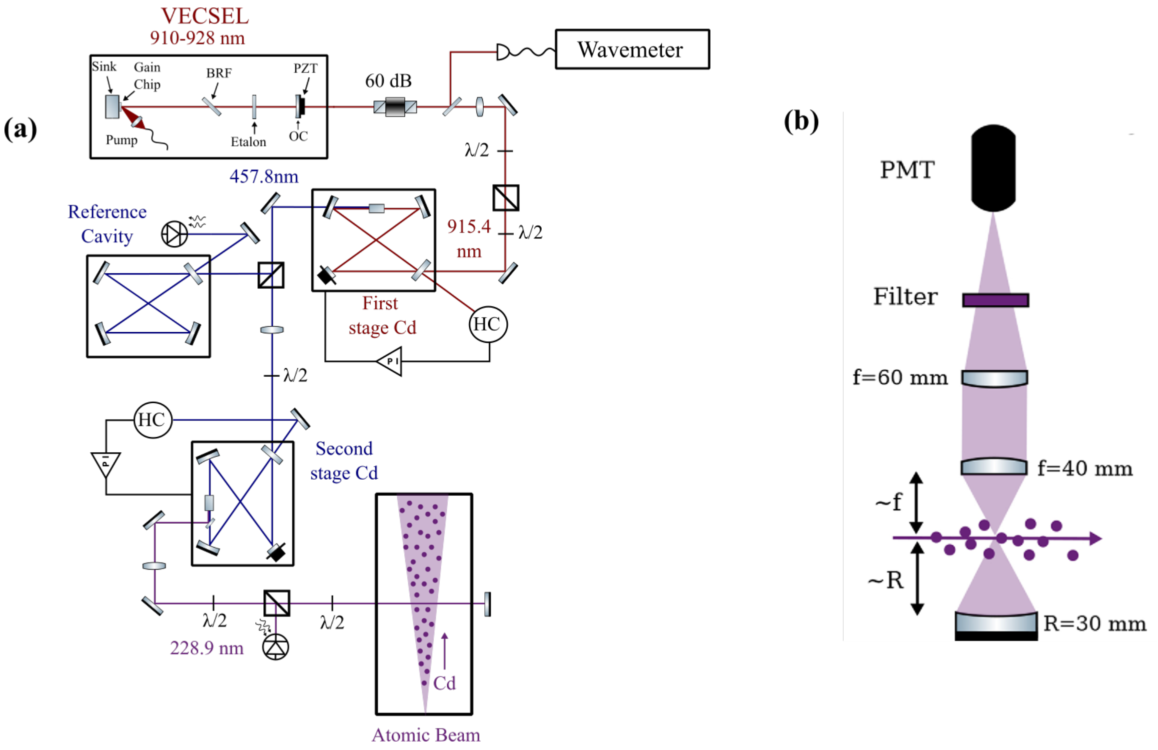

Figure 6.6: (a) Optical schematic of the spectroscopy measurement. The BBO cavity for UV production is locked to the first-stage doubling cavity, which is in turn locked to the VECSEL. The laser frequency is swept by sending a triangular wave to the VECSEL PZT. Frequency calibration is ensured by sending a small fraction of the master IR light to a wavemeter and also by using a reference bow-tie cavity in the visible region. (b) Optical schematic diagram on top of the chamber which collects the fluorescence emitted by the atoms.

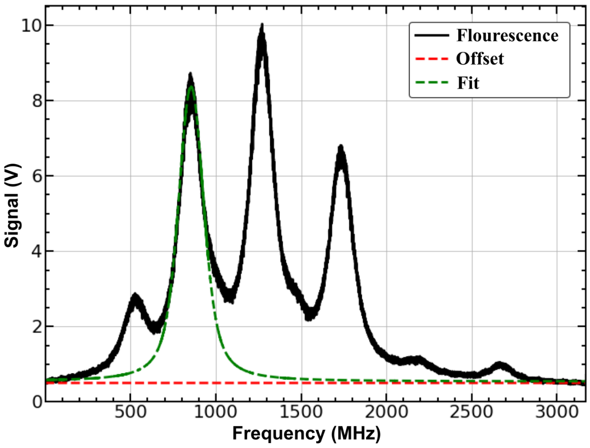

Figure 6.7: Sample fit of a Voigt fit to the ^{114}Cd peak, taken for an oven temperature of 107 °C, used to determine the flow rate and divergence of the oven output. Adapted from [162].

assuming the transverse distribution of the velocities is Gaussian, ignoring the time taken by the light to interact with the atoms. At 100 °C, time-of-flight broadening can be estimated based on the measured beam radius and the most probable velocity of the beam as ∼200 kHz, which is much smaller than the ∼40 MHz width typically seen in the fits. Similarly, the amplitude of the fitted signal is used to estimate the flow rate of the atoms. Figure 6.7 shows a sample fit, which is performed for all the peaks taken at temperatures ranging from 85 - 120 °C.

From the Gaussian part of the fit of the fluorescence peaks, the divergence can be estimated. Assuming the transverse velocity of the beam follows a Gaussian distribution, the divergence of the atomic beam is given by equation 6.1, where σ_t is estimated from the performed fit and $v_{beam} = \sqrt{3k_BT/m}$ is the longitudinal velocity of the atomic beam [159].

$$\theta = \frac{\sigma_t\sqrt{2\ln 2}}{v_{beam}} \tag{6.1}$$

With this estimate of divergence, the dependency on the temperature is shown in Figure 6.8, where a slight a linear dependence of the beam divergence as a function of temperature is measured. The large error bars are mainly systematic uncertainty, rather than statistical, explaining the seemingly excellent fit compared to the error bars. This divergence of ∼40 mrad is similar to that measured for the previous oven design [159], which in both cases is broader than expected from theory, in this case around a factor of 2.

The fitted amplitude of the peak can be converted to the flow rate using the following method.

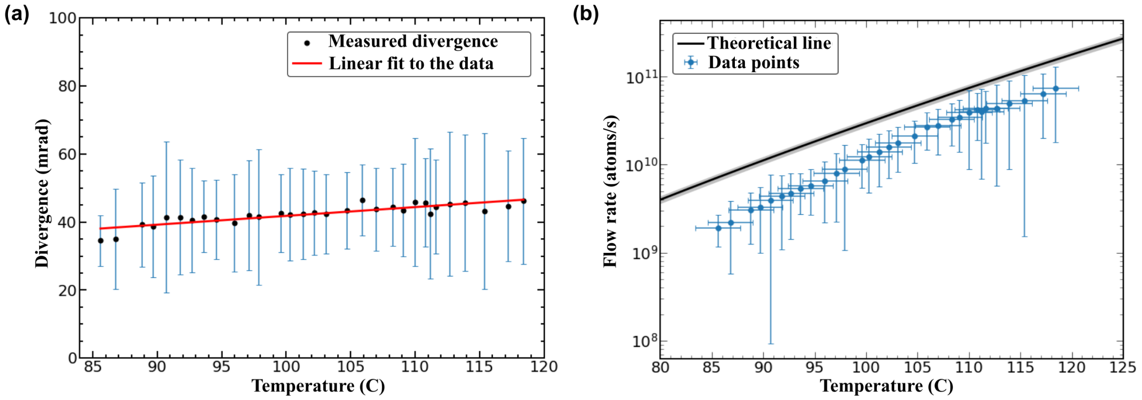

Figure 6.8: (a) The divergence of the atomic beam from the oven as a function of temperature. (b) Flow rate of the atomic beam as a function of oven temperature. See text for details about error bars, which are dominated by systematic error. Adapted from [162].

Firstly, the voltage of the signal obtained is converted to optical power using the sensitivity of the photomultiplier tube at the used control voltage. This is used to estimate the total power emitted by the atoms, keeping in account all the optical losses (e.g. viewports, optics, filter) as well as the solid angle of the fluorescence pattern and the collection optics. This gives us the atomic density ρ at respective temperatures expressed as the equation 6.2, where V_{int} is the interaction volume, P_{max} is the optical power of the peak chosen, $\Omega_{tot} = 8\pi/3$ is the total solid angle of the dipole emission and Ω_{ph} is the total angle as seen by the photodiode.

$$\rho = \frac{1}{V_{int}} P_{max} \frac{\Omega_{tot}}{\Omega_{ph}} \left(\frac{\hbar\omega_0 \Gamma s}{2\sigma_t \sqrt{2\pi}} \int_{-\infty}^{\infty} \frac{\exp\left[-v^2/(2\sigma_t^2)\right]}{1 + 4(kv_t/\Gamma)^2} dv_t \right)^{-1} \tag{6.2}$$

The results from the measurements are shown in Figure 6.8. The vertical error bars come from the uncertainty of the fit and the conversion of the measured voltage to the emitted fluorescence power. This conversion gives a large error due to the logarithmic dependency of the gain, making it difficult to measure precisely. The horizontal error bars arise from the systematic uncertainty of the temperature reading as specified by the manufacturer. A full description and discussion of the various error sources is given in [162]. This measurement gives a flow rate of about 10^{10} atoms/s at a temperature of 100 °C.

With this performance of about 10^{10} atoms/s and a divergence of about 40-50 mrad, this oven can be used as the source of atoms in order to generate the ultra-cold samples using the standard state-of-the-art cooling techniques and also to perform spectroscopy.

6.2.3 Precision frequency measurement of the $^1S_0$-$^1P_1$ transition

The atomic beam is used to measure the absolute frequency and isotope shift values of the $^1S_0$-$^1P_1$ transition of cadmium. Earlier absolute frequency measurements of this transition are limited and often decades old [163, 164]. Many of these earlier measurements used interferometers operating in air for their frequency calibration and therefore require the refractive index at 229 nm to be well known. The refractive index of air as a function of wavelength can be calculated from empirical formulae [165], but it also depends upon ambient environmental factors, such as temperature, pressure and humidity. Moreover, a full measurement of the isotope shift values of this transition has not been performed before, with values for only some of these shifts published [166]. Otherwise, the only available data comes from the frequency dependence of MOTs [56, 99]. Furthermore, precise and accurate measurements of isotope shifts have gained considerable recent attention due to the possibility to search for and constrain potential extensions to the standard model, including new long-range or Higgs-like forces [167–169]. They can also provide valuable data for atomic structure calculations [170].

At the above discussed parameters of ambient pressure of the chamber, divergence and flow rate of the atomic beam at 100 °C, we identify the peaks clearly from all the eight isotopes of cadmium in a single 3 GHz sweep in the DUV. In order to convert the time axes of the obtained fluorescence spectrum, a frequency reference is necessary, which in this experiment is another home-made bow-tie cavity which is designed to have a long path length in order to reduce the free spectral range and increase the number of resonances observed during a spectrosocopy measurement. To this cavity, a part of the blue light generated by the first frequency doubling step at 458 nm is sent.

The design length of the cavity results in a free spectral range of 210 MHz. This was further measured by simultaneously monitoring the transmission of the cavity and the wavelength of the VECSEL as it was slowly swept in frequency. The frequency positions of the resonances were then estimated and fit with a straight line, in both the frequency sweeping up and down configurations. The slope of the fitted lines can be used to extract the free spectral range and a mean of the sweep up and down values, weighted with the error of the fit, is taken to give a measured value of free spectral range of 204.2 ± 0.9 MHz.

During a spectroscopy measurement, the transmission of this reference cavity is monitored. The time-to-frequency conversion is performed by fitting a parabola to the measured cavity resonances

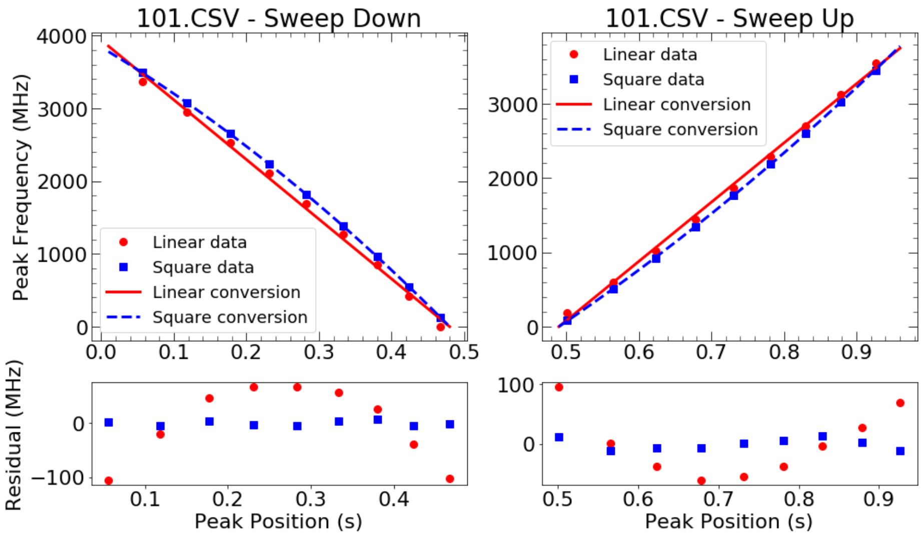

Figure 6.9: Frequency linearization of the PZT sweep. Left plot is for the negative slope of the voltage change and the right is for positive slope. Lower panel shows the residual when performing linear (red circle) and quadratic linearizations (blue square).

and using the measured FSR, allowing the non-linear response of the PZT to be corrected for. Figure 6.9 shows how the frequency of the UV changes with time when applying a linear change in voltage to the PZT. The hysteresis effect is observed as the PZT position is varied at the same frequency while the sweep is in different direction, with both nonlinear and asymmetric behaviour observed. As seen in Figure 6.9, a linear fit does not describe the change in frequency well, though it was found that fitting with both 2nd-order and 3rd-order polynomials provide a good fit, with minimal difference in the observed fit residuals. The 2nd-order (quadratic) fit was chosen for converting the temporal data into smooth and continuous frequency data.

Simultaneously, a fraction of IR light, directly from the master laser source is sent to a wave meter (Bristol Instruments, 621) using fibers. This helps in providing an absolute reference of the frequency with a stated accuracy of 0.2 ppm.

After having obtained the complete fluorescence spectrum from the atoms, it is first converted to the frequency spectrum and the signal is cleaned by using the monitored UV power to remove amplitude noise. This cleaned signal is then fit using a simultaneous fit to ten Voigt profiles where in the weighted distribution from the natural abundance of the cadmium isotopes is assumed. For

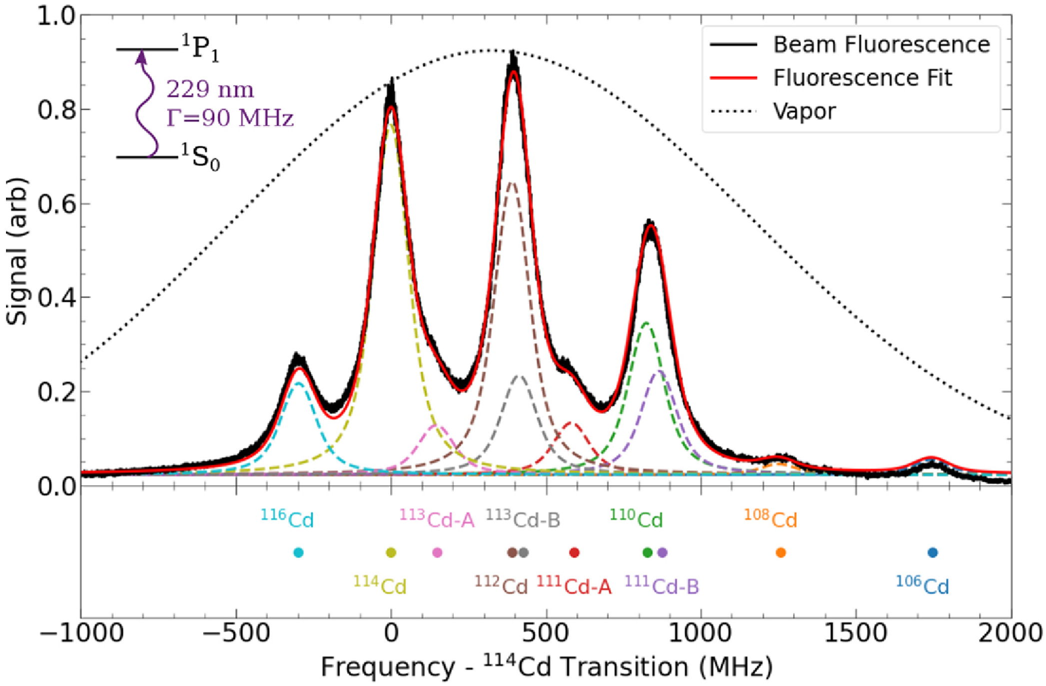

Figure 6.10: Isotope shift measurement. Black line is the fluorescence signal and the red is the fit. The dashed colored lines are the individual isotope contributions and the dashed black line is the Doppler broadened spectrum of a vapor at same temperature as the oven. The lower panel shows the mean values of the frequencies obtained from ten fits. From [57].

the fermionic ^{111}Cd and ^{113}Cd isotopes, the strength of the hyperfine splitting is used. With this fit the relative frequency spacing between all the transitions is extracted.

Figure 6.10 shows the fluorescence signal where all the peaks are fit as mentioned above. The relative frequency separations with respect to ^{114}Cd are presented in Table 6.1, which is the average value from 10 spectra. The first error in the frequency values arises from the statistical error from the fitting procedure and the second one is the systematic error from the frequency conversion.

However in order to measure the absolute value of the transition frequency, the Bristol wave meter is used to the frequency calibrate the signal. Similarly like the relative frequency measurement, we take multiple sweeps obtaining the ^{114}Cd trace, which as shown in Figure 6.10 has negligible contributions from other isotopes. Instead of using the reference cavity, the value of the wavemeter is recorded simultaneously to the sweep. The fluorescence is plotted against the wavemeter reading

Table 6.1: Summary of measured isotope shift relative to the ^{114}Cd isotope. Error values for this work sequentially represent the combined statistical and fitting error and the systematic error of the frequency conversion – see text for details. Two measurements are also presented from [166].

Transition	**Determination 1 [166]**	**Determination 2 [166]**	**This work / MHz**
^{106}Cd	-	-	1748.1 ± 5.2 ± 9.7
^{108}Cd	-	-	1258.5 ± 5.3 ± 7.0
^{110}Cd	878 ± 17	905 ± 35	826.2 ± 4.2 ± 4.6
^{111}Cd - F′=1/2	-	-	591.5 ± 4,4 ± 3.3
^{111}Cd - F′=3/2	878 ± 17	-	874.7 ± 4.3 ± 4.8
^{112}Cd	375 ± 15	395 ± 30	391.6 ± 4.0 ± 2.2
^{113}Cd - F′=1/2	-	-	148.0 ± 4.2 ± 0.8
^{113}Cd - F′=3/2	375 ± 15	-	426.5 ± 4.5 ± 2.4
^{116}Cd	-	-	-298.7 ± 4.0 ± 1.7

and fit to a Voigt profile to find its central value. Again we take multiple spectra and average the result. We obtain the frequency of this transition to be 1309864506 ± 4 ± 262 MHz, where the first error is the statistical error arising by taking the mean of all the measurements and the second error is coming from the uncertainty of the wavemeter. This is much larger than the first and second order Doppler shift and the recoil energy, which are therefore ignored. For example, the first-order Doppler shift is given by $\delta\nu = \vec{k} \cdot \vec{v}$, so the measured beam angle of <4 mrad gives $\delta\nu$ <200 kHz. This measured value is consistent with the previous value reported in [163].

Since the publication of these spectroscopic measurements [57], more precise and accurate measurements have been very recently reported [171]. These measurements use a temperature-stabilized cavity as a reference and fully calibrate the non-linearity of their wavemeter for improved accuracy. They also use enriched sources of cadmium to allow for the fermionic transitions to be identified more clearly. The measured absolute frequency value of the ^{114}Cd transition is consistent with the value reported here, but there is some discrepancy between the isotope shift values. In particular, there appears to be a systematic difference in the frequency calibration, which most likely arises due to the non-linear response of the wavemeter used here.

6.3 Spectroscopy of the $^1S_0$ - $^3P_1$ transition at 326 nm

The laser system for generating light at 326 nm, described in Chapter 4, is also tested by performing high-precision spectroscopy on narrow $^1S_0$ - $^3P_1$ transition, as described in [58]. The goal here is to observe saturation absorption spectroscopy and to generate an error signal for locking the laser to these signals. This will verify that the noise properties of the laser are suitable for addressing this narrow linewidth transition.

The optical set-up of the fluorescence collection optics is similar to those employed in the 229 nm spectroscopy, except, a different optical filter and a higher sensitivity photo-multiplier tube is used, due to the reduce fluorescence from this transition. Likewise the oven temperature is raised to ~150 °C to increase the flow of atoms.

A beam of 326 nm with 6 mW of power and a radius of 5 mm is sent in an orthogonal direction to the atomic beam. The polarization is optimized to be horizontal using the fluorescence signal. A triangular wave is sent to the PZT of the pre-stabilization cavity, which allows a sweep of about 4 GHz in the UV with which all the eight stable isotopes are visible, the isotope shifts of which have

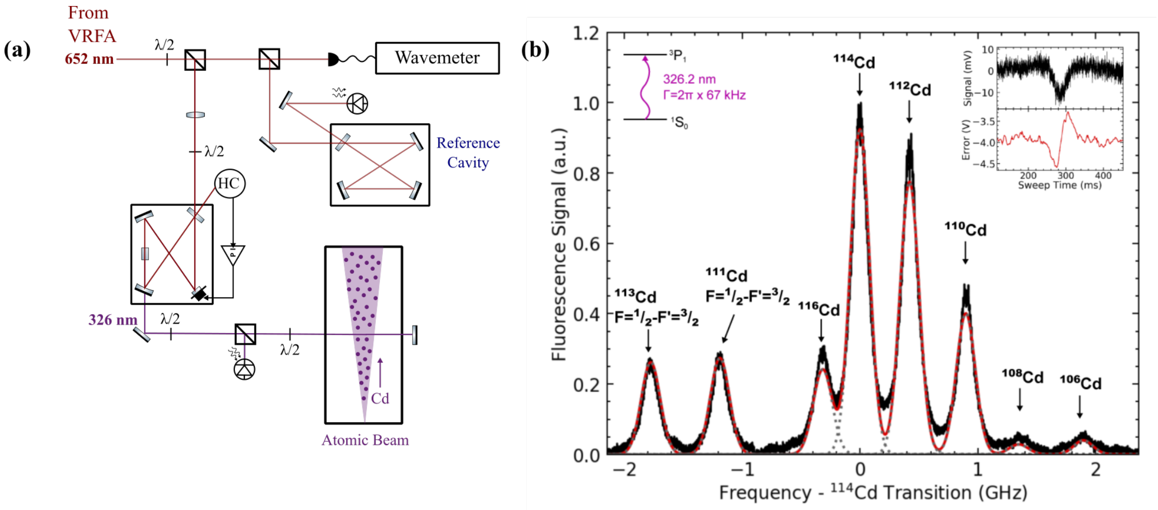

Figure 6.11: (a) shows the optical schematic of the 326 nm interacting with the atoms while (b) shows the signal from the atoms. Black line is the fluorescence signal and the red is the fit. The dashed gray lines are the individual isotope contributions to the complete spectrum. The inset panel shows the error saturation absorption spectroscopy signal and generated error signal. Adapted from [58].

previously been measured [100, 172]. The Voigt fitted peaks of the signals from all the isotopes is shown in Figure 6.11, where the fit performed is assumed to have the amplitude based on natural abundances, as in the previous section.

The saturation absorption spectroscopy is also performed on the cadmium vapor which requires a pump and probe beam, overlapped in an approximately in counter-propagating manner at the atomic beam position. The inset of Figure 6.11 (b) shows the saturated dip obtained and also its error signal. The error signal is derived by modulating the laser frequency at 10 kHz with an acousto-optical modulator (AOM) and then using a lock-in amplifier.

6.4 Oven reliability

The oven used for generating the cadmium beam did pose certain experimental challenges. This section briefly discusses the reasons which lead to the breakdown of the oven, i.e, loss of the signal from atoms, and the solutions and plans to counteract these problems.

After the first time that the oven was opened after use for spectroscopy, it was noticed that cadmium had been reacting with the copper gasket used to seal the oven reservoir. This reaction was severe and the copper gasket had been almost entirely eroded, as can be seen in Figure 6.12 which shows the image of the copper gasket after re-opening the oven. This was solved by replacing it with a silver-plated copper gasket which seems to successfully prevent this reaction, which we were not previously aware of and may not have been reported elsewhere.

Another more critical problem seems to have been related to the high vapor pressure of cadmium. While the beam worked very well for some months at the temperatures needed for 229 nm, since the 326 nm fluorescence is fainter than 229 nm, this required a higher working temperature of the oven. At high temperatures of the oven (>150 °C), there was a gradual loss in signal and opening the chamber revealed clogging of the capillaries (Figure 6.12). Capillary clogging tends to occur because the surface area of the capillaries is large, so they cool faster than the rest of the chamber, leading cadmium to preferentially condense there [173]. Clogging can therefore in principle be solved by maintaining the capillaries at a higher temperature than the rest of the oven and the oven has been redesigned for this purpose.

At another instance, problems with the ion pump was observed. It is suspected that this may have occurred due to the pump being filled with cadmium, again due to operating the source at high temperatures. This has made it difficult to subsequently achieve the lowest pressures of $\sim 10^{-9}$ mbar.

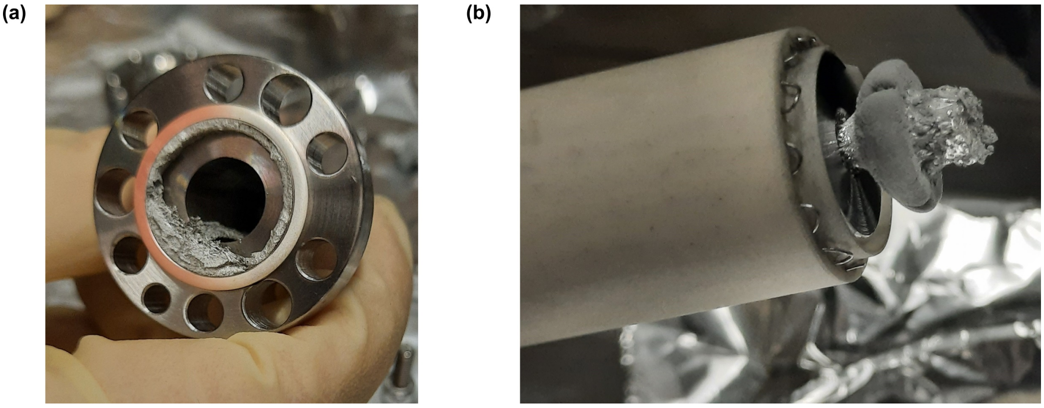

Figure 6.12: (a) The copper-cadmium reaction on the gasket. Almost the entire inner section of the gasket has reacted and the cadmium is attracted out of the main oven chamber. (b) Clogging of the oven capillaries with cadmium following operation at high temperatures (T >150 °C).

The vacuum pump companies don't seem certain about their performance so this remains an open technical question which requires more research.

Chapter 7

Towards the production of ultra-cold cadmium ensembles

This chapter mainly discusses the optical system and vacuum chamber design of a state-of-the-art source of ultra-cold cadmium. It presents thorough numerical simulations of the cooling and trapping of cadmium which is divided into two stages: firstly on the broad dipole-allowed transition at 229 nm; and then on the intercombination transition at 326 nm. The design begins with an atomic oven and uses a minimal amount of laser radiation at 229 nm light due to the known problems with using and producing the light at this wavelength. This is achieved by using the 229 nm light only to slow the output from an atomic oven, allowing for subsequent direct loading into a 3D magneto-optical trap (MOT) at 326 nm. The atomic trajectories throughout the full vacuum chamber is also presented, giving a complete picture of the position and velocity evolution of the atoms and is used to estimate the loading rate of the 3D MOT for a range of experimentally feasible parameters. The final part of the chapter discusses the future prospects towards the realization of the degenerate source of atoms in an optical dipole trap. The theory and the simulations of the power and beam waist requirements to generate the dipole trap for cadmium atoms are discussed.

7.1 Introduction

7.1.1 State-of-the-art and system requirements

A cold, continuous and an efficient source of atoms enables table-top experiments on a broad range of topics such as atom interferometry, quantum information, quantum simulation and many more [174]. Historically, alkali elements have been primarily used to test the initial theories of laser cooling and trapping techniques, often due to the availability of laser sources. For example, high power single-mode sources are readily available for laser cooling and trapping of rubidium due to the principle cooling transition being at 780 nm.

Alkaline-earth elements and alkaline-earth-like elements are often rather recently studied in comparison to alkali atoms, and this is especially true of cadmium. Until now, the production of cold cadmium samples have been done directly from a vapor source onto the $^1\mathrm{S}_0 \rightarrow {}^1\mathrm{P}_1$ via a MOT [56, 99]. While more recently, cadmium has been cooled using the narrow linewidth intercombination transition, $^1\mathrm{S}_0 \rightarrow {}^3\mathrm{P}_1$ [54]. The loading of atoms directly from the vapor can cause limitations in the background pressure of the chamber. For this purpose we developed the novel cadmium beam to be used instead of a vapor source (Chapter 6). Furthermore, standard cooling and atom source techniques like a Zeeman slower or a 2D MOT, or further cooling to quantum degeneracy, have not yet been demonstrated with cadmium.

State-of-the-art cooling systems often employ such techniques using spatially separated regions where each transition is addressed consecutively and independently. In strontium, for example, this architecture has been used to develop continuous ultra-cold sources, including the first continuous Bose-Einstein condensate [86, 175, 176]. The aim of this chapter is to design and simulate a similar system for cadmium, having the qualities of fast loading rates, μK or lower temperature atoms, and excellent vacuum for long-lived coherence for the application to atom interferometry.

7.1.2 Laser cooling and trapping of cadmium

Given the novelty of using cadmium as a quantum source and also the power limitations experienced during the development of laser systems in the UV regime, it is important to clearly understand the parameter space required to generate ultra-cold cadmium sources. Therefore, in this chapter, each cooling and trapping stage with the 229 nm and the 326 nm transition is considered in detail, to understand the parameter space as allowed by the developed lasers discussed in Chapters 3 and 4. This will also help to elucidate the specific challenges posed by cadmium in producing a cold atom

Table 7.1: Relevant properties of the main cooling transitions for Cd, Sr and Yb. Values for the wavelength (λ), corresponding natural linewidth (Γ), saturation intensity (I_s), Doppler temperature (T_D) and the minimum stopping distance for atoms at the most probable velocity ($v = \sqrt{2k_B m/T}$) of a Maxwell-Boltzmann distributed 100 °C sample (d_{stop}) are reported.

Atom	λ (nm)	$\Gamma/2\pi$	I_s (mW/cm^2)	T_D	d_{stop} (m)
			^{1}S$_0$-^{1}P$_1$		
Cd	228.9	91 MHz	992	2.2 mK	6×10^{-3}
Sr	460.9	32 MHz	42.5	0.8 mK	4×10^{-2}
Yb	398.9	28 MHz	57.7	0.7 mK	4×10^{-2}
			^{1}S$_0$-^{3}P$_1$		
Cd	326.1	66.6 kHz	0.252	1.6 μK	12
Sr	689.4	7.4 kHz	0.003	180 nK	230
Yb	555.8	182.2 kHz	0.139	4.4 μK	7.5

source.

Information on the relevant transitions of cadmium are given in Table 7.1, alongside the more commonly employed strontium and ytterbium for comparison. The singlet transition is the main dipole-allowed cooling transition at 229 nm with the highest linewidth among the three atoms (Γ=2$\pi\times$90.9 MHz). However, production of high-power continuous-wave light at this wavelength is challenging, as detailed in Chapter 3, with only around 100 mW available for stable operation. The design presented here mitigates for this comparative lack of power by making the capture efficiency of the system as high as possible.

Moreover, the use of high power 229 nm light poses technical and fundamental problems in producing high atom numbers in a magneto-optical trap. As discussed in Section 2.3.1, the 229 nm light is able to photoionize the atoms from the ^{1}P$_1$ state and this has a limiting effect on the atom number in the MOT [99]. The energy of the 229 nm photons is also in principle sufficient to cause photoionization from the ^{3}P$_1$ state.

Additionally, high-power DUV light is known to be damaging to optical coatings and degrades their performance, especially those under vacuum, where this degradation can be rapid. The complete damage mechanisms are not fully understood, though there seems to be contributions from both oxygen depletion of the coating material and from UV-induced ionisation of hydrocarbons which subsequently bond to the coating surface. Although research into improving optical coatings under vacuum is ongoing [177, 178] and fluoride-based coatings seem to perform much better [147], this problem is not currently solved. Excessive use of 229 nm light would therefore require the system to be regularly opened or purged with oxygen to recover the coating performance. Furthermore, not all standard optical components are easily available for 229 nm. For example, while single-mode fibres for the UV have been demonstrated, they are not commercially available and require a complex production procedure for a still limited performance [179, 180].

Nevertheless, given its high scattering rate and low wavelength, the 229 nm transition has the ability to slow down fast atoms at very short stopping distances (Table 7.1), which is useful for efficient loading of atoms coming from the oven source. Cadmium has very recently been trapped without using 229 nm, but since this system requires three additional repumping lasers [100], this approach is not considered further here.

Following initial cooling with the 229 nm, atoms can be further cooled down with the 326 nm intercombination transition using optical molasses configuration and also a three-dimensional MOT. Experimentally, the production of the 326 nm doesn't pose as many challenges as the 229 nm production. A maximum usable power of 1 W has been produced with the system described in Section 4.2 and similar powers have been achieved in this region of the UV elsewhere [151, 181]. This is also true in terms of damage to the vacuum viewports and optics. Furthermore, as shown in Table 7.1, the linewidth of the 326 nm transition is between that of cadmium and ytterbium. This is interesting because it is possible to load $\sim 10^8$ atoms/s directly into a MOT on the $^1S_0$ - $^3P_1$ ytterbium transition [182], but this is very difficult on strontium. This suggests that it may be possible to load a MOT on the intercombination transition of cadmium without using a MOT at 229 nm first.

7.1.3 Basic idea of the cold atom system

The basic idea of the cold atom apparatus for producing cadmium is shown in Figure 7.1. It is inspired by similar designs for strontium [175]. Most of the remainder of this chapter consists of the numerical simulations this system to understand its feasibility and performance.

In brief, however, the proposal is to load atoms from a collimated source into a 2D MOT at 229 nm. There is the option to additionally perform Zeeman slowing on this collimated beam to increase the atom number in the 2D MOT. The 2D MOT will act as a source of slow atoms, which are

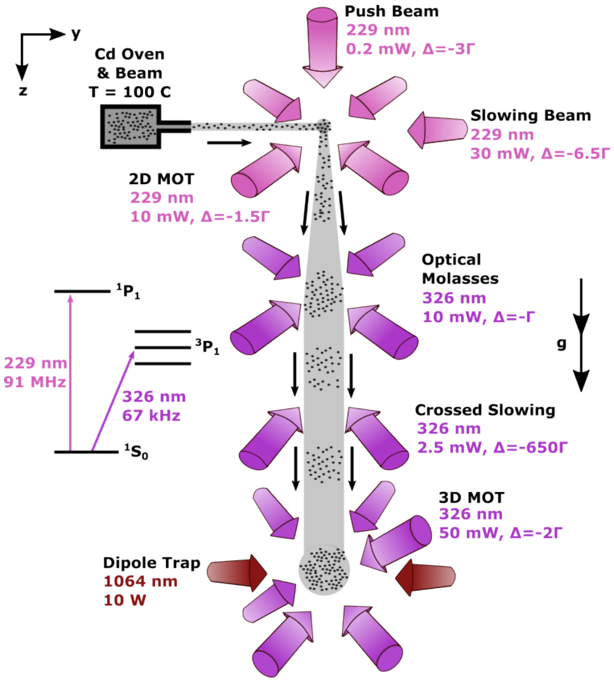

Figure 7.1: Cartoon of the basic idea of the cold cadmium source and a simplified energy level diagram of cadmium, showing the relevant transitions for cooling and trapping. An estimation of the necessary powers (per beam) and detunings required are shown for each stage.

pushed vertically downwards by a low-intensity beam. The remainder of the system uses only 326 nm light to generate lower temperatures, reduced optics damage and no photoionization. Furthermore, spatially separating the oven from the 3D MOT region will assist in achieving better background pressure, as well as isolating the high-energy 229 nm photons from interacting with the 3D MOT and potentially reducing the trap life times and atom number.

Firstly in this second-stage 326 nm section, the atoms are transversely cooled in 2D optical molasses to collimate the falling atoms. They are then slowed vertically by angled beams before being loaded into a 3D MOT, which would ultimately be transferred from the 3D MOT chamber using an moving optical dipole trap to a science chamber to perform interferometry with cold strontium atoms generated elsewhere (see Chapter 8). However, this design is also aimed in such a way that interferometry can be performed in the main chamber on cadmium alone, by leaving the vertical axis open.

This design may also be of use for other alkaline-earth-like systems who have transitions in the DUV. For example, zinc has similar transitions to cadmium, with its $^1\mathrm{S}_0$ - $^1\mathrm{P}_1$ and $^1\mathrm{S}_0$ - $^3\mathrm{P}_1$ transitions being at 214 nm with $\Gamma=2\pi\times71$ MHz and 308 nm with $\Gamma=2\pi\times4$ kHz, respectively. Laser cooling and trapping of zinc is only in its very early stages [183] and the system presented here could prove a guide for future experiments sharing similarities in the transition properties.

7.2 Numerical simulation description

The numerical simulation is performed using the Monte-Carlo method with the Python programing language and calculates the trajectories of the atoms by updating their spatial and velocity values in discrete steps of time. This method has been used successfully to simulate a broad range of MOTs and related cold atomic sources, including standard 3D and 2D MOT implementations [184, 185]. It begins with atoms being assigned a particular position and velocity in a pseudo-random sampling method. At each constant time interval (greater than the lifetime of the transition), the acceleration of the atom is determined from the forces acting on the atom at that point in the space, which are the radiation pressure force derived from the semi-classical theory of atom-light interaction (see Section 2.1.2). The time interval is chosen to be 50 μs and the complete simulation time is assigned as 500 ms. At each cooling stage in the complete simulation, the simulation is terminated based on the final fate of the atom, such as being lost or trapped. That is, when the atoms fulfill certain pre-defined criteria of having velocities below a critical limit and being at a particular spatial position (e.g. within the central MOT region).

The laser beams are assumed to be Gaussian and the tails on both sides are truncated depending on the radius of the viewport they are assumed to pass through. The interaction is modeled by having the circular polarization of the light decomposed into its respective σ^+, σ^- and π components [186]. This is helpful when the laser beam and the magnetic field interact off axis, i.e. allowing for the possibility of π transitions. Also considering the direction of the magnetic field (not just the magnitude), the locally induced acceleration onto the atom by a laser beam with a unit vector $\hat{k}$ is given by the equation 7.1, where $s = I/I_{sat}$ is the saturation parameter of the laser beam, s_{tot} is the total saturation parameter from all the beams, Δ_Γ is the detuning of the beam in units of linewidth, $k_\Gamma = 1/\lambda\Gamma$, $\mu_\Gamma = \frac{\mu_B}{2\pi\lambda}$ and for the bosonic isotopes of cadmium, $\Delta g_F = g'_F m'_F - g_F m_F$, which is 1 for 229 nm transition and 1/6 for the 326 nm transition.

$$a = \frac{\hbar\pi\Gamma}{m\lambda} s\hat{k} \sum_{n=-1,0,1} \frac{\eta_n}{1 + s_{\text{tot}} + 4\left(\Delta_\Gamma - k_\Gamma\right)\hat{k}\cdot\vec{v} - \Delta g_F \mu_\Gamma n\left|\vec{B}\right|} \tag{7.1}$$

The parameter η_n is given by $\eta_0 = \left(1 - \left(\hat{k}_i \cdot \hat{B}\right)^2\right)/2$ and $\eta_{\pm 1} = \left(1 \pm \alpha \hat{k}_i \cdot \hat{B}\right)^2/4$, where $\alpha = \pm 1$ is the handedness of the circularly polarised light relative to the propagation direction and the subscript i refers to the beam in question [186]. The summation over n corresponds to the decomposition of the circularly polarized light into its respective three components. This formalism is also extended to account for linear polarisation, as well as circular. In this case the η parameters are changed to $\eta_0 = \left(\hat{E}_i \cdot \hat{B}\right)^2$ and $\eta_{\pm 1} = \left(1 - \left(\hat{E}_i \cdot \hat{B}\right)^2\right)/2$, where $\hat{E}_i$ is the unit linear polarisation vector of the beam.

Another feature while accessing the 326 nm transition is spectrally modulating the beam in order to increase the capture velocity [92]. All the individual modes are considered to behave as an independent beam while the total power in the beam is evenly distributed amongst all the modes. These modes are assumed to be a linewidth away from each other.

The various magnetic fields are pre-calculated in a grid like format in 3 dimensions and then interpolated. The interpolation functions are saved and loaded separately into the main simulation to save computational time. At a given point all the magnetic fields from the various coils and magnets are summed to give the complete field. The magnetic field of Earth is assumed to be cancelled throughout the whole experimental region and therefore not considered.

Finally, the simulation also considers spontaneous emission, which is assumed to be isotropic in nature and results in a heating effect (see Section 2.1.4). It is modeled by $\hbar k \sqrt{R\tau}\hat{x}$ where R is the total scattering rate which can be estimated from equation 7.1, τ is the simulation step time, and $\hat{x}$ is the direction of the emission chosen pseudo-randomly [134]. This helps to limit minimal velocities the atoms can reach to the respective Doppler temperature of the interacting transition.

7.3 Preparation of cold cadmium: Numerical simulation

7.3.1 Phase space of the oven output

This section describes the numerical Monte Carlo simulation of the position and velocity spread of the atoms emitted from the oven, which serves as the distributions for the laser cooling simulation. The oven design assumed in the simulation has a single 32 mm long capillary with a 1 mm diameter aperture. This is a simplified design due to the reliability difficulties encountered with the original oven, as discussed in Section 6.4. The theoretical flow rate is estimated using equation 7.2 which determines the flow rate in the collision-free regime and also assumes the atoms experiencing half

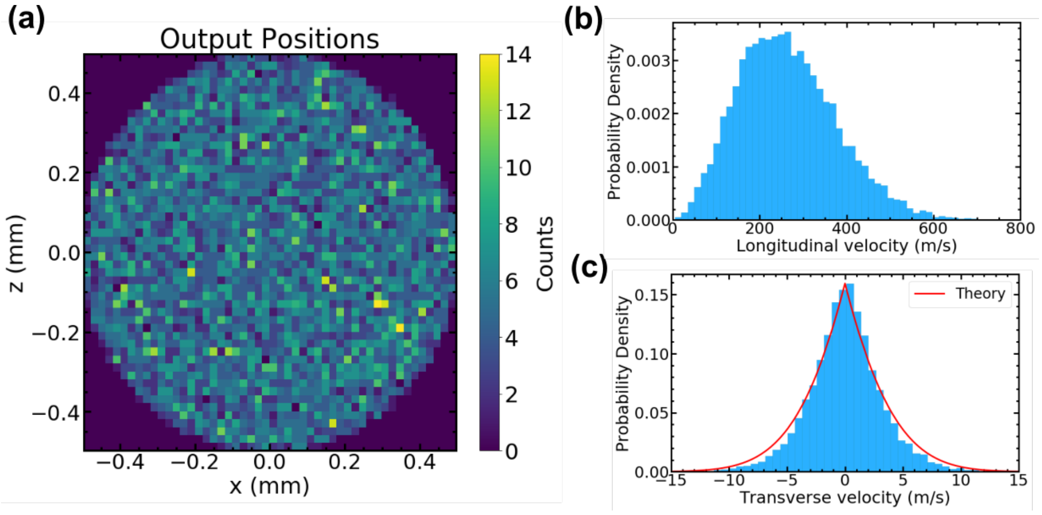

Figure 7.2: Simulated oven output at 100 °C. (a) Atom density in the transverse cross-section at the oven output. (b) Probability density function of atom number as a function of longitudinal velocity. (c) Probability density function of atom number as a function of transverse velocity in agreement with the theoretical distribution.

solid angle from the oven [159].

$$N\left(s^{-1}\right) = \frac{2\pi n \bar{v} r_{cap}^{3} N_{cap}}{3L} \tag{7.2}$$

where L and r_{cap} are the length and the internal radius of the capillaries, respectively, and N_{cap} is the number of capillaries used, which is 1 in this case. $\bar{v}$ is the mean atomic speed given by $(8k_BT/\pi M)^{1/2}$ and n is the atomic density given by P/k_BT. This gives an estimate of 1.1×10^{10} atoms/s at a temperature of 100 °C, similar to the previous oven design (see Figure 6.8).

Despite knowing the velocity distribution of this particular oven design [159, 187], a simulation is performed numerically in order to avoid a bias arising when the transverse and longitudinal velocities are chosen independently. Independent pseudo-random sampling from the known longitudinal and transverse distributions doesn't account for the dependency of the transverse velocity on the longitudinal velocity or vice-versa. Instead, here a simulation geometrically determines the fate of the atom, i.e. if it will exit the oven capillary, beginning with a velocity from the Maxwell-Boltzmann distribution in three dimensions and a position within the diameter of the capillary.

Figure 7.2 (a), shows the position distribution in the x-z position plane of 10^4 atoms selected as exiting the capillary, where the colour code represents the number of atoms in the bin. Gravity is

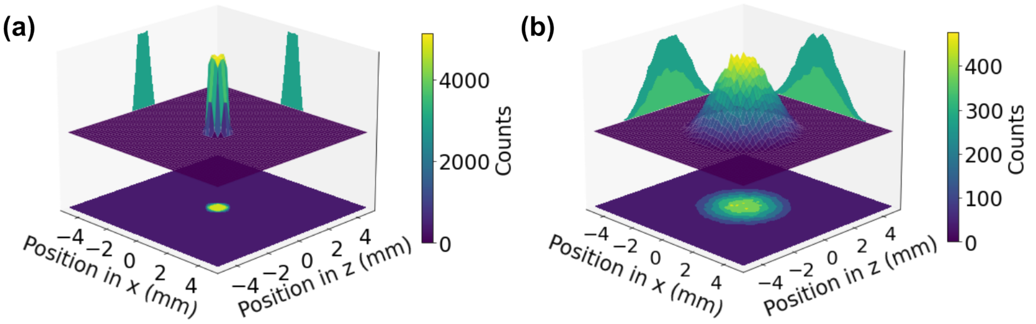

Figure 7.3: Spatial distribution of the simulated output of the Cd oven: (a) at the oven output (y=0 mm); (b) at the position of the 2D MOT (y=75 mm), showing that most atoms are within a radius of 2 mm at this point.

assumed to be along the z axis while the atoms are emitted from the oven along the y axis. The expected uniform distribution across the capillary output diameter is observed.

In Figure 7.2 (b) and (c) panels, the normalized atom density is plotted against the longitudinal and transverse velocity in histogram style. Panel (c) shows this simulated velocity distribution in the transverse dimension to be almost in agreement with the theoretical distribution [187], calculated independently (with a different software). This theoretical distribution for a capillary structure is calculated using the equation 7.3, where $d = 2r_{cap}$ and L are the internal diameter and length of the capillary, respectively, v_0 is the most probable velocity for the Maxwell-Boltzmann distribution and $\Gamma\left(-1/2, v^2L^2/v_0^2d^2\right)$ is the gamma function.

$$P(v,d) = \frac{|v|\exp(-v/v_0^2)\Gamma(-1/2, v^2L^2/v_0^2d^2)}{\sqrt{8\pi v_0^2(1+d^2/L^2)^{1/2}}} \tag{7.3}$$

Finally, the evolution of this atomic beam is studied at distance of 75 mm from the oven output which is the approximate location of the 2D MOT based on the 229 nm transition. Figure 7.3 shows the evolution of the spatial distribution in the x and z dimensions. This serves as preliminary input position distribution that the 2D MOT beams would need to slow the atoms down from. Based on the expanded size of the oven output, it can be seen that most of the atoms are within a few mm, allowing for small beams and CF16 vacuum windows (optical access of 8 mm diameter) as viable choices.

Due to the good agreement between the simulated and theoretical oven outputs and the reasonable flow rate values ($\sim 10^{10}$), these simulated distributions can be used as the first stage of the remaining numerical simulations.

7.3.2 First cooling stages – 229 nm

Permanent bar magnets

One challenge when dealing with the 229 nm transition is the generation of the necessary magnetic fields. Accounting for the high scattering rate of this broad transition, it naturally demands a large magnetic field and magnetic field gradient for both slowing and MOTs. Employment of magnetic coils for these tasks is ruled out not only due to the caused optical blockage around the chamber, but also due to the high currents required to generate the large magnetic field gradients which in turn are responsible for eddy currents and necessitate undesirable water cooling mechanisms. Permanent bar magnets can be used to generate these fields instead of coils. This is further advantageous as the field dies faster thereby avoiding stray magnetic fields penetrating into the subsequent cooling regimes. This also offers easy assemblage and removal along with a homogeneous field.

The design follows what has been previously done for 2D MOTs [188] and it is based upon neodymium bar magnets for the 2D MOT and Zeeman slower. Each bar magnet is of dimensions 25 mm × 10 mm × 3 mm (RS components, N750-RB) therefore compact and weighs only about 5.6 g. The magnetization of the neodymium bar magnets is 8.8×10^5 A/m and measurements have been performed on 18 magnets using a Hall probe. By fitting the measured magnet field as a function of distance from the magnet, the magnetization of each magnet can be found. Reasonable agreement with the theoretical value is found, as summarized in Figure 7.4, but due to the extreme sensitivity of the measurement to position, it is hard to measure precise values.

For the Monte Carlo simulations, the magnetic field is approximated by assuming a point-like ideal dipole from these rectangular, discrete bar magnets, and use the nominal value of the magnetization. Although analytical solutions for rectangular bar magnets exist, only a small error is found when considering an ideal dipole instead, as has also been found previously [189]. The ideal magnetic dipole moment given by equation 7.4 where $\vec{m}$ is the magnetic moment, μ_0 is the vacuum permeability and $\vec{r}$ is the position vector from the magnet.

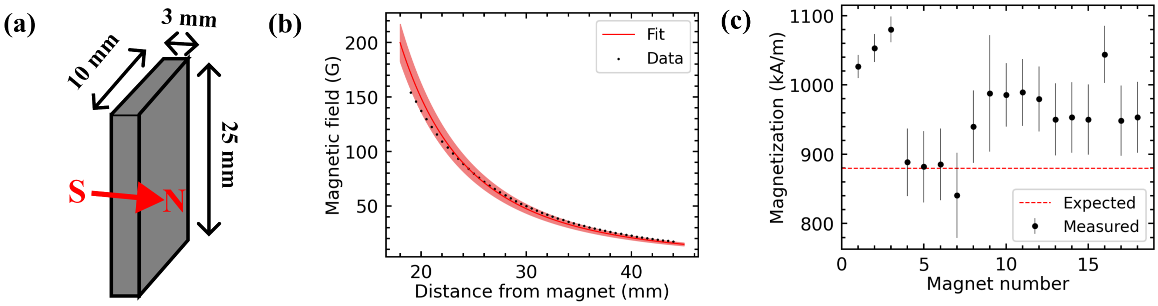

Figure 7.4: (a) Geometry and dipole orientation of the bar magnets. (b) Field measured with a Hall probe along the dipole axis fit to equation 7.4 with the magnetization as a free parameter. Shaded region is from the fit uncertainty. (c) Deduced magnetization for 18 tested magnets. The error bars come from the uncertainty of the fit.

$$B\left(\vec{r}\right) = \frac{\mu_0}{4\pi}\left[\frac{3\vec{r}\left(\vec{m}\cdot\vec{r}\right)}{r^5} - \frac{\vec{m}}{r^3}\right] \tag{7.4}$$

2D MOT with permanent magnets: Simulation and vacuum design

The 2D MOT beams are in the x-y plane, 45° to the oven output (Figure7.5). As mentioned earlier, due to the high linewidth of this transition there is a requirement of high magnetic field gradients. Previous 3D MOT implementations have used gradients of 170 G/cm in the axial direction, so about 85 G/cm in the radial directions is assumed [54, 56]. To estimate the required gradient needed for the 2D MOT, the capture velocity can be determined to the nearest m/s for atoms moving on axis and with no transverse velocity. The MOT beams are assumed to have radius w = 2 mm and detuning Δ = -2 Γ . Furthermore, the magnetic field is assumed to be an ideal gradient $\vec{B} = B_0\left(-a, b, 0\right)$ according to the co-ordinate system defined in Figure 7.5. Velocities up to around 80 m/s can be captured, provided large gradients (>200 G/cm) can be achieved, as shown in Figure 7.5 (a).

To generate such a high field gradient, it is necessary to get the magnets as close as possible to the MOT. For this purpose, instead of housing viewports, the faces of the chamber adjacent to the MOT beams are used to place the permanent magnets. Figure 7.5 shows the chamber design where a cuboid cut is made on two sides of the octagon where the magnets are placed, with the possibility to stack a total of 3 magnets on each side. With this configuration, the closest point of these magnets is only about 22 mm from the center of the MOT, but the magnets remain outside

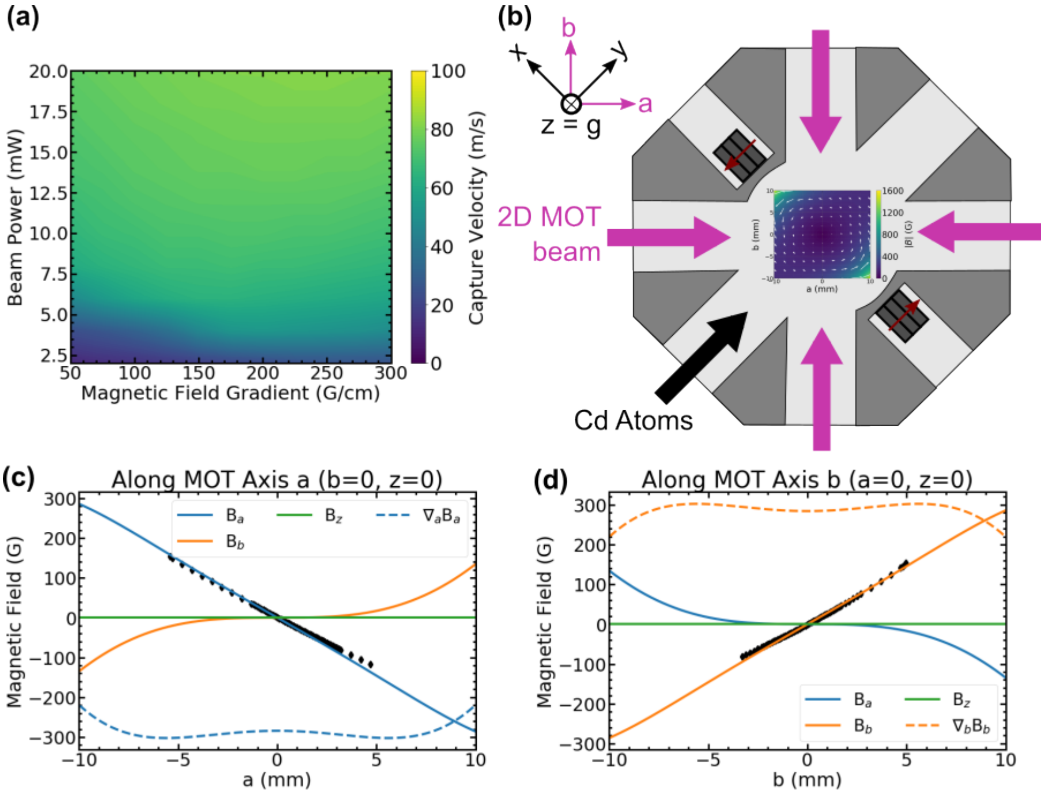

Figure 7.5: (a) Capture velocity with an ideal magnetic field gradient. (b) To-scale design of the 2D MOT chamber and magnets including a scale drawing of the calculated magnetic field. (c) and (d) Calculated (lines) and measured (black diamonds) magnetic fields along the MOT beam axes. See text for more details.

the vacuum chamber for simplicity.

The field generated by these magnets can be analytically simulated according to equation 7.4 and with the magnets orientated as in Figure 7.5 (b). This simulation is done for 2 stacks each composed of 1, 2 and 3 magnets. The calculated and measured magnetic fields for the set of 3 magnets are shown in Figure 7.5 (c) and (d). In the central region the field is almost entirely along the MOT beam axes and very large magnetic field gradients >250 G/cm are achievable with this permanent magnetic set-up. The measurements are made in a test set-up with a Hall probe. There is good agreement between the measured and calculated values, with a measured gradient of 260 G/cm.

These calculated fields can be used to determine the capture velocity of the MOT in a more

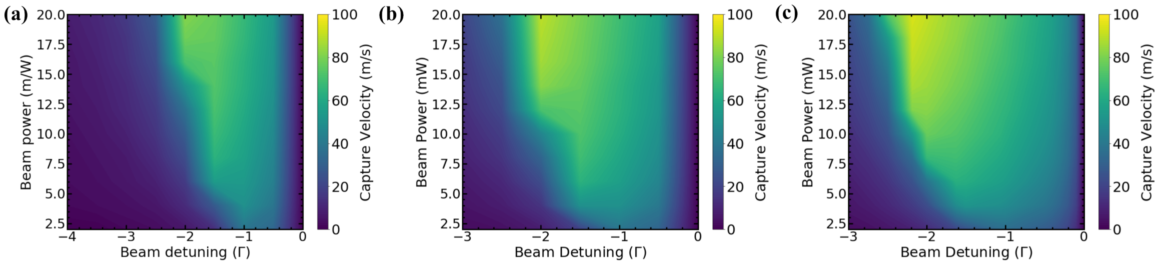

Figure 7.6: Capture velocity of 2D MOT as a function of beam power and beam detuning for 1, 2 and 3 magnets per stack ((a), (b) and (c), respectively). Increasing the number of magnets increases both the capture velocity and the range of usable detunings.

realistic manner than previously. Figure 7.6 shows the contour plot estimating the capture velocity as a function of beam power and beam detuning for 1, 2 and 3 magnets per stack and Figure 7.7 shows the capture velocity as a function of beam power and beam radius for 1, 2 and 3 magnets per stack. The variation in the colour gradient is observed as the number of magnets per stack is increased, showing the advantage of using more magnets. Assuming 3 magnets in 2 stacks, the 2D MOT beams of waist about 2 mm with reasonable powers of 10 - 15 mW and a beam detuning of -2 Γ can capture atoms with initial velocities from 80 - 100 m/s (yellow region).

Values of the beam parameters are chosen for further simulations, using the capture velocity contour plots shown above and the known performance of the 229 nm source (Chapter 3). A beam power of 10 mW, a waist of 2 mm, and 2 stacks of 3 magnets are fixed. At these beam and field

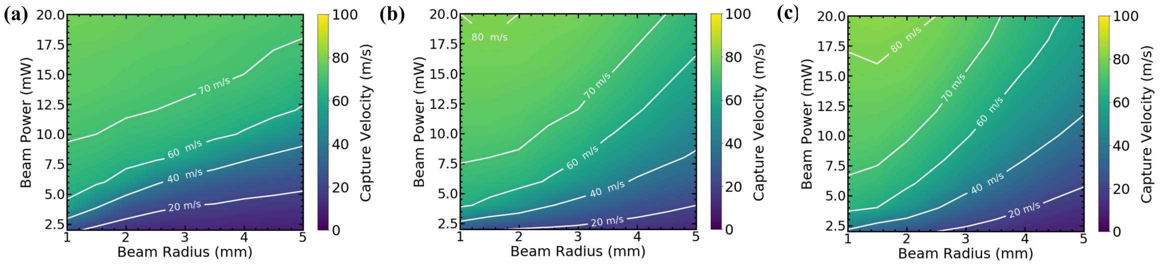

Figure 7.7: Capture velocity of 2D MOT as a function of beam power and radius for 1, 2 and 3 magnets per stack ((a), (b) and (c), respectively). Increasing the gradient increases the capture velocity, especially for smaller beam radii.

parameters, the detuning is set to Δ=-1.5 Γ, which is a choice made to be safe for stable operation. Although higher capture velocities are available at larger detunings, the capture velocity falls quickly with the increasing detuning or decreasing intensity once the optimum is reached (Figure 7.6 (c)), meaning that effects such as power fluctuations or UV damage to viewports could cause problems with daily operation at the nominally optimum value.

Zeeman slower - Simulation

Although the capture velocity of the 2D MOT presented above is relatively high, the captured number of atoms can still be enhanced by the use of a Zeeman slower [66]. This component allows the slowing of atoms from the 100 °C beam down to a few 10s of m/s before they enter the 2D MOT at 229 nm transition. As shown in Table 7.1, the minimum stopping distance of cadmium atoms at this temperature is of the order of 6 mm. Such short stopping distances require powers above the saturation intensity, which, however is not considered due to the main goal of keeping the 229 nm power minimal.

In the semi-classical approach, for an atom interacting with a red-detuned counter-propagating laser beam in a magnetic field, the detuning is given by $\Delta = \Delta_0 + kv + \frac{\mu_B B}{\hbar}$, where Δ_0 is the detuning for the atoms in zero magnetic field at rest, k is the light wave number and v is the velocity of the atoms, with μ_B and B being Bohr magneton and external magnetic field strength respectively. Assuming this detuning is constant throughout the interaction, energy conservation also demands that $v\left(y\right)^2 = v\left(0\right)^2 - \eta\frac{\hbar k}{m}\Gamma y$, where $\eta = \frac{s_0}{1+s+4\Delta^2/\Gamma^2}$ and s is the saturation parameter. This sets the ideal field to be that of equation 7.5, where $B\left(0\right) = \hbar\left[\Delta - \Delta_0 - kv\left(0\right)\right]/\mu_B$, $\Delta B = \hbar kv\left(0\right)/\mu_B$ and $L = mv\left(0\right)^2/\left(\eta\hbar k\Gamma\right)$ [190].

$$B\left(y\right) = B\left(0\right) + \Delta B\left(1 - \sqrt{1 - \frac{y}{L}}\right) \tag{7.5}$$

Generating the required large field gradients over the short distances requested (∼ 60mm) is difficult. One option is again to consider using permanent magnets [191]. In particular, a Halbach array of magnets can be used to generate a uniform field within the array, but dies quickly outside the array structure. Zeeman slowers using Halbach arrays have been demonstrated and studied in detail with e.g. Rb [190, 192] and Yb [193]. However, slowing the most probable velocity of the atoms from the oven (∼ 280 m/s) to 70 m/s (less than the capture velocity of the 2D MOT), requires a change in field of 680 G over ∼7 cm. For comparison, the Halbach schemes with permanent magnets used previously generated fields of only 3 G/cm [192], 12 G/cm [190] and 20 G/cm [193], an order

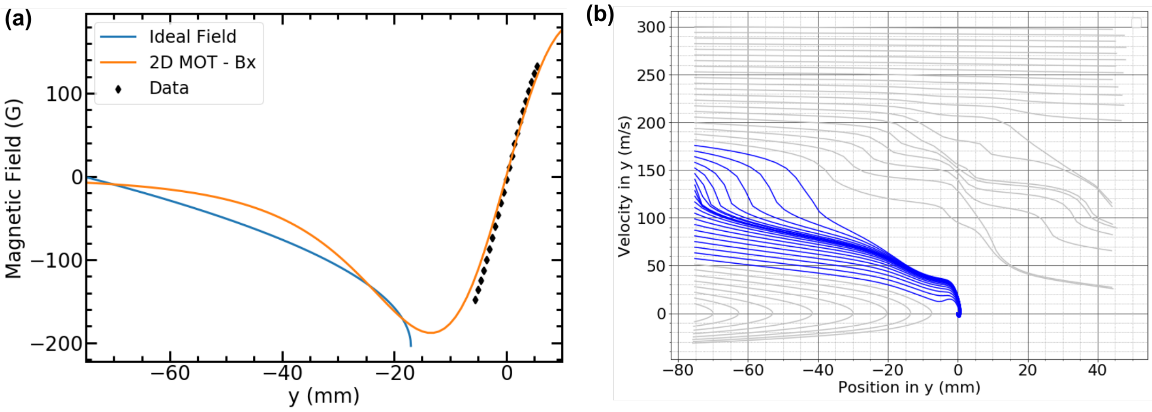

Figure 7.8: (a) Blue line shows the ideal field of the Zeeman slower for slowing atoms from 135 m/s to 75 m/s over 58 mm with Δ = -6.5 Γ. The orange line shows the transverse field from the 2D MOT magnets and the black diamonds the data measured with a Hall probe. (b) The longitudinal velocity of atoms coming from the oven to the 2D MOT when the Zeeman slower beam power is set to 20 mW. Blue traces are those captured in the 2D MOT.

of magnitude smaller.

Interestingly, however, the magnetic field from the 2D MOT magnets already gives a reasonable approximation to the ideal field. The magnetic field in the x dimension (transverse to the atomic beam) with respect to position in y (along the atomic beam) is shown in Figure 7.8 (a). Therefore, like in a Halbach configuration, this field is transverse to the atomic beam direction and requires orthogonal and linear polarization of the slowing beam [191]. This is equally decomposed into σ^+ and σ^- components, so only half the input power is available to drive the σ^+ needed for our decreasing field configuration (see Section 7.2). This effectively doubles the power requirements compared to a configuration where the field and the beam are parallel (longitudinal field Zeeman slower) [194].

The performance of a Zeeman slower using this field is shown in Figure 7.9 as a function of the slowing beam power. The beam waist is 2 mm (focused at the oven output) and the detuning $\Delta = -6.5\ \Gamma$ to match the ideal field as closely as possible. Here the range of oven output velocities captured by the 2D MOT is given is shown, as atoms that are too slow can be pushed backwards by the Zeeman slower beam, especially at higher powers (Figure 7.8 (b)). This range can be approximately converted into a normalized atom number by integrating the longitudinal velocity distribution of the oven output (see Figure 7.2) within the capture velocity range. As can be seen

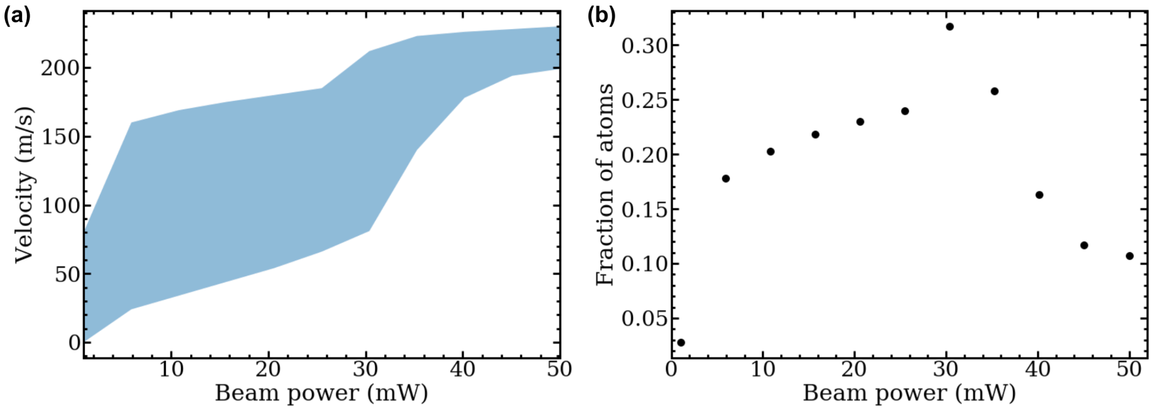

Figure 7.9: (a) The shaded region shows the oven output velocities captured in the 2D MOT when adding a Zeeman slowing beam. (b) The corresponding fraction of the oven output. This value peaks for 30 mW of beam power.

at around 30 mW of power, the fraction of atoms it is in principle possible collect is increased to around 30%, an order or magnitude improvement from the case without the Zeeman slower.

The Zeeman slower therefore tremendously increases the effective capture velocity of the 2D MOT, but at the cost of increasing demands on 229 nm production and use. It is consequently generally ignored in the following sections, although interestingly there is still some potential gain even with just a few mW, though this will require some work for generating the necessary -6.5 Γ frequency offset (~590 MHz).

Push beam: Simulation

Once the atoms are trapped in the 2D MOT in the x and y dimensions, a low-intensity push beam is used to direct the atoms in the direction of gravity (z axis). This beam is orthogonal to the 2D MOT plane and the longitudinal velocity of the slow beam of atoms exiting the 2D MOT (z axis) is controlled by the intensity of this beam. The push beam has two purposes. One is to push the atoms in the vertical direction and stop them from escaping upwards out of the 2D MOT. The other is to direct the atoms to the main chamber where they will be loaded into the 3D MOT. In general, it is good to push the atoms as fast as possible to minimize their transverse spread during the flight. However, here power on the order of 100 μW is preferred as the atoms can otherwise acquire large velocities along with the existing gravitational acceleration and can be out of the small capture

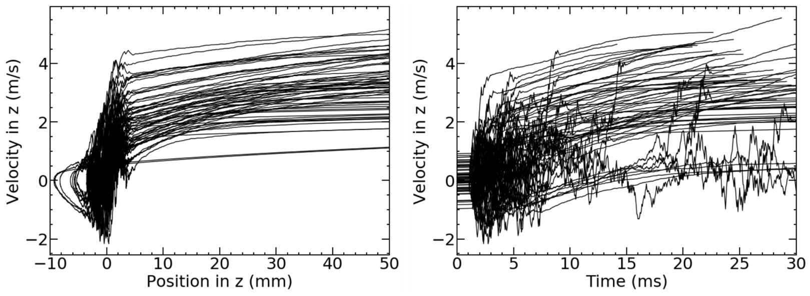

Figure 7.10: Longitudinal velocity as a function of (left) longitudinal position and (right) time after interaction with the push beam.

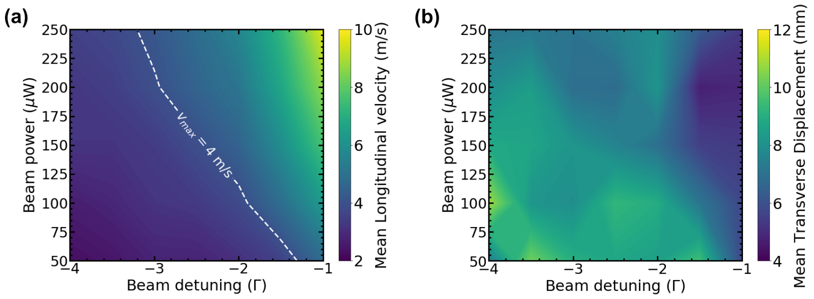

Figure 7.11: (a) Mean longitudinal velocity (v_z) of the slow atomic beam at a position $z = 50$ mm beneath the 2D MOT. The white dashed line is the approximate target value and atoms should be at or beneath this value. (b) Mean transverse displacement at the same location.

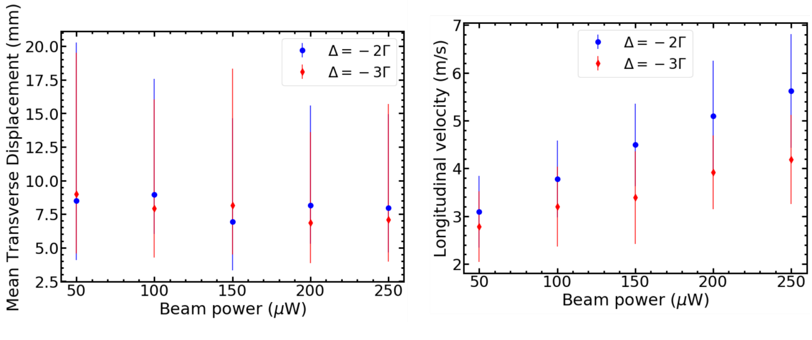

Figure 7.12: (a) Mean transverse displacement (points) and the interquartile range (error bars) of the atoms at $z = 50$ mm. (b) Mean longitudinal velocity (points) and ± the standard deviation (error bars) at the same position. Using $\Delta = -3\ \Gamma$ reduces the dependence on power fluctuations.

velocity regime of the 3D intercombination transition MOT, which is ∼5 m/s (see Section 7.3.3). This output is hereafter referred to as the slow atomic beam, in contrast to the fast beam from the oven. For such low velocities (a few m/s) the effect of gravity can become significant if the atoms are pushed horizontally and alignment between the 2D and 3D MOTs can be complicated. For example, for 2D and 3D MOT chambers separated horizontally by 30 cm and with atoms moving at 4 m/s, the atoms will fall ∼3 cm off axis due to gravity. To counteract this effect, the 2D MOT chamber is placed directly above the 3D MOT chamber meaning the atoms stay on axis throughout their travel.

Sample trajectories of the atoms being pushed from the 2D MOT are shown in Figure 7.10. These trajectories are performed setting the beam radius to 3 mm (to be larger than the 2D MOT) and using a power of 150 μW and a detuning of $-3\ \Gamma$. Panel (a) shows the change in longitudinal velocity as a function of position in z. After exiting the 2D MOT region under the influence of the push beam, the atomic velocities have smoother trajectories and slow acceleration due to the small force of the push beam. Panel (b) shows the longitudinal velocity as a function on time, which shows that most of the scattering events occur in the first 10 ms or so. Keeping this time low is important to help reduce the effect of photo-ionization.

The performance of the push beam is quantified for a range of beam powers and detunings at an offset of 50 mm in the z direction. Once the interactions with the 2D MOT and push beam have subsided, the key parameter is the longitudinal velocity, which should be kept below the capture velocity of the 3D MOT. This plot shows there is a broad parameter space to achieve this value and that only small powers similar to 100 μW are required. Also shown in Figure 7.11 is the transverse displacement, which is a parameter that needs to be minimized in order to keep the atoms sufficiently confined to the vertical axis before the subsequent transverse cooling and collimation in optical molasses on the 326 nm transition. The mean transverse displacement is inversely proportional to the longitudinal velocity, so the longitudinal velocity should be as fast as permissible.

It is also important to check the spread of the velocity and spatial distributions, not just their mean values. Figure 7.12 shows the dependence of longitudinal velocity and mean transverse displacement as a function of the push beam power. The mean transverse displacement is slightly reduced as the intensity in the push beam power is increased but the dependence isn't seen to be major. However, the spread of the distribution is reduced with increasing intensity, as represented by the vertical error bars. The error bars represent the inter-quartile range, which is chosen instead of standard deviation as the transverse displacement of the atoms is a wide distribution with long

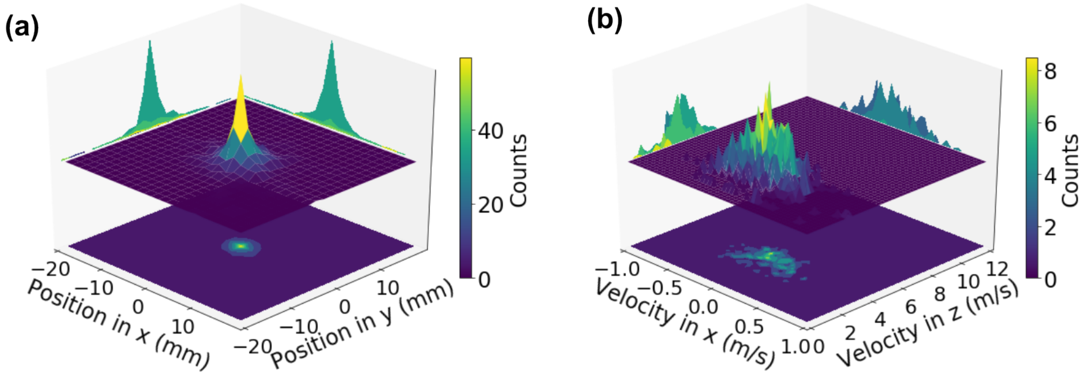

Figure 7.13: Slow atomic beam exiting the 2D MOT cooling region (z = 50 mm). (a) Transverse position distribution and (b) transverse and longitudinal velocity distributions.

tails and doesn't seem to be fully Gaussian. Conversely, the longitudinal velocity and its spread increases with the push beam power. Here the vertical error bars represent the standard deviation of the velocity spread. At a push beam detuning of $-2\,\Gamma$, the longitudinal velocity is seen to be more sensitive to changes in beam power. Hence a detuning of $-3\,\Gamma$ is selected to reduce this sensitivity and a power of 170 μW is chosen to select the desired longitudinal velocity.

With the optimized values of power and detuning from the contour plots, the slow beam of atoms exiting the 229 nm cooling region can be fully simulated beginning from the oven output. Figure 7.13 shows the simulated cold atoms after the interaction with the 2D MOT beams in the x-y plane and the push beam in the z direction. Only atoms which have been successfully cooled, trapped and pushed make up the displayed cross sections of this slow atomic beam in the transverse plane in position (x-y) and in the velocity distribution in the transverse and longitudinal domain (v_x-v_z). This is the cross section 50 mm below the 2D MOT (whose centre defines the origin) and represents about 1% of the atoms from the oven. The position distribution in the x and y dimensions look identical as expected from the symmetry of the cooling thus far. In velocity space, the transverse spread is lower after the cooling due to the 2D MOT beams within a range of around ±0.5 m/s, whereas in the longitudinal direction, the velocity peaks around 4 m/s as desired with a spread of around 1 m/s.

7.3.3 Intercombination transition - 326 nm

Transverse cooling with optical molasses: Simulation

Following the 2D MOT and push beam stage, the atoms are traveling in the direction of gravity towards the 3D MOT on the 326 nm transition. During this path (∼35 cm), the atoms will acquire a significant transverse spread in the spatial regime (∼±4 cm) which can lead to a reduction in trapping efficiencies. To counteract this spread, molasses cooling is performed in the transverse (x-y) plane, 84 mm below the 2D MOT as shown in Figure 7.14, aiming for the minimum achievable velocity, limited by the Doppler limit. These molasses beams are assumed to be frequency modulated to enhance the capture velocity. Each frequency mode is spaced at a frequency distance equal to the linewidth of the transition (66.6 kHz) and is treated as an individual beam in the simulation (see Section 7.2).

To understand the feasibility of this approach, a simplified source of atoms is considered where they all begin from a fixed point in space (0,0,50) mm. The initial transverse velocities are assumed to be a Gaussian around 0 m/s where the σ of the distribution is 0.3 m/s, while the longitudinal velocity is set to 4 m/s, to approximate the output of the 2D MOT and push beam (Figure 7.13). These trajectories are simulated using 100 frequency modes (full span of 6.6 MHz, similar to an earlier demonstration [54]), 10 mW of power in each beam of waist 5 mm. The beams are centred at a height of z=84 mm. The transverse position distribution is shown in Figure 7.14 (b) as a function of position in z. As the atoms travel down in z, the transverse position, both x and y (not shown), remains effectively constant after the interaction with the molasses beams. All the atoms are collimated suggesting that the transverse cooling beams are functioning effectively at these intensity and frequency modulation levels.

Similarly, the transverse velocity shown in Figure 7.15 (a) as a function of position in z shows the initial velocity spread up to 0.7 m/s. These atoms attain velocities close to zero from the point of interaction (about 80 mm in z) and are limited by the Doppler limit thereafter. Also the transverse velocity as a function of time is shown in Figure 7.15 (b), showing that this interaction occurs rapidly on the ms time scale. However, the effect of this molasses interaction causes a small increase in the spread in the longitudinal velocity, as shown in Figure 7.15 (b). This is due to the random kicks from the scattering process and the absence of cooling in the longitudinal direction. Although this heating effect is not prohibitive (±0.3 m/s), it highlights the need to keep the beam intensity as low as functional.

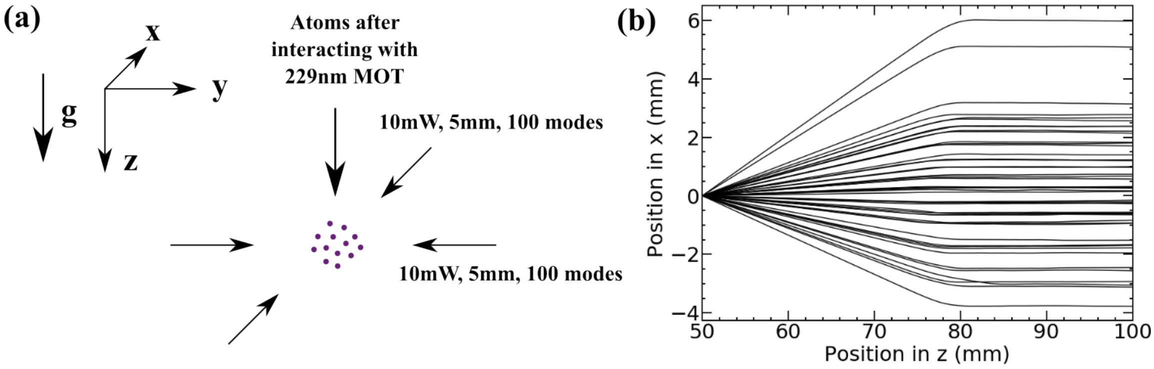

Figure 7.14: (a) Schematic of molasses cooling at 326 nm. (b) Simulated demonstration of the collimation provided by the molasses beams. See text for details.

Following this proof-of-principle validation, more realistic position and velocity distributions can be considered. The initial position and velocities of atoms from the 2D MOT and push beam are considered to interact with the molasses beams (i.e. the distributions from Figure 7.13). The mean transverse speed of the atoms is simulated as a function of the number of frequency modes and beam power (Figure 7.16 (a)) and as a function of beam power and beam radius (Figure 7.16 (b)). The darkest regions in Figure 7.16 represent atoms close to the Doppler limit set by the intercombination transition. In Figure 7.16 (a), as the number of modes is increased at low powers, the atoms aren't slowed down to the lowest limit. This is due to the descreasing saturation parameter of each mode, which becomes significantly less than 1 (beam radius of 5 mm). In Figure 7.16 (b), the number of frequency modes is fixed to 100 and the beam radius and power are varied. It is preferable to stay in the top right region of this plot, but this comes with increased random kicks which results in the heating in the longitudinal velocities. However, it can be seen that for radii above ∼5 mm, there is limited dependence on beam power above around 5 mW.

As with the output from the push beam, it is necessary to consider the distributions and not just the mean values, which is done with simulations where the beam power is set to 5 mm and the number of frequency modes to 100. The transverse speed and its inter-quartile range as a function of the beam power is shown in Figure 7.17 (a). Increasing the beam power not only reduces the transverse speed but also its spread as parameterized by the inter-quartile range, meaning that a larger fraction of the atoms are fully cooled down. Figure 7.17 (b) shows the probability density function of the transverse velocity, for a beam power of 5 mW around the zero transverse velocity in a

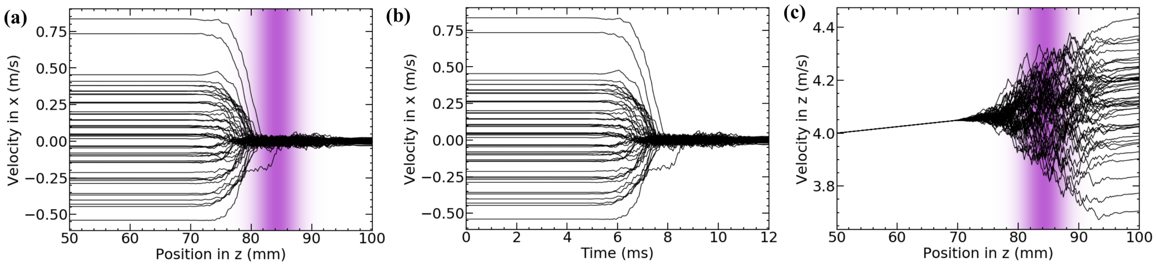

Figure 7.15: Simulated atom trajectories following the interaction with the molasses cooling beams. (a) Transverse velocity of the of the atoms as a function of position in z. Shading approximates the beam intensity. (b) Transverse velocity as a function of time. Collimation occurs efficiently and rapidly. (c) Longitudinal velocity as a function of position – a random heating walk is observed.

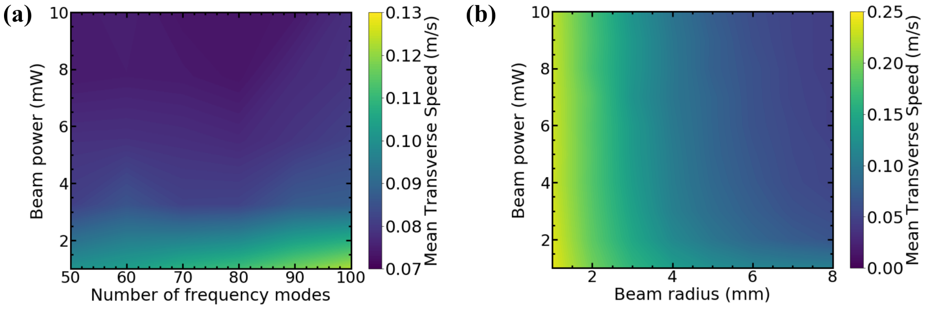

Figure 7.16: (a) Mean transverse speed as a function of molasses beam power and frequency modes (radius = 5 mm) and (b) molasses beam power and beam radius (modes = 100).

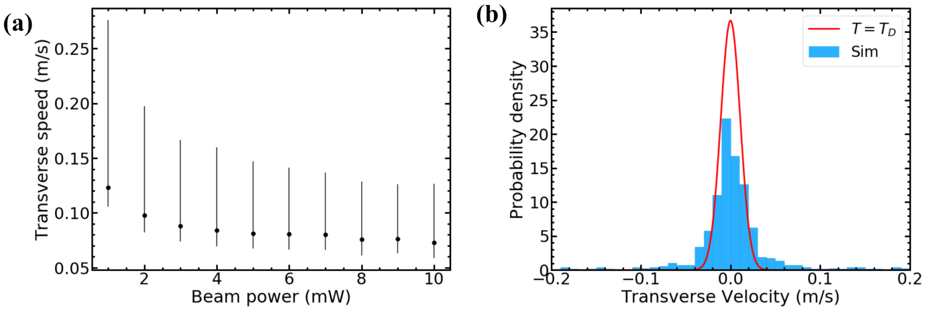

Figure 7.17: (a) Transverse speed as a function of molasses beam power (modes = 100, radius = 5 mm). Error bars show the inter-quartile range. (b) Probability density of the transverse velocity (power = 10 mW) along with the calculated distribution for Doppler-temperature-limited atoms.

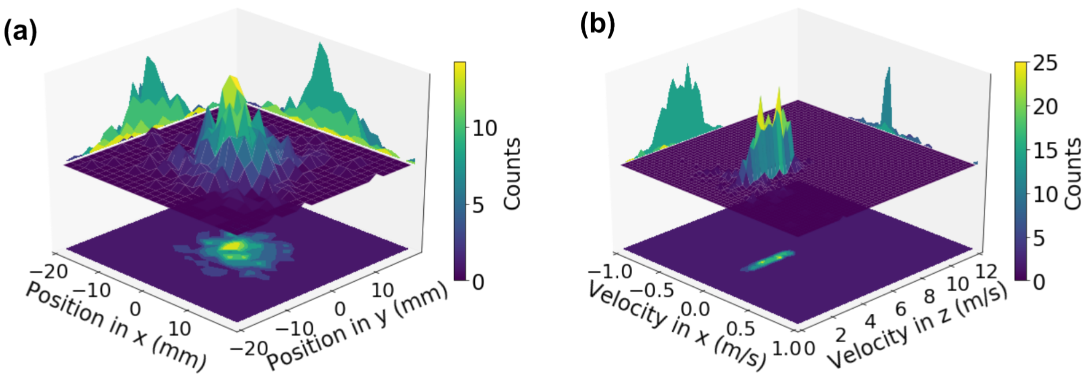

Figure 7.18: (a) Transverse beam cross-section and (b) velocity distribution after the molasses beam interaction (z=100 mm). The narrowing of the transverse velocity is evident and nearly total.

histogram fashion. The red curve is the calculated velocity distribution at the Doppler temperature and the simulated distribution can be seen to approach this limit.

These simulations allow for parameters of the molasses beam to be selected as 5 mW power, 5 mm radius and 100 frequency modes. These values allow for efficient cooling close to the Doppler limit, but keep the saturation parameter per mode at almost exactly 1. This will prevent excess heating in the longitudinal direction, as well as saving laser power for other purposes.

Similarly to the case after the push beam, the velocity and position of the slow atomic beam can be considered using these finalized parameters. This is done at a distance of z =100 mm from the 2D MOT location, where the simulated atoms begin at the oven and are slowed and pushed from the 2D MOT before the molasses interaction occurs at 84 mm below the origin. Figure 7.18 shows this slow atomic beam cross section in the transverse position space and also the transverse and longitudinal dimensions of velocity. In comparison to Figure 7.13, the near total narrowing of the transverse velocity peak towards the Doppler limit of the intercombination transition can be observed after the interaction with the molasses. The longitudinal velocity spread is slightly widened due to the random heating in the z axis and also the lack of cooling. The position spread is significantly larger than in Figure 7.13 even though the vertical travel distance is only 50 mm. This highlights the importance of the molasses beams for collimating the slow atomic beam. Without this transverse slowing the atoms would continue to expand transversely at the rate between Figure 7.13

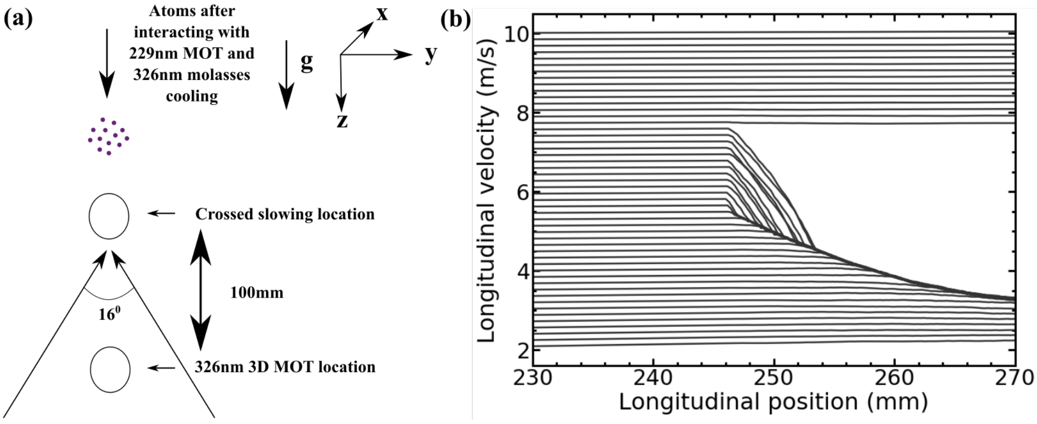

Figure 7.19: (a) Schematic of the crossed slowing beams. (b) Simulation of longitudinal slowing from the crossed slowing beams for atoms on axis and with no transverse velocity.

and Figure 7.18 and most would be lost before reaching the 3D MOT.

Crossed slowing beams: Simulations

Once the atoms have been slowed and effectively collimated in the transverse direction, another way to increase the 3D MOT efficiency is by reducing the longitudinal velocity the atoms achieve as they progress downwards along the gravitational axis. To avoid heating the atoms in the transverse direction and to protect the 3D MOT, this slowing should be done on the intercombination transition. A set-up for strontium has used a Zeeman slower type configuration on the 689 nm transition [175, 176], but very recently, crossed (or angled) slowing beams have been shown to be effective with demonstrations on systems with erbium, dysprosium and ytterbium [195–197].

To perform this in our case, crossed slowing beams at a full opening angle of 16° are designed to be sent from below the 3D MOT chamber as shown in Figure 7.19 (a). These beams intersect at 100 mm above the 3D MOT (251 mm below the 2D MOT) where the effect of the magnetic field is reduced. The principle of the angled slowing is demonstrated in Figure 7.19 (b), where atoms are simulated falling under gravity along the z axis with variable velocities in v_z and without transverse velocity. Here 2.5 mW of power per beam of 5 mm radius, with each beam having 100 frequency modes. As can be seen, atoms can be cooled efficiently where the range of velocities cooled is determined by the detuning and the frequency modulation.

Aside from successfully overlapping the crossed beams, the main experimental challenge of these

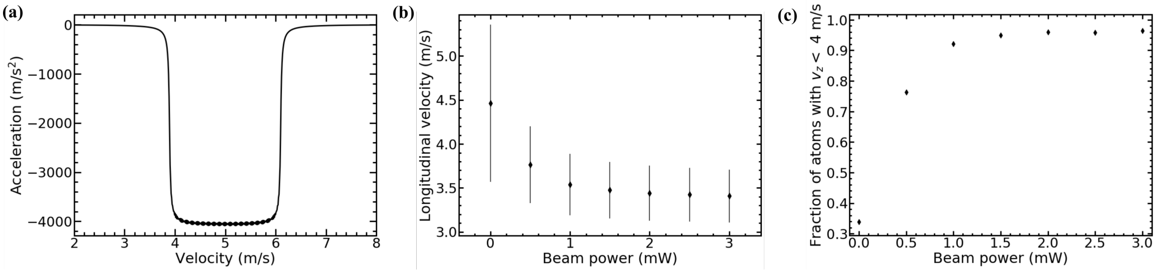

Figure 7.20: (a) Deceleration on the atoms due to the crossed slowing beams. (b) Mean value (black diamonds) and standard deviation (error bars) of the longitudinal velocity following the crossed slowing beams. (c) Fraction of the atoms having a longitudinal velocity less than 4 m/s.

slowing beams is getting them on resonance with the desired velocity class, as even the modulated intercombination transition beams have only about 2 m/s width as deducible from Figure 7.19 (b). Care must be taken to account for the Zeeman shift introduced by the magnetic field at the position of the crossed slowing beams when selecting the detuning. Figure 7.20 (a) shows the expected deceleration from the crossed slowing beams (2.5 mW, 5 mm, 100 modes), when the detuning has been tuned to cool atoms with v_z >4 m/s. In this case the detuning of the highest frequency mode is $\Delta = -650\ \Gamma$, with each successive mode red-detuned by a further linewidth.

With this detuning and deceleration, it is possible to slow the fastest atoms down to below the

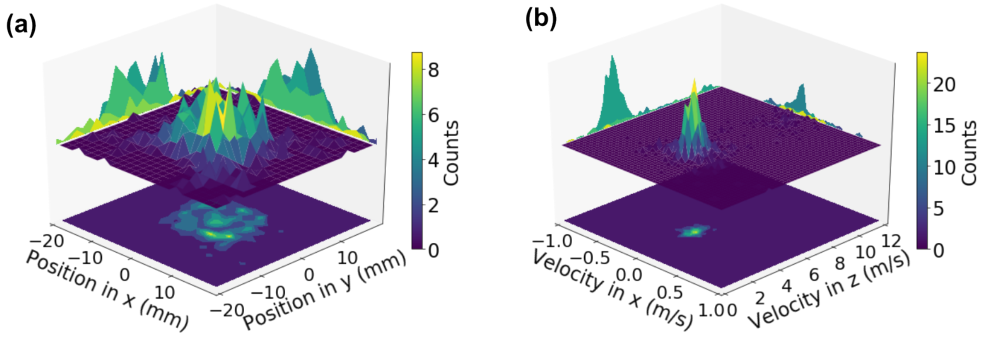

Figure 7.21: (a) Transverse beam cross-section and (b) velocity distribution after the interaction with cross-slowing beams (z=300 mm).

capture velocity of the 3D MOT and to enhance the loading rate (see below and Section 7.3.4). This is shown in Figure 7.20 (b) where only a few mW of beam power is required to reduce the mean longitudinal velocity of the slow atomic beam and also to narrow its distribution, as represented by the error bars. Figure 7.20 (c) shows the fraction of atoms in the cold atomic beam having a longitudinal velocity less than 4 m/s and shows that nearly all the atoms can be slowed to this limit, with this fraction saturating at around 1.5 mW of beam power. This shows that like with the molasses beams, the planned cooling is efficient.

The effect of the crossed slowing on the position and velocity distributions of the cold atomic beam is studied at a longitudinal position of 300 mm below the 2D MOT, i.e, about 50 mm after the interaction with the modulated crossed slowing beams and 50 mm above the 3D MOT. The transverse cross section is determined in the spatial domain and the velocity spread in the transverse and longitudinal dimensions, as shown in Figure 7.21. The transverse positional spread is similar to that shown in Figure 7.18, although there is some broadening due to random scattering as only one pair of crossed beams being used. However, the narrowing of the velocity distribution in the longitudinal axis is clear and is a result of the crossed slowing.

3D MOT with magnetic coils: Simulation, vacuum chamber

The 3D MOT on the intercombination transition at 326 nm is designed 351 mm below the origin (center of the 2D MOT). Such a MOT has recently been demonstrated for the first time with cadmium [54, 100]. The minimum velocity achievable with this transition is defined by the Doppler

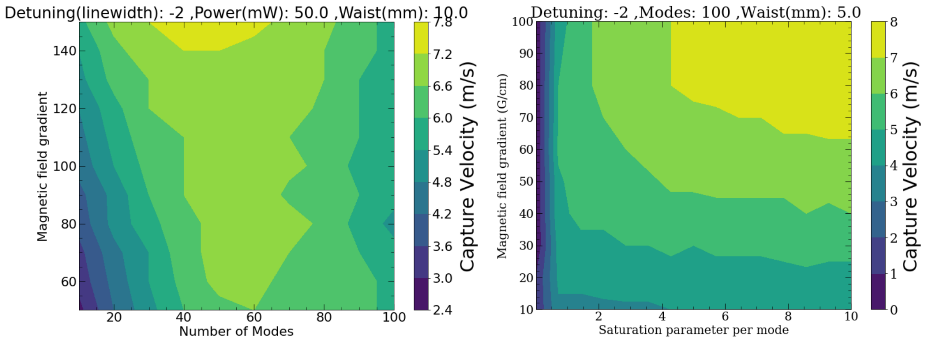

Figure 7.22: Capture velocity of 3D MOT as a function of magnetic field gradient and as a function of mode number (left) and magnetic field gradient-saturation parameter per mode (right).

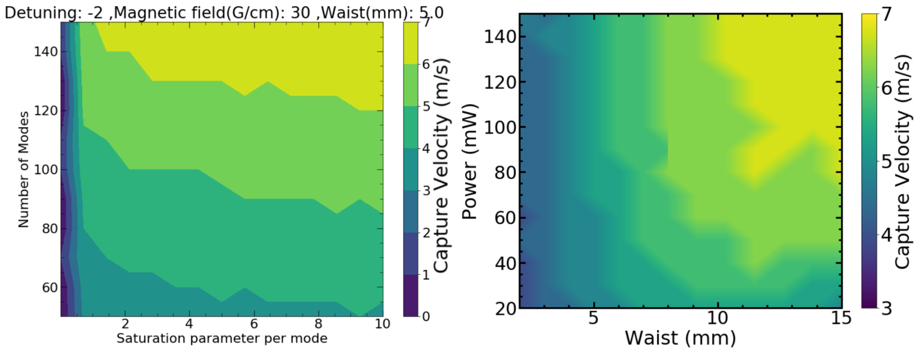

Figure 7.23: Capture velocity of 3D MOT as a function of mode number-saturation parameter per mode and beam power-waist.

temperature limit which is 1.6 μK, which is a good initial level for further cooling or atom interferometry, being similar to the level achievable in e.g. a rubidium MOT.

The above preliminary cooling techniques leading to this intercombination MOT have been designed carefully keeping in mind the desired final position and velocity regime of the atoms entering the 3D MOT, as should now become clear by considering its simulated capture velocity. The capture velocity of the MOT is plotted in a contour fashion as a function of the number of modes and the magnetic field gradient, and also as a function of saturation parameter per mode and magnetic field gradient as shown in Figure 7.22. In Figure 7.22 (a) the MOT beam power is fixed at 50 mW and the waist is 10 mm. In this fixed power configuration, there is an optimized set of mode numbers where the capture velocity is maximized. Outside of this region, either the number of modes is too few to enhance the velocity range of the radiative force or the saturation parameter per mode is too small as the number of modes is too high. In Figure 7.22 (b), conversely, the number of modes is fixed at 100 and the saturation parameter per mode is increased. This shows that for a given field gradient, increasing the saturation parameter per mode above around 5 does not lead to improved performance. Capture velocities approaching 8 m/s can be achieved, though with experimentally challenging beam powers of 100 mW and magnetic field gradients of 80 G/cm.

Figure 7.23 shows the capture velocity for a magnetic field gradient of 30 G/cm, as used in [54] and feasible with the coil design presented below. Figure 7.23 (a) shows that for this magnetic field gradient of 30 G/cm and 100 modes, atoms with longitudinal velocities from 4 - 6 m/s can be captured, depending on the saturation parameter per mode. This is approximately the longitudinal

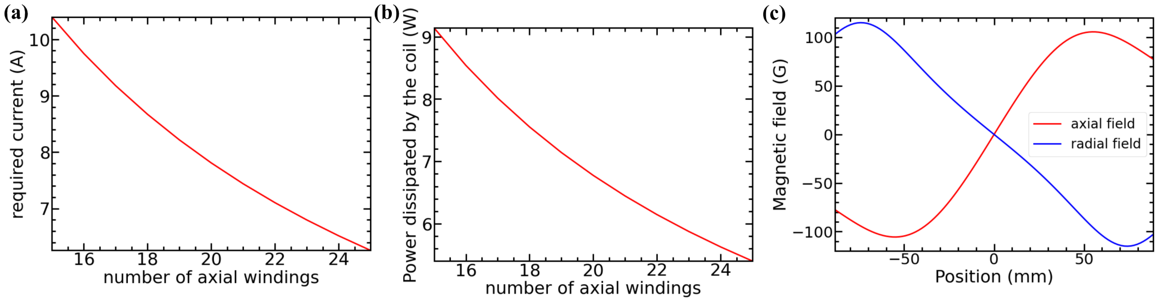

Figure 7.24: (a) The current required to produce 30 G/cm as a function of the number of axial windings. (b) The respective power dissipated by the coils. (c) The calculated magnetic field in the radial and axial directions for 20 windings producing 30 G/cm.

velocity range of the atoms arriving after the interaction with the molasses cooling and the crossed slowing beams, meaning this field gradient and frequency modulation is a good choice for our slow atomic beam. Figure 7.23 (b) shows the capture velocity as a function of beam waist and power, with 30 G/cm and 100 modes. The capture velocity can be increased by increasing both the beam waist and the beam power at these settings. This shows that the MOT has the potential to benefit from the high powers achieved with the developed laser system (Section 4.2). In any case, capturing atoms from the slow atomic beam (∼4 m/s) should be achievable with a broad range of experimentally feasible parameters.

The above calculations considered the magnetic field as calculated from current-carrying magnetic coils wrapped around the vacuum chamber viewports. These coils are to be run in an anti-Helmholtz configuration to produce the quadrupole magnetic field required for the MOT. They are made up of copper with a diameter of 1 mm and have an assumed spacing of 0.1 mm between each coil. The 3D MOT chamber is a spherical octagon design where the electromagnetic coils with CF100 viewports and the two sets of coils are separated by a distance of 90 mm to each other, 45 mm being the distance to the MOT (see the design in Figure 7.25 below). The minimum winding radius is taken as 77 mm (the radius of the flange is 75.82 mm), while the maximum radius is set to 90 mm to prevent blockage elsewhere in the system. This gives a maximum number of horizontal windings of 11. There is, however, in principle no maximum on the axial number of windings. Figure 7.24 shows the current required to generate a field gradient of 30 G/cm and the corresponding power dissipated by the coils, as a function of number of axial windings. Figure 7.24 (c) shows the calculated radial and axial magnetic field generated for 20 axial windings, when generating a field gradient of 30 G/cm in the axial direction. This requires a current of about 6 - 10 A and a power dissipation of 5 - 10 W, requirements which are easily achieved in the laboratory.

7.3.4 Chamber design and loading rate of 3D MOT

With the above information it is possible to finalize the design of the vacuum chamber and numerically simulate the atomic trajectories throughout the full system using the finalized distances and magnetic fields. The atomic trajectories throughout each stage of interaction with the 229 nm and 326 nm beams in the form of 2D MOT, push beam, transverse molasses, crossed slowing beams and the 3D MOT are determined in a single simulation, whose beam parameters are given in Table 7.2. The finalized computer-aided design (CAD) of the chamber is shown in Figure 7.25 (a). As can be seen, the 2D MOT chamber is extremely compact to allow for the transverse cooling to occur as soon as possible and to minimize the travel distance to the 3D MOT chamber. There is a gate valve between the two MOT chambers to allow for the top chamber to be opened without breaking the vacuum of the main system, for example if the cadmium has to be reloaded or if the 229 nm viewports need to be replaced due to UV-induced damage. The vacuum pump by the 2D MOT is capable of being operated with its internal components held at high temperatures (∼200 °C), which may help to prevent problems due to cadmium condensing and damaging the pump operation (see Section 6.4). Currently, there is no differential pumping between the two MOT chambers to allow for vertical interferometry beams as a first test of atom interferometry with cadmium, but once the atoms start being transferred to the main science chamber (see Section 8.2 below), this can be inserted. With differential pumping, the system may be a good option for the continuous production of ultra-cold or even quantum degenerate sources [86].

A complete pictorial representation of the path the atoms follow in the vacuum chamber, is presented in Figure 7.25 (b), which is shown to scale. To summarize the optical design, the atoms are first loaded from an oven operating at 100 °C into the 2D MOT on the 229 nm transition. Using a low-intensity push beam on the same transition, the atoms are directed downwards and encounter the transverse molasses beams on the 326 nm transition where they get collimated in the x-y plane. In order to optimize the efficiency of the 3D MOT on the intercombination transition, a cross-slowing beams are employed at an angle of 16° from below, 100 mm above the 3D MOT, to reduce the longitudinal velocity of the atoms to match with the capture velocity of the subsequent 3D MOT below. The effect of all these stages are visible in the trajectories of Figure 7.25.

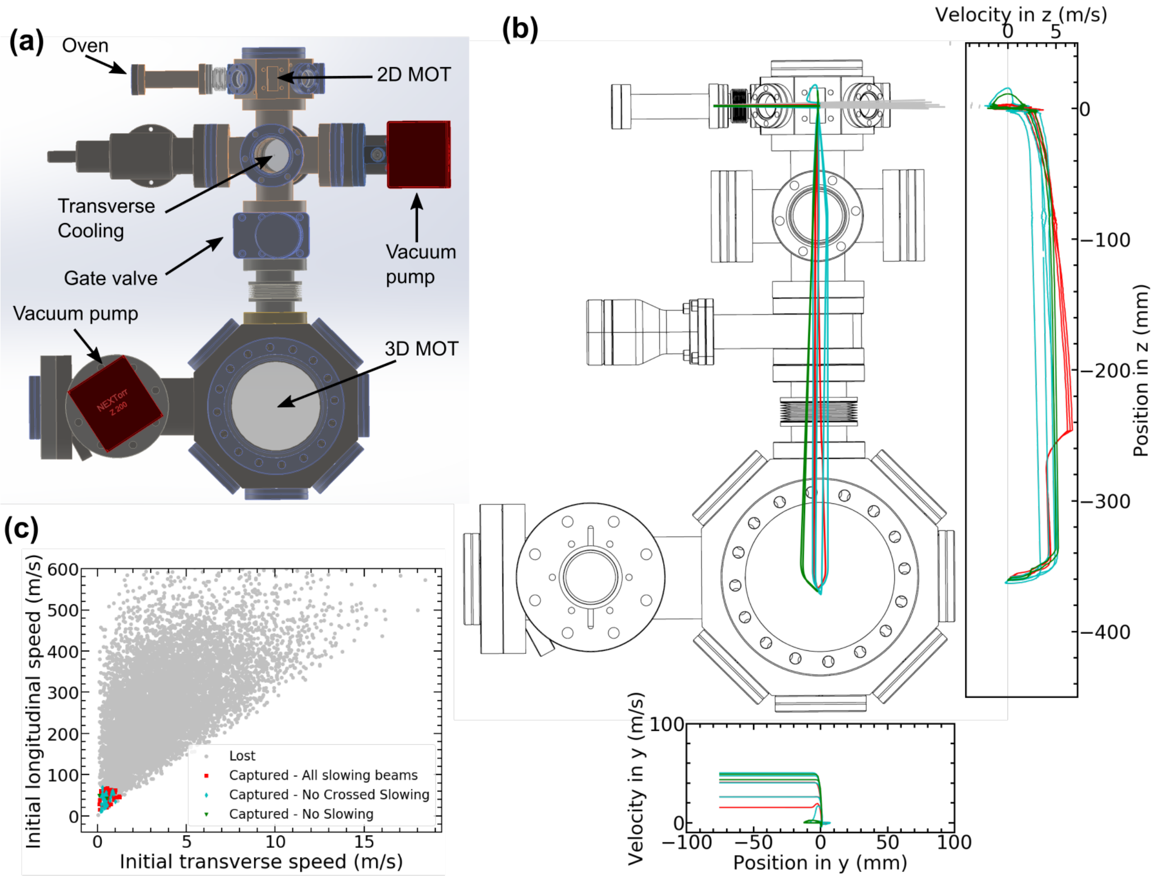

Figure 7.25: (a) The vacuum chamber designed for the production of ultra-cold cadmium with each individual part labelled, (b) Schematic of the same chamber showing some simulated trajectories of atoms, all the way from the oven until they are captured in the 3D MOT. The grey lines are those atoms which are lost (top region). Green lines are atoms that are captured without the transverse or crossed slowing beam active. Light blue lines are those atoms captured only once the transverse cooling is turned on. Red lines are atoms captured only once both the transverse and crossed slowing beams are activated. (c) The initial velocity distribution of the atoms. The same colour scheme is used as in (b).

Table 7.2: Properties of the laser beams in the final simulation of the system, including optical power per beam P, beam waist w, detuning Δ, number of frequency modes and the saturation parameter per mode s. The Zeeman slower is not used unless specifically mentioned.

Beam (number)	P (mW)	w (mm)	Δ (Γ)	Modes	s
		229 nm – $^1S_0$-$^1P_1$			
2D MOT (×4)	10	2	-1.5	1	0.16
Push beam (×1)	0.17	3	-3	1	10^{-3}
Zeeman Slower (×1)	30	2	-6.5	1	0.48
		326 nm – $^1S_0$-$^3P_1$			
3D MOT (×6)	50	5	-2	100	5.1
Molasses (×4)	10	5	-1	100	1.0
Angled Slowing (×2)	2.5	3	-650	100	0.71

Furthermore, it is now possible to estimate the real benefits of the various cooling stages above by running the simulation with the same initial set of atoms, but with and without certain cooling stages. For example, the red coloured trajectories are the atoms successfully captured in the 3D MOT only when both the transverse molasses and the crossed slowing beams are used. The light blue trajectories are atoms captured in the 3D MOT without the crossed beam slowing, but with the transverse molasses cooling. The green trajectories are the atoms captured in the 3D MOT directly from the 2D MOT, even in the case without the transverse or crossed beam slowing. Grey trajectories are atoms which are always lost. These results are also shown in Figure 7.25 (c) which considers the results as a function of initial velocities from the oven. This shows that when the transverse and the crossed slowing beams are active, the system is very efficient at transferring slow atoms from the oven all the way to the 3D MOT.

These improvements can be quantified by considering the loading rate of the 3D MOT. This is estimated from the simulated efficiency of the system in loading atoms into the 3D MOT from the oven scaled by the oven flow rate. These rates can be further scaled as per the fraction of the abundance of the ^{114}Cd isotope which is 0.29. This gives an idea of the upper bound of the key feature of the system, i.e. the rate at which cold atoms are loaded. The discussed loading rates are to be considered the upper limit of the performance because the simulation doesn't account for losses

Table 7.3: Capture Efficiency and loading rates of the 3D MOT at 326 nm for natural ^{114}Cd and an oven temperature of 100 °C. These simulations use 10^4 atoms. Errors are from the counting statistics of the simulation.

	Capture Efficiency	Loading Rate
2D MOT & 3D MOT	0.02 %	$6\pm4 \times10^5$ atoms/s
+ Transverse Cooling	0.34 %	$1.0\pm0.2 \times10^7$ atoms/s
+ Longitudinal Cooling	0.85 %	$2.6\pm0.3 \times 10^7$ atoms/s

emerging from the intra-atomic collision and also the collisions with the background gases or other atom-atom interactions. The results of this are shown in Table 7.3 for an for an oven temperature of 100 °C. As can be seen, the key feature is the introduction of the transverse cooling which increases the capture efficiency by about a factor of 20. The crossed slowing beams seem to further improve the efficiency by a factor of around 2. The estimated loading rate is $2.6\pm0.3 \times 10^7$ atoms/s, which compares favourably to that measured using a two-stage 3D MOT process, where 10^6 atoms are loaded in 200 ms with 30 mW of 229 nm power (s =0.2) and a sourced enriched for 93% ^{111}Cd [54].

By looking at the loading rate, the parameters of the beams can be optimized and their criticality understood. For example, Figure 7.26 shows the loading rate when varying the beam power and

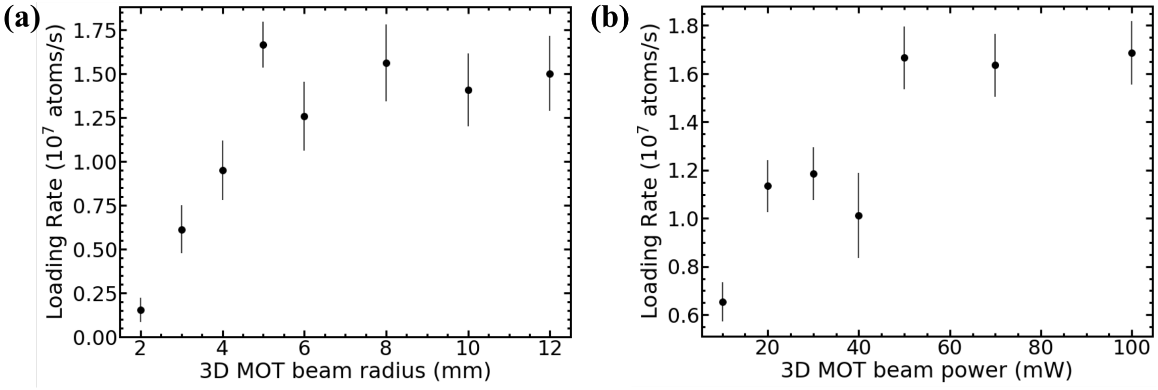

Figure 7.26: Loading rate of the 3D MOT for ^{114}Cd when varying the (a) MOT beam radius and (b) MOT beam power. These simulations use 3×10^4 atoms and the error bars are from the counting statistics of the simulation.

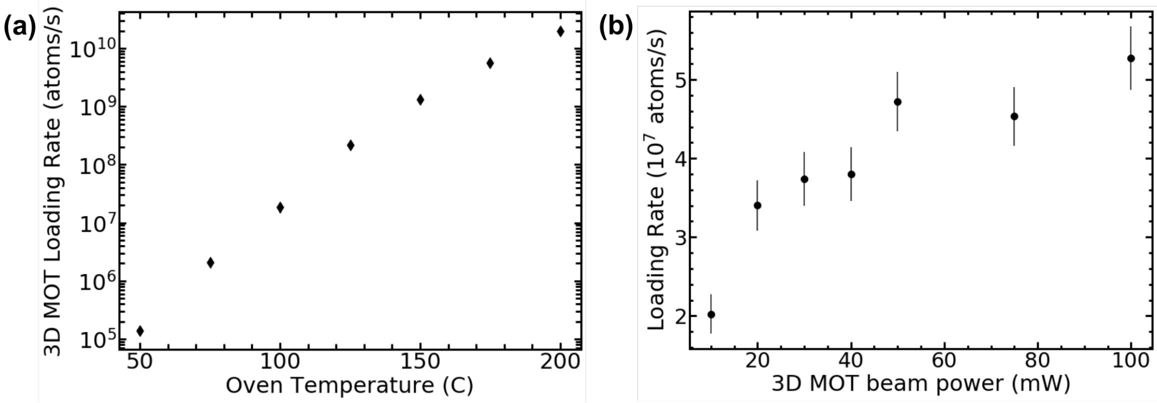

Figure 7.27: (a) Loading rate of ^{114}Cd into the 3D MOT as a function of oven temperature and (b) as a function of the 2D MOT beam powers. Simulations with 10^4 atoms and parameters as in Table 7.2.

waist of the 3D MOT beams, with the other values kept the same as in Table 7.2. As can be seen, the loading rate saturates with around 50 mW per MOT beam and a beam radius of 5 mm, allowing these values to be selected as optimum values.

Figure 7.27 shows the change in loading rate as a function of the oven temperature. This is one of the simplest way to increase the flux of atoms. At a temperature of 100 °C, around 10^7 atoms/s is estimated. At higher temperatures the capture efficiency of the system decreases (as there are proportionally more fast atoms) but this is compensated for by the non-linear increase in flow rate and the capture rate continues to rise. While higher temperatures are experimentally possible, around 100 °C is chosen to prevent problems with background pressure and to minimize the losses due the collisions within the cadmium gas and also with other background gases.

Finally, Figure 7.27 compares the loading rate as a function of the power in the 229 nm beams in the 2D MOT and the power in the 326 nm beams in the 3D MOT (varying waists). For a workable 229 nm power of 10 mW in each beam, a loading rate up to 10^7 atoms/s in 3D MOT is estimated. The loading rate here seems to saturate around 40 mW of power per 2D MOT beam. The design is still limited to 10 mW powers, however, due to the problems with DUV-induced damage and generation. If these can be overcome with technological advances, then this represents an excellent way to increase the atom number of the 3D MOT, so the loading rates given above should not be considered a fundamental limit for this design. Furthermore, cadmium sources with natural abundance have been considered. The use of isotope-enriched sources [54, 171] would allow for an increase in the loading rate by a factor 4.

7.4 Preparation of quantum degenerate sources

7.4.1 Nd:YAG laser set-up – 1064 nm

Once the atoms are trapped in the 3D MOT on the intercombination transition at the temperature of the order of μK [54], an optical dipole trap with a far-off-resonant beam can be employed, to further cool the atomic ensemble down to nK level, such that interferometry with the highest precision can be performed. By slowly lowering the trap depth, evaporative cooling can occur and quantum degenerate sources can be produced [198], although this remains an open question for cadmium as its cold collisional properties are yet to be measured.

In order to have a large trap depth but minimal spontaneous single-photon scattering, the trapping laser should produce high intensities at large detunings from the atomic transition (see Section 2.1.7). Such intensities require a tight focus which also means that the laser should have excellent mode quality and should be low noise (frequency and intensity) to prevent heating inside the trap. These requirements can be met by amplified Nd:YAG lasers operating at 1064 nm or doubled to 532 nm.

The laser to be used in this case is a commercial system with a maximum output power of about 45 W at 1064 nm (ALS-IR, Azur Light). It consists of a single-frequency seed laser which is amplified in Yb-doped fibre, with a specified linewidth of 50 kHz and a root-mean-squared RIN value of 0.02%. An important feature is that the laser is air-cooled only and does not need a chiller, which is useful for reducing noise in the laboratory and complexity. The measured properties of the laser are shown in Figure 7.28. A maximum measured power of 46 W is achieved and the beam is nearly circular and close to diffraction-limited ($M^2 < 1.1$). The beam profile is power dependent, however, in terms of both size and focal position, which means that the laser must be operated at the same power settings for consistent results. Nevertheless, the laser has the required characteristics for optical dipole trapping and for lattice launching (see Section 8.4).

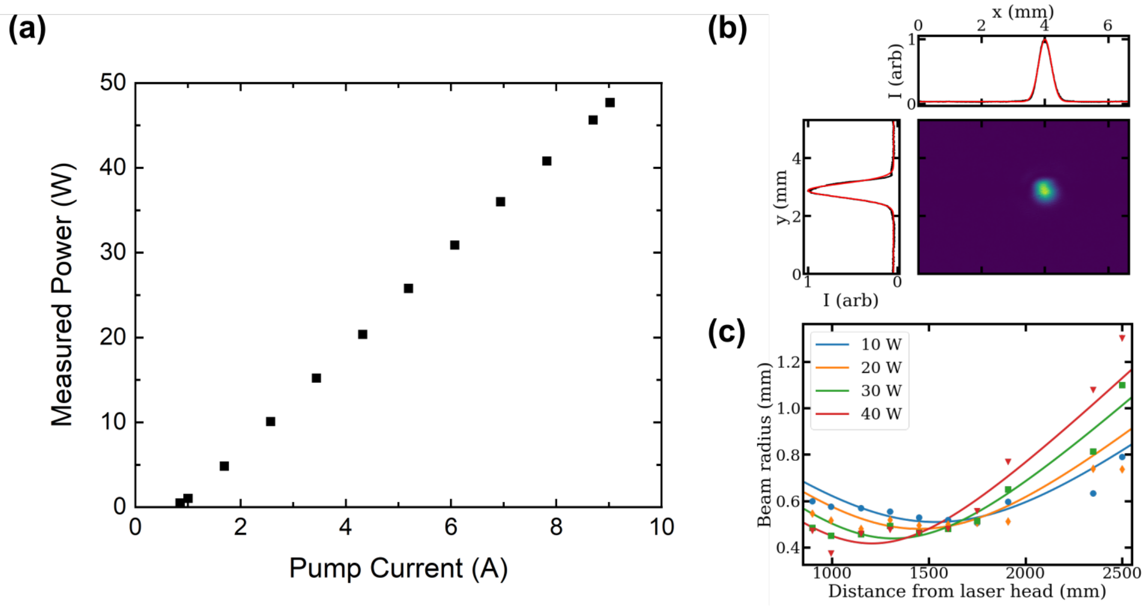

Figure 7.28: (a) Measured output power of the 1064 nm laser as a function of pump laser current. (b) Sample image of the mode. (c) Measured beam profile from the laser at different output powers.

7.4.2 Optical dipole trap calculations

This dipole trap is designed to be in the transverse (x-y) plane at the location of the 3D MOT in the main chamber, before the atoms are transferred to the science chamber (see Section 8.2). The potential is calculated according to equation 2.30 and assuming atoms in the ground state and a two-level system spanned by the ^{1}S$_0$ - ^{1}P$_1$ transition. Figure 7.29 shows the case of two circular Gaussian beams (A and B) of equal waists and orthogonal polarization considered to overlap at the 3D MOT location and with a full opening angle of θ =60°. The power of both the beams is 6 W and the waist of the beams is 35 μm. This power is limited so as to allow for the potential to use the laser simultaneously on strontium and the used waist is smaller than typical for e.g. strontium [199]. This is due to the strong dependence of equation 2.30 on the transition frequency ($U_{dipole} \propto \omega_0^{-3}$), meaning that the trap is relatively shallow for cadmium. This can be compensated by decreasing the waist, as here, or by increasing the power.

The calculated potential in the x-y plane is shown in Figure 7.29 (b). The generated potential is used to calculate the depth of the trap in the x, y and z dimensions as shown in Figure 7.29 (c), where the dipole trap beams make an angle $\theta/2$ with the x axis. For beams crossed at 90°, the x

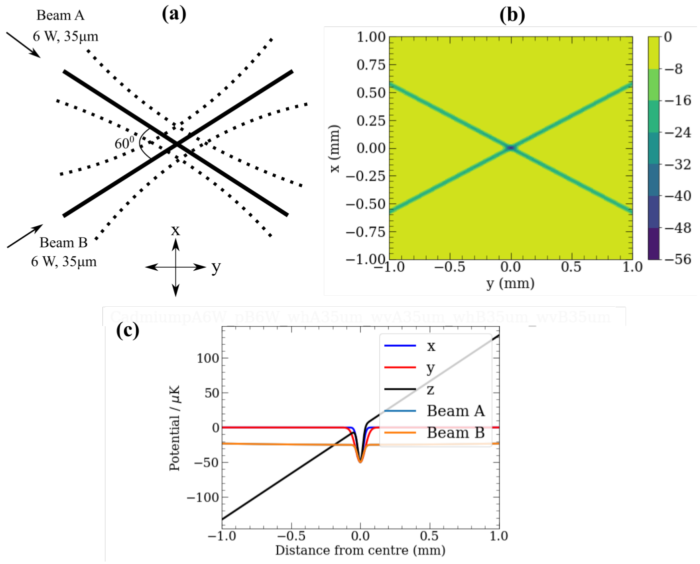

Figure 7.29: (a) Schematic of the optical dipole trap beams showing the co-ordinate system and approximate beam powers and waists. (b) The same beams in x-y plane where the color code represents the dipole potential in μk. (c) The 1D potentials in x, y, z and along the beam axes.

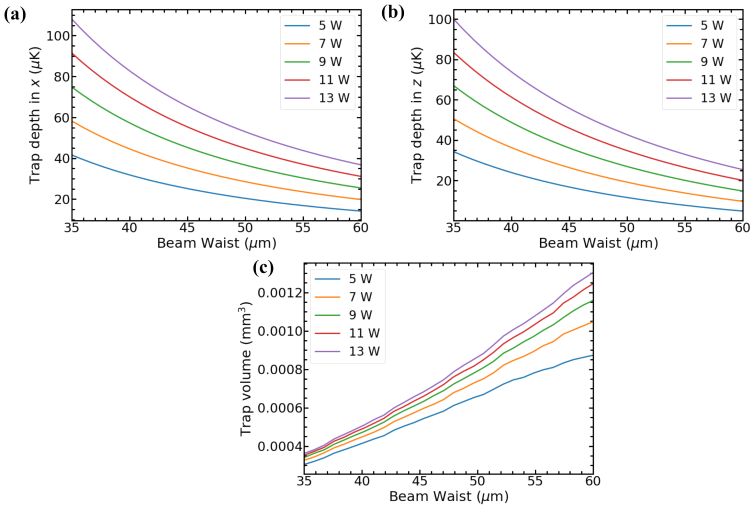

Figure 7.30: (a) The trap depth potential in x as a function of the beam waist for different powers (similar for y). (b) The trap depth in z (direction of gravity) as a function of waist for different powers. This is lower than the corresponding depth in x. (c) The trap volume as a function of the beam waist for variable powers.

and y traps are identical, but even with angled beams the trap depth is the same and can be taken as the minimum value of the potential. The trap in the z dimension, however, must consider the effect of gravity, which is why the two trap beams are orientated in the horizontal plane. In this case the trap depth is taken as the difference between the minimum and the turning point of the potential, i.e. at the trap centre and the position of the turning point below z=0. In this particular case, the trap depth in x, y and z (given in μK) is an order of magnitude larger than the assumed temperature of the atomic ensemble in the 3D MOT ($\sim$2 μK) thereby allowing for efficient loading into the optical dipole trap. The trap depth in z is approximately 42 μK.

The effect of the trapping beam parameters on the trap performance can be considered in more detail. Figure 7.30 (a) shows the trap depth potential as a function of the waist of the beam. This is in the x direction, but similar behaviour is observed in the y dimension. This is shown for different powers and the higher the power the deeper the trap. This trap depth is seen to decrease as the waist of the beam is increased. However, even at the lowest calculated beam power of 5 W, a trap depth in x of about 40 μK can be achieved with a 35 μm waist, already an order of magnitude higher the Doppler temperature of the MOT, highlighting that there is a large parameter space available for this laser to generate sufficiently deep traps ($>$ 20 T$_D$). Figure 7.30 (b) shows the trap depth potential in the z direction for different powers as the waist varies, where similar though slightly reduced depths are achieved.

Figure 7.30 (c) shows the dependence of the trap volume as a function of the waist for different powers. This trap volume is calculated by multiplying the trap size in the x, y and z dimensions and increases with the waist of the beam. The trap size is taken from the sigma of the Gaussian fitted to the potential along the dimensions x and y (see Figure 7.29 for the geometry). Higher waists and powers corresponds to a wider trap thereby increasing the trap volume, which is beneficial for loading more atoms from the 3D MOT.

Chapter 8

Vacuum chamber design for the dual-species atom interferometer

This chapter describes the design of the chamber in the dual-species interferometer which is utilized for generating strontium atoms and the plans for bringing the two systems together. This includes the calculation of the optical set-up for transferring the atoms from the MOT regions to a fountain region, where the two species can be launched simultaneously in a chirped 1064 nm lattice. The efficiency of this launch is investigated, with a focus on losses due to Landau-Zener tunneling, is studied for both the species. Finally, a full design of the dual-species vacuum chamber is presented and its suitability for atom interferometry discussed.

8.1 Design of upgraded vacuum apparatus for strontium

The generation of ultra-cold samples of strontium is advanced and the techniques are therefore well-known and studied, as previously discussed. Therefore a full simulation as in Chapter 7 is not required. Instead, previously implemented systems from the University of Florence for generating ultra-cold atomic strontium atoms can be used to design a system suited for the specific task of atom inteferometry, rather than for atomic clocks as previously [200]. For example, one important requirement for a fountain interferometer is good optical access in the vertical direction, not typically required for clocks [82].

Figure 8.1 shows the vacuum chamber design for the strontium atomic ensemble. This design

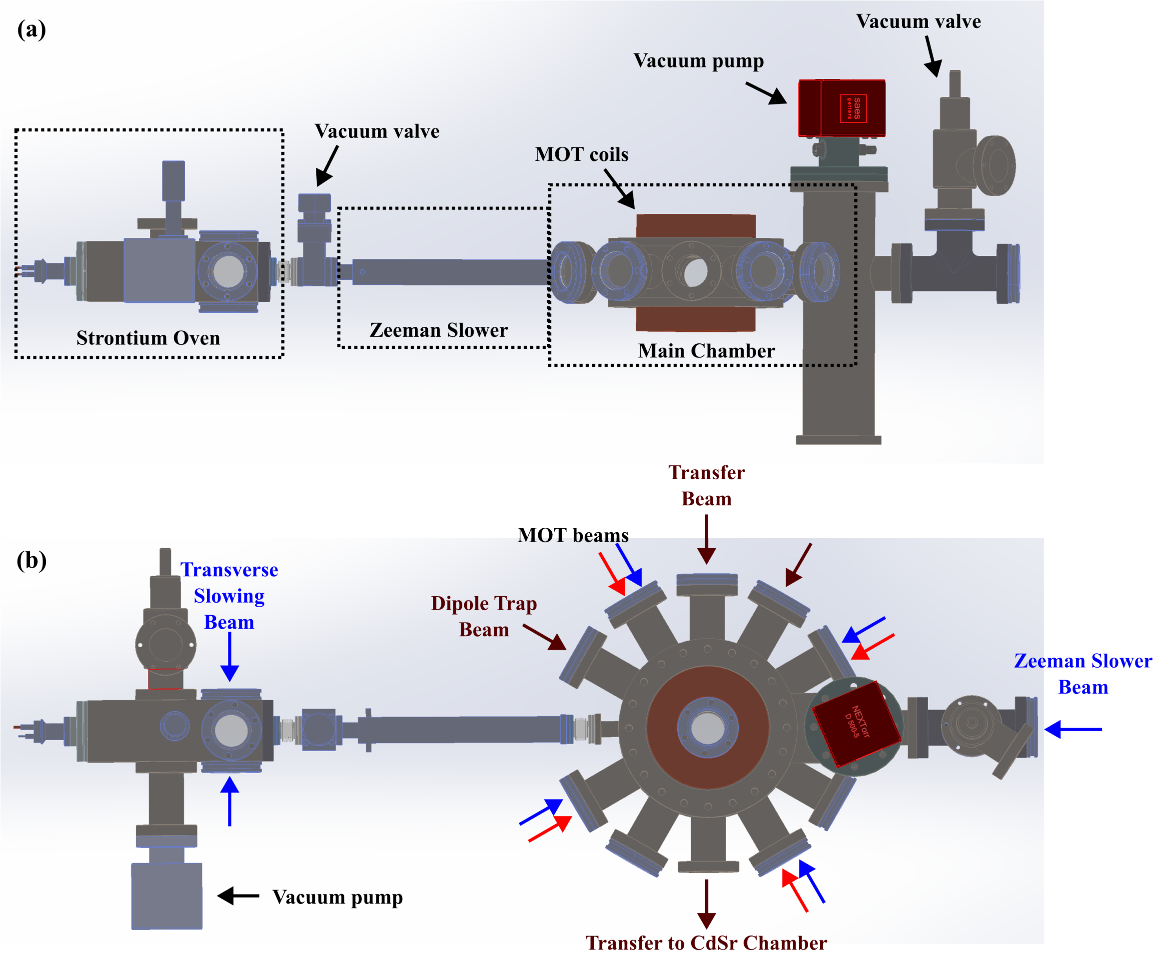

Figure 8.1: Vacuum chamber design for the new strontium apparatus. (a) Side view of the chamber showing the different regions. The magnetic coils for the Zeeman slower are not shown. (b) Top view of the chamber showing the optical set-up. See text for more details.

consists of an oven similar to that presented in Chapter 6. The atoms from the oven are slowed using a Zeeman slower on the 461 nm transition, whose design can be taken directly from previous demonstrations. The extra blue power now available due to the VECSEL-based system can be utilized in a transverse cooling scheme of these atoms before they enter the Zeeman slower. After slowing, these atoms are first trapped in a MOT on the 461 nm transition, a so-called blue MOT, before being further cooled down using a red MOT on the 689 nm transitions. Following the cooling in the red MOT to the μK level, atoms can be loaded into an optical dipole trap (see Section 7.4.2) and undergo further cooling to quantum degeneracy [87]. Figure 8.1 also shows space left for the connection to the dual-species interferometer and the optical transfer beams used to to transport the ultra-cold strontium ensemble from the main chamber towards the science chamber, as outlined in Section 8.2.

One important detail for generating ultra-cold sources of strontium compared to cadmium, is that a 3D MOT on the broad ^{1}S$_0$ - ^{1}P$_1$ transition is in general required, although direct capture on the 689 nm transition is possible in a highly optimized system [175]. This is due to the weak force generated by the ^{1}S$_0$ - ^{3}P$_1$ transition of strontium which is an order of magnitude less than for the same transition in cadmium. It is generally simpler to perform two 3D MOTs sequentially on 461 nm and then on 689 nm in the same position which rules out the possibility of using permanent magnets to generate the large gradients required for the dipole-allowed transition, as this cannot easily be changed during an experiment. It is therefore important to design magnetic coils which are capable of generating large gradients of 50 G/cm and also consider how the power dissipation will be removed from the coils.

The typical configuration of generating the field required for a 3D MOT is an anti-Helmholtz configuration, as discussed in Section 2.1.5. In this case the magnetic field gradient in the axial (z) direction can be written as shown in equation 8.1. Here the case of a pair of single coils with radius a and separation $2d$ are considered, through which a current of I is running.

$$\frac{\partial B}{\partial z} = 3\mu_0 \frac{Ia^2 d}{\left(a^2 + d^2\right)^{5/2}} \tag{8.1}$$

As can be seen in equation 8.1, the key requirement for a large field gradient is that the axial separation between the two coils is as small as possible, because of the approximate $1/d^4$ dependence. For this reason a re-entrant flange has been designed to house the MOT coils and minimize the axial separation of the coils. The flange is also designed to minimize a without reducing the optical access afforded by the CF40 viewport. Figure 8.2 (a) shows the re-entrant flange placed above the MOT

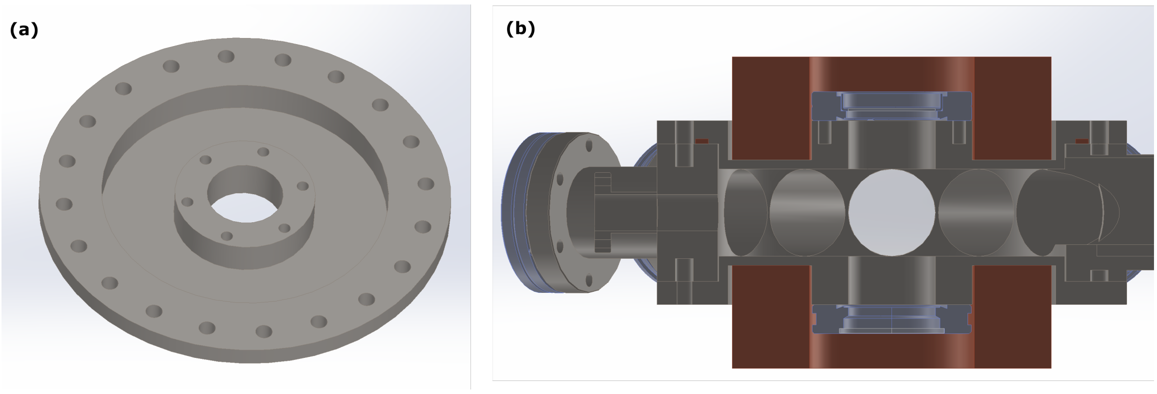

Figure 8.2: (a) Re-entrant flange which is to be placed on the top of the MOT chamber (b) The MOT chamber showing the design of the electromagnetic coils required for the 3D MOT field gradients.

chamber which holds the magnetic coils required to generate the gradients required for the 3D MOT while Figure 8.2 (b) shows the positioning of the electromagnetic coils above the chamber. It should be noted that the axial direction of these coils is vertical so that the strongest field gradient is in the direction of gravity (see equation 2.22). This is to help support the weak 689 nm MOT which tends to sag under gravity [201], especially for the fermionic ^{87}Sr.

The size of this re-entrant flange decides the minimum inner and maximum outer radius of the coils. A design of these coils is made using cuboidal copper tubes (cross-section of 5 mm×5 mm) with an internal hole (3 mm diameter) through which cooling water can flow and the large surface area of the coils of 25 mm^2 allows for large currents to be safely used. This design is highly efficient in removing heat as the cooling is internal and follows a recently demonstrated design [202]. The current required to produce 50 G/cm is simply estimated using equation 8.1 where each coil windings is considered as a current loop at the winding's geometrical centre. The number of windings in the axial direction can be altered, while the number of radial windings is fixed at 6 by the re-entrant flange geometry. Figure 8.3 shows the required current and the power that must be dissipated as a function of axial windings. A winding number of 8 is selected as this is at the minimum of the power to be dissipated and requires 35 A of current, producing 21 W of heat. The estimated mass of the coils is 2.5 kg.

The magnetic field in the axial direction can also be calculated analytically according to equation 8.2, while the radial field requires a numerical approach using the Biot-Savart law. Figure 8.3

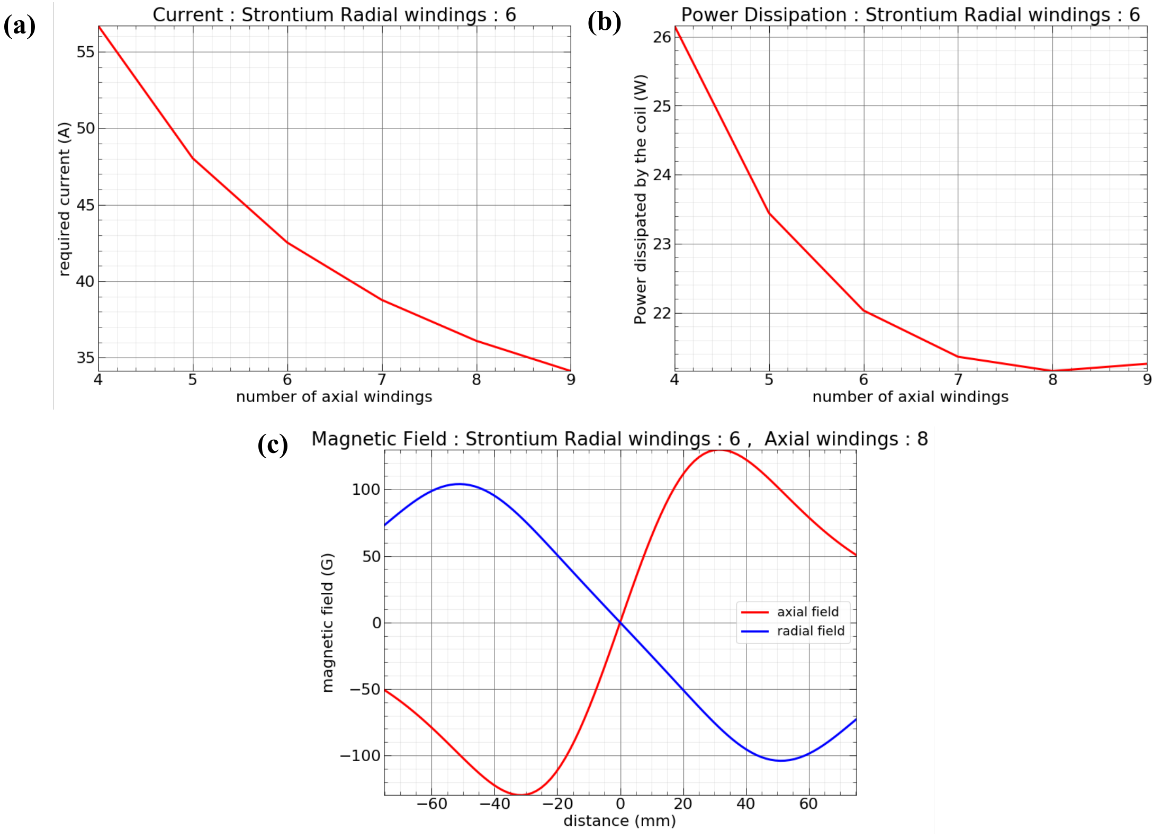

Figure 8.3: (a) Current required for generating 50 G/cm as a function of the number of axial windings. (b) Power dissipated by the coils operating at this current. (c) Magnetic field in the radial and axial directions generated by the coils.

shows the calculated radial and axial fields about the MOT centre.

$$B_z\left(z\right) = \mu_0 \frac{I}{2a}\left[\left(1+\left[z/a-d/a\right]^2\right)^{-3/2} - \left(1+\left[z/a+d/a\right]^2\right)^{-3/2}\right] \tag{8.2}$$

8.2 Optical transfer: 3D MOT chamber to science chamber

In the final vacuum chamber design of the dual-species interferometer, the atoms must be transferred from the separate cadmium and strontium chambers to the main science chamber. This requires the atoms to be transferred a distance of ∼40 cm. The plan to perform this is based on the design of an optically compensated zoom lens consisting of 5 lenses (symmetrically) whose effective focal length

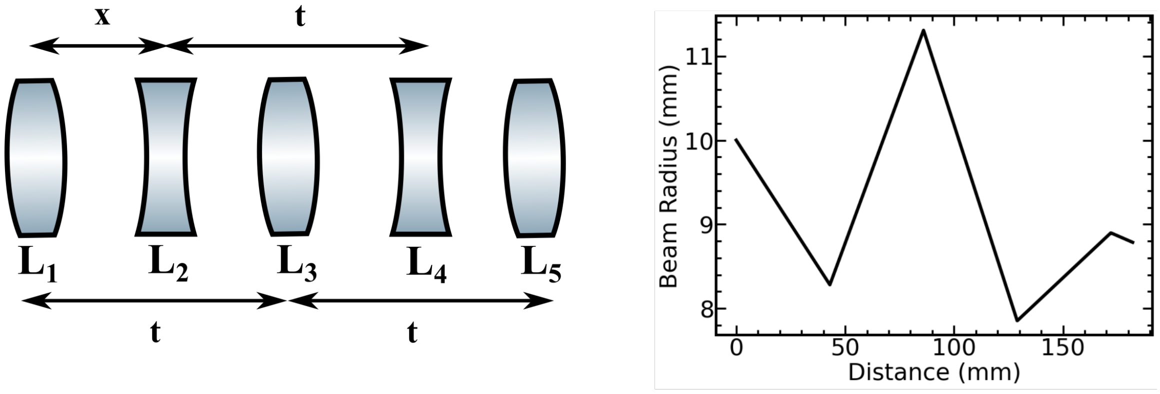

(a) **(b)**

Figure 8.4: (a) Optical schematic of the transfer scheme consisting of five lenses. L1 and L5 have f = 250 mm; L2 and L4 have f = −75 mm; L3 has f = 75 mm; and t=86 mm (b) The evolution of the beam radius as it propagates through the lens system.

is tunable to perform the transfer. This has been recently demonstrated as an efficient method for transferring ultra-cold atomic samples [203]. This set-up reduces the mechanical foot print and cost by a large amount, in comparison to a set-up using a translation stage to linearly shift the lens by the transfer distance [204].

The optical schematic and the chosen lens focal lengths are shown in Figure 8.4. In the optical schematic, the first, third and the fifth lenses in the sequence are the convex lenses whereas the second and the fourth lenses are concave. The spacing between the convex lenses and between the concave lenses is fixed, however these two lens sets move relative to each other which results in a change in effective focal length. The displacement parameter is labelled as x, which is the distance between L1 and L2. As x changes adiabatically using e.g. an air-bearing translation stage, the waist position of the optical dipole trap beam (1064 nm) can be shifted to the desired position, without changing the waist size.

The lenses L1, L3 and L5 are designed to be spaced at a distance of t (86 mm) and the lenses L2 and L4 are also at a distance of t from each other. For L1 and L5 of focal length 250 mm and L3, 75 mm and L2 and L4 being -75 mm, Figure 8.5 shows the effective distance from the last lens where the focal spot is formed as a function of the displacement parameter. These focal lengths are chosen based on the availability of 50 mm diameter achromatic doublets coated at this wavelength. Figure 8.4 (b) shows the Gaussian beam propagation through the lenses for an input beam of waist

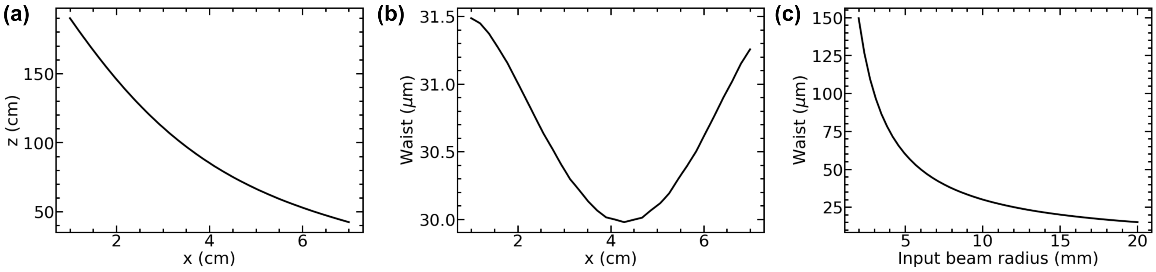

Figure 8.5: (a) Waist position for the designed optically compensated zoom lens. (b) Related for waist size for an input beam radius of 10 mm. (c) Expected waist as a function of input beam radius ($x = t/2$).

10 mm. Each sharp transition represents the position of a lens and the negative focal length lenses are placed at the mid-point between the positive length lenses. As can be seen, the beam radius does not change much throughout the lens system and so it is requested to use the lenses of diameter of 50 mm to reduce diffraction effects.

The waist position changes with the displacement parameter as shown in Figure 8.5 (a). For example, to shift the waist from a position of from 60 cm to 100 cm, the displacement parameter x, i.e. the relative positions of lenses L2 and L4, needs to be changed from only 5.4 cm to 3.3 cm. The corresponding change is the waist is negligible as shown in Figure 8.5 (b). The waist size is determined from the input beam waist, as shown in Figure 8.5 (c). For example, to generate the tight focus of around 30 μm required for cadmium (see Section 7.4.2), an input beam radius of ∼10 mm is required.

8.3 Design of full vacuum apparatus

This section shows the complete design of the atom interferometer with its two arms designed for generating ultra-cold cadmium and strontium ensembles, to scale. The interferometry region is 1 m long with a detection possibility on the top as well as bottom as shown in Figure 8.6. The material is chosen to be stainless steel 316 while the viewports are made up of excimer-grade UV-fused silica which are capable of better withstanding the intense UV radiation required for cadmium.

The main science chamber is a spherical octagon laid horizontally so that the vertical axis is of size CF100. This large tube is chosen to minimize diffraction effects on the interferometry beam,

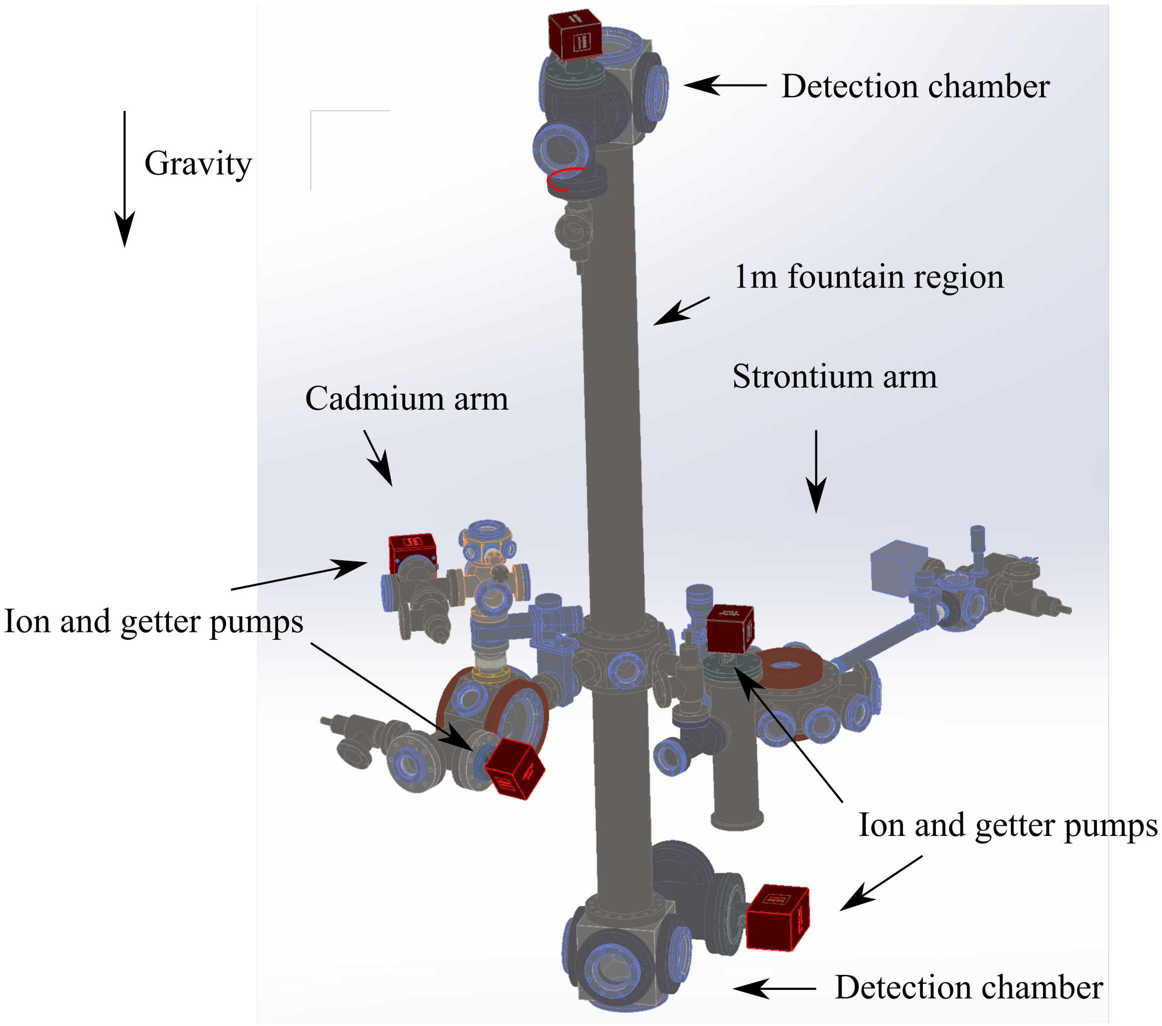

Figure 8.6: The complete design of the vacuum chamber showing both the arms to generate the ultra-cold ensembles of cadmium and strontium along with the 1 m interferometric arm with the detection chambers.

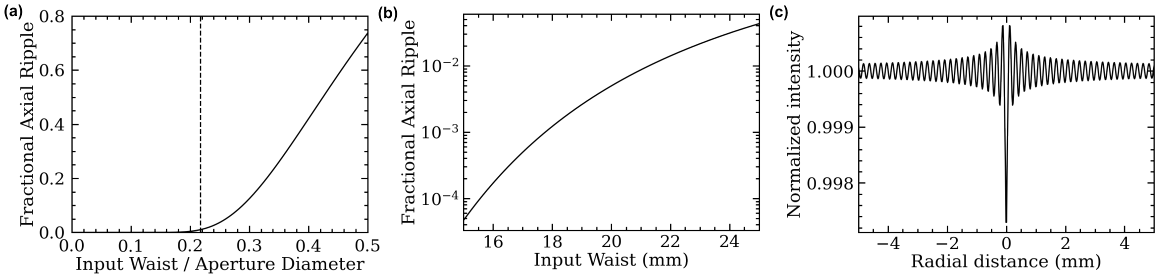

Figure 8.7: (a) Axial ripple as a function of the input waist to the beam diameter (solid line) showing the 1% ripple criterion (dashed line). (b) Calculated ripple in the axial direction for diffraction from a CF100 viewport. (c) Radial ripple at a propagation distance of z ~1 m from the viewport and with the beam waist at the 1% ripple criterion ($\lambda = 326$ nm).

which should be as close as possible to a plane wave in the ideal case (see Section 2.2). The intensity ripple introduced by the viewport can be calculated in the axial and radial directions by considering the diffraction of a Gaussian beam from a circular aperture [105]. For a circular aperture of radius a this results in equation 8.3, where J_0 is the zeroth-order Bessel function of the first kind and $w\left(z\right)$ is the Gaussian beam propagation formula and $N = a^2/z\lambda$ is the Fresnel number. This formula is valid assuming that $r \ll a$, i.e. close to the optical axis, and is exact along the beam axis ($r = 0$) [105].

$$I\left(r, z\right) \approx \left[\frac{w_0}{w\left(z\right)}\right]^2 \left|1 - e^{-a^2/w_0^2} e^{-i\pi N} J_0\left(2\pi N r/a\right)\right|^2 \tag{8.3}$$

From equation 8.3, it can be deduced that the axial intensity varies approximately as e^{-a^2/w_0^2}. This leads to the definition of a 1% ripple criterion of $w_0 = 2a/4.6$ [205], which has been used in designing state-of-the-art atom interferometry experiments [27]. At this ratio of the input waist and the aperture size, there is a ripple in the intensity of approximately 1% along the beam axis. The magnitude of this ripple is independent of the propagation distance, but the spatial frequency of this ripple is dependent on distance, with higher frequency oscillations occurring nearer the aperture. Figure 8.7 shows the calculated ripple and how it dramatically increases once the beam waist is greater than the 1% value. Also shown is the ripple in the radial direction, highlighting how the maximum ripple is along the axis.

For a CF100 viewport of diameter 98 mm, the 1% criterion allows for a beam with a waist of 21.3 mm, more than sufficient to be considered very large compared to an ultra-cold source of atoms. The Rayleigh length at this diameter is 4.4 km and 2.1 km for 326 nm and 689 nm, respectively, orders of magnitude larger than the length of the fountain, meaning the laser can be considered fully collimated during an e.g. Bragg interferometry sequence and other effects such as the Gouy phase can be neglected.

Atoms from the cadmium and strontium cold apparatus can be transferred into this science chamber, as outlined in Section 8.2, and then launched a total height of 1 m in the main interferometry region, limited by the tube in the design. The laboratory supports the option of increasing this height to over 2 m. Due to the potential difficulties of launching cadmium with an optical lattice, discussed above in Section 8.4, the possibility to instead drop the atoms around 50 cm is also present. This length is chosen to leave room underneath the fountain for optics for the interferometric beams optics, a vibration-isolation stage etc.

8.4 Lattice launch efficiency

This section describes the calculation of the simultaneous launch of the cadmium and strontium atoms in the interferometer. Once the atoms are transferred into the science chamber, they can be launched using optical lattice beams which are sent in a retro-reflected configuration to trap the atoms in the periodic lattice maxima [43]. This fountain configuration enhances flight time and therefore the interferometry sensitivity, as discussed in Section 2.2, and the current design has a 1 m launch tube for this purpose (Figure 8.6).

It is important that both species are launched with the same velocity, which means that the same mechanism should be used for both. Therefore a lattice based on a high-power, single-mode 1064 nm laser as presented in Section 7.4.1, is preferable to launching with sequential Bragg pulses or a lattice based on intercombination transitions, which are atom specific. Atoms can be launched using a lattice by chirping the frequency of the lattice laser to generate a moving standing-wave pattern. For a lattice formed from light with a wave number k and with a chirp rate α, the acceleration a of the launch is given by equation 8.4.

$$a = \frac{\alpha}{2k} \tag{8.4}$$

There are two main fundamental sources of loss when using this lattice launch: spontaneous emission due to the lattice light and Landau-Zener tunneling. In practice, other losses due to e.g. the temperature of the atoms and imperfections in the lattice will also be present. The losses due to spontaneous emission can be calculated simply according to equation 2.13 and will be small for such a far detuned lattice. Landau-Zener tunneling, in classical terms, is when atomic are forcefully pushed

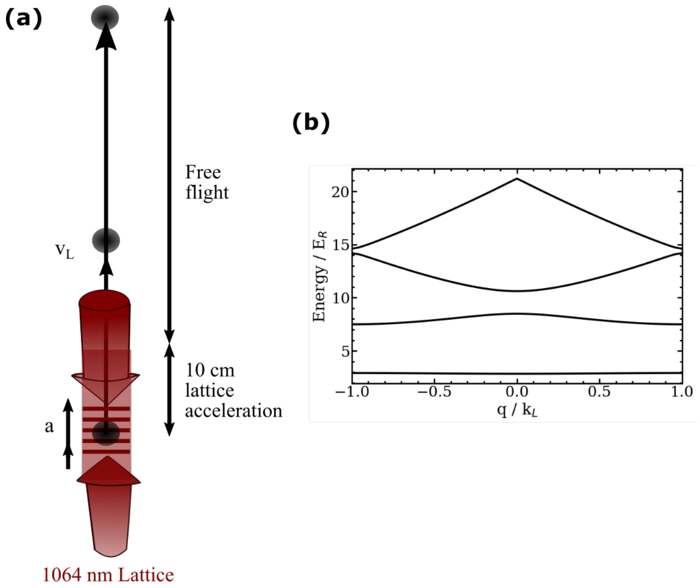

Figure 8.8: (a) Scheme for launching the atoms with a 1064 nm lattice. (b) Calculated energy bands for cadmium for a trap depth of 10 E_R, where E_R is the lattice recoil energy.

out of the lattice sites when the lattice acceleration is too much for the atoms to bear compared to their trapped potential energy arising from the lattice depths. Quantum mechanically, these losses occur even when the lattice depths are larger than the atomic energy due to the tunneling effect.

The losses due to Landau-Zener tunnelling can be estimated by considering the launch as a sequence of Bloch oscillations [205, 206]. For a launch velocity v_L the atoms will pass through a number of avoided crossings N given by equation 8.5.

$$N = \frac{mv_L}{2\hbar k} \tag{8.5}$$

Also required is the band gap energy $\hbar\Omega$ of the lattice potential, which can be calculated by numerically solving the Schrödinger equation [207]. From this the fraction of surviving atoms f can then be calculated according to equation 8.6.

$$f = \left(1 - \exp\left[-\frac{\pi\Omega^2}{2\alpha}\right]\right)^N \tag{8.6}$$

Equation 8.6 shows that large trap depths and slow chirp rates minimize tunnelling losses. These atom losses are investigated by fixing the distance over which the atoms are accelerated for to 10 cm, as shown in Figure 8.8. The target launch height is around 1 m. Based on the launch height, the final

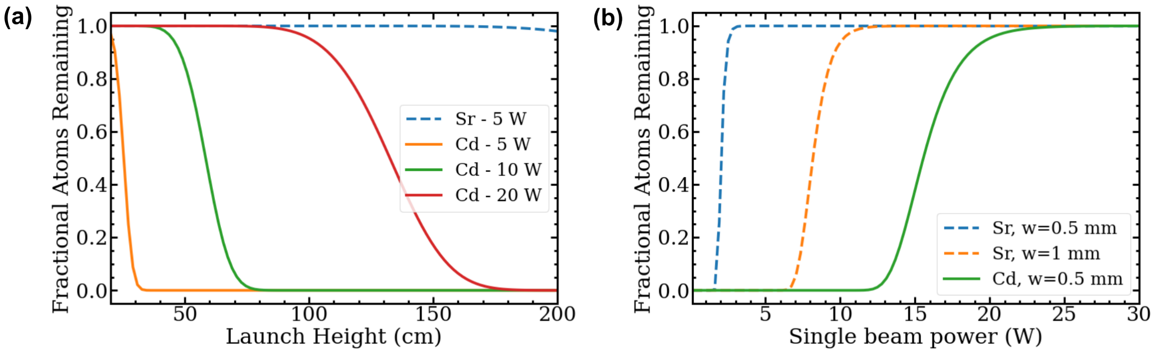

Figure 8.9: Fraction of atoms surviving the launch sequence for cadmium (solid lines) and strontium (dashed lines). (a) Varying the total launch height with fixed beam waist w=0.5 mm. (b) For a launch height of 1 m.

velocity of the atoms when released from the lattice can be calculated, and therefore the required acceleration and chirp rate can be determined allowing the losses to be calculated according to equation 8.6.

Figure 8.9 shows the estimated number of atoms surviving the launch for cadmium and strontium at different lattice and launch parameters. It is clearly seen that losses are much worse for cadmium and efficient launching requires very high intensity beams. This is a consequence of the $1/\omega_0^3$ dependence of equation 2.30 which reduces the band gap energy and therefore increases Landau-Zener tunnelling. It is clear that this will be a challenge for the dual-species interferometer, but reasonable launch heights and atom numbers (>50%) should be achievable for the experimental powers. In the case, for strontium, the laser seems to be a very good option with efficient launches up to 2 m available.

Chapter 9

Summary and future prospects

This thesis has presented the experimental and simulation work performed towards the construction of a dual-species atom interferometer with atomic cadmium and strontium. Complete baseline lasers systems for both cadmium and strontium have been presented, including lasers with W-level power and Hz-level linewidth for performing clock atom interferometry. Designs of the cadmium and strontium vacuum apparatus have been presented, including a full numerical simulation in the former case. Based on these systems, a design for a vacuum chamber for a dual-species fountain atom interferometer is presented, including information about the optical transfer and lattice launching.

The systems for accessing the relevant UV transitions of cadmium have been developed and characterized in house using novel designs [57–59]. They have further been used to perform spectroscopy on a novel cadmium atomic beam [57, 58], whose performance has likewise been characterized. The most challenging of these systems is the 229 nm laser system for the ^{1}S$_0$ - ^{1}P$_1$ due to the difficulty in achieving high-power continuous-wave light with long-term stability and even sourcing suitable optics and non-linear crystals at such a low wavelength. Nevertheless, stable production up to a maximum value of 100 mW has been observed. The 326 nm and the 332 nm laser set-ups for addressing the ^{1}S$_0$ - ^{3}P$_1$ and ^{1}S$_0$ - ^{3}P$_0$ transitions, respectively, share a common design which allows for the reduction of the linewidth in the UV to kHz level in the case of 326 nm and down to the Hz level for the ultra-narrow 332 nm clock wavelength. These laser set-ups are furthermore capable of generating powers of 1 W and 1.2 W at 326 nm and 332 nm, respectively. The laser systems for strontium are also developed.

The laser which generates the 461 nm light has the same master laser set-up as that of the

229 nm laser, but with one frequency-doubling step fewer, highlighting the technical advantage of using cadmium and strontium as a pair. It can produce powers up to 1.4 W. The light for the strontium intercombination transitions at 689 nm and 698 nm is generated using a Ti-Sapph laser with which the intercombination transitions are accessible.

The production of a cold source of cadmium is thoroughly simulated, due to it being an unproven element for generating quantum degenerate gases or performing atom interferometry with. These simulations were performed keeping in mind the experimental and technical limitations of the powers produced at the less-explored UV wavelengths. Nevertheless, a state-of-the-art system based on segmented regions for improving vacuum is presented, with loading rates of $>10^7$ atoms/s into the 3D MOT is expected.

In the very near future, work will begin on the construction of this system. The vacuum chamber is currently being manufactured at the time of writing and is expected to be delivered imminently. Once the chamber has been constructed it will be baked at a high temperature for a considerable time (more than one month) to make it as clean as possible to try to reduce problems of damage induced by the UV. Following this, the production of ultra-cold cadmium will be established according to the simulated design.

There is a great deal of physics to be studied that will be possible with these ultra-cold cadmium atoms. Naturally, early attention will be focused towards an initial demonstration of atom interferometry with cadmium by using Bragg interferometry with the high power 326 nm laser developed here (Section 4.2). However, many properties of cadmium are still to be explored, such as its cold collisional properties. These can be measured in conjunction with trying to make a quantum degenerate source of cadmium. From such measurements an isotope with the lowest scattering length in its ground state can be known from an available pool of eight isotopes. Such an isotope would be useful to maintain higher coherence time in interferometric sequences.

Furthermore, cadmium atoms can be a good frequency reference for future optical clocks due to the presence of their clock transition at 332 nm. High intrinsic sensitivity clocks can be prepared due to their low wavelength and reduced sensitivity to the black-body radiation. High precision frequency measurements can be performed with cadmium species to measure their internal properties, such as the mass and field shifts by looking at the isotope frequency shifts with high accuracy. If this is done with two intercombination states, such as the 326 nm and 332 nm transitions, it represents an ideal case for making King's plots and searching for new physics due to the high number of isotopes of cadmium and its nuclear structure [57, 100].

In parallel, work will also begin to establish the upgraded strontium apparatus presented in Chapter 8. In the further future, the dual-species atom interferometer can be used to probe general relativity in a quantum mechanical context [57]. It can be used to test Einstein's weak equivalence principle, especially by using quantum states of matter, such as superpositions of clock states, not available to classical tests. A very interesting yet challenging possibility is that it can also be useful to determine the time dilation effects and thereby may help in explaining the theory of gravity at minuscule scales, where it intersects in a meaningful way with quantum mechanics. These works will benefit from the growing technique of clock atom interferometry and the high-power clock lasers developed here.

Appendices

Appendix A

List of publications

The author is a co-author on the following articles published during the duration of the PhD program, listed beginning with the most recent.

1. S. Bandarupally, J. N. Tinsley, M. Chiarotti, N. Poli, "Design and simulation of a source of cold cadmium for atom interferometry", arXiv (2023)
2. I. Alonso et al., "Cold Atoms in Space: Community Workshop Summary and Proposed Road-Map", EPJ Quantum Technology **9**, 30 (2022)
3. M. Chiarotti, J. N. Tinsley, S. Bandarupally, S. Manzoor, M. Sacco, L. Salvi, N. Poli, "Practical Limits for Large-Momentum-Transfer Clock Atom Interferometers", PRX Quantum **3**, 030348 (2022)
4. S. Manzoor, J. N. Tinsley, S. Bandarupally, M. Chiarotti, N. Poli, "High-power, frequency-quadrupled UV laser source resonant with the $^1S_0$ - $^3P_1$ narrow intercombination transition of cadmium at 326.2 nm", Optics Letters **47**, 2582-2585 (2022)
5. J. N. Tinsley, S. Bandarupally, M. Chiarotti, S. Manzoor, L. Salvi, N. Poli, "Prospects for a simultaneous atom interferometer with ultracold cadmium and strontium for fundamental physics tests", Proc. SPIE **12016**, 1201602 (2022)
6. J. N. Tinsley, S. Bandarupally, J.-P. Penttinen, S. Manzoor, S. Ranta, L. Salvi, M. Guina, N. Poli, "Watt-level blue light for precision spectroscopy, laser cooling and trapping of strontium and cadmium atoms", Optics Express **29**, 25462-25476 (2021)

Appendix B

Ultra-high vacuum preparation

This appendix describes the procedure performed to reduce the pressure of the spectroscopy chamber used in Chapter 6 to the ultra-high vacuum regime.

B.1 Vacuum pump technology

The removal the internal particles in the chamber is firstly done by connecting it to a scroll pump which sucks out the internal matter and thereby reducing the chamber pressure from atmospheric pressure to about a level of 10^{-2} mbar. The scroll pump consists of two co-scrolls, out of which one is fixed and the other scroll performs a spiral/circular motion against the fixed one, contrary to the functioning of a piston. The particles enter the scroll set-up from the open end and they slowly get transferred to the center of these scrolls due to the circular motion, where there they finally exit from. During the travel of these gas particles, they reduce in volume and the increased pressure of the collected ensemble aids in the flushing out of the gas. The pump used here is IDP-7 from Agilent Technologies.

Simultaneously, while the scroll pump is connected, we attach the turbo pump (TwisTorr 74 FS, Agilent Technologies) which reduces the pressure from 10^{-2} mbar down to about 10^{-7} mbar. Any traces of hydrogen, water vapor and various other elements are removed with a combination of high temperatures and the pumping mechanism. The turbo pump functions using high speed rotating blades, like a turbine, which are fixed within a chamber-like structure. These blade type structures sit throughout the length of this chamber. The high speeds gives the gas particles momentum in the axial direction and they are consequently pushed down and experience pressure compression before they are pushed out through an exhaust valve. Rotation speeds can be of the order of tens of thousand rpm, although our pumps operates at around 1000 Hz.

Finally we use an ion pump (StarCell, Agilent Technologies) which gets the vacuum down to the ultra-high vacuum regime of 10^{-9} - 10^{-10} mbar. This is the final stage of pumping which allows to attain the desired ultra-high vacuum system. Unlike any mechanical rotatory movements mentioned in the previous pumps, the ion pump functions by the generation of high voltage within a cell surrounded by a magnetic field for motional control. This high voltage generates free electrons which acquire spiral motion due to the Lorentz force experienced. Collision of these electrons with the gas particles generates ions and more electrons. This allows for the collision of the generated ions with the cathode thereby generating titanium atoms and get trapped in the cathode. The titanium atoms help in adsorption of the gas molecules within the chamber. This system allows for less mechanical noise. However for ion pumps to function, high vacuum is a prerequisite, which is why the scroll and turbo pumps must be first employed.

Nevertheless, limitations in the pressure can arise despite pumping the chamber using these various pumps to low pressures. These can arise due to the particles which remain trapped inside the chamber. The particles mainly exist within the chamber due to four ongoing processes, vaporisation through the surfaces, diffusion of some elements through the mass of the material, permeation of gas particles from the outer atmosphere via the chamber walls and desorption of weakly bound particles on the inner surface of the chamber which might have been introduced during the construction or the maintenance of the material [199]. Although permeation is impossible to prevent, the effect of the other three processes can be reduced by using a clean and baked vacuum chamber, with our procedures discussed in the following section.

B.2 Oven preparation & baking procedure

In order to obtain the ultra-high vacuum regime and reduce the effects of trapped gas, it is mandatory to carefully prepare the oven and spectroscopy chamber. The chamber and the individual oven parts were first cleaned with distilled and soapy water to remove any oil remaining from the manufacturing process. A hand cleaning with acetone was then performed and, for those parts which were small enough, a final cleaning in a heated ultrasonic bath with acetone is performed.

The chamber is then constructed. We make sure to place in the cadmium sample very carefully in the oven while wearing a chemical mask, pair of gloves and a fully covering lab coat as it is highly dangerous to consume cadmium in the form of dust. It is then crucial to tighten all the viewports and other flanges used for connecting the oven and the chamber and also the connection to the ion pump. Care must be taken to tighten the bolts in the correct sequence to achieve an even seal without leaks. In addition to being required for maintaining the vacuum, this is important in avoiding any kind of cadmium leaks to the environment.

In order to obtain the ultra-high vacuum regime, it is mandatory to bake the chamber whilst reducing the pressure in gradual steps from the atmospheric pressure as described previously. Baking the chamber at high temperatures helps to remove any water molecules within and also other elements trapped in the chamber walls and is therefore necessary for attaining the lowest pressures. Also the particles from the air which settle on the windows of the viewports are targeted. Any vacuum system with the best background pressure is always limited by these gas particles. As one of the main contaminants is water vapor, it is best to bake at a minimum temperature of 100 °C. Heating is performed using heating tape and variacs to control the current flow and hence temperature. Current is also run through the tantalum wire to heat the oven part inside the chamber. Without this heating, there is a large difference in temperature between the oven and the rest of the chamber, showing that the thermal isolation of the oven works well.

The temperature during the baking is increased gradually avoiding any sudden gradients, as various vacuum parts have different thermal expansions. The mechanical stress can have negative affects such as breakage of the components, especially the glass viewports. To quantify the temperature gradient in the chamber, we measure the temperatures at various locations of the vacuum chamber using thermocouples to make sure the heating occurs uniformly. The chamber is wrapped in aluminium foil mainly to reduce the losses to the environment by radiation and thereby creating a insulation barrier from the chamber to the surrounding environment. The aluminium foil also helps to reduce gradients and ensure an even temperature. These sequential pumping stages allows us to keep an eye on the leakage during prolonged baking periods. This process can take up to a month till we reach the ultra-high vacuum stage. At this point we turn off the heating and let the system cool down gradually to room temperature and close the valve which connects the turbo pump to the chamber, leaving only the ion pump operating. With this the final background pressure of the system is about 10^{-10} mbar.

Bibliography

1. L. de Broglie. *Recherches sur la théorie des Quanta*. PhD Thesis (University of Paris, November 1924).
2. C. J. Davisson & L. H. Germer. "Reflection of Electrons by a Crystal of Nickel". *Proceedings of the National Academy of Sciences of the United States of America* **14,** 317–22 (April 1928).
3. H. Rauch & S. A. Werner. *Neutron Interferometry: Lessons in Experimental Quantum Mechanics, Wave-Particle Duality, and Entanglement* (Oxford University Press, January 2015).
4. R. P. Berman. *Atom Interferometry* (Academic Press, 1997).
5. A. D. Cronin, J. Schmiedmayer & D. E. Pritchard. "Optics and interferometry with atoms and molecules". *Rev. Mod. Phys.* **81,** 1051–1129 (July 2009).
6. G. M. Tino & M. A. Kasevich. *Atom Interferometry, Proceedings of the International School of Physics "Enrico Fermi," Course CLXXXVIII, Varenna 2013* (Società Italiana di Fisica and IOS Press, 2014).
7. N. F. Ramsey. "A Molecular Beam Resonance Method with Separated Oscillating Fields". *Phys. Rev.* **78,** 695–699 (June 1950).
8. C. J. Bordé, C. Salomon, S. Avrillier, A. van Lerberghe, C. Bréant, D. Bassi & G. Scoles. "Optical Ramsey fringes with traveling waves". *Phys. Rev. A* **30,** 1836–1848 (October 1984).
9. O. Carnal & J. Mlynek. "Young's double-slit experiment with atoms: A simple atom interferometer". *Phys. Rev. Lett.* **66,** 2689–2692 (May 1991).
10. D. W. Keith, C. R. Ekstrom, Q. A. Turchette & D. E. Pritchard. "An interferometer for atoms". *Phys. Rev. Lett.* **66,** 2693–2696 (May 1991).
11. M. Kasevich & S. Chu. "Atomic interferometry using stimulated Raman transitions". *Phys. Rev. Lett.* **67,** 181–184 (July 1991).

12. T. Kovachy, P. Asenbaum, C. Overstreet, C. A. Donnelly, S. M. Dickerson, A. Sugarbaker, J. M. Hogan & M. A. Kasevich. "Quantum superposition at the half-metre scale". *Nature* **528,** 530–533 (December 2015).

13. B. Stray *et al.* "Quantum sensing for gravity cartography". *Nature* **602,** 590–602 (February 2022).

14. G. M. Tino. "Testing gravity with cold atom interferometry: results and prospects". *Quantum Science and Technology* **6,** 024014 (March 2021).

15. A. Peters, K. Y. Chung & S. Chu. "Measurement of gravitational acceleration by dropping atoms". *Nature* **400** (August 1999).

16. M. J. Snadden, J. M. McGuirk, P. Bouyer, K. G. Haritos & M. A. Kasevich. "Measurement of the Earth's Gravity Gradient with an Atom Interferometer-Based Gravity Gradiometer". *Phys. Rev. Lett.* **81,** 971–974 (August 1998).

17. G. Rosi, L. Cacciapuoti, F. Sorrentino, M. Menchetti, M. Prevedelli & G. M. Tino. "Measurement of the Gravity-Field Curvature by Atom Interferometry". *Phys. Rev. Lett.* **114,** 013001 (January 2015).

18. P. Asenbaum, C. Overstreet, T. Kovachy, D. D. Brown, J. M. Hogan & M. A. Kasevich. "Phase Shift in an Atom Interferometer due to Spacetime Curvature across its Wave Function". *Phys. Rev. Lett.* **118,** 183602 (May 2017).

19. J. B. Fixler, G. T. Foster, J. M. McGuirk & M. A. Kasevich. "Atom Interferometer Measurement of the Newtonian Constant of Gravity". *Science* **315,** 74–77 (January 2007).

20. G. Rosi, L. Sorrentino F. Cacciapuoti, M. Prevedelli & G. M. Tino. "Precision measurement of the Newtonian gravitational constant using cold atoms". *Nature* **510** (June 2014).

21. C. Overstreet, P. Asenbaum, J. Curti, M. Kim & M. A. Kasevich. "Observation of a gravitational Aharonov-Bohm effect". *Science* **375,** 226–229 (January 2022).

22. W. Chaibi, R. Geiger, B. Canuel, A. Bertoldi, A. Landragin & P. Bouyer. "Low frequency gravitational wave detection with ground-based atom interferometer arrays". *Phys. Rev. D* **93,** 021101 (January 2016).

23. B. Canuel *et al.* "Exploring gravity with the MIGA large scale atom interferometer". *Scientific Reports* **8,** 14064 (September 2018).

24. A. Lenef, T. D. Hammond, E. T. Smith, M. S. Chapman, R. A. Rubenstein & D. E. Pritchard. "Rotation Sensing with an Atom Interferometer". *Phys. Rev. Lett.* **78,** 760–763 (February 1997).

25. T. L. Gustavson, P. Bouyer & M. A. Kasevich. "Precision Rotation Measurements with an Atom Interferometer Gyroscope". *Phys. Rev. Lett.* **78,** 2046–2049 (March 1997).

26. B. Canuel, F. Leduc, D. Holleville, A. Gauguet, J. Fils, A. Virdis, A. Clairon, N. Dimarcq, C. J. Bordé, A. Landragin & P. Bouyer. "Six-Axis Inertial Sensor Using Cold-Atom Interferometry". *Phys. Rev. Lett.* **97,** 010402 (July 2006).

27. S. M. Dickerson, J. M. Hogan, A. Sugarbaker, D. M. S. Johnson & M. A. Kasevich. "Multiaxis Inertial Sensing with Long-Time Point Source Atom Interferometry". *Phys. Rev. Lett.* **111,** 083001 (August 2013).

28. K. Bongs, M. Holynski, J. Vovrosh, P. Bouyer, G. Condon, E. Rasel, C. Schubert, W. P. Schleich & A. Roura. "Taking atom interferometric quantum sensors from the laboratory to real-world applications". *Nature Reviews Physics* **1,** 731–739 (December 2019).

29. M. Hauth, C. Freier, V. Schkolnik, A. Senger, M. Schmidt & A. Peters. "First gravity measurements using the mobile atom interferometer GAIN". *Applied Physics B* **113,** 49–55 (April 2013).

30. R. Bouchendira, P. Cladé, S. Guellati-Khélifa, F. Nez & F. Biraben. "New Determination of the Fine Structure Constant and Test of the Quantum Electrodynamics". *Phys. Rev. Lett.* **106,** 080801 (February 2011).

31. L. Morel, Z. Yao, P. Cladé & S. Guellati-Khélifa. "Determination of the fine-structure constant with an accuracy of 81 parts per trillion". *Nature* **588,** 61–65 (December 2020).

32. R. H. Parker, C. Yu, W. Zhong, B. Estey & H. Müller. "Measurement of the fine-structure constant as a test of the Standard Model". *Science* **360,** 191–195 (April 2018).

33. P. Hamilton, M. Jaffe, P. Haslinger, Q. Simmons, H. Müller & J. Khoury. "Atom-interferometry constraints on dark energy". *Science* **349,** 849–851 (August 2015).

34. L. Salvi, N. Poli, V. Vuletić & G. M. Tino. "Squeezing on Momentum States for Atom Interferometry". *Phys. Rev. Lett.* **120,** 033601 (January 2018).

35. A. Shankar, L. Salvi, M. L. Chiofalo, N. Poli & M. J. Holland. "Squeezed state metrology with Bragg interferometers operating in a cavity". *Quantum Science and Technology* **4,** 045010 (October 2019).

36. G. P. Greve, C. Luo, B. Wu & J. K. Thompson. "Entanglement-Enhanced Matter-Wave Interferometry in a High-Finesse Cavity". *Nature* **610,** 472–477 (October 2022).

37. N. Huntemann, C. Sanner, B. Lipphardt, C. Tamm & E. Peik. "Single-Ion Atomic Clock with 3×10^{-18} Systematic Uncertainty". *Phys. Rev. Lett.* **116,** 063001 (February 2016).

38. W. F. McGrew, X. Zhang, R. J. Fasano, S. A. Schäffer, K. Beloy, D. Nicolodi, R. C. Brown, N. Hinkley, G. Milani, M. Schioppo, T. H. Yoon & A. D. Ludlow. "Atomic clock performance enabling geodesy below the centimetre level". *Nature* **564,** 87–90 (December 2018).

39. T. Mazzoni, X. Zhang, R. Del Aguila, L. Salvi, N. Poli & G. M. Tino. "Large-momentum-transfer Bragg interferometer with strontium atoms". *Phys. Rev. A* **92,** 053619 (November 2015).

40. A. O. Jamison, B. Plotkin-Swing & S. Gupta. "Advances in precision contrast interferometry with Yb Bose-Einstein condensates". *Phys. Rev. A* **90,** 063606 (December 2014).

41. R. P. del Aguila, T. Mazzoni, L. Hu, L. Salvi, G. M. Tino & N. Poli. "Bragg gravity-gradiometer using the $^1S_0$–$^3P_1$ intercombination transition of ^{88}Sr". *New Journal of Physics* **20,** 043002 (April 2018).

42. X. Zhang, R. P. del Aguila, T. Mazzoni, N. Poli & G. M. Tino. "Trapped-atom interferometer with ultracold Sr atoms". *Phys. Rev. A* **94,** 043608 (October 2016).

43. L. Hu, E. Wang, L. Salvi, J. N. Tinsley, G. M. Tino & N. Poli. "Sr atom interferometry with the optical clock transition as a gravimeter and a gravity gradiometer". *Classical and Quantum Gravity* **37,** 014001 (November 2019).

44. N. Yu & M. Tinto. "Gravitational wave detection with single-laser atom interferometers". *General Relativity and Gravitation* **43,** 1943–1952 (July 2011).

45. P. W. Graham, J. M. Hogan, M. A. Kasevich & S. Rajendran. "New Method for Gravitational Wave Detection with Atomic Sensors". *Phys. Rev. Lett.* **110,** 171102 (April 2013).

46. L. Hu, N. Poli, L. Salvi & G. M. Tino. "Atom Interferometry with the Sr Optical Clock Transition". *Phys. Rev. Lett.* **119,** 263601 (December 2017).

47. J. Rudolph, T. Wilkason, M. Nantel, H. Swan, C. M. Holland, Y. Jiang, B. E. Garber, S. P. Carman & J. M. Hogan. "Large Momentum Transfer Clock Atom Interferometry on the 689 nm Intercombination Line of Strontium". *Phys. Rev. Lett.* **124,** 083604 (February 2020).

48. T. Wilkason, M. Nantel, J. Rudolph, Y. Jiang, B. E. Garber, H. Swan, S. P. Carman, M. Abe & J. M. Hogan. "Atom Interferometry with Floquet Atom Optics". *Phys. Rev. Lett.* **129,** 183202 (October 2022).

49. L. Badurina *et al.* "AION: an atom interferometer observatory and network". *Journal of Cosmology and Astroparticle Physics* **2020,** 011–011 (May 2020).

50. M. Abe *et al.* "Matter-wave Atomic Gradiometer Interferometric Sensor (MAGIS-100)". *Quantum Science and Technology* **6,** 044003 (July 2021).

51. G. M. Tino *et al.* "SAGE: A proposal for a space atomic gravity explorer". *The European Physical Journal D* **73** (November 2019).

52. Y. A. El-Neaj *et al.* "AEDGE: Atomic Experiment for Dark Matter and Gravity Exploration in Space". *EPJ Quantum Technology* **7** (March 2020).

53. J. N. Tinsley, S. Bandarupally, M. Chiarotti, S. Manzoor, L. Salvi & N. Poli. *Prospects for a simultaneous atom interferometer with ultracold cadmium and strontium for fundamental physics tests*. in *Optical and Quantum Sensing and Precision Metrology II* (eds J. Scheuer & S. M. Shahriar) **12016** (SPIE, 2022), 1–16.

54. A. Yamaguchi, M. S. Safronova, K. Gibble & H. Katori. "Narrow-line Cooling and Determination of the Magic Wavelength of Cd". *Phys. Rev. Lett.* **123,** 113201 (September 2019).

55. S. G. Porsev & M. S. Safronova. "Calculation of higher-order corrections to the light shift of the $5s^{21}S_0 - 5s5p^3P_0^o$ clock transition in Cd". *Phys. Rev. A* **102,** 012811 (July 2020).

56. Y. Kaneda, J. M. Yarborough, Y. Merzlyak, A. Yamaguchi, K. Hayashida, N. Ohmae & H. Katori. "Continuous-wave, single-frequency 229 nm laser source for laser cooling of cadmium atoms". *Opt. Lett.* **41,** 705–708 (February 2016).

57. J. N. Tinsley, S. Bandarupally, J.-P. Penttinen, S. Manzoor, S. Ranta, L. Salvi, M. Guina & N. Poli. "Watt-level blue light for precision spectroscopy, laser cooling and trapping of strontium and cadmium atoms". *Optics Express* **29,** 25462–25476 (August 2021).

58. S. Manzoor, J. N. Tinsley, S. Bandarupally, M. Chiarotti & N. Poli. "High-power, frequency-quadrupled UV laser source resonant with the $^1S_0$-$^3P_1$ narrow intercombination transition of cadmium at 326.2 nm". *Opt. Lett.* **47,** 2582–2585 (May 2022).

59. M. Chiarotti, J. N. Tinsley, S. Bandarupally, S. Manzoor, M. Sacco, L. Salvi & N. Poli. "Practical Limits for Large-Momentum-Transfer Clock Atom Interferometers". *PRX Quantum* **3,** 030348 (September 2022).

60. M. Zych, F. Costa, I. Pikovski & Č. Brukner. "Quantum interferometric visibility as a witness of general relativistic proper time". *Nature Communications* **2,** 505 (October 2011).

61. S. Loriani, A. Friedrich, C. Ufrecht, F. D. Pumpo, S. Kleinert, S. Abend, N. Gaaloul, C. Meiners, C. Schubert, D. Tell, É. Wodey, M. Zych, W. Ertmer, A. Roura, D. Schlippert, W. P. Schleich, E. M. Rasel & E. Giese. "Interference of clocks: A quantum twin paradox". *Science Advances* **5,** eaax8966 (October 2019).

62. S. Chu. "Nobel Lecture: The manipulation of neutral particles". *Rev. Mod. Phys.* **70,** 685–706 (July 1998).

63. C. N. Cohen-Tannoudji. "Nobel Lecture: Manipulating atoms with photons". *Rev. Mod. Phys.* **70,** 707–719 (July 1998).

64. W. D. Phillips. "Nobel Lecture: Laser cooling and trapping of neutral atoms". *Rev. Mod. Phys.* **70,** 721–741 (July 1998).

65. D. J. Wineland, R. E. Drullinger & F. L. Walls. "Radiation-Pressure Cooling of Bound Resonant Absorbers". *Phys. Rev. Lett.* **40,** 1639–1642 (June 1978).

66. W. D. Phillips & H. Metcalf. "Laser Deceleration of an Atomic Beam". *Phys. Rev. Lett.* **48,** 596–599 (March 1982).

67. C. J. Foot. *Atomic Physics* (Oxford University Press, 2005).

68. S. Chu, L. Hollberg, J. E. Bjorkholm, A. Cable & A. Ashkin. "Three-dimensional viscous confinement and cooling of atoms by resonance radiation pressure". *Phys. Rev. Lett.* **55,** 48–51 (July 1985).

69. V. S. Letokhov, V. G. Minogin & B. D. Pavlik. "Cooling and capture of atoms and molecules by a resonant light field". *Soviet Journal of Experimental and Theoretical Physics* **45,** 698 (April 1977).

70. H. J. Metcalf & P. van der Straten. *Laser Cooling and Trapping* (Springer, 1999).

71. P. D. Lett, R. N. Watts, C. I. Westbrook, W. D. Phillips, P. L. Gould & H. J. Metcalf. "Observation of Atoms Laser Cooled below the Doppler Limit". *Phys. Rev. Lett.* **61,** 169–172 (July 1988).

72. J. Dalibard & C. Cohen-Tannoudji. "Laser cooling below the Doppler limit by polarization gradients: simple theoretical models". *J. Opt. Soc. Am. B* **6,** 2023–2045 (November 1989).

73. P. D. Lett, W. D. Phillips, S. L. Rolston, C. E. Tanner, R. N. Watts & C. I. Westbrook. "Optical molasses". *J. Opt. Soc. Am. B* **6,** 2084–2107 (November 1989).

74. C. Salomon, J. Dalibard, W. D. Phillips, A. Clairon & S. Guellati. "Laser Cooling of Cesium Atoms Below 3 μK". *Europhysics Letters* **12,** 683 (August 1990).

75. E. L. Raab, M. Prentiss, A. Cable, S. Chu & D. E. Pritchard. "Trapping of Neutral Sodium Atoms with Radiation Pressure". *Phys. Rev. Lett.* **59,** 2631–2634 (December 1987).

76. D. A. Steck. *Quantum and Atom Optics* revision 0.11.0, 2016 (http://steck.us/teaching, 2007).

77. R. Grimm, M. Weidemüller & Y. B. Ovchinnikov. "Optical Dipole Traps for Neutral Atoms". *Advances In Atomic, Molecular, and Optical Physics* **42,** 95–170 (2000).

78. M. Kasevich & S. Chu. "Measurement of the gravitational acceleration of an atom with a light-pulse atom interferometer". *Applied Physics B* **54,** 321–332 (May 1992).

79. Pippa Storey & Claude Cohen-Tannoudji. "The Feynman path integral approach to atomic interferometry. A tutorial". *J. Phys. II France* **4,** 1999–2027 (November 1994).

80. A. Peters, K. Y. Chung & S. Chu. "High-precision gravity measurements using atom interferometry". *Metrologia* **38,** 25 (February 2001).

81. K. Bongs, R. Launay & M. Kasevich. "High-order inertial phase shifts for time-domain atom interferometers". *Applied Physics B* **84,** 599–602 (September 2006).

82. J. N. Tinsley. *Construction of a Rubidium Fountain Atomic Interferometer for Gravity Gradiometry*. PhD thesis (University of Liverpool, 2019).

83. N. Poli, C. W. Oates, P. Gill & G. M. Tino. "Optical atomic clocks". English. *Rivista del Nuovo Cimento* **36,** 555–624 (December 2013).

84. T. Bothwell, C. J. Kennedy, A. Aeppli, D. Kedar, J. M. Robinson, E. Oelker, A. Staron & J. Ye. "Resolving the gravitational redshift across a millimetre-scale atomic sample". *Nature* **602,** 420–424 (February 2022).

85. X. Zheng, J. Dolde, V. Lochab, B. N. Merriman, H. Li & S. Kolkowitz. "Differential clock comparisons with a multiplexed optical lattice clock". *Nature* **602,** 425–430 (February 2022).

86. C.-C. Chen, R. González Escudero, J. Minář, B. Pasquiou, S. Bennetts & F. Schreck. "Continuous Bose–Einstein condensation". *Nature* **606,** 683–687 (June 2022).

87. S. Stellmer, R. Grimm & F. Schreck. "Production of quantum-degenerate strontium gases". *Phys. Rev. A* **87,** 013611 (January 2013).

88. G. Ferrari, N. Poli, F. Sorrentino & G. M. Tino. "Long-Lived Bloch Oscillations with Bosonic Sr Atoms and Application to Gravity Measurement at the Micrometer Scale". *Phys. Rev. Lett.* **97,** 060402 (August 2006).

89. N. Poli, F.-Y. Wang, M. G. Tarallo, A. Alberti, M. Prevedelli & G. M. Tino. "Precision Measurement of Gravity with Cold Atoms in an Optical Lattice and Comparison with a Classical Gravimeter". *Phys. Rev. Lett.* **106,** 038501 (January 2011).

90. V. Xu, M. Jaffe, C. D. Panda, S. L. Kristensen, L. W. Clark & H. Müller. "Probing gravity by holding atoms for 20 seconds". *Science* **366,** 745–749 (November 2019).

91. C. D. Panda, M. Tao, J. Egelhoff, M. Ceja, V. Xu & H. Müller. "Quantum metrology by one-minute interrogation of a coherent atomic spatial superposition". *arXiv:2210.07289* (October 2022).

92. T. Kuwamoto, K. Honda, Y. Takahashi & T. Yabuzaki. "Magneto-optical trapping of Yb atoms using an intercombination transition". *Phys. Rev. A* **60,** R745–R748 (August 1999).

93. H. L. Xu, A. Persson, S. Svanberg, K. Blagoev, G. Malcheva, V. Pentchev, E. Biémont, J. Campos, M. Ortiz & R. Mayo. "Radiative lifetime and transition probabilities in Cd *I* and Cd *II*". *Phys. Rev. A* **70,** 042508 (October 2004).

94. F. W. Byron, M. N. McDermott & R. Novick. "Self-Broadening of Optical Double Resonance Lines in Cadmium". *Phys. Rev.* **134,** A615–A624 (May 1964).

95. R. H. Garstang. "Hyperfine Structure and Intercombination Line Intensities in the Spectra of Magnesium, Zinc, Cadmium, and Mercury". *J. Opt. Soc. Am.* **52,** 845–851 (August 1962).

96. W. M. Itano, L. L. Lewis & D. J. Wineland. "Shift of $^2\mathrm{S}_{\frac{1}{2}}$ hyperfine splittings due to blackbody radiation". *Phys. Rev. A* **25,** 1233–1235 (February 1982).

97. T. Bothwell, D. Kedar, E. Oelker, J. M. Robinson, S. L. Bromley, W. L. Tew, J. Ye & C. J. Kennedy. "JILA SrI optical lattice clock with uncertainty of 2.0×10^{-18}". *Metrologia* **56,** 065004 (October 2019).

98. I. Ushijima, M. Takamoto, M. Das, T. Ohkubo & H. Katori. "Cryogenic optical lattice clocks". *Nature Photonics* **9,** 185–189 (March 2015).

99. K.-A. Brickman, M.-S. Chang, M. Acton, A. Chew, D. Matsukevich, P. C. Haljan, V. S. Bagnato & C. Monroe. "Magneto-optical trapping of cadmium". *Phys. Rev. A* **76,** 043411 (October 2007).

100. B. Ohayon, S. Hofsäss, J. E. Padilla-Castillo, S. C. Wright, G. Meijer, S. Truppe, K. Gibble & B. K. Sahoo. "Isotope shifts in cadmium as a sensitive probe for physics beyond the standard model". *New Journal of Physics* **24,** 123040 (December 2022).

101. J. S. Schelfhout & J. J. McFerran. "Multiconfiguration Dirac-Hartree-Fock calculations for Hg and Cd with estimates for unknown clock-transition frequencies". *Phys. Rev. A* **105,** 022805 (February 2022).

102. K. Kotru, D. L. Butts, J. M. Kinast & R. E. Stoner. "Large-Area Atom Interferometry with Frequency-Swept Raman Adiabatic Passage". *Phys. Rev. Lett.* **115,** 103001 (August 2015).

103. H. Müller, S.-w. Chiow, Q. Long, S. Herrmann & S. Chu. "Atom Interferometry with up to 24-Photon-Momentum-Transfer Beam Splitters". *Phys. Rev. Lett.* **100,** 180405 (May 2008).

104. S. S. Szigeti, J. E. Debs, J. J. Hope, N. P. Robins & J. D. Close. "Why momentum width matters for atom interferometry with Bragg pulses". *New Journal of Physics* **14,** 023009 (February 2012).

105. A. E. Siegman. *Lasers* (University Science Books, 1986).

106. R. Nourshargh, S. Lellouch, S. Hedges, M. Langlois, K. Bongs & M. Holynski. "Circulating pulse cavity enhancement as a method for extreme momentum transfer atom interferometry". *Communications Physics* **4,** 257 (December 2021).

107. P. Touboul *et al.* "*MICROSCOPE* Mission: Final Results of the Test of the Equivalence Principle". *Phys. Rev. Lett.* **129,** 121102 (September 2022).

108. F. Hofmann & J. Müller. "Relativistic tests with lunar laser ranging". *Classical and Quantum Gravity* **35,** 035015 (January 2018).

109. S. Fray, C. A. Diez, T. W. Hänsch & M. Weitz. "Atomic Interferometer with Amplitude Gratings of Light and Its Applications to Atom Based Tests of the Equivalence Principle". *Phys. Rev. Lett.* **93,** 240404 (December 2004).

110. L. Zhou, S. Long, B. Tang, X. Chen, F. Gao, W. Peng, W. Duan, J. Zhong, Z. Xiong, J. Wang, Y. Zhang & M. Zhan. "Test of Equivalence Principle at 10^{-8} Level by a Dual-Species Double-Diffraction Raman Atom Interferometer". *Phys. Rev. Lett.* **115,** 013004 (July 2015).

111. P. Asenbaum, C. Overstreet, M. Kim, J. Curti & M. A. Kasevich. "Atom-Interferometric Test of the Equivalence Principle at the 10^{-12} Level". *Phys. Rev. Lett.* **125,** 191101 (November 2020).

112. L. Zhou, C. He, S.-T. Yan, X. Chen, D.-F. Gao, W.-T. Duan, Y.-H. Ji, R.-D. Xu, B. Tang, C. Zhou, S. Barthwal, Q. Wang, Z. Hou, Z.-Y. Xiong, Y.-Z. Zhang, M. Liu, W.-T. Ni, J. Wang & M.-S. Zhan. "Joint mass-and-energy test of the equivalence principle at the 10^{-10} level using atoms with specified mass and internal energy". *Phys. Rev. A* **104,** 022822 (August 2021).

113. D. Schlippert, J. Hartwig, H. Albers, L. L. Richardson, C. Schubert, A. Roura, W. P. Schleich, W. Ertmer & E. M. Rasel. "Quantum Test of the Universality of Free Fall". *Phys. Rev. Lett.* **112,** 203002 (May 2014).

114. J. Hartwig, S. Abend, C. Schubert, D. Schlippert, H. Ahlers, K. Posso-Trujillo, N. Gaaloul, W. Ertmer & E. M. Rasel. "Testing the universality of free fall with rubidium and ytterbium in a very large baseline atom interferometer". *New Journal of Physics* **17,** 035011 (March 2015).

115. K. Zhang, M.-K. Zhou, Y. Cheng, L.-L. Chen, Q. Luo, W.-J. Xu, L.-S. Cao, X.-C. Duan & Z.-K. Hu. "Testing the Universality of Free Fall by Comparing the Atoms in Different Hyperfine States with Bragg Diffraction". *Chinese Physics Letters* **37,** 043701 (April 2020).

116. X.-C. Duan, X.-B. Deng, M.-K. Zhou, K. Zhang, W.-J. Xu, F. Xiong, Y.-Y. Xu, C.-G. Shao, J. Luo & Z.-K. Hu. "Test of the Universality of Free Fall with Atoms in Different Spin Orientations". *Phys. Rev. Lett.* **117,** 023001 (July 2016).

117. G. Rosi, G. D'Amico, L. Cacciapuoti, F. Sorrentino, M. Prevedelli, M. Zych, Č. Brukner & G. M. Tino. "Quantum test of the equivalence principle for atoms in coherent superposition of internal energy states". *Nature Communications* **8,** 15529 (June 2017).

118. M. G. Tarallo, T. Mazzoni, N. Poli, D. V. Sutyrin, X. Zhang & G. M. Tino. "Test of Einstein Equivalence Principle for 0-Spin and Half-Integer-Spin Atoms: Search for Spin-Gravity Coupling Effects". *Phys. Rev. Lett.* **113,** 023005 (July 2014).

119. G. Varoquaux, R. A. Nyman, R. Geiger, P. Cheinet, A. Landragin & P. Bouyer. "How to estimate the differential acceleration in a two-species atom interferometer to test the equivalence principle". *New Journal of Physics* **11,** 113010 (November 2009).

120. C. W. Chou, D. B. Hume, T. Rosenband & D. J. Wineland. "Optical Clocks and Relativity". *Science* **329,** 1630–1633 (September 2010).

121. J. Grotti *et al.* "Geodesy and metrology with a transportable optical clock". *Nature Physics* **14,** 437–441 (February 2018).

122. M. Takamoto, I. Ushijima, N. Ohmae, T. Yahagi, K. Kokado, H. Shinkai & H. Katori. "Test of general relativity by a pair of transportable optical lattice clocks". *Nature Photonics* **14,** 411–415 (April 2020).

123. S. Khandelwal, M. P. Lock & M. P. Woods. "Universal quantum modifications to general relativistic time dilation in delocalised clocks". *Quantum* **4,** 309 (August 2020).

124. I. Pikovski, M. Zych, F. Costa & Č. Brukner. "Universal decoherence due to gravitational time dilation". *Nature Physics* **11,** 668–672 (August 2015).

125. M. Carlesso & A. Bassi. "Decoherence due to gravitational time dilation: Analysis of competing decoherence effects". *Physics Letters A* **380,** 2354–2358 (July 2016).

126. K. E. Khosla & N. Altamirano. "Detecting gravitational decoherence with clocks: Limits on temporal resolution from a classical-channel model of gravity". *Phys. Rev. A* **95,** 052116 (May 2017).

127. A. Roura. "Gravitational Redshift in Quantum-Clock Interferometry". *Phys. Rev. X* **10,** 021014 (April 2020).

128. H. Verma, M. Zych & F. Costa. "Effect of environment on the interferometry of clocks". *Quantum* **5,** 525 (August 2021).

129. N. Bohr. "The Quantum Postulate and the Recent Development of Atomic Theory". *Nature* **121,** 580 (April 1928).

130. A. J. Paige, A. D. K. Plato & M. S. Kim. "Classical and Nonclassical Time Dilation for Quantum Clocks". *Phys. Rev. Lett.* **124,** 160602 (April 2020).

131. A. R. H. Smith & M. Ahmadi. "Quantum clocks observe classical and quantum time dilation". *Nature Communications* **11,** 5360 (October 2020).

132. P. T. Grochowski, A. R. H. Smith, A. Dragan & K. Debski. "Quantum time dilation in atomic spectra". *Phys. Rev. Research* **3,** 023053 (April 2021).

133. O. Carraz, F. Lienhart, R. Charrière, M. Cadoret, N. Zahzam, Y. Bidel & A. Bresson. "Compact and robust laser system for onboard atom interferometry". *Applied Physics B* **97,** 1432–0649 (August 2009).

134. M. Barbiero, M. G. Tarallo, D. Calonico, F. Levi, G. Lamporesi & G. Ferrari. "Sideband-Enhanced Cold Atomic Source for Optical Clocks". *Phys. Rev. Applied* **13,** 014013 (January 2020).

135. M. Guina, A. Rantamäki & A. Härkönen. "Optically pumped VECSELs: review of technology and progress". *Journal of Physics D: Applied Physics* **50,** 383001 (August 2017).

136. S. C. Burd, D. T. C. Allcock, T. Leinonen, J. P. Penttinen, D. H. Slichter, R. Srinivas, A. C. Wilson, R. Jördens, M. Guina, D. Leibfried & D. J. Wineland. "VECSEL systems for the generation and manipulation of trapped magnesium ions". *Optica* **3,** 1294–1299 (December 2016).

137. P. H. Moriya, Y. Singh, K. Bongs & J. E. Hastie. "Sub-kHz-linewidth VECSELs for cold atom experiments". *Opt. Express* **28,** 15943–15953 (May 2020).

138. S. C. Burd, J.-P. Penttinen, P.-Y. Hou, H. M. Knaack, S. Ranta, M. Mäki, E. Kantola, M. Guina, D. H. Slichter, D. Leibfried & A. C. Wilson. "VECSEL systems for quantum information processing with trapped beryllium ions". *arXiv:2003.09060* (2020).

139. M. G. Tarallo. *Development of a Strontium optical lattice clock.* PhD thesis (Università degli Studi di Firenze, 2009).

140. G. D. Domenico, S. Schilt & P. Thomann. "Simple approach to the relation between laser frequency noise and laser line shape". *Appl. Opt.* **49,** 4801–4807 (September 2010).

141. M. Pizzocaro, D. Calonico, P. C. Pastor, J. Catani, G. A. Costanzo, F. Levi & L. Lorini. "Efficient frequency doubling at 399 nm". *Appl. Opt.* **53,** 3388–3392 (June 2014).

142. G. D. Boyd & D. A. Kleinman. "Parametric Interaction of Focused Gaussian Light Beams". *Journal of Applied Physics* **39,** 3597–3639 (July 1968).

143. T. Freegarde, J. Coutts, J. Walz, D. Leibfried & T. W. Hänsch. "General analysis of type I second-harmonic generation with elliptical Gaussian beams". *J. Opt. Soc. Am. B* **14,** 2010–2016 (August 1997).

144. T. Rossetti. *Realizzazione di una sorgente laser visibile tramite duplicazione in frequenza in cavità ottica risonante.* Diploma thesis (Università degli Studi di Firenze, 2020).

145. B. Boulanger, I. Rousseau, J. Feve, M. Maglione, B. Menaert & G. Marnier. "Optical studies of laser-induced gray-tracking in KTP". *IEEE Journal of Quantum Electronics* **35,** 281–286 (March 1999).

146. T. Hansch & B. Couillaud. "Laser frequency stabilization by polarization spectroscopy of a reflecting reference cavity". *Optics Communications* **35,** 441–444 (December 1980).

147. Z. Burkley, L. de Sousa Borges, B. Ohayon, A. Golovizin, J. Zhang & P. Crivelli. "Stable high power deep-uv enhancement cavity in ultra-high vacuum with fluoride coatings". *Opt. Express* **29,** 27450–27459 (August 2021).

148. D. Preißler, D. Kiefer, T. Führer & T. Walther. "Evolutionary algorithm-assisted design of a UV SHG cavity with elliptical focusing to avoid crystal degradation". *Applied Physics B* **125,** 220 (November 2019).

149. K. Takachiho, M. Yoshimura, Y. Takahashi, M. Imade, T. Sasaki & Y. Mori. "Ultraviolet laser-induced degradation of $CsLiB_6O_{10}$ and β-BaB_2O_4". *Opt. Mater. Express* **4,** 559–567 (March 2014).

150. J. C. Shaw, S. Hannig & D. J. McCarron. "Stable 2 W continuous-wave 261.5 nm laser for cooling and trapping aluminum monochloride". *Opt. Express* **29,** 37140–37149 (November 2021).

151. S. Hannig, J. Mielke, J. A. Fenske, M. Misera, N. Beev, C. Ospelkaus & P. O. Schmidt. "A highly stable monolithic enhancement cavity for second harmonic generation in the ultraviolet". *Review of Scientific Instruments* **89,** 013106 (January 2018).

152. J.-I. Kim & D. Meschede. "Continuous-wave coherent ultraviolet source at 326 nm based on frequency trippling of fiber amplifiers". *Opt. Express* **16,** 10803–10808 (July 2008).

153. Y. Wang, K. Wang, E. F. Fenton, Y.-W. Lin, K.-K. Ni & J. D. Hood. "Reduction of laser intensity noise over 1 MHz band for single atom trapping". *Opt. Express* **28,** 31209–31215 (October 2020).

154. R. Drever, J. Hall, F. Kowalski, J. Hough, G. Ford, A. Munley & H. Ward. "Laser Phase and Frequency Stabilization Using an Optical Resonator". *Appl. Phys. B* **31,** 97–105 (June 1983).

155. E. S. Polzik & H. J. Kimble. "Frequency doubling with $KNbO_3$ in an external cavity". *Opt. Lett.* **16,** 1400–1402 (September 1991).

156. M. Chiarotti. *Sviluppo di una sorgente laser UV in continua per spettroscopia di alta precisione della transizione di orologio del cadmio a 332 nm.* Master's thesis (Università degli Studi di Firenze, 2021).

157. M. G. Tarallo, N. Poli, M. Schioppo, D. Sutyrin & G. M. Tino. "A high-stability semiconductor laser system for a ^{88}Sr-based optical lattice clock". *Applied Physics B: Lasers & Optics* **103,** 17–25 (April 2011).

158. *Matisse User's Guide.* Version 2.2. Sirah Lasertechnik (2015).

159. M. Schioppo, N. Poli, M. Prevedelli, S. Falke, C. Lisdat, U. Sterr & G. M. Tino. "A compact and efficient strontium oven for laser-cooling experiments". *Review of Scientific Instruments* **83,** 103101 (October 2012).

160. N. Grani. *Studio di un sistema di rallentamento e intrappolamento laser di atomi di cadmio ad alta efficienza.* Diploma thesis (Università degli Studi di Firenze, 2019).

161. J. M. Khosrofian & B. A. Garetz. "Measurement of a Gaussian laser beam diameter through the direct inversion of knife-edge data". *Appl. Opt.* **22,** 3406–3410 (November 1983).

162. A. Vignoli. *Caratterizzazione di un fascio atomico di cadmio per spettroscopia di precisione di transizioni nell'UV.* Diploma thesis (Università degli Studi di Firenze, 2020).

163. K. Burns & K. B. Adams. "Energy Levels and Wavelengths of Natural Cadmium and of Cadmium-114". *J. Opt. Soc. Am.* **46,** 94–99 (February 1956).

164. C. E. Moore. *Atomic Energy Levels As Derived From the Analyses of Optical Spectra* (National Standards Reference Data System, 1958).

165. E. R. Peck & K. Reeder. "Dispersion of Air". *J. Opt. Soc. Am.* **62,** 958–962 (August 1972).

166. F. M. Kelly & E. Tomchuk. "Isotope Shift in the CdI Resonance Line λ 2288 Å". *Proceedings of the Physical Society* **78,** 1304–1306 (December 1961).

167. C. Delaunay, R. Ozeri, G. Perez & Y. Soreq. "Probing atomic Higgs-like forces at the precision frontier". *Phys. Rev. D* **96,** 093001 (November 2017).

168. J. C. Berengut, D. Budker, C. Delaunay, V. V. Flambaum, C. Frugiuele, E. Fuchs, C. Grojean, R. Harnik, R. Ozeri, G. Perez & Y. Soreq. "Probing New Long-Range Interactions by Isotope Shift Spectroscopy". *Phys. Rev. Lett.* **120,** 091801 (February 2018).

169. I. Counts, J. Hur, D. P. L. Aude Craik, H. Jeon, C. Leung, J. C. Berengut, A. Geddes, A. Kawasaki, W. Jhe & V. Vuleti ć. "Evidence for Nonlinear Isotope Shift in Yb^+ Search for New Boson". *Phys. Rev. Lett.* **125,** 123002 (September 2020).

170. H. Miyake, N. C. Pisenti, P. K. Elgee, A. Sitaram & G. K. Campbell. "Isotope-shift spectroscopy of the $^1S_0 \rightarrow^3 P_1$ and $^1S_0 \rightarrow^3 P_0$ transitions in strontium". *Phys. Rev. Research* **1,** 033113 (November 2019).

171. S. Hofsäss, J. E. Padilla-Castillo, S. C. Wright, S. Kray, R. Thomas, B. G. Sartakov, B. Ohayon, G. Meijer & S. Truppe. "High-resolution isotope-shift spectroscopy of Cd I". *Phys. Rev. Res.* **5,** 013043 (January 2023).

172. P. Masłowski, K. Bielska, A. Cygan, D. J., D. Lisak, R. Ciuryło, A. Bielski & R. S. Trawiński. "The hyperfine and isotope structure of the Cd intercombination line – revisited". *Eur. Phys. J. D* **51,** 295–302 (March 2009).

173. E. Staub. *Developing a High-Flux Atomic Beam Source for Experiments with Ultracold Strontium Quantum Gases*. Master's thesis (Ludwig-Maximilians-Universität München, 2019).

174. F. Schreck & K. v. Druten. "Laser cooling for quantum gases". *Nature Physics* **17,** 1296–1304 (December 2021).

175. S. Bennetts, C.-C. Chen, B. Pasquiou & F. Schreck. "Steady-State Magneto-Optical Trap with 100-Fold Improved Phase-Space Density". *Phys. Rev. Lett.* **119,** 223202 (December 2017).

176. C.-C. Chen, S. Bennetts, R. G. Escudero, B. Pasquiou & F. Schreck. "Continuous Guided Strontium Beam with High Phase-Space Density". *Phys. Rev. Applied* **12,** 044014 (October 2019).

177. D. Gangloff, M. Shi, T. Wu, A. Bylinskii, B. Braverman, M. Gutierrez, R. Nichols, J. Li, K. Aichholz, M. Cetina, L. Karpa, B. Jelenković, I. Chuang & V. Vuletić. "Preventing and reversing vacuum-induced optical losses in high-finesse tantalum (V) oxide mirror coatings". *Opt. Express* **23,** 18014–18028 (July 2015).

178. Z. Hubka, J. Novák, I. Majerová, J. T. Green, P. K. Velpula, R. Boge, R. Antipenkov, V. Šobr, D. Kramer, K. Majer, J. A. Naylon, P. Bakule & B. Rus. "Mitigation of laser-induced contamination in vacuum in high-repetition-rate high-peak-power laser systems". *Appl. Opt.* **60,** 533–538 (January 2021).

179. F. Gebert, M. H. Frosz, T. Weiss, Y. Wan, A. Ermolov, N. Y. Joly, P. O. Schmidt & P. S. J. Russell. "Damage-free single-mode transmission of deep-UV light in hollow-core PCF". *Opt. Express* **22,** 15388–15396 (June 2014).

180. C. D. Marciniak, H. B. Ball, A. T.-H. Hung & M. J. Biercuk. "Towards fully commercial, UV-compatible fiber patch cords". *Opt. Express* **25,** 15643–15661 (July 2017).

181. A. C. Wilson, C. Ospelkaus, A. P. VanDevender, J. A. Mlynek, K. R. Brown, D. Leibfried & D. J. Wineland. "A 750-mW, continuous-wave, solid-state laser source at 313 nm for cooling and manipulating trapped ^{9}Be$^+$ ions". *Applied Physics B* **105,** 741–748 (December 2011).

182. A. Guttridge, S. A. Hopkins, S. L. Kemp, D. Boddy, R. Freytag, M. P. A. Jones, M. R. Tarbutt, E. A. Hinds & S. L. Cornish. "Direct loading of a large Yb MOT on the ^{1}S$_0$ $\rightarrow$^{3}P$_1$ transition". *Journal of Physics B: Atomic, Molecular and Optical Physics* **49,** 145006 (June 2016).

183. M. Büki, D. Röser & S. Stellmer. "Frequency-quintupled laser at 308nm for atomic physics applications". *Appl. Opt.* **60,** 9915–9918 (November 2021).

184. W. Wohlleben, F. Chevy, K. Madison & J. Dalibard. "An atom faucet". *The European Physical Journal D - Atomic, Molecular, Optical and Plasma Physics* **15,** 237–244 (August 2001).

185. S. Chaudhuri, S. Roy & C. S. Unnikrishnan. "Realization of an intense cold Rb atomic beam based on a two-dimensional magneto-optical trap: Experiments and comparison with simulations". *Phys. Rev. A* **74,** 023406 (August 2006).

186. M. Vangeleyn, P. F. Griffin, E. Riis & A. S. Arnold. "Single-laser, one beam, tetrahedral magneto-optical trap". *Opt. Express* **17,** 13601–13608 (August 2009).

187. F. Gao, H. Liu, P. Xu, X. Tian, Y. Wang, J. Ren, H. Wu & H. Chang. "Precision measurement of transverse velocity distribution of a strontium atomic beam". *AIP Advances* **4,** 027118 (February 2014).

188. G. Lamporesi, S. Donadello, S. Serafini & G. Ferrari. "Compact high-flux source of cold sodium atoms". *Review of Scientific Instruments* **84,** 063102 (June 2013).

189. S. Bennetts. *1000 times closer to a continuous atom laser: Steady-state strontium with unity phase-space density*. PhD thesis (Universiteit van Amsterdam, 2019).

190. D. B. Ali, T. Badr, T. Brézillon, R. Dubessy, H. Perrin & A. Perrin. "Detailed study of a transverse field Zeeman slower". *Journal of Physics B: Atomic, Molecular and Optical Physics* **50,** 055008 (February 2017).

191. Y. B. Ovchinnikov. "A Zeeman slower based on magnetic dipoles". *Optics Communications* **276,** 261–267 (August 2007).

192. P. Cheiney, O. Carraz, D. Bartoszek-Bober, S. Faure, F. Vermersch, C. M. Fabre, G. L. Gattobigio, T. Lahaye, D. Guéry-Odelin & R. Mathevet. "A Zeeman slower design with permanent magnets in a Halbach configuration". *Review of Scientific Instruments* **82,** 063115 (June 2011).

193. E. Wodey, R. J. Rengelink, C. Meiners, E. M. Rasel & D. Schlippert. "A robust, high-flux source of laser-cooled ytterbium atoms". *Journal of Physics B: Atomic, Molecular and Optical Physics* **54,** 035301 (February 2021).

194. I. R. Hill, Y. B. Ovchinnikov, E. M. Bridge, E. A. Curtis & P. Gill. "Zeeman slowers for strontium based on permanent magnets". *Journal of Physics B: Atomic, Molecular and Optical Physics* **47,** 075006 (March 2014).

195. W. Lunden, L. Du, M. Cantara, P. Barral, A. O. Jamison & W. Ketterle. "Enhancing the capture velocity of a Dy magneto-optical trap with two-stage slowing". *Phys. Rev. A* **101,** 063403 (June 2020).

196. B. Seo, P. Chen, Z. Chen, W. Yuan, M. Huang, S. Du & G.-B. Jo. "Efficient production of a narrow-line erbium magneto-optical trap with two-stage slowing". *Phys. Rev. A* **102,** 013319 (July 2020).

197. B. Plotkin-Swing, A. Wirth, D. Gochnauer, T. Rahman, K. E. McAlpine & S. Gupta. "Crossed-beam slowing to enhance narrow-line ytterbium magneto-optic traps". *Review of Scientific Instruments* **91,** 093201 (September 2020).

198. M. D. Barrett, J. A. Sauer & M. S. Chapman. "All-Optical Formation of an Atomic Bose-Einstein Condensate". *Phys. Rev. Lett.* **87,** 010404 (June 2001).

199. S. Piatchenkov. *A versatile ultracold strontium apparatus: from construction to new tools for quantum simulation*. PhD thesis (Universiteit van Amsterdam, 2020).

200. N. Poli, M. Schioppo, S. Vogt, S. Falke, U. Sterr, C. Lisdat & G. M. Tino. "A transportable strontium optical lattice clock". *Applied Physics B* **117,** 1107–1116 (December 2104).

201. H. Katori, T. Ido, Y. Isoya & M. Kuwata-Gonokami. "Magneto-Optical Trapping and Cooling of Strontium Atoms down to the Photon Recoil Temperature". *Phys. Rev. Lett.* **82,** 1116–1119 (February 1999).

202. G. Verma, E. Wang, J. Assendelft, N. Poli, G. Rosi, G. M. Tino & L. Salvi. "A scalable laser system at 461 nm for laser cooling and trapping of Sr atoms". *Applied Physics B* **128,** 1432–0649 (May 2022).

203. J. H. Lee, H. Jung, J.-y. Choi & J. Mun. "Transporting cold atoms using an optically compensated zoom lens". *Phys. Rev. A* **102,** 063106 (December 2020).

204. T. L. Gustavson, A. P. Chikkatur, A. E. Leanhardt, A. Görlitz, S. Gupta, D. E. Pritchard & W. Ketterle. "Transport of Bose-Einstein Condensates with Optical Tweezers". *Phys. Rev. Lett.* **88,** 020401 (December 2001).

205. A. Sugarbaker. *Atom Interferometry in a 10 m Fountain*. PhD thesis (Stanford University, 2014).

206. J. Hogan. *Towards precision tests of general relativity using an atom interferometer*. PhD thesis (Stanford University, 2010).

207. T. Kovachy, J. M. Hogan, D. M. S. Johnson & M. A. Kasevich. "Optical lattices as waveguides and beam splitters for atom interferometry: An analytical treatment and proposal of applications". *Phys. Rev. A* **82,** 013638 (July 2010).